Molecular-Modified Materials for Solar Fuels Generation

by

Nghi Do Phuong Nguyen

A Dissertation Presented in Partial Fulfillment
of the Requirements for the Degree
Doctor of Philosophy

Approved July 2023 by the
Graduate Supervisory Committee:

Gary F. Moore, Chair
Dong-Kyun Seo
Scott G. Sayres

ARIZONA STATE UNIVERSITY

August 2023

ABSTRACT

Surface modification of (semi)conducting materials with polymers provides a strategy for interfacing electrodes with electrocatalysts for reactions of industrial importance. The resulting constructs create opportunities to capture, convert and store solar energy in the form of chemical bonds, generating solar fuels. This thesis describes III-V semiconductors, modified with molecular catalysts embedded in thin-film polymeric coatings. Overarching goals of this work include building protein-like, soft-material environments on solid-state electrode surfaces. This approach enables coordination of earth-abundant metal centers within the three-dimensional molecular coatings to modulate the electronic and catalytic properties of the overall assembly and provide assemblies for studying the effects of polymeric-encapsulation on electrocatalytic as well as photoelectrosynthetic performance. In summary, this work provides 1) new approaches to designing, interfacing, and characterizing (semi)conducting and catalytic materials to effectively power chemical transformations (including hydrogen evolution and carbon dioxide reduction), and 2) kinetic models for better understanding the structure-function relationships governing the performance of these assemblies.

DEDICATION

for my family
to my Mother, for her love and unwavering support
and to Ryan, who understands the significance of this journey

"New things turn up all the time. How can we be so fortunate to work in a business like this? It has been and continues to be a very exciting life and I feel so deeply privileged to have been able to share it with so many fine, intelligent, and unbelievably enjoyable colleagues both in this country and around the world. To all of you, only a few of whom I have found ways to mention here, I say a heartfelt "Thank you!" and "Let there be more"."

C. Austen Angell

ACKNOWLEDGMENTS

Professor Gary F. Moore's mentorship, encouragement, and support have been invaluable throughout the completion of this work. I am forever grateful for the countless opportunities he has given me and for the love of (photo)electrochemistry.

I would like to thank my PhD committee member Professor Dong-Kyun Seo and Professor Scott Sayres for providing feedback and encouragement along the way. I have greatly enjoyed Professor Dong-Kyun Seo's class on Material Characterization Methods and it has provided me with much knowledge throughout my research. I would never forget how Prof. Scott Sayres has been incredibly helpful and patient when I was a first-time TA for Physical Chemistry lab.

This journey could not have been possible without Dr. Brian L. Wadsworth. He taught me pretty much all I know about surface modification and electrochemistry. He inspired me with his sharp mind and kind heart. There is no word that can describe how thankful I am to have his mentorship and friendship.

I want to thank Dr. Diana Khusnutdinova for her encouragement and helpful advice since when I first started in the lab until now when I am about to finish my PhD journey. Her constant support has been tremendously important to my research and career.

Completion of this work would not be possible without my labmates. Edgar A. Reyes Cruz has been a mentor and a friend, giving solid advice and listening to all my problems all throughout five years. No one works harder and is as caring as Daiki Nishiori. He is such a blessing to this world. I can't say enough how much I appreciate my friendship with Lillian K. Hensleigh. Our conversations (while sweeping the lab) have brought me much knowledge and joy.

I want to thank Prof. Timothy C. Steimle for believing in me and giving me the opportunity to pursue my PhD at Arizona State University. A special thank you is extended to Dr. Anh T. Le for her support in my years at ASU.

I also want to thank the staff at Arizona State University, especially Dr. Tim Karcher, Dr. Xin Guo, Dr. Diana Convey, Dr. Gwyneth Gordon, Mary Zhu and David Nutt.

The financial support from the National Science Foundation (Early Career Award 1653982), United States Department of Energy (Office of Science, Early Career Award DE-SC0021186), School of Molecular Sciences, ASU Graduate College, the ASU Graduate and Profession Student Association (GPSA), and the Innovation Award (Prof. Professor William Glaunsinger and Lorna Glaunsinger) is gratefully acknowledged.

My mother, Thuy Thi Nguyen, has been incredibly loving, understanding, encouraging and patient with me. I am lucky to be her daughter and I cannot ask for a more perfect role model. Her love for education and her humanity have guided me throughout all my life.

Ryan D. Miller, my partner, has been my fierce advocate and strongest supporter throughout graduate school. He has given me unconditional love in all of my successes and failures. He keeps me sane and safe.

TABLE OF CONTENTS

Page

LIST OF TABLES x

LIST OF FIGURES xiii

LIST OF ABBREVIATION.. xxxvii

CHAPTER

1 INTRODUCTION 1

1.1 Solar Fuels Generation...2

1.2 PV-electrolysis versus Photoelectrochemical Systems 4

1.3 Artitificial Photosynthesis and Photoelectrosynthetic Cells 6

1.4 Molecular-Modified Electrodes for Electrocatalysis and Photoelectrosynthesis..15

1.5 Efficiencies of Photochemical Systems 17

1.6 Outlook and Conclusion 22

1.7 References..23

2 UNDERSTANDING AND CONTROLLING THE PERFORMANCE-LIMITING STEPS OF CATALYSTS-MODIFIED SEMICONDUCTORS 29

2.1 Introduction.. 30

2.1.1 Homogeneous and Heterogeneous Hydrogen Evolution Reaction Using Cobaloxime-type Catalyst 30

2.1.2 Cobaloxime-catalysts Immobilization on III-V Semiconductors..... 32

CHAPTER Page

2.2. Results and Discussion 34

2.2.1 Materials Preparation 34

2.2.2 Surface Characterization of Cobaloxime-polypyridyl GaAs 37

2.2.3 Photoelectrochemical Measurements and Mechanisms for Hydrogen Evolution Reaction at Molecular-Modified Photoelectrode 46

2.2.4 Quantum Efficiencies 57

2.2.5 Product Detection 61

2.2.6 Determination of Per Cobalt Hydrogen Evolution Reaction Activities 62

2.3 Conclusion 66

2.4 References 67

3 DEGRADE – REPAIR CYCLE OF A FUEL-FORMING PHOTOELECTRODE 74

3.1 Introduction 75

3.2 Results and Discussion 78

3.2.1 Materials and Electrode Preparation 78

3.2.2 Workflow and Processes used for Surface Characterization 82

3.2.3 Analysis of Catalyst Degradation and Regeneration on Co|PPy|GaP Surfaces via GATR-FTIR, XP Spectroscopy, and Ellipsometry. 85

3.2.4 Photoelectrochemical Performance 93

3.2.5 Product Detection via Gas Chromatography 97

3.2.6 Structural Characterization for Degradation and Repair Mechanism 100

3.3 Conclusions.................... 109

3.4 References.................... 111

4 ADDRESSING THE ORIGIN OF PHOTOCURRENTS AND FUEL PRODUCTION ACTIVITIES IN CATALYST-MODIFIED SEMICONDUCTOR ELECTRODES 116

4.1 Introduction.................... 117

4.1.1 Cobalt Porphyrin-modified Photocathode for Hydrogen Evolution Reaction 117

4.1.2 Photoelectrosynthesis vs. Screening vs. Dye-Sensitized Hole Injection 119

4.2 Results and Discussion 123

4.2.1 Material Preparation....................123

4.2.2 Optical Characterization of Cobalt Porphyrin-modified-GaP 125

4.2.3 Photoelectrochemical Characterization....................128

4.2.4 Comparisons between Heterogeneous-Homogeneous Semiconductor Electrodes and Homogeneous Solutions Containing the Molecular Electrocatalyst.....................135

4.2.5 Apparent Dye-Sensitization Efficiencies....................143

4.3 Conclusion 149

4.4 References....................150

CHAPTER Page

5 EXPERIMENTAL METHODS 160
    5.1 Experimental Methods for Chapter 2 161
        5.1.1 Experimental Methods 161
        5.1.2 X-ray Photoelectron Spectroscopy Data 166
        5.1.3 Photoelectrochemical Data 172
        5.1.4 References 173
    5.2 Experimental Methods for Chapter 3 174
        5.2.1 Experimental Methods 174
        5.2.2 Fourier Transform Infrared Spectroscopy Data 177
        5.2.3 X-ray Photoelectron Spectroscopy Data 178
        5.2.4 Photoelectrochemical Data 186
        5.2.5 References 188
    5.3 Experimental Methods for Chapter 4 189
        5.3.1 Experimental Methods 189
        5.3.2 Electrochemical Data 192
        5.3.3 References 194
COMPLETE BIBLIOGRAPHY 196

APPENDIX

A. ACKNOWLEDGEMENTS FOR PERMISSION TO REPRODUCE PORTIONS OF CHAPTER 1 FROM JOULE 213
B. ACKNOWLEDGEMENTS FOR PERMISSION TO REPRODUCE PORTIONS OF CHAPTER 1 FROM ACS CHEMICAL REVIEWS 215

APPENDIX Page

C. ACKNOWLEDGEMENTS FOR PERMISSION TO REPRODUCE PORTIONS OF CHAPTER 2 FROM ACS C JOURNAL OF PHYSICAL CHEMISTRY LETTERS 217
D. ACKNOWLEDGEMENTS FOR PERMISSION TO REPRODUCE PORTIONS OF CHAPTER 3 FROM ACS APPLIED ENERGY MATERIAL 219
E. ACKNOWLEDGEMENTS FOR PERMISSION TO REPRODUCE PORTIONS OF CHAPTER 4 FROM ACS APPLIED ENERGY MATERIALS 221

LIST OF TABLES

Table Page

2.1. Total Cobalt Surface Loadings Determined Using ICP-MS............................. 39

2.2. Ratios of Absorbance Between NO^- Stretch Feature at 1235 cm^{-1} and Features at 1600 cm^{-1} or 1419 cm^{-1} Associated With The Polymer. In Order To Exclude Discrepancies in Intensities Arising from Sample-To-Sample Variations in The Degree of Contact With The ATR Crystal, We Compared The Ratios Of Absorption Bands Centered at 1600 cm^{-1} and at 1419 cm^{-1}, Assigned to C=N and C-N Vibrational Modes of The Polymer Graft, to Peaks Assigned to The NO^- Mode of The Intact Catalysts. We Then Used These Ratios to Obtain The Fraction of Catalyst Species Present in The Polymer and Information on The Overall Surface Composition. These Results Are Summarized in Table 2.2 and Indicate A Decrease in The Amount of Cobaloximes Remaining in The Film Following PEC Testing. We Estimate ~ 40% of The Cobaloximes Detach From The Polymeric Coating Following Our Photoelectrochemical Studies. These Results Are Consistent With More Detailed Reports On This Topic From Our Research Group Indicating That Cobaloximes Loosely Associated With The Polymeric Coating Can Detach During Photoelectrochemical Operation. 45

2.3. Open-Circuit Voltages, Short-Circuit Current Densities, Maximum Power Points, And Fill Factors Extracted From Linear Sweep Voltammetry Data Recorded at A Scan Rate of 100 mV s^{-1} Using PPy|GaAs or Cobaloxime|PPy|GaAs Working Electrodes in 0.1 M Phosphate Buffer (pH 7) Or 0.1 M NaOH (pH 13). All Data Were Recorded Under Simulated 1-Sun Illumination. 50

Table Page

3.1. Percentage of Initial Cobaloximes That Degrade Following Photoelectrochemical Operation (% Degradation), and The Percentage of Initial Cobaloximes Present Following Chemical Repair (% Repair), As Determined Via GATR-FTIR Relative Peak Intensity Analysis..87

3.2. Fraction of Total Pyridyl-Nitrogen Sites Coordinated to Cobaloxime Cobalt Centers As Determined Via Deconvolution of N 1s Core Level XP Spectra.............88

3.3. Fraction of Total Pyridyl-Nitrogen Sites Coordinated to Cobaloxime Cobalt Centers As Determined Via Co:N XP Spectral Intensity Ratios. 90

3.4. Per-Geometric-Area Cobaloxime Loadings 92

3.5. Open-Circuit Voltages, Short-Circuit Current Densities, Maximum Power Points, And Fill Factors Extracted From Linear Sweep Voltammetry Data Recorded At A Scan Rate Of 100 mV s^{-1} Using GaP, PPy|GaP, And Co|PPy|GaP Working Electrodes In 0.1 M Phosphate Buffer (pH 7) Before (Indicated As Initial) and After 15 Minutes Controlled-Potential Electrolysis (Indicated As Post-Degrade), and After Regeneration of Catalyst (Indicated As Post-Repair). All Data Were Recorded Under Simulated 1-Sun Illumination. 95

4.1. Open-Circuit Voltages, Short-Circuit Current Densities, Maximum Power Points, And Fill Factors Recorded Using GaP, PPy|GaP, and Co|PPy|GaP Electrodes in 0.1 M Phosphate Buffer (pH 7) Under Simulated 1-Sun Illumination 130

4.2. Current Densities Associated With PPy|Gap Or CoTTP|PPy|Gap Electrodes Polarized At 0 V Vs RHE in 0.1 M Phosphate Buffer (pH 7) Determined Using Three

Table Page

Different Methods. 134

4.3. Soret And Q-Type Absorption Bands (Δ_{abs}) As Well As Associated Extinction Coefficients (ε) of 5,10,15,20-Tetra-P-Tolylporphyrin Cobalt(II) (CoTTP) in Chloroform Recorded Prior To And Following 26 Hours After The Addition of ~1 Equivalent of Pyridine 137

4.4. Soret and Q-Type Absorption Bands (Δ_{abs}) As Well As Associated Extinction Coefficients (ε) Recorded Using CoP|NanoITO or CoTTP|PVP|NanoITO Electrodes in Propylene Carbonate As Described in Reference 12 of This Chapter. 140

5.1. Open-Circuit Voltages, Short-Circuit Current Densities, Maximum Power Points, And Fill Factors Extracted From Linear Sweep Voltammetry Data Recorded at A Scan Rate Of 100 mV s^{-1} Using GaP, PPy|GaP, and Co|PPy|GaP Working Electrodes in 0.1 M Phosphate Buffer (pH 7) in The Dark. 187

5.2. Midpoint Potentials For The Reduction and Oxidation (${}^{n}E_{1/2}$) Of 5,10,15,20-tetra-p-tolylporphyrin Cobalt(II) (CoTTP) in The Presence of 0 and 2,282 Equivalents of Pyridine As Determined By Cyclic Voltammetry. Peak-To-Peak Separations (Δe_p) Are Reported in Parentheses. For Irreversible Redox Couples, The Anodic Peak Potential (${}^{n}E_a$) and/or Cathodic Peak Potential (${}^{n}E_c$) Is Reported. All Voltammograms Were Recorded in Dimethylformamide Containing 0.1 M $TBAPF_6$ As The Supporting Electrolyte Under Argon Using A 3 mm Diameter Glassy Carbon Working Electrode At Room Temperature and The Ferrocenium/Ferrocene Redox Couple As An Internal Reference. 193

LIST OF FIGURES

Figure Page

1.1. Schematic Comparing Photovoltaic-Powered Electrolysis (PV-Electrolysis) (Left) and Photoelectrochemical (PEC) (Right) Device Concepts, Including Tradeoffs In Their Current Use, Projected Costs, Required Amount of Raw Materials, and Current Technology Readiness Level (TRL). 5

1.2 Illustration of A p-Type (a–d) and n-Type (e–h) Semiconductor Showing The Energy Level of Conduction Band-Edge Potential (E_{CB}), Valence Band-Edge Potential (E_{VB}), Fermi Level (E_F), Quasi-Fermi Levels of Electrons ($E_{F,n}$) And Holes ($E_{F,p}$), And Solution Potential (E_{sol}), Along With Associated Differences in Potential. (a and e) Before Equilibrium, (b and f) After Equilibration With Electrolyte in The Dark, (c and g) Under Illumination in Steady-State Conditions Under The Open-Circuit Potential, and (d and h) Under Illumination in Steady-State Conditions Under Applied Bias Potentials. $E_{H+/H2}$ Is The Redox Potential of The H^+/H_2 Couple, W_{sc} Is The Width Of The Space-Charge Region, V_{ph} Is The Photovoltage, V_{bi} Is The Built-In Potential Of The Space-Charge Region, and η_o Is The Overpotential, And η_u Is The Underpotential. The Barrier Height, Φ_b, Is The Maximum Internal Energy That Can Be Extracted From An Electron–Hole Pair. 8

2.1. Molecular Structures Of (a) $Co(dmgH_2)(dmgH)Cl_2$ and (b) $Co(dmgH)_2PyCl$. 35

2.2. Schematic Representation of The Synthetic Method Used To Prepare Polypyridyl-Modified GaAs Electrodes (PPy|GaAs) Alongside Photos of The UV Reaction Apparatus (Top Image) And A Custom-Built Working Electrode (Bottom

Image). In This Scheme, Assembly of The Cobaloxime-Type Catalysts Occurs by Replacing One of The Axial Chloride Ligands of The Precursor Complex, $Co(dmgH_2)(dmgH)Cl_2$, With A Pyridyl Functional Group of The Polymeric Surface Coating. Charge Balance When Replacing Chloride, An Anionic X-Type Ligand, With Pyridyl, A Neutral L-Type Ligand, Is Accounted for by The Base-Promoted Conversion of The Dimethylglyoxime Ligand To The Dimethylglyoximate Monoanion. 36

2.3. Photos Collected During Determination of Contact Angles Using Drops Of Deionized Water On (A) GaAs (Contact Angle = 34 ± 1^o), (B) PPy|GaAs (Contact Angle = 50 ± 3^o), And (C) Cobaloxime|PPy|GaAs (Contact Angle = 76 ± 1^o). The Increase in Contact Angles Following Each Chemical-Modification Step Indicates Increased Hydrophobicity of The Resulting Surfaces. 37

2.4. Ellipsometry Spectra Recorded Using PPy|GaAs At Incidence Angles of 70° (Dotted), 75° (Solid), And 80° (Dashed). Using These Ellipsometry Measurements, The Thickness of The Polypyridyl Layer On GaAs Was Determined To Be 2.0 ± 0.3 nm. Using The Bulk Polymer Density of 1.15 g cm^{-3} and 4-Vinylpyridine Molecular Weight of 105.14 g mol^{-1}, The Related Polypyridyl Site Density Is 2.2 nmol cm^{-2}. 38

2.5. N 1s Core Level XP Spectra of (a) A Powder Sample of $Co(dmgH)_2PyCl$, (b) Cobaloxime|PPy|GaAs, (c) PPy|GaAs, and (d) GaAs. The Circles Are The Spectral Data, and The Solid Lines Represent The Backgrounds (Light Gray), A Component Fit Associated With Nitrogens Bound To Co (Red), A Component Fit Associated

With Unbound Pyridyl Nitrogens (Blue), And Overall Fits (Black). The Feature at 397.6 eV Present in XP Spectra of Unmodified GaAs Surfaces Is Assigned to A Satellite Feature of The Ga LMM Auger Line at 393 eV. The Peak Position and Full Width At Half Maximum (fwhm) of This Feature Was Used to Guide The Fitting and Assist With Identifying Components in XP Spectra of PPy|GaAs. The XP Spectrum of PPy|GaAs Was Fit With A Component at 397.6 eV, Assigned To A Satellite Feature Of The Ga LMM Auger Line, And An Additional Component at 398.8 eV, Assigned to Pyridyl Nitrogens of The Polymeric Coating (Figure 2.3c). Using The Peak Positions and fwhm of These Two Components to Guide The Fitting of The N 1s Core Level Spectrum of Cobaloxime|PPy|GaAs, At Least One Additional Nitrogen Component Could Be Fit to The Data (Figure 2.3d). This Additional Contribution at 400.1 eV Is Ascribed to Nitrogen Atoms Coordinated to Cobalt Ions, Including Pyridyl-Type Nitrogens As Well As Glyoximate- and Glyoxime-Type Nitrogens. Inspection of The XP Spectra Collected Using Powder Samples of $Co(dmgH)_2PyCl$ and $Co(dmgH_2)(dmgH)Cl_2$ Show The Nitrogen Signals Arising From The Glyoximate and Glyoxime Ligands Overlap With The Nitrogen Contributions From Co-Coordinated Pyridine Ligands (See Figure 2.4).. 40

2.6. (A) N 1s Core Level Spectra Collected Using Powder Samples of Either The Model Compound $Co(dmgH)_2PyCl$ (Red) or Precursor Compound $Co(dmgH_2)(dmgH)Cl_2$ (Olive) (Data Taken From Reference 27 in This Chapter).....41

2.7. Co 2p Core Level XP Spectra of PPy|GaAs (Blue) And Cobaloxime|PPy|GaAs (Red). The Circles Are The Spectral Data, and The Solid Lines Represent The Background (Light Gray) and Overall Fit (Black). 42

Figure Page

2.8. (a) GATR-FTIR Absorption Spectra Of GaAs (Black Solid Line) And PPy|GaAs (Blue Solid Line), As Well As FTIR Transmission Spectra of 4-Vinylpyridine in KBr (Purple Dashed Line) and Polyvinylpyridine in Kbr (Blue Dashed Line). (b) GATR-FTIR Absorption Spectra of Cobaloxime|PPy|GaAs (Red Solid Line) As Well As FTIR Transmission Spectra of The Precursor Complex, $Co(dmgH_2)(dmgH)Cl_2$, in KBr (Olive Dashed Line) and The Model Cobaloxime Complex, $Co(dmgH)_2PyCl$, in KBr (Red Dashed Line)... 43

2.9. GATR-FTIR Absorption Spectra of Cobaloxime|PPy|GaAs Collected (a) Prior To and (b) Following 3 Cyclic Voltammograms (Scanning From +0.58 V Vs RHE to -1.12 V Versus RHE at A Scan Rate Of 100 mV s^{-1}) Recorded in pH 13 Electrolyte (0.1 M NaOH) Under Simulated 1-Sun Illumination. The Absorption Feature at 1235 cm^{-1}, Assigned to The NO- Stretch Of The Immobilized Cobaloxime Units, Is Present in The GATR-FTIR Spectra Collected Prior To And Following Photoelectrochemical Experiments, Indicating The Immobilized Catalysts Present Following These Experiments Are Intact.. 45

2.10 Plots of The Percentage of Light Transmitted (Dotted), Reflected (Dashed), or Absorbed (Solid) By Cobaloxime|PPy|GaAs versus The Wavelength of Illumination. The Percentage of Light Reflected Is Equal to The Sum of The Specular Percent Reflectance, Collected at An Incident Angle of 5° To The Normal of The Sample Surface, and Diffuse Percent Reflectance. The Data Shown In This Figure Were Used to Prepare IQE Plots from The Related EQE Plots 46

2.11 (a) The Air Mass 1.5 Global Tilt Solar Flux Spectrum (Black Solid) As Well As

Transmission Spectra Of The Gap (Bandgap = 2.26 Ev) (Blue Dash) And GaAs (Bandgap = 1.43 Ev) (Red Dash) Semiconductors Used In This Work. (b) Linear Sweep Voltammograms Recorded At A Scan Rate Of 100 MV S^{-1} Using Cobaloxime-Polypyridyl-Modified GaAs (Cobaloxime|PPy|GaAs) Electrodes in pH 7 (Dash Traces) or pH 13 (Solid Traces) Solutions Under Simulated 1-Sun Illumination (Red Traces) or in The Dark (Black Traces). (c) Linear Sweep Voltammograms Recorded At A Scan Rate Of 100 mV s^{-1} Using Cobaloxime-Polypyridyl-Modified Gap (Cobaloxime|PPy|Gap) Electrodes in pH 7 (Dash Traces) or pH 13 (Solid Traces) Solutions Under Simulated 1-Sun Illumination (Blue Traces) or in The Dark (Black Traces). 48

2.12 Linear Sweep Voltammograms Recorded At 100 MV S^{-1} Using Either GaAs (Black), PPy|GaAs (Blue), Or Cobaloxime|PPy|GaAs (Red) Working Electrodes Under 100 Mw Cm^{-2} Illumination In Either (A) Ph Neutral (0.1 M Phosphate Buffer) Or (B) Ph 13 (0.1 M NaOH) Electrolyte Solutions. The Black Dashed Lines Represent The H^+/H_2 Equilibrium Potential 49

2.13 Linear Sweep Voltammograms Recorded Under 100 mW cm^{-2} Illumination Using Cobaloxime|PPy|GaAs Working Electrodes in pH 13 (0.1 M NaOH) Electrolyte Solutions And The Following Scan Rates: 10 (Red), 50 (Orange), 100 (Yellow), 200 (Green), 500 (Cyan), 700 (Blue) And 1000 (Violet) mV s^{-1}. 52

2.14 Linear Sweep Voltammograms Recorded Under 150 mW cm^{-2} Illumination Using Cobaloxime|PPy|GaAs Working Electrodes in pH Neutral (0.1 M Phosphate Buffer) Electrolyte Solutions and The Following Scan Rates: 10 (Red), 50 (Orange), 100 (Yellow), 200 (Olive), 500 (Cyan), 700 (Blue), 1000 (Violet), 1200 (Grey), 1500 (Black), 1700 (Pink), 2000 (Dark Yellow), 2500 (Navy), and 3000 (Green) mV s^{-1} 52

2.15 (a) Linear Sweep Voltammograms Recorded at 100 mV s^{-1} Using Cobaloxime|PPy|GaAs Electrodes in 0.1 M Phosphate Buffer (pH 7) and The Following Illumination Intensities: 0 (Black Dash), 75 (Red), 125 (Olive), 175 (Blue), and 200 (Violet) mW cm^{-2}. (b) Plots of The Limiting Current Densities Recorded in The Low Polarization Region (Squares) and High Polarization Region (Circles) versus The Illumination Intensity. (c) Linear Sweep Voltammograms Recorded Under 100 mW cm^{-2} Illumination Using Cobaloxime|PPy|GaAs Electrodes in 0.1 M Phosphate Buffer (pH 7) And The Following Scan Rates: 10 (Red), 50 (Orange), 100 (Green), 200 (Olive), 500 (Cyan), 700 (Blue), 1000 (Violet), 1200 (Grey), And 1500 (Black) mV s^{-1}. (D) Plots of The Limiting Current Densities Recorded in The Low Polarization Region (Squares) and High Polarization Region (Circles) versus The Scan Rate. 54

2.16 Linear Sweep Voltammograms Recorded at A Scan Rate Of 100 mV s^{-1} Using Cobaloxime|PPy|GaAs Working Electrodes in pH 13 (0.1 M NaOH) Electrolyte Solutions And The Following Illumination Conditions: 25 (Red), 50 (Orange), 100 (Olive), 150 (Blue), And 200 (Purple) mW cm^{-2}. 55

2.17 Plots of The Limiting Peak Current Densities versus (a) Scan Rate and (b) Scan Rate$^{1/2}$ Recorded Under 100 mW cm^{-2} Illumination in The Low Polarization Region (Squares) and High Polarization Region (Circles) Using Cobaloxime|PPy|GaAs

Working Electrodes in pH Neutral (0.1 M Phosphate Buffer) Electrolyte Solutions and The Following Scan Rates: 10 (Red), 50 (Orange), 100 (Green), 200 (Olive), 500 (Cyan), 700 (Blue), 1000 (Violet), 1200 (Grey), And 1500 (Black) mV s^{-1}. 56

2.18 (a) External Quantum Efficiency (EQE) Action Spectra Recorded at pH 7 Using Either Cobaloxime|PPy|GaAs (Red) or Cobaloxime|PPy|Gap (Blue) Working Electrodes Polarized at 0 V vs RHE. (b) Electron Flux Spectra for Cobaloxime|PPy|GaAs (Red) and Cobaloxime|PPy|Gap (Blue) Calculated Using The EQE Action Spectra Shown in Figure 2.20a and The Solar Flux Spectrum Shown in Figure 2.9a. (c) EQE Action Spectra Recorded at oH 13 Using Either Cobaloxime|PPy|GaAs (Red) or Cobaloxime|PPy|Gap (Blue) Working Electrodes Polarized at 0 V vs RHE. (d) Electron Flux Spectra for Cobaloxime|PPy|GaAs (Red) and Cobaloxime|PPy|Gap (Blue) Calculated Using The EQE Action Spectra Shown In Figure 2.20c And The Solar Flux Spectrum Shown In Figure 2.9a. 59

2.19 Internal Quantum Efficiency (IQE) Action Spectra of Cobaloxime|PPy|GaAs Working Electrodes Polarized at 0 V vs RHE in (a) 0.1 M Phosphate Buffer pH 7 (Green) or (b) 0.1 M NaOH pH 13 (Red). These IQE Spectra Were Constructed Using The Related EQE Spectra (Figure 2.20) and The Plot Of Percentage of Light Absorbed by Cobaloxime|PPy|GaAs (i.e., The Light Harvesting Efficiency of Cobaloxime|PPy|GaAs) versus The Wavelength of Illumination (Solid Line In Figure 2.8). 60

2.20 (a) Irradiance and (b) Photon Flux Spectra of An LSC-100 Series Oriel Solar Simulator Collected With An AM 1.5 G Filter (Red Circles). For Comparison, The

Air Mass 1.5 Global Tilt (Olive) and Direct Circumsolar (Blue) Irradiance and Photon Flux Spectra Are Included 61

2.21 A Representative Gas Chromatogram Obtained from Chromatography of A Headspace Gas Sample Taken From A Sealed Photoelectrochemical Cell Containing A Cobaloxime|PPy|GaAs Working Electrode Polarized at 0 V vs RHE In A pH 13 Solution Before (Dashed Line) And After (Solid Line) 20 Min Of Illumination At 100 mW cm^{-2}. In These Experiments, Quantification of Hydrogen Confirmed Near Unity Faradaic Efficiencies When Polarizing Cobaloxime|PPy|GaAs Working Electrode at 0 V, -0.2 V, -0.58 V, -0.98 V, Or -1.38 V Vs RHE in pH 7 Electrolyte Solutions or at 0 V, -0.2 V, -0.52 V, Or -1.92 V Vs RHE in pH 13 Electrolyte Solutions. 62

2.22 Plots of The Limiting Per Cobalt Site HER Activity of Cobaloxime|PPy|GaAs Working Electrodes in The Low Polarization Region (Squares) and High Polarization Region (Circles) versus The Illumination Intensity When Immersed in Phosphate Buffer (pH 7) And Using A Scan Rate Of 100 mV s^{-1} (See Experimental Methods For Further Details). 64

2.23 Plots of The Limiting Per Cobalt Site HER Activity Versus (a) Scan Rate And (b) Scan Rate$^{1/2}$ Recorded Under 100 mW cm^{-2} Illumination in The Low Polarization Region (Squares) and High Polarization Region (Circles) Using Cobaloxime|PPy|GaAs Working Electrodes in pH Neutral (0.1 M Phosphate Buffer) Electrolyte Solutions and The Following Scan Rates: 10 (Red), 50 (Orange), 100 (Green), 200 (Olive), 500 (Cyan), 700 (Blue), 1000 (Violet), 1200 (Grey), And 1500

(Black) MV S^{-1}. The Related Linear Sweep Voltammetry Data Is Shown in Figure 2.13c. 64

2.24 (a) Linear Sweep Voltammograms of Cobaloxime|PPy|GaAs (Red) Recorded at 100 mV s^{-1}, Under Increasing Illumination, in 0.1 M Solution Of Phosphate Buffer (pH 7). (b) Plot of The Turnover Frequency (TOF) Recorded at 0 V vs RHE versus Illumination Intensity. From The Current Densities Collected in Linear Sweep Experiments With Varying Illumination Conditions, We Can Derive The TOF (H_2 Molecule Per Co Site Per Second). A Plot of This TOF Versus The Illumination Intensity Show That TOF Increases Linearly As The Light Intensity Increase But Eventually Reach A Maximum Value Of ~20 H2 Co^{-1} S^{-1} Under 200 mW cm^{-2} Illumination (Figure 2.27c-D). 65

3.1 Schematic Representations of A Degrade-Repair Cycle For A Molecular Modified Phototelectrode. 75

3.2 Schematic Representation of The Synthetic Method Used To Prepare Cobaloxime-Polypyridyl-Modified GaP Electrodes (Co|PPy|GaP). In This Scheme, Assembly of The Cobaloxime-Type Catalysts Occurs by Replacing One of The Axial Chloride Ligands of The Precursor Complex, $Co(dmgH_2)(dmgH)Cl_2$, With A Pyridyl Functional Group of The Polymeric Surface Coating. Charge Balance When Replacing Chloride, An Anionic X-Type Ligand, With Pyridyl, A Neutral L-Type Ligand, Is Accounted For by The Base-Promoted Conversion of The Dimethylglyoxime Ligand to The Dimethylglyoximate Monoanion. 80

3.3 (a) Components of The Customized Photoelectrochemical Cell Used in This

Work And (b) The Assembled Cell in Operation Using A Modified-GaP Working Electrode, A Pt Counter Electrode And Ag/AgCl Reference Electrode.................... 81

3.4 Work and Processing Scheme Used For Characterizing Samples via GATR-FTIR and Ellipsometry. 83

3.5 Work and Processing Scheme Used For Characterizing Samples via XP Spectroscopy. 85

3.6 (a) Schematic Representation of The Co|PPy|GaP Degrade-Repair Cycle. (b) Schematic Illustration of The Three-Electrode Assembly Featuring A Molecular-Modified p-Type Semiconductor Working Electrode Under Steady-State Illumination at Open-Circuit Conditions. E_{CB} Is Conduction Band-Edge Potential and E_{VB} Is Valence Band-Edge Potential, $E_{F,n}$ Is The Electron Quasi-Fermi Level, $E_{F,p}$ Is The Hole Quasi-Fermi Level, E_{cat} Is The Catalyst Potential, $E_{H+/H2}$ Is The Thermodynamic Hydrogen Potential, and V_{ph} Is The Photovoltage. (c) Voltammograms Recorded Using Co|PPy|GaP Electrodes Prior to (Red) and Following (Red Dash) Degradation via Controlled-Potential Electrolysis At 0 V vs RHE (See Figure 1d And Related Caption), As Well As Subsequent Repair Via Wet-Chemical Processing (Green). Voltammograms Recorded Using PPy|GaP Electrodes Prior To (Blue) And Following (Blue Dash) The Same Controlled-Potential Electrolysis Experiments Are Included For Comparison. All Voltammograms Were Recorded in 0.1 M Phosphate Buffer (pH 7) Solution, at A Scan Rate of 100 mV s^{-1}, and Under 100 mW cm^{-2} Illumination. (d) Current Density versus Time Plots Obtained via 15 Minutes of Controlled-Potential Electrolysis At 0 V Vs RHE Using Either Co|PPy|GaP (Red) Or PPy|Gap

Figure Page

(Blue) Electrodes in 0.1 M Phosphate Buffer (pH 7), and Under 100 mW cm^{-2} Illumination. 94

3.7 (A) Linear Sweep Voltammograms Recorded at A Scan Rate of 100 mV s^{-1} Using A Co|PPy|GaP Working Electrodes in 0.1 M Phosphate Buffer (pH 7), Under 100 mW cm^{-2} Before Controlled-Potential Electrolysis Experiment (Red) and After The Third Degrade-Repair Cycle (Light Green). (b) Current Density versus Time Plots Obtained Via 15 Minutes of Controlled-Potential Electrolysis at 0 V vs RHE Using The Electrodes Described in (a). 97

3.8 (a) Linear Sweep Voltammogram Recorded Using Post-Degrade Co|PPy|GaP Samples (Post Controlled-Potential Electrolysis Experiment) at A Scan Rate of 100 mV s^{-1} and A Freshly Prepared Solution of 0.1 M Phosphate Buffer That Was Not Previously Exposed To The Co|PPy|GaP Electrodes. These Post-Degrade Electrodes Showed Near-Unity Faradaic Efficiency at Activities Equal To Those Obtained in The Initial Phosphate Buffer Solutions. This Result Indicates No Photocatalysis in Solution Happening. (b) Current Density versus Time Plots Obtained During Controlled-Potential Electrolysis at 0 V vs RHE For Gas Chromatography Experiments. All Data Are Averaged From Three Separate Working Electrodes 98

3.9 A Representative Gas Chromatogram Obtained From Chromatography Of A Headspace Gas Sample Taken From A Sealed Photoelectrochemical Cell Containing A Post-Degrade Co|PPy|GaP Working Electrode Before (Dotted) and After (Dashed) 20 Minutes Of Controlled-Potential Electrolysis at 0 V vs RHE in a pH 7 Phosphate Buffer Solution, Under Illumination at 100 mW cm^{-2}. 99

Figure Page

3.10 (a) Linear Sweep Voltammogram Recorded Using Post-Repair Co|PPy|GaP Samples (Post Controlled-Potential Electrolysis Experiment) at A Scan Rate of 100 mV s^{-1}. (b) Current Density Versus Time Plots Obtained During Controlled-Potential Electrolysis at 0 V vs RHE For Gas Chromatography Experiments. All Data Are Averaged From Three Separate Working Electrodes. 99

3.11 A Representative Gas Chromatogram Obtained From Chromatography of A Headspace Gas Sample Taken From A Sealed Photoelectrochemical Cell Containing A Post-Repair Co|PPy|GaP Working Electrode Before (Dotted) And After (Solid) 20 Minutes of Controlled-Potential Electrolysis at 0 V vs RHE in A pH 7 Phosphate Buffer Solution, Under Illumination At 100 mW cm^{-2}. 100

3.12 Ellipsometry Spectra Recorded Using Co|PPy|GaP Samples (a) Prior To Photoelectrochemical Characterization/Degradation, (b) Following Photoelectrochemical Characterization/Degradation and (c) Following Chemical Repair. The Spectra Shown Here Are Obtained From An Average of Measurements Involving Three Separately Prepared Samples. All Individual Spectra Were Recorded at Incidence Angles of Either 55° (Solid), 65° (Dashed), Or 75° (Dash-Dot). Averaging Between Three Samples, The Thickness of The Co-Polypyridyl Layer On GaP Was Determined To Be 5.16 ± 0.01 nm For The Initial Co|PPy|GaP Samples, 5.34 ± 0.03 nm For The Post-Degrade Co|PPy|GaP Samples, And 3.96 ± 0.01 nm For The Post-Repair Co|PPy|GaP Samples. 102

3.13 The PPy|GaP Ellipsometry Data Was Analyzed (a) Prior To Photoelectrochemical Characterization/Degradation And (b) Following

Photoelectrochemical Characterization/Degradation. The Plots Shown Here Are Obtained by Averaging Data From Three Separately Prepared Samples. All Individual Spectra Were Recorded at Incidence Angles of Either 55° (Solid), 65° (Dashed), or 75° (Dash-Dot). Averaging Between Three Samples, The Thickness Of The Polypyridyl Layer On Gap Was Determined To Be 2.31 ± 0.01 nm For The Initial PPy|GaP Samples, and 3.56 ± 0.03 nm For The Post-Degrade PPy|GaP Samples. 103

3.14 Refractive Index of the Polypyridyl Layer On Gap For Initial PPy|Gap (Solid) and Post-Degrade PPy|Gap (Dashed) Samples 103

3.15 Refractive Index of the Cobaloxime-Polypyridyl Layer On Gap For Initial Co|PPy|GaP (Solid Red), Post-Degrade PPy|Gap (Dashed Red) and Post-Repair Co|PPy|GaP (Solid Green) Samples. 104

3.16 (a) FTIR Transmission Spectrum of The Model Cobaloxime Complex, $Co(dmgH)_2PyCl$, in KBr (Red Solid). (b) GATR-FTIR Spectrum Of PPy|Gap Recorded Using Initial Sample (Blue Solid). (c) GATR-FTIR Spectra Of Co|PPy|GaP Samples Recorded Using Initial (Red Solid), Post-Degrade (See Fig. 1d And Related Caption) (Red Dash), And Post-Repair (Green Solid) Samples. All Spectra Are Normalized to The Absorbance Peak At 1600 cm^{-1} 105

3.17 VariGATR-FTIR Spectra Of PPy|GaP Samples Recorded Prior To (Solid) and Following (Dashed) The Controlled-Potential Electrolysis Experiments. Spectral Contributions at ~1126 cm^{-1}, 1464 cm^{-1} And at 1655 cm^{-1} Are Attributed To Bending of PO_x^- Groups, Stretching of Ch_x Groups From Adventitious Carbon and

Figure Page

Deformation/Bending of OH Groups, Respectively, Arising From Air Exposure and Handling of The Samples. 106

3.18 (a) Structure of The Pyridyl And Cobaloxime Units of Co|PPy|GaP Indicating the PyN, GlyN, And PyN-Co Nitrogen Sites. (b-d) N 1s Core Level XP Spectra of Co|PPy|GaP Recorded Using (b) *Initial*, (c) *Post-Degrade* (See Figure 3.2d and Related Caption), and (d) *Post-Repair* Samples. Solid Lines Represent The Background (Gray) and Indicated Components (Cyan for Remnant Pyridyl Nitrogens (PyN), Yellow for Glyoximate Nitrogens Bound to Cobalt Centers (GlyN), and Purple for Pyridyl Nitrogens Bound To Cobaloximes (PyN-Co))............................107

3.19 Co 2p Core Level Spectra of Co|PPy|GaP Recorded (a) Prior To and (b) Following Degradation via Controlled-Potential Electrolysis at 0 V vs RHE As Well As (c) Subsequent Repair via Wet-Chemical Processing. Circles Represent The Spectral Data.. 108

4.1 Schematic Representation of The Cobalt Porphyrin-Polypyridyl GaP Photoelectrode (CoTTP|PPy|GaP). 118

4.2 Schematic Diagram Highlighting The Molecular Structure of A Cobalt Porphyrin Coordinated to A Surface-Grafted Polypyridyl Chain On A CoTTP|PPy|GaP Working Electrode Wired in A Three-Electrode Configuration Under Illumination Using A Broadband or Monochromatic Light Source. 119

4.3 Photoelectrosynthesis Vs. Screening Vs. Dye-Sensitized Hole Injection* 122

4.4 Plots of The Probabilities of (a) Absorption (Φ_{abs}) (Squares), (b) Reflection (Φ_{ref}) (Circles), and (c) Transmission (Φ_{trans}) (Triangles) for Gap (Black), PPy|Gap

(Blue), And CoTTP|PPy|Gap (Purple). The Dashed and Dotted Black Lines Indicate Energies Associated With The Direct and Indirect Bandgaps of GaP, Respectively. 126

4.5 Plots of The Probabilities of (a) Absorption (Φ_{abs}) (Squares), (b) Reflection (Φ_{ref}) (Circles), and (c) Transmission (Φ_{trans}) (Triangles) Measured Using Samples of GaP (Black), PPy|GaP (Blue), And CoTTP|PPy|GaP (Purple)........ 127

4.6 Plots of The Absorption Coefficients For Unmodified GaP (Black), PPy|GaP (Blue), And CoTTP|PPy|GaP (Purple) From 540 To 850 nm. Error Bars Are Included For Each Data Point Shown........ 128

4.7 Linear Sweep Voltammograms Recorded Using A Gap (Black Solid), PPy|GaP (Blue Solid), or CoTTP|PPy|GaP (Purple Solid) Electrode In 0.1 M Phosphate Buffer (pH 7) Under Simulated 1-Sun Illumination. The Vertical Dashed Line At 0 V Vs RHE Indicates The Potential Of The H^+/H_2 Couple........ 129

4.8 Wavelength-Resolved (a) External (Circles) and (b) Internal (Squares) Quantum Efficiency Plots Recorded Using PPy|Gap (Blue) Or CoTTP|PPy|Gap (Purple) Electrodes Polarized At 0 V Vs RHE In 0.1 M Phosphate Buffer (pH 7). The Dashed and Dotted Black Lines Indicate Energies Associated With The Direct And Indirect Bandgaps of GaP........ 131

4.9 Plots of Wavelength-Resolved Electron Flux Associated With PPy|GaP (Blue) or CoTTP|PPy|Gap (Purple) Electrodes Polarized At 0 V Vs RHE in 0.1 M Phosphate Buffer (Ph 7). All Plots Were Generated Using Related EQE Data and Considering Illumination Under AM1.5 Global Tilt Solar Flux. At The Equilibrium Potential (0 V

Vs RHE) The Activities Associated With Both The PPy|GaP And CoTTP|PPy|GaP Electrodes Are Approaching Their Limiting Values (See Figure 4.5). 133

4.10 External Quantum Efficiency Action Spectra Collected Using PPy|GaP (Blue) or CoTTP|PPy|GaP (Purple) Electrodes Polarized At 0 V vs RHE in 0.1 M phosphate buffer (pH 7) Normalized At 300 nm As Well As Absorption Spectra of 5,10,15,20-Tetra-P-Tolylporphyrin Cobalt(II) (CoTTP) Recorded in Chloroform in The Absence (Solid Green) and Presence of ~1 Equivalent of Pyridine (Dashed Green) in The Wavelength Ranges Where (a) The Porphyrin Soret Absorption Band (300 To 500 Nm) and (b) The Porphyrin Q-Type Absorption Bands (500 To 650 nm) Occur. .. 136

4.11 (A) Absorption Spectra of 5,10,15,20-tetra-p-tolylporphyrin Cobalt(II) (CoTTP) in Chloroform Recorded Prior To (Solid Green) and Following 26 Hours After The Addition of ~1 Equivalent of Pyridine (Dashed Green). The Gray Lines Show Data Recorded Following 5 Min, 1h, 2h, 7h, 10h, and 12h After The Addition Of ~1 Equivalent Of Pyridine. (b) Extinction Coefficients Of CoTTP in Chloroform Recorded Prior To (Solid Green) And Following 26 Hours After The Addition of ~1 Equivalent of Pyridine (Dashed Green). 136

4.12 Wavelength-Resolved LHE Plots Collected Using Gap (Black), PPy|Gap (Blue), Or CoTTP|PPy|Gap (Purple) Electrodes As Well As Extinction Coefficients Of CoTTP In Chloroform Recorded in The Absence (Solid Green) Or Presence of ~1 Equivalent of Pyridine (Dashed Green). The Data Were Collected At Wavelengths Where Porphyrin (a) Soret Absorption Bands (300 To 500 nm) Occur and (b) Q-Type Absorption Bands (500 To 650 nm) Occur... 137

4.13 Schematic Representation of The CoTTP, CoTTP-Pyridine, and CoTTP-Pyridine-O_2 Equilibria. Oxygen Binds to The Cobalt Center To Form A CoTTP-Pyridine-O_2 Complex, Where The Oxygen Exists Formally As A Superoxide Ion. 139

4.14 Absorption Spectra of (a) Cobalt Porphyrin-Modified Nanostructured Indium Tin Oxide (CoP|NanoITO) at Open Circuit Potential (Green Solid) and Polarized at Potentials Required To Generate The Co^{iii} Species (Grey Solid And Black Dashed) As Well As (b) Cobalt Porphyrin-Polyvinylpyridine-Modified Nanostructured Indium Tin Oxide (CoTTP|PVP|NanoITO) at Open Circuit Potential (Purple Solid) and Polarized At Potentials Required To Generate The Co^{ii} Species (Grey Solid And Black Dashed). The Black Dashed Traces In Both Panels Represent Spectra Of Cop|NanoITO and CoTTP|PVP|NanoITO Electrodes That No Longer Change Upon Further Biasing The Applied Potential. This Data Is Taken from Reference 12 of This Chapter. 139

4.15 (A) Plots of The Wavelength-Resolved LHE Measured Using CoTTP|PPy|GaP Electrodes (Purple Solid) and An Approximated LHE Associated With The CoTTP|PPy Layer (Green Dashed). As Expressed in Eq. 4.1, The LHE Associated with The CoTTP|PPy Layer Is Approximated Using The Measured Per Geometric Area Loading Of Cobalt Porphyrins On CoTTP|PPy|GaP Surfaces (1 nmol cm^{-2}), The Polypyridyl Layer Thickness On CoTTP|PPy|GaP Surfaces (~4 nm), And The Extinction Coefficients of CoTTP In Chloroform Recorded In The Presence of ~1 Equivalent of Pyridine. (b) Plot of The Percent of Light Attenuated By The Cobalt

Porphyrin-Polypyridyl Coating of The CoTTP|PPy|GaP Assemblies (Green Dashed). Using The LHE Values Associated With The CoTTP|PPy Layer From Panel (a), The Percent of Light Attenuated by The Cobalt Porphyrin-Polypyridyl Coating Is Estimated To Be ~39% At The Wavelength Associated With The Soret Absorption Band at 441 nm, ~3% At The Wavelength Associated With The Q-Type Absorption Band at 554 nm, and ~2% At The Wavelength Associated With The Q-Type Absorption Band at 592 nm. 141

4.16 (A) External Quantum Efficiency Action Spectra Calculated For A Cobalt Porphyrin-Polypyridyl-Modified GaP Electrode Assuming The Immobilized Porphyrins Serve Strictly As Light-Screening Pigments (Not Catalysts) and All Photons Absorbed By The Porphyrin Layer Are Screened From The Underlying Gap Semiconductor (Red). (b) External Quantum Efficiency Action Spectra Calculated for A Cobalt Porphyrin-Polypyridyl-Modified GaP Electrode Assuming The Immobilized Porphyrins Serve Strictly As Dye-Sensitizers (Not Catalysts) and All Photons Absorbed by The Porphyrin Layer Contribute To Production Of Photocurrent via A Dye-Sensitization Mechanism (Teal). For Comparison, The External Quantum Efficiency Action Spectrum Collected Using PPy|Gap Electrodes Polarized At 0 V vs RHE in 0.1 M Phosphate Buffer (Blue) Is Included in Both Panels (a) and (b). 143

4.17 EQE Action Spectrum Collected Using CoTTP|PPy|GaP Electrodes Polarized at 0 V Vs RHE in 0.1 M Phosphate Buffer (pH 7) (Purple) And A Hypothetical EQE Action Spectrum Of CoTTP|PPy|GaP Electrodes Assuming The Immobilized

Porphyrins Serve Strictly As Pigments, Not Catalysts, and That All Photons Absorbed by The Porphyrin Layer Are Screened From The Underlying GaP and Do Not Contribute To Production of Current (I.E. The DSE Is 0%) (Red). 145

4.18 EQE Action Spectrum Collected Using CoTTP|PPy|GaP Electrodes Polarized At 0 V vs RHE in 0.1 M Phosphate Buffer (pH 7) (Purple) and A Hypothetical EQE Action Spectrum of CoTTP|PPy|GaP Electrodes Assuming The Immobilized Porphyrins Serve Strictly As Pigments, Not Catalysts, and That All Photons Absorbed by The Porphyrin Layer Are Screened From The Underlying Gap But Contribute To Production of Current Via A Dye-Sensitization Mechanism (I.E. The DSE Is 100%) (Teal). 146

4.19 A Plot of The Apparent DSE (As Defined In Equation 4.7) Required To Achieve The Eqes Measured Using CoTTP|PPy|Gap Electrodes (Purple). For Comparisons, The Dses Used io Construct The Hypothetical EQE Action Spectra Shown In Figure 4.17, Where The DSE of The CoTTP|PPy|Gap Electrodes Is 0%, (Red) And Figure 4.18, Where The DSE of The CoTTP|PPy|Gap Electrodes Is 100% (Teal) Are Also Included. These Results Further Demonstrate That Enhancements in EQE Following Porphyrin Modification Cannot Be Accounted For By Porphyrin Dye Sensitization. For Example, The Apparent DSE Required To Achieve The EQEs Measured Following Porphyrin Modification At Wavelengths Between 300 And 400 nm Would Be Almost 250%. 148

5.1 XP Survey Spectrum of GaAs (111)A. 166

5.2 Ga 2p Core Level XP Spectrum of GaAs (111)A. The Circles Are The Spectral

Data, and The Solid Lines Represent The Background (Light Gray), Component Fits (Dark Gray), and Overall Fit (Black). 166

5.3 As 2p Core Level XP Spectrum of GaAs (111)A. The Circles Are The Spectral Data, and The Solid Lines Represent The Background (Light Gray), Component Fits (Dark Gray), and Overall Fit (Black). 167

5.4 N 1s Core Level XP Spectrum of GaAs (111)A. The Circles Are The Spectral Data, and The Solid Lines Represent The Background (Light Gray) and Overall Fit (Black). 167

5.5 XP Survey Spectrum Of PPy|GaAs. 168

5.6 Ga 2p Core Level XP Spectrum of PPy|GaAs. The Circles Are The Spectral Data, and The Solid Lines Represent The Background (Light Gray), Component Fits (Blue), and Overall Fit (Black). 168

5.7 As 2p Core Level XP Spectrum of PPy|GaAs. The Circles Are The Spectral Data, and The Solid Lines Represent The Background (Light Gray), Component Fits (Blue), and Overall Fit (Black). 169

5.8 N 1s Core Level XP Spectrum of PPy|GaAs. The Circles Are The Spectral Data, and The Solid Lines Represent The Background (Light Gray), Component Fits (Blue), and Overall Fit (Black). 169

5.9 C 1s Core Level XP Spectrum of PPy|GaAs. The Circles Are The Spectral Data, and The Solid Lines Represent The Background (Light Gray) and Overall Fit (Black). 170

5.10 XP Survey Spectrum of Cobaloxime|PPy|GaAs. 170

Figure Page

5.11 Ga 2p Core Level XP Spectrum of Cobaloxime|PPy|GaAs. The Circles Are The Spectral Data, and The Solid Lines Represent The Background (Light Gray), Component Fits (Red), and Overall Fit (Black).. 170

5.12 As 2p Core Level XP Spectrum of Cobaloxime|PPy|GaAs. The Circles Are The Spectral Data, and The Solid Lines Represent The Background (Light Gray), Component Fits (Red), and Overall Fit (Black).. 171

5.13 N 1s Core Level XP Spectrum of Cobaloxime|PPy|GaAs. The Circles Are The Spectral Data, and The Solid Lines Represent The Background (Light Gray), Component Fits (Red), And Overall Fit (Black). 171

5.14 C 1s Core Level XP Spectrum of Cobaloxime|PPy|GaAs. The Circles Are The Spectral Data, And The Solid Lines Represent The Background (Light Gray) and Overall Fit (Black). 172

5.15 Linear Sweep Voltammograms Recorded Using Cobaloxime|PPy|GaAs Working Electrodes in pH Neutral (0.1 M Phosphate Buffer) Electrolyte Solutions Under 100 mW cm^{-2} Illumination at Scan Rates of 100 (Green) and 1500 (Black) mV s^{-1} As Well As Under 150 mW cm^{-2} Illumination At A Scan Rate Of 1500 mV s^{-1} (Black Dashed)... 172

5.16 Linear Sweep Voltammograms Recorded Under 150 mW cm^{-2} Illumination Using Cobaloxime|PPy|GaAs Working Electrodes In pH 13 (0.1 M NaOH) Electrolyte Solutions And The Following Scan Rates: 10 (Red), 50 (Orange), 100 (Yellow), 200 (Olive), 500 (Cyan), And 1000 (Violet) mV s^{-1}. 173

5.17 FTIR Transmission Spectra of The Precursor Complex, $Co(dmgH_2)(dmgH)Cl_2$, in KBr (Green) And The Model Cobaloxime Complex, Co(dmgH)$_2$PyCl, In Kbr (Red). Transmission Spectra of Co(dmgH)$_2$PyCl Display A Relatively Strong Transmission Band at 1240 cm^{-1} That Is Assigned to The NO- Stretch Of This Complex. The Frequency of This Band Is Diagnostic of Cobaloxime Complexes Featuring Axial Coordination to Pyridyl Nitrogens. For Comparison, The NO- Stretch of The Precursor Complex, Co(dmgH$_2$)(dmgH)Cl$_2$, Is Located at 1225 Cm^{-1}. 177

5.18 FTIR Transmission Spectra of 4-Vinylpyridine in KBr (Purple) and Polyvinylpyridine in KBr (Blue). The Absorption Bands Centered at 1600 cm^{-1} and 1417 cm^{-1} Are Assigned To C=N And C-N Vibrational Modes, Respectively. The Feature Observed at 1453 cm^{-1} in The Polyvinylpyridine Spectrum (Blue) Is Indicative of The Planar Deformation Vibration of The CH$_2$ Groups Along The Polymer Chain Backbone. 177

5.19 GATR-FTIR Absorbance Spectra of Unmodified Gap Before (Gray) and After (Black) Etching With Buffered Hydrofluoric Acid (6:1 HF/NH$_4$F In H$_2$O) for Five Minutes. In This Figure, ν and δ Denote Stretching And Deformation (Bending) Vibrational Modes, Respectively. 178

5.20 XP Survey Spectrum of an Initial Co|PPy|GaP Sample. 178

5.21 Ga 2p Core-Level XP Spectrum of an Initial Co|PPy|GaP Sample. The Circles Are The Spectral Data, The Solid Lines Represent The Background (Light Gray), Component Fit (Red), and Overall Fit (Black). 179

5.22 P 2p Core-Level XP Spectrum of An Initial Co|PPy|GaP Sample Collected Prior to Photoelectrochemical Characterization and Associated Degradation. The Circles Are The Spectral Data, and The Solid Lines Represent The Background (Light Gray), Component Fit (Red), and Overall Fit (Black). 179

5.23 C 1s Core-Level XP Spectrum of An Initial Co|PPy|GaP Sample. The Circles Are The Spectral Data, and The Solid Lines Represent The Background (Light Gray), and Overall Fit (Black). 180

5.24 O 1s Core-Level XP Spectrum of An Initial Co|PPy|GaP Sample. The Circles Are The Spectral Data, and The Solid Lines Represent The Background (Light Gray), and Overall Fit (Black). 180

5.25 XP Survey Spectrum of A Postdegrade Co|PPy|GaP Sample. 181

5.26 Ga 2p Core-Level XP Spectrum of A Postdegrade Co|PPy|GaP Sample. The Circles Are The Spectral Data, and The Solid Lines Represent The Background (Light Gray), Component Fit (Red), and Overall Fit (Black). 181

5.27 P 2p Core-Level XP Spectrum of A Postdegrade Co|PPy|GaP Sample. The Circles Are The Spectral Data, and The Solid Lines Represent The Background (Light Gray), Component Fit (Red), and Overall Fit (Black). 182

5.28 C 1s Core-Level XP Spectrum of A Postdegrade Co|PPy|GaP Sample. The Circles Are The Spectral Data, and The Solid Lines Represent The Background (Light Gray), and Overall Fit (Black). 182

5.29 O 1s Core-Level XP Spectrum of A Postdegrade Co|PPy|GaP Sample. The Circles Are The Spectral Data, and The Solid Lines Represent The Background (Light Gray), and Overall Fit (Black). 183

Figure Page

5.30 XP Survey Spectrum of A Postrepair Co|PPy|GaP Sample............................ 183

5.31 Ga 2p Core-Level XP Spectrum of A Postrepair Co|PPy|GaP Sample. The Circles Are The Spectral Data, The Solid Lines Represent The Background (Light Gray), Component Fit (Green), and Overall Fit (Black). 184

5.32 P 2p Core-Level XP Spectrum of A Postrepair Co|PPy|GaP Sample. The Circles Are The Spectral Data, And The Solid Lines Represent The Background (Light Gray), Component Fit (Green), and Overall Fit (Black). 184

5.33 1s Core-Level XP Spectrum of A Postrepair Co|PPy|GaP Sample. The Circles Are The Spectral Data, and The Solid Lines Represent The Background (Light Gray), and Overall Fit (Black). 185

5.34 O 1s Core-Level XP Spectrum of A Postrepair Co|PPy|GaP Sample. The Circles Are The Spectral Data, and The Solid Lines Represent The Background (Light Gray), and Overall Fit (Black).. 185

5.35 Linear Sweep Voltammograms Recorded at A Scan Rate of 100 mV s^{-1} Using Unmodified Gap Working Electrodes Prior To (Solid) and Following (Dashed) Controlled-Potential Electrolysis Experiments. All Data Are Averages Obtained Using Three Separate Unmodified Gap Working Electrodes In 0.1 M Phosphate Buffer (Ph 7) As The Electrolyte And 100 mW cm^{-2} Illumination Conditions........ 186

5.36 Current Density Versus Time Plot Obtained During 15 Minutes of Controlled-Potential Electrolysis at 0 V Vs RHE Using Unmodified Gap Working Electrodes. All Data Are Averages Obtained Using Three Separate Unmodified Gap Working Electrodes in 0.1 M Phosphate Buffer (pH 7) As The Electrolyte And 100 mW cm^{-2}

Figure Page

Illumination Conditions. 186

5.37 Linear Sweep Voltammograms Recorded at A Scan Rate Of 100 mV s^{-1} Using Gap (Black), PPy|Gap (Blue), Or Co|PPy|GaP (Red) Working Electrodes in 0.1 M Phosphate Buffer (pH 7) in The Dark. All Data Are Averages Obtained Using Three Separately Prepared Working Electrodes. 187

5.38 (A) Cyclic Voltammograms of 5,10,15,20-tetra-p-tolylporphyrin Cobalt(II) (CoTTP) (0.34 Mm) Recorded in Dimethylformamide Containing 0.1 M Tetrabutylammonium Hexafluorophosphate (TBAPF6) As The Supporting Electrolyte, Ferrocene As An Internal Standard, and 0 (Solid Green) or 2,282 (Dashed Green) Equivalents Of Pyridine. (B) Cyclic Voltammogram Of CoTTP Recorded In Dimethylformamide Containing 0.1 M TBAPF6 In The Absence Of Ferrocene. This Voltammogram Is Included for Comparison Given The Overlap Between The Ferrocenium/Ferrocene (Fc^+/Fc) Redox Couple and The Redox Feature Assigned To The $Co^{iii/II}$ Couple of CoTTP. All Voltammograms Were Collected at Room Temperature Under An Argon Atmosphere Using A 3 Mm Diameter Glassy Carbon Working Electrode And Referenced To The Ferrocenium/Ferrocene Redox Couple.... 192

LIST OF ABBREVIATIONS

Abbreviation	Meaning
APCE	Absorbed Photon-To-Current Efficiency
C_A^0	Concentration of The Chemical Substrate
Co|PPy|GaP	Cobaloxime-Polypyridyl-Modified Gap
CO_2RR	Carbon Dioxide Reduction Reaction
Cobaloxime|PPy|GaAs	Cobaloxime-Polypyridyl-Modified GaAs PPy|GaAs Polypyridyl-Modified GaAs
CR	Correction Multiplier of The AC Measurement
E	Energy of A Photon at A Given Wavelength
E_{cat}	Catalyst Potential
E_{CB}	Valence Band-Edge Energy
E_F	Fermi Level
$E_{F,n}$	Non-equilibrium Steady-state Electron Population
$E_{F,p}$	Non-equilibrium Steady-state Hole Population
$E_{H+/H2}$	Thermodynamic Potential Associated With The Proton/Hydrogen Couple
E_{PQ}^0	Standard Reduction Potential Of The Catalyst
EQE	External Quantum Efficiency
E_{sol}	Solution Potential
E_{VB}	Conduction Band-Edge Energy
F	Faraday Constant
ff	Fill Factor

Ftir	Fourier-Transform Infrared
Fwhm	Full Width At Half Maximum
Gain	Gain Set For The Detector
GATR	Grazing-Angle Attenuated Total Reflectance
Glyn	Glyoximate Nitrogen Bound To Cobalt Center
HER	Hydrogen Evolution Reaction
I_0	Incident Photon Flux on The Semiconductor After Correcting For Interface Reflection And Electrolyte Absorption Losses
ICP-MS	Inductively coupled plasma mass spectrometry
IPCE	Incident Photon-to-Current Efficiency
IQE	Internal Quantum Efficiency
J_g	Minority Carrier Current Density
J_0	Limiting Current Density
j_{ph}	Photocurrent Density
$j$sc	Short-Circuit Current Density
J_p	current density due to holes
J_n	current density due to electrons
J_{SCR}	Electron Photocurrent Density in The Space-Charge Region
J_w	Electron Current Density at The Depletion Edge
k_{cat}	Pseudo First-Order Rate Constant
k	Apparent Rate Constant

L	Pathlength
LHE	Light Harvesting Efficiency
LSV	Linear Sweep Voltammogram
N	Amount of Chemical Product
Ncat	Total Amount of Catalyst on The Surface
$N_{\text{per Unit Of Time}}$	Amount of Product Generated Per Unit of Time
n	Number of Electrons Required To Form The Product
n_0	Electron Density In The Bulk
n_W	Electron Density at The Depletion Edge
PEC	Photoelectrochemical
PPy|GaAs	Polypyridyl-Modified GaAs
PPy|Gap	Polypyridyl-Modified Gap
Pv	Photovoltaics
Pyn	Pyridyl Nitrogen
PyN-Co	Pyridyl Nitrogen Bound To Cobaloxime
Q	Total Amount Of Charge Passed During The Photoelectrochemical Reaction
q	Unit Charge
q_p	Photon Flux
RHE	Reversible Hydrogen Electrode
Sr	Spectral Responsivity Of The Reference Detector
Sth	Solar-To-Hydrogen
t	Time

T	Temperature
TOF	Turnover Frequency
$\mathrm{TOF}_{\mathrm{max}}$	Potential Independent Maximum Turnover Frequency
TON	Turnover Number
TRL	Technological Readiness Level
V	Detector Voltage
$\mathrm{V}b$	Bias Potential
V_{bi}	Built-In Potential Of The Space-Charge Region
$\mathrm{V}_{\mathrm{flatband}}$	Flatband Potential
$V\mathrm{OC}$	Open-Circuit Potential
V_{ph}	Photovoltage
W_{SC}	Width Of The Space-Charge Region
XP Spectroscopy	X-ray Photoelectron Spectroscopy
α	Absorption Coefficient
η_{F}	Faradaic Efficiency
η_{o}	Overpotential
η_{u}	Underpotential
ϕ_{abs}	Probability Of Photon Absorption
Φ_{B}	Barrier Height
ϕ_{inj}	Probability Of Charge Separation
ϕ_{sep}	Probability Of Charge Transfer Across The Interface
$\Gamma_{\mathrm{C'}}$	Concentration Of Immobilized Catalysts Present In Their Activated Form

ΔG	Gibbs Free Energy Change
τ	minority carrier average lifetime

CHAPTER 1 INTRODUCTION

Portions of this chapter are excerpted and reproduced from:

Nguyen, N. P.; Moore, G. F. Storing Sunlight at Low Temperatures? *Joule* **2021**, *5*, 2254-2256 with permission from The Royal Society of Chemistry.

and

Reyes Cruz, E. A.; Nishiori, D.; Wadsworth, B. L.; Nguyen, N. P.; Hensleigh, L. K.; Khusnutdinova, D.; Beiler, A. M.; Moore, G. F. Molecular-Modified Photocathodes for Applications in Artificial Photosynthesis and Solar-to-Fuel Technologies. *Chem. Rev*. **2022**, *122*, 16051-16109 with permission from The American Chemical Society.

1.1 Solar Fuels Generation

The development of a sustainable energy-transduction systems is one of the most critical challenges facing humanity over the few decades.[1-11] Not only do humanity have to meet a huge power demand of an estimated 40 TW by 2050, we also have to access it using sustainable and environmental-friendly methods. Although fossil fuels are now abundant and accessible, these are finite resources as it is estimated that we have enough oil for 50 -150 years, natural gas for 207 to 590 years and coal for 1000 to 2000 years.[12] Carbon dioxide (CO_2) emissions from fossil fuel consumption has remarkably increased over the years, creating negative environmental impacts on our planet.[1-12]

Since Giacomo Ciamician's prediction of a solar-fueled future published in 1912,[13] scientists have been inspired by the biochemical process of photosynthesis to develop artificial leaves that use sunlight to create fuels and other value-added chemical products. Such solar-to-fuel devices could enable carbon-free or carbon-neutral pathways to powering the planet. Artificial systems capable of generating fuels from sustainable and renewable energy sources provide a strategy to satiating modern societies' energy demands, with minimal environmental impact.[14-19] Approaches to solve the energy conundrum often take inspiration from the biological process of photosynthesis that powers our biosphere and supplied the fossil fuels global economies rely on.[4-6,8-10,14-19] The functions and chemical processes of photosynthesis have inspired artificial photosynthesis systems to convert solar energy into chemical energy and store it as synthetic chemical fuels. Solar energy can be directly converted into chemical fuels via photoelectrochemical reactions. Many properties associated with solid-state heterogeneous catalysts have motivated several molecular-based, surface-modification strategies such as discrete local three-dimensional environments for binding substrates, lowering transition state energies, and releasing the products. Molecular systems also provide tunability, which can be achieved by designing the ligation environment around the catalyst.[8-19]

1.2 PV-electrolysis *versus* Photoelectrochemical systems

The construction of artificial leaves has been pursued using a continuum of design concepts. As depicted in Figure 1.1, these range from more decoupled approaches such as photovoltaic-powered electrolysis (PV-electrolysis), to more integrated designs such as those used in photoelectrochemistry (PEC). In PV-electrolysis, photovoltaic components are interconnected to power physically separated electrolyzer units. The electrolyzers contain catalysts—chemical sites providing low-energy pathways for driving energetically uphill reactions such as the splitting of water into oxygen and hydrogen. These chemical products can be used as fuels or stored for later use, including chemical upgrading. The other approach of PEC offers the same advantages regarding its chemical products, but here the light-harvesting and electrocatalytic components are co-located and/or assembled into a single architecture.[4]

Both design strategies are inspired by the biological process of photosynthesis, where plants and other organisms store the sun's energy in the form of chemical bonds that constitute the foods we eat and ultimately, on longer geological time scales, the carbon-based fossil fuels our modern societies rely on. However, key distinctions between PV-electrolysis and PEC include their technological readiness level (TRL), raw material requirements, cost, and potential for scalability. PV-electrolysis is a more mature technology that benefits from its modularity, enabling the individual components to be optimized for their integrated operation. PEC devices, on the other hand, promise simplification of device architecture and thereby lower costs, but are technologically less mature and thus remain active areas of research with correspondingly more limited market penetration.[4,20]

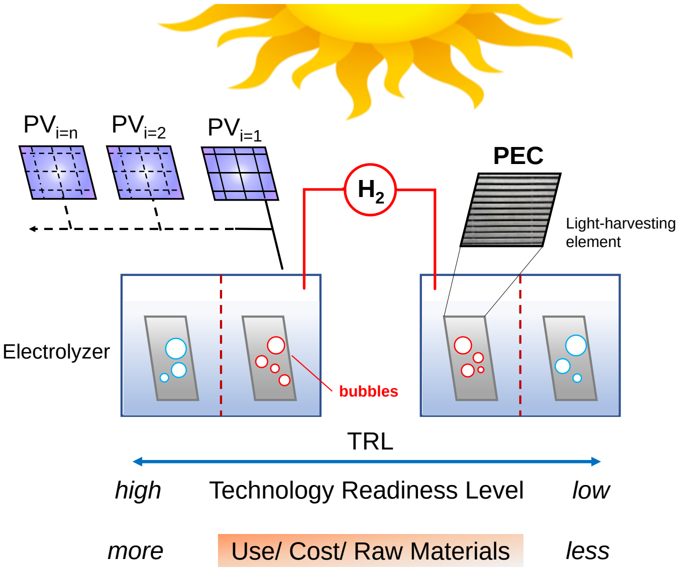

Figure 1.1. Schematic comparing photovoltaic-powered electrolysis (PV-electrolysis) (left) and photoelectrochemical (PEC) (right) device concepts, including tradeoffs in their current use, projected costs, required amount of raw materials, and current technology readiness level (TRL). Adapted with permission from ref 4. Copyright 2018 The Royal Society of Chemistry.

1.3 Artificial Photosynthesis and Photoelectrosynthetic Cells

The construction of molecular-based light-harvesting complexes and electron donor-acceptors has provided insights to fundamental principles governing energy and charge transfer processes.[21-28] This includes the construction of purely molecular assemblies as well as molecular components interfaced with solid-state materials to form dye-sensitized solar cells and dye-sensitized photoelectrosynthesis cells.[29–35] However, this thesis specifically focuses on fuel production applications involving visible-light absorbing semiconductors modified with molecular fuel-forming electrocatalysts.

Engineering of nanostructured semiconductor materials, including the synthesis of nanowire composites, can mitigate reflective losses and improve light-trapping effects.[36.37] For example, pillared nanowire arrangements have relatively long dimensions for effectively absorbing light, but also have relatively short (radial) dimensions for diffusing carriers.

Unlike conducting/metallic electrodes which have a relatively high density of states at the Fermi level, semiconducting electrodes have Fermi levels that lie within the band gap (i.e., an energy range where no electronic states can exist), and any charge transfer across the semiconductor|electrolyte solution interface occurs via the energy bands.[38] The highest energy continuum of electronic states below the Fermi level is the valence band and is fully occupied by electrons at the absolute zero temperature.[39] The lowest energy continuum of electronic states above the Fermi level is the conduction band and is vacant at the absolute zero temperature. Fermi level in semiconductors is defined as the energy level for which the occupational probability for an electron or hole is 50% in thermal equilibrium conditions,[40] and E_F is defined with respect to a reference state. The conduction band edge potential and valence band edge potential (E_{CB} and E_{VB}, respectively, with units of V versus E_{ref}), are defined as the electrode potentials of the lowest energy electronic state of the conduction band and the highest energy electronic state of the valence band, respectively. When the material absorbs particles of light with energies exceeding the energy of the semiconductor band gap energy (E_g), a transition of photoexcited electrons from the valence band to the conduction creates electron-hole pairs. Intrinsic semiconductors (i.e., undoped semiconductor materials such as Si or Ge) have less conductivity than metals because their Fermi levels lie approximately in the middle of the band gap and thus have lower free carrier concentrations in the dark (about 1010 cm–3 at 300 K in the case of Si with Eg = 1.11 eV).[41] However, the addition of electron-accepting impurities (dopants) can shift the E_F toward the E_{VB} and increase their conductivity. Conversely, the addition of dopants that are electron-donating can shift the E_F toward the E_{CB} and increase their conductivity. Materials doped with electron-accepting impurities are referred to as p-type semiconductors, whereas those doped with electron-donating impurities are referred to as n-type semiconductors.

Upon contacting a semiconductor with a liquid, a semiconductor|liquid junction is formed, and the difference in potential between the semiconductor Fermi level (E_F) and the potential of the liquid solution (which is defined by the Nernst equation and the concentrations of reduced and oxidized species) must equilibrate. This equilibration process occurs via an exchange of carriers across the resulting interface until the potential of the semiconductor and solution are the same and equilibrium is established. In the case of p-type semiconductors, the energetic positioning of the E_F, which is relatively closer to the E_{VB} rather than the E_{CB}, causes the material to behave like an anode in the dark. Thus, equilibrium between E_F and the solution potential results in the net transfer of holes from the semiconductor to the solution (**Figure 1.2a and 1.2b**).[42,43] This movement of charge across the semiconductor liquid interface yields a difference in potential within the semiconductor and a built-in voltage (V_{bi}, defined as the built-in potential corresponding to the potential drop across the space charge region). For a p-type semiconductor, this potential difference is manifested as a 'downward' bending (**Figure 1.2b and 1.2c**) of the E_{CB} and E_{VB} due to the net removal of holes from the semiconductor and the concomitant 'drop' in electric-field intensity within the semiconductor.

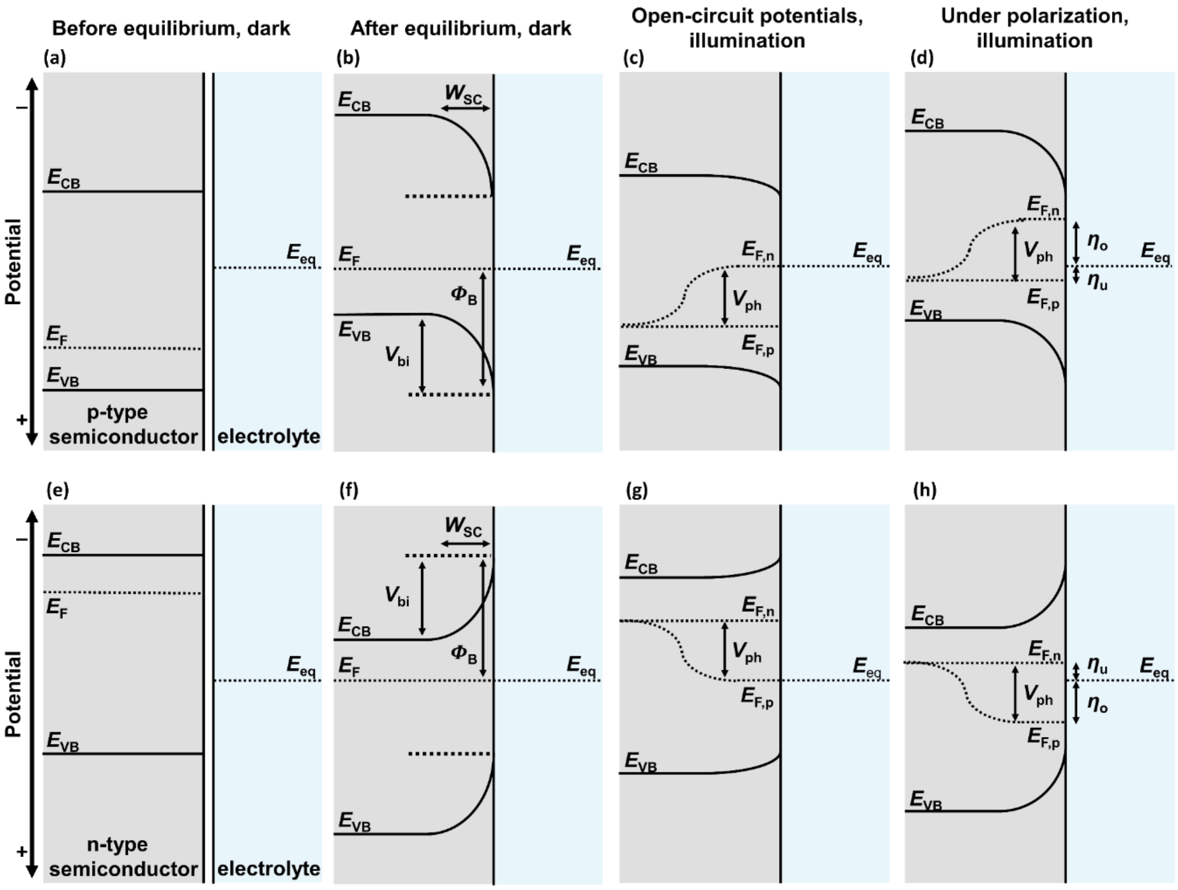

Figure 1.2. Illustration of a p-type (a–d) and n-type (e–h) semiconductor showing the energy level of conduction band-edge potential (E_{CB}), valence band-edge potential (E_{VB}),

Fermi level (E_F), quasi-Fermi levels of electrons ($E_{F,n}$) and holes ($E_{F,p}$), and solution potential (E_{sol}), along with associated differences in potential. (a and e) before equilibrium, (b and f) after equilibration with electrolyte in the dark, (c and g) under illumination in steady-state conditions under the open-circuit potential, and (d and h) under illumination in steady-state conditions under applied bias potentials. Eeq is the equilibrium potential equal to the reduction potential of the half-reaction (Ox + ne– ⇄ Red. W_{sc} is the width of the space-charge region, V_{ph} is the photovoltage, V_{bi} is the built-in potential of the space-charge region, and η_o is the overpotential, and η_u is the underpotential. The barrier height, ϕ_B, is the maximum internal energy that can be extracted from an electron–hole pair. Figures are adapted from Reyes Cruz et al. Molecular-Modified Photocathodes for Applications in Artificial Photosynthesis and Solar-to-Fuel Technologies. Chem. Rev. 2022, 122, 16051-16109.

Under illumination of the semiconductor material with a photon flux of energy greater than the band-gap width ($h\nu > E_g$) causes absorption of photons and generation of electron–hole pairs. As a result of the generation, an increase in the concentration of the excess electrons in the conduction band and the excess holes in the valence band takes place. This creates a hole quasi- Fermi level ($E_{F,p}$) and electron quasi-Fermi level ($E_{F,n}$) that are related to E_{VB} and E_{CB}, respectively, as given in Eq. 1.1a and 1.1.b,[44,45]

$$E_{\mathrm{F,p}} = E_{\mathrm{VB}} + \frac{RT}{F}\ln\left(\frac{p}{N_{\mathrm{V}}}\right) \qquad \text{(Eq. 1.1a)}$$

$$E_{\mathrm{F,n}} = E_{\mathrm{CB}} - \frac{RT}{F}\ln\left(\frac{n}{N_{\mathrm{C}}}\right) \qquad \text{(Eq. 1.1.b)}$$

where N_C and N_V are the conduction and valence band densities of states. n (= $n_{eq} + \Delta n$) and p (= $p_{eq} + \Delta p$) are non-equilibrium steady-state concentration of electrons and holes respectively, n_{eq} and p_{eq} are semiconductor electron and hole concentrations in the dark, respectively. When a semiconductor is illuminated, equal excess concentrations (Δn and Δp) of electrons in the conduction band and holes in the valence band are created. For a p-type semiconductor, the equilibrium electron density in the dark is very low, $p_{eq} + \Delta p \approx p_{eq}$, $E_{F,p}$ is position-independent and approximately equal in value to the majority-carrier Fermi level in the bulk.[46] However, since $n_{eq} + \Delta n \gg n_{eq}$, illumination results in $E_{F,n}$ that is position-dependent and displaced toward E_{CB} as shown in Figure. 1.2c and 1.2d. Since for an n-type semiconductor, the equilibrium hole density in the dark is very low, $n_{eq} + \Delta n \approx n_{eq}$, so that the electron quasi-Fermi level ($E_{F,n}$) is almost the same as in the equilibrium Fermi level E_F in the dark. However, since $p_{eq} + \Delta p >> p_{eq}$, the quasi-Fermi level for holes ($E_{F,p}$) is displaced downward toward the valence band, increasing the driving force for oxidation reactions, as shown in Figure 1.2f and 1.2g.

This splitting of E_F of a semiconductor into two quasi-Fermi levels associated with non-equilibrium steady-state electron, $E_{F,n}$, and hole, $E_{F,p}$, populations gives rise to a corresponding photovoltage, V_{ph}, and a decrease in the degree of band bending (Figure 1.2c and 1.2g). The photovoltage (V_{ph}) is defined as the difference in the electron and hole quasi-Fermi levels at the semiconductor surface under illumination) and can be obtained via measurement of E_{eq} in the dark versus the open-circuit potential under illumination, E_{oc}.[42] The maximum V_{ph} of a semiconductor is smaller than the band gap due to the intrinsic bulk recombination, and the presence of surface states can further reduce V_{ph} by lowering the barrier height (φ_B) (which is the maximum internal energy that can be extracted from electron–hole pairs). Forward electrochemical biasing of the semiconductor enhances the band bending and the fraction of minority-carrier electrons reaching the semiconductor surface. For an ideal p-type semiconductor,[47] the driving force for the cathodic reaction at the semiconductor|liquid interface is equal to the difference between $E_{F,n}$ and the solution potential. For an ideal n-type semiconductor,[47] the driving force for the anodic reaction at the semiconductor|liquid interface is equal to the difference between $E_{F,p}$ and the solution potential.[45] In both cases, the position of the quasi-Fermi level associated with the minority carriers is dependent on the applied potential (V) as well as the illumination intensity (which also affects the value of V_{ph}). In the example of a p-type semiconductor, as $E_{F,n}$ changes, the associated rate constant for electron transfer remains constant and is independent of V and illumination intensity.[45] Thus, for a well-behaved semiconductor electrode, the dependence of J (a reaction rate) on the electrochemical potential (a driving force) is established by changing the degree of band bending within the semiconductor, which in turn controls the steady-state concentration of minority charge carriers reaching the electrode surface.[47] This is in stark contrast to electrocatalytic reactions involving conducting metallic electrodes, where the potential of the electrode is defined by a single E_{F} and differences in V appear mostly outside the electrode in the solution phase. Thus, in accordance with Marcus-Hush-Levich theory and Butler-Volmer kinetics,[60–64] enhancement of electrocatalytic reaction rates upon increasing the η is due to the driving-force-dependent nature of the charge-transfer rate constant, not changes in the surface concentrations of charge carriers.

The current density produced by a semiconductor|liquid junction under illumination has been modeled by Gärtner.[48,49] For p-type semiconductors, which are a focus of this review, the minority carrier current density (J_{g}) is obtained by summing the electron current density at the depletion edge (J_{w}) (*i.e.*, the boundary between the space-charge region and bulk semiconductor) and the electron photocurrent density in the space-charge region (J_{SCR}) when recombination effects within the space-charge region and at the interface are neglected (Eq. 2 – Eq. 4):

$$J_g = J_w + J_{SCR} \qquad \text{(Eq. 2)}$$

$$J_w = J_0 \left[\frac{n_w}{n_0} - 1\right] - qI_0 \alpha L \frac{e^{(-\alpha W)}}{1+\alpha L} \qquad \text{(Eq. 3)}$$

$$J_{SCR} = -qI_0(1 - e^{-\alpha W}) \qquad \text{(Eq. 4)}$$

In Eq. 2 – Eq. 4, n_{w} is the electron density at the depletion edge, n_0 is the electron density in the bulk, q is the unit charge, I_0 is the incident photon flux on the semiconductor after correcting for interface reflection and electrolyte absorption losses, α is the absorption coefficient of the photoelectrode, and J_0 is the limiting current density. As the electron concentration in the bulk (n_0) is relatively small, $|J_w|$ is limited to J_0 as shown in Eq. 5 in the absence of illumination, even at large applied V_{b}:

$$|J_w| \approx J_0 = \frac{qn_0L}{\tau} \qquad \text{(Eq. 5)}$$

where τ is the minority carrier average lifetime. Under the boundary condition used in the Gärtner model, where $n_{\mathrm{w}} = 0$ at the depletion edge, J_{g} can be expressed as shown in Eq. 6:

$$J_g = -J_0 - qI_0\left(1 - \frac{e^{-\alpha W}}{1+\alpha L}\right) \qquad \text{(Eq. 6)}$$

In this form, the equation addresses monochromatic illumination conditions. To address broad-band illumination conditions, integration can be applied over a selected spectral range. In summary, the Gärtner model gives a relatively simplified description of the current density produced upon illumination of a photoelectrode where carrier recombination within the space-charge region is not accounted for. Thus the predicted current can deviate from experimental results under conditions where the band bending is relatively low and recombination rates are relatively high.[45]

The Gärtner model was further extended by Reichman[49] to account for contributions from recombination in the space-charge region. In this revised model, the current density due to holes (J_p) and electrons (J_n) is described in terms of the surface concentrations of charge carriers (p_s and n_s) relative to their values at equilibrium (p_{s0} and n_{s0}), meaning the surface concentrations of charge carriers when no net current flows as expressed in Eq.7a and 7b, respectively:

$$J_p = J_p^0 \left[\frac{p_s}{p_{s_0}} - 1\right] \quad \text{(Eq. 7a)}$$

$$J_n = -J_n^0 \left[\frac{n_s}{n_{s_0}} - 1\right] \quad \text{(Eq. 7b)}$$

where J_p^0 and J_n^0 are the exchange current densities (*i.e.*, the current densities at equilibrium where no net current flows) for holes and electrons, respectively. For a p-type semiconductor under illumination, the surface concentration of holes (defined as p_s/p_{s0}) is a function of V and is independent of the light intensity (Eq. 8a).[49] Conversely, the surface concentration of electrons (n_s/n_{s0}) is a function of V as well as the illumination intensity, and is dependent on recombination losses in the space-charge region (K_r) ((Eq.8 – Eq. 11):

$$\frac{p_s}{p_{s_0}} = e^{\frac{qV}{k_BT}} \quad \text{(Eq. 8a)}$$

$$\frac{n_s}{n_{s_0}} = \left(\frac{-K_r + \left({K_r}^2 + 4AB\right)^{\frac{1}{2}}}{2A}\right)^2 \quad \text{(Eq. 8b)}$$

$$K_r = \frac{\pi k_B T n_i W}{4\tau(V_{bi} - V)} \cdot e^{\frac{qV}{2k_BT}} \quad \text{(Eq. 9)}$$

$$A = J_n^0 + J_0 \cdot e^{\frac{qV}{k_B T}} \qquad \text{(Eq. 10)}$$

$$B = J_n^0 - J_g \qquad \text{(Eq. 11)}$$

where n_i is the intrinsic carrier concentration and V is the applied potential.

1.4 Molecular-Modified Electrodes for Electrocatalysis and Photoelectrosynthesis

Advances in interfacial chemistry and rational synthetic design have accelerated development of catalyst-modified semiconductors that convert energy between photonic, electronic, and chemical forms. These constructs hold promise for unleashing renewable-energy technologies that convert sunlight to fuels and other value-added chemical products. Various functionalization strategies and characterization methods have been used to assemble and study visible-light-absorbing semiconductors modified with molecular, fuel-forming catalysts.[29-36,50-52] Such constructs have demonstrated promising performance; however, there is currently insufficient understanding of how charge carriers move through these systems to provide rational design principles. Related to this, the development of new methods to interface electrocatalysts with semiconductor electrodes and characterize the resulting assemblies are active areas of research investigation undertaken by both relatively large collaborative teams and individual research groups.

Although the current availability of ligand platforms able to withstand oxidative operating conditions may limit their applications, in general, molecular-based modification of semiconductors offers opportunities to combine the relatively high activity, selectivity, and tunability of molecular components with the favorable solar energy capture and conversion properties of solid-state semiconducting materials.

The immobilization of molecular electrocatalysts to a semiconductor surface results in formation of semiconductor|catalyst interfaces. When these modified semiconductors are immersed in liquids, semiconductor|catalyst|liquid junctions are formed. Application of relatively thick catalytic films (i.e., those that are ion-impermeable and can be formed by metallic electrocatalytic coatings) give rise to ‘buried’ junctions. Under these conditions, the catalytic processes occurring at the catalyst|liquid interface are physically separated from the photovoltage generation and charge separation processes occurring at the semiconductor|catalyst interface.[53,54] Unlike semiconductor|liquid junctions, the E_{CB} and E_{VB} edges associated with ‘buried’ junctions are not required to straddle the thermodynamic potentials of the redox half-reactions occurring in the liquid phase because the photovoltages are not fixed relative to a material-specific flatband potential ($V_{flatband}$).[42,54] Thus, the overall system is analogous to having a photovoltaic connected in series with an electrochemical load. Alternatively, catalytic surface coatings that are ion-permeable, including molecular catalyst layers and coatings of porous oxide materials, form interfaces that have been referred to as ‘adaptive’ junctions.[55,56] Because the electrocatalyst layer (molecular or other) is permeable to the electrolyte solution, the maximum internal energy that can be extracted from electron – hole pairs (i.e., the barrier height) increases as a function of the catalyst redox states.[53] Thus, in comparison with non-porous metallic electrocatalyst coatings, the ‘adaptive’ junctions do not require a potential drop across the electrocatalyst|liquid interface as the free motion of ions from the electrolyte solution enables the potential drop to occur mostly inside the semiconductor across the space-charge region. For this reason, the E_{CB} and E_{VB} band edge positions associated with adaptive junctions must be appropriately positioned with respect to their potentials and the thermodynamics of the fuel-forming half-reactions (e.g., for a photocathode driving a reductive chemical process, the E_{CB} needs to be poised negative of the fuel-forming half-reaction equilibrium potential).

1.5 Efficiencies of Photochemical Systems

The efficiencies of photoelectrochemical systems can be broadly separated into either benchmarking- or diagnostic- type efficiencies. *Benchmarking efficiencies* are ratios of total power output to total power input. In the case of solar photoelectrochemical hydrogen production from water, this is the solar-to-hydrogen (STH) conversion efficiency; however, related equations for other chemical products can be expressed more generally as solar-to-fuel (STF) conversion efficiency.[54,57,58] As shown in Eq. 1.12,[59] the STF conversion efficiency is the ratio of chemical power produced to total incident solar power. In this particular example involving hydrogen evolution and STH, the chemical power is the product of the Gibbs free energy change (ΔG) per mole of hydrogen gas (H_2) formed via the splitting of water (237.14 kJ mol H_2^{-1} at 25 ^{o}C) and the rate of hydrogen evolution, which can be determined via chemical analysis methods. The total incident solar power is the product of the area of the light absorber and the incident illumination power density (P_{total}), which is 100 mW cm^{-2} under air mass 1.5 global tilt (AM 1.5 G)[59,60] conditions. As shown in Eq. 1.13, the chemical energy output can also be expressed as the product of the thermodynamic potential of the overall chemical reaction (1.23 V in the case of water-splitting), the short circuit current density (j_{SC}), and the faradaic efficiency of the reaction (η_F).[52] This latter approach involves (photo)electrochemical methods of determining the chemical energy output, but also requires knowledge (or an assumption) of η_F, which as shown in Eq 1.14 is the ratio of the amount of chemical product (N) to the total amount of charge passed during the photoelectrochemical reaction (Q) multiplied by the Faraday constant (F) and the number of electrons required to form the product (n).

$$STH = \left[\frac{(237\ kJ\ mol\ H_2{}^{-1}) \times (mol\ H_2\ s^{-1})}{Area\ (cm^2) \times P_{total}\ (mW\ cm^{-2})}\right]_{AM\ 1.5\ G} \qquad \text{(Eq. 1.12)}$$

$$STH = \left[\frac{(1.23\ V) \times |j_{SC}\ (mA\ cm^{-2})| \times \eta_F}{P_{total}\ (mW\ cm^{-2})}\right]_{AM\ 1.5\ G} \qquad \text{(Eq. 1.13)}$$

$$\eta_F = \frac{n \times N\ (mol) \times F\ (C\ mol^{-1})}{Q\ (C)} \qquad \text{(Eq. 1.14)}$$

Unlike benchmarking efficiencies, which strictly involve measurements using two-electrodes (*i.e.*, a cathode and an anode) with no electrochemical or chemical biasing, *diagnostic efficiencies* can involve applications of bias potentials and/or the use of three-electrodes (*i.e.*, working, counter, and reference electrodes) which enable decoupling and determination of kinetic and thermodynamic properties associated with the cathode or anode components of a photoelectrochemical cell. The applied bias photon-to-current efficiency (ABPE) is an example of a diagnostic efficiency and it differs from the STH because it involves application of a bias potential (V_b) between the working and counter electrode to produce a photocurrent density (j_{ph}), as shown in Eq. 1.15:[52]

$$ABPE = \left[\frac{[1.23\ V - |V_b|\ (V)] \times j_{ph}\ (mA\ cm^{-2})}{P_{total}\ (mW\ cm^{-2})}\right]_{AM\ 1.5\ G} \qquad \text{(Eq. 1.15)}$$

If an ABPE is reported for a three-electrode measurement, it is recommended the potential difference between the working electrode and the counter electrode as well as the potential difference between the working electrode and reference electrode are reported.[59]

Other diagnostic-type efficiencies involve counting of particles rather than energy or power. For example, the external quantum efficiency (EQE) (sometimes referred to as the incident photon-to-current efficiency (IPCE)) is defined as the ratio of electron flux measured as current to incident photon flux (*i.e.*, particles of light, and not power of light) as shown in Eq. 1.16. EQE can also be defined as the product of the probability of photon absorption (Φ_{abs}), the probability of charge separation (Φ_{sep}), and the probability of charge injection across a semiconductor junction (Φ_{inj}). As shown in Eq. 1.17. Φ_{abs} represents the fraction of incident photons absorbed by a material and is synonymous with the terms light harvesting efficiency (LHE) as well as absorptance. The internal quantum efficiency (IQE) (sometimes referred to as the absorbed photon-to-current efficiency (APCE)), represents another type of benchmarking efficiency, and it is defined as the ratio of electron flux measured as current to absorbed photon flux as shown in Eq. 1.18.[59] IQE can also be defined as the product of Φ_{sep} and Φ_{inj}, and is thus equal to the EQE divided by LHE.

$$EQE = IPCE = \frac{electrons\ (cm^{-2}\ s^{-1})}{incident\ photons\ (cm^{-2}\ s^{-1})} = \Phi_{abs}\Phi_{sep}\Phi_{inj} \qquad \text{(Eq. 1.16)}$$

$$\Phi_{abs} = LHE = \frac{absorbed\ photons\ (cm^{-2}\ s^{-1})}{incident\ photons\ (cm^{-2}\ s^{-1})} \qquad \text{(Eq. 1.17)}$$

$$IQE = APCE = \frac{electrons\ (cm^{-2}\ s^{-1})}{absorbed\ photons\ (cm^{-2}\ s^{-1})} = \Phi_{sep}\Phi_{inj} \qquad \text{(Eq. 1.18)}$$

Although they are not necessarily types of efficiencies, parameters for describing durability and activity include the turnover number (TON) and turnover frequency (TOF). TON is defined as the number of moles of substrate transformed by one mole of catalyst. and TOF is the time derivative of TON.[60] For one-electron reduction reactions and two-electron reduction reactions where the first one-electron reaction between the catalyst and substrate is rate-determining,[60] TON and TOF are expressed using Eq. 1.19 and 1.20:

$$TON = \frac{N}{N_{cat}} = \frac{kC_A^0\, t}{1+exp\left[\frac{F}{RT}\left(E-E_{PQ}^0\right)\right]} \qquad \text{(Eq. 1.19)}$$

$$TOF = \frac{N_{per\ unit\ of\ time}}{N_{cat}} = \frac{kC_A^0}{1+exp\left[\frac{F}{RT}\left(E-E_{PQ}^0\right)\right]} \qquad \text{(Eq. 1.20)}$$

where N is the amount of chemical product, N_{cat} is the total amount of catalyst on the surface, k is the apparent rate constant associated with the catalytic reaction, $C_{\mathrm{A}}{}^0$ is the concentration of the chemical substrate, t is time, E is the electrode potential, $E_{\mathrm{PQ}}{}^0$ is the standard reduction potential of the catalyst, R is the gas constant, T is the temperature, and $N_{\text{per unit of time}}$ is the amount of product generated per unit of time. When the electrode activity is limited only by kinetics associated with chemical catalysis, and not by electron-transfer kinetics or mass-transfer phenomena, all the catalysts at the electrode surface are effectively in their activated forms and the concentration of chemical substrate at the electrode surface is approximately equal to its bulk concentration. Under these conditions, the plateau current of the voltammogram will not increase upon increasing the scan rate, and the TOF equals the maximum turnover frequency ($\mathrm{TOF_{max}}$) as shown in Eq. 21:[60]

$$TOF_{max} = kC_A^0 \qquad \text{(Eq. 1.21)}$$

Given that electron flux can be expressed as a product of n (the number of electrons required for the reaction), TOF, Γ_{CT} (per geometric area density of the total catalyst), and Avogadro constant (NA), Eq. 1.16 can be transformed into Eq. 1.22, which shows the connection between EQE and TOF:

$$EQE = \frac{n \times TOF\ (s^{-1}) \times \Gamma_{C_T}\ (mol\ cm^{-2}) \times N_A\ (mol^{-1})}{incident\ photons\ (cm^{-2}\ s^{-1})} \qquad \text{(Eq. 1.22)}$$

If the photoelectrosynthetic illumination intensity, charge transfer rate constants, and the concentration of chemical substrates are sufficiently high, TOF in Eq. 1.22 will be replaced with TOF_{max} upon sufficiently biasing the electrode potential, meaning that the overall efficiency (EQE) associated with the fuel-forming reaction can become limited by the value of TOF_{max}.

For all types of efficiencies reported in the literature, it is informative to know where the counting starts (e.g., number of incident photons or incident power versus number of absorbed photons or absorbed power) and where the counting ends (e.g., carriers measured as current moving a potential versus enthalpies or Gibbs free energies associated with the chemical products). The implementation and limitations associated with these types of efficiencies have been described elsewhere. The implementation and limitations associated with these types of efficiencies have been described elsewhere.[47,49] While these efficiency calculations provide a standardized approach for making comparisons between photoelectrochemical assemblies, other important considerations include monetary costs and stability of the materials.[11,60]

1.6 Outlook and Conclusion

Outstanding challenges in the field of solar fuels and artificial photosynthesis include not only achieving higher efficiencies, but also fabricating materials that use relatively low-cost components that are robust and thus scalable. In the context of hydrogen production, how to store and transport this product for applications in global markets also remains an outstanding issue. Further challenges include using the principles of green catalysis to reengineer or entirely recreate the processes and technologies required to produce the range of chemicals our modern societies rely on. This includes manufacturing reduced forms of carbon dioxide and dinitrogen as well as creating imaginative ways of rebalancing the planet's phosphorus cycle.

This dissertation focuses on synthesizing, characterizing and performance evaluation of hybrid photoelectrosynthetic assemblies for hydrogen evolution and carbon dioxide reduction. Synthetic strategies for immobilizing molecular electrocatalysts onto solid-state conductive/semiconducting surfaces using polymeric interfaces are explored and analyzed with various surface-sensitive spectroscopic techniques.

These systems are utilized to investigate fuel forming reactions and identify fundamental performance-limiting bottlenecks encountered at relatively high rates of fuel formation. The key findings and discussions are likely relevant to other materials and chemical transformations involving proton-transfer reactions. Thus, the photoelectrochemical techniques highlighted in this work (including applications of varying electrochemical polarization, pH, illumination intensity, and scan rate) provide a general yet useful strategy for better understanding, and ultimately controlling, the performance of catalyst-modified semiconductors.

1.7 References

(1) Hemminger, J.; Fleming, G. R.; Ratner, M. A. Directing Matter and Energy: Five Challenges for Science and the Imagination; U.S. Government Printing Office: Washington, DC, 2007.

(2) Ort, D. R.; Merchant, S. S.; Alric, J.; Barkan, A.; Blankenship, R. E.; Bock, R.; Croce, R.; Hanson, M. R.; Hibberd, J. M.; Long, S. P.; Moore, T. A.; Moroney, J.; Niyogi, K. K.; Parry, M. A. J.; Peralta-Yahya, P. P.; Prince, R. C.; Redding, K. E.; Spalding, M. H.; van Wijk, K. J.; Vermaas, W. F. J.; von Caemmerer, S.; Weber, A. P. M.; Yeates, T. O.; Yuan, J. S.; Zhu, X. G. Redesigning Photosynthesis to Sustainably Meet Global Food and Bioenergy Demand. Proc. *Natl. Acad. Sci*. **2015**, *112* (28), 8529–8536.

(3) Smil, V. Harvesting the Biosphere: The Human Impact. *Popul. Dev. Rev*. **2011**, *37* (4), 613–636.

(4) Ardo, S.; Rivas, D. F.; Modestino, M. A.; Greiving, V. S.; Abdi, F. F.; Llado, E. A.; Artero, V.; Ayers, K.; Battaglia, C.; Becker, J.-P.; Bederak, D.; Berger, A.; Buda, F.; Chinello, E.; Dam, B.; Di Palma, V.; Edvinsson, T.; Fuji, K.; Gardeniers, H.; Geerlings, H.; Hashemi, S. M. H.; Haussener, S.; Houle, F.; Huskens, J.; James, B. D.; Konrad, K.; Kudo, A.; Kunturu, P. P.; Lohse, D.; Mei, B.; Miller, E. L.; Moore, G. F.; Muller, J.; Orchard, K. L.; Rosser, T. E.; Saadi, F. H.; Schüttauf, J.-W.; Seger, B.; Sheehan, S. W.; Smith, W. A.; Spurgeon, J.; Tang, M. H.; van de Krol, R.; Vesborg, P. C. K.; Westerik, P. Pathways to Electrochemical SolarHydrogen Technologies. *Energy Environ. Sci.* **2018**, *11*(10), 2768–2783.

(5) Faunce, T. A.; Lubitz, W.; Rutherford, A. W.; MacFarlane, D.; Moore, G. F.; Yang, P.; Nocera, D. G.; Moore, T. A.; Gregory, D. H.; Fukuzumi, S.; Yoon, K. B.; Armstrong, F. A.; Wasielewski, M. R.; Styring, S. Energy and Environment Policy Case for a Global Project on Artificial Photosynthesis. *Energy Environ. Sci*. **2013**, *6* (3), 695–698.

(6) Faunce, T.; Styring, S.; Wasielewski, M. R.; Brudvig, G. W.; Rutherford, A. W.; Messinger, J.; Lee, A.F.; Hill, C.L.; Degroot, H.; Fontecave, M.; MacFarlane, D.

R.; Hankamer, B.; Nocera, D. G.; Tiede, D. M.; Dau, H.; Hiller, W.; Wang, L.; Amal, R. Artificial Photosynthesis as a Frontier Technology for Energy Sustainability. *Energy Environ. Sci.* **2013,** *6* (4), 1074–1076.

(7) Gray, H. B, Powering the Planet with Solar Fuel. *Nat. Chem*. **2009**, *1*, 7.

(8) Najafpour, M. M.; Barber, J.; Shen, J.-R.; Moore, G. F. Running on Sun. *Chem. World* **2012**, 43.

(9) Hambourger, M.; Moore, G. F.; Kramer, D. M.; Gust, D.; Moore, A. L.; Moore, T. A. Biology and Technology for Photochemical Fuel Production. *Chem. Soc. Rev*. **2009**, *38* (1), 25–35.

(10) Lewis, N. S. Research Opportunities to Advance Solar Energy Utilization. *Science* **2016**, *351* (6271), aad1920.

(11) Blankenship, R. E.; Tiede, D. M.; Barber, J.; Brudvig, G. W.; Fleming, G.; Ghirardi, M.; Gunner, M. R.; Junge, W.; Kramer, D. M.; Melis, A; Moore, T. A.; Moser, C. C.; Nocera, D. G.; Nozik, A. J.; Ort, D. R.; Parson, W. W.; Prince, R. C.; Sayre, R. T. Comparing Photosynthetic and Photovoltaic Efficiencies and Recognizing the Potential for Improvement. *Science* **2011**, *332* (6031), 805–809.

(12) Lewis, N. S., and Nocera, D. G., Powering the planet: Chemical challenges in solar energy utilization, *Proc. Natl. Acad. Sci.* **2006**, *103*, 15729 – 15735.

(13) Ciamician, G. The Photochemistry of the Future. Science 1912, 36, 385−394.

(14) Tran, P. D.; Wong, L. H.; Barber, J.; Loo, J. S. C. Recent Advances in Hybrid Photocatalysts for Solar Fuel Production. *Energy Environ. Sci.* **2012**, *5*, 5902-5918.

(15) Woolerton, T. W.; Sheard, S.; Chaudhary, Y. S.; Armstrong, F. A. Enzymes and Bio-Inspired Electrocatalysts in Solar Fuel Devices. *Energy Environ. Sci*. **2012**, *5* (6), 7470–7490.

(16) Nozik, A. J. Photoelectrochemistry: Applications to Solar Energy Conversion. *Annu. Rev. Phys. Chem*. **1978**, *29* (1), 189–222.

(17) Bard, A. J.; Fox, M. A. Artificial Photosynthesis: Solar Splitting of Water to Hydrogen and Oxygen. *Acc. Chem. Res.* **1995**, *28* (3), 141–145.

(18) Gust, D.; Moore, T. A.; Moore, A. L. Solar Fuels via Artificial Photosynthesis. *Acc. Chem. Res.* **2009**, *42* (12), 1890–1898.

(19) Moore, G. F.; Brudvig, G. W. Energy Conversion in Photosynthesis: A Paradigm for Solar Fuel Production. *Annu. Rev. Condens. Matter Phys*. **2011**, *2* (1), 303–327.

(20) Modestino, M. A. and Haussener, S. An Integrated Device View on Photo-Electrochemical Solar-Hydrogen Generation. *Annu. Rev. Chem. Biomol. Eng*., **2015**, *6*, 13-34.

(21) Alcala-Torano, R.; Sommer, D. J.; Bahrami Dizicheh, Z.; Ghirlanda, G. Methods in Enzymology, Volume 580: Peptide, Protein and Enzyme Design; Academic Press: Cambridge, **2016**; p 389−416.

(22) Sakimoto, K. K.; Kornienko, N.; Yang, P. Cyborgian Material Design for Solar Fuel Production: The Emerging Photosynthetic Biohybrid Systems. *Acc. Chem. Res.* **2017**, *50*, 476−481.

(23) Berggren, G.; Adamska, A.; Lambertz, C.; Simmons, T. R.; Esselborn, J.; Atta, M.; Gambarelli, S.; Mouesca, J. M.; Reijerse, E.; Lubitz, W.; et al. Biomimetic assembly and activation of [FeFe]-hydrogenases. *Nature* **2013**, *499*, 66−69.

(24) Slater, J. W.; Marguet, S. C.; Monaco, H. A.; Shafaat, H. S. Going beyond Structure: Nickel-Substituted Rubredoxin as a Mechanistic Model for the [NiFe] Hydrogenases. *J. Am. Chem. Soc*. **2018**, *140*, 10250−10262.

(25) Helm, M. L.; Stewart, M. P.; Bullock, R. M.; Dubois, M. R.; Dubois, D. L. A Synthetic Nickel Electrocatalyst with a Turnover Frequency Above 100,000 s−1 for H_2 Production. *Science* **2011**, *333*, 863−866.

(26) Das, A. K.; Engelhard, M. H.; Bullock, R. M.; Roberts, J. A. S. A Hydrogen-Evolving $Ni(P_2N_2)_2$ Electrocatalyst Covalently Attached to a Glassy Carbon Electrode: Preparation, Characterization, and Catalysis. Comparisons with the Homogeneous Analogue. *Inorg. Chem*. **2014**, *53*, 6875−6885.

(27) Leung, J. J.; Warnan, J.; Nam, D. H.; Zhang, J. Z.; Willkomm, J.; Reisner, E. Photoelectrocatalytic H2 evolution in water with molecular catalysts immobilised

on p-Si via a stabilising mesoporous TiO_2 interlayer. *Chem. Sci.* **2017**, *8*, 5172−5180.

(28) Reback, M. L.; Ginovska-Pangovska, B.; Ho, M. H.; Jain, A.; Squier, T. C.; Raugei, S.; Roberts, J. A. S.; Shaw, W. J. The Role of a Dipeptide Outer-Coordination Sphere on H_2-Production Catalysts: Influence on Catalytic Rates and Electron Transfer. *Chem. Eur. J.* **2013**, *19*, 1928−1941.

(29) Ginovska-Pangovska, B.; Dutta, A.; Reback, M. L.; Linehan, J. C.; Shaw, W. J. Beyond the Active Site: The Impact of the Outer Coordination Sphere on Electrocatalysts for Hydrogen Production and Oxidation. *Acc. Chem. Res*. **2014**, *47*, 2621−2630.

(30) Gust, D.; Moore, T. A.; Makings, L. R.; Liddell, P. A.; Nemeth, G. A.; Moore, A. L. Photodriven Electron Transfer in Triad Molecules: A Two-Step Charge Recombination Reaction. *J. Am. Chem. Soc*. **1986**, *108*, 8028−8031.

(31) Yang, J.; Yoon, M. C.; Yoo, H.; Kim, P.; Kim, D. Excitation energy transfer in multiporphyrin arrays with cyclic architectures: Towards artificial light-harvesting antenna complexes. *Chem. Soc. Rev*. **2012**, *41*, 4808−4826.

(32) Rudolf, M.; Kirner, S. V.; Guldi, D. M. A multicomponent molecular approach to artificial photosynthesis - the role of fullerenes and endohedral metallofullerenes. *Chem. Soc. Rev*. **2016**, *45*, 612−630.

(33) Kosco, J.; Moruzzi, F.; Willner, B.; McCulloch, I. Photocatalysts Based on Organic Semiconductors with Tunable Energy Levels for Solar Fuel Applications. *Adv. Energy Mater*. **2020**, *10*, 2001935.

(34) Cheng, Y.-Z.; Ding, X.; Han, B.-H. Porous Organic Polymers for Photocatalytic Ca Carbon Dioxide Reduction. *ChemPhotoChem* **2021**,*5*, 406−417.

(35) X.; Fan, K.; Li, F.; Sun, L. Molecular Engineering of Photocathodes based on Polythiophene Organic Semiconductors for Photoelectrochemical Hydrogen Generation. *ACS Appl. Mater. Interfaces* **2021**, *13*, 40602−40611.

(36) Guldi, D. M. Fullerene-porphyrin architectures; photosynthetic antenna and reaction center models. *Chem. Soc. Rev*. **2002**, *31*, 22−36.

(37) Alstrum-Acevedo, J. H.; Brennaman, M. K.; Meyer, T. J. Chemical Approaches to Artificial Photosynthesis. 2. *Inorg. Chem*. **2005**, *44*, 6802−6827.

(38) Memming, R, Semiconductor Electrochemistry, 2nd Ed, *John Wiley & Sons, Incorporated*, **2015**, 169–266.

(39) Alverty, R. A, and Silbey, and R.J. Physical Chemistry, 1st Ed. *Wiley & Sons*, **1992**.

(40) Ramette. R. W., *J. Chem. Edu*. **1987**, *64*, 885.

(41) Osterloh, F. E. Photocatalysis versus Photosynthesis: A Sensitivity Analysis of Devices for Solar Energy Conversion and Chemical Transformations. *ACS Energy Lett*. **2017**, *2*, 445−453.

(42) Walter, M. G.; Warren, E. L.; McKone, J. R.; Boettcher, S. W.; Mi, Q.; Santori, E. A.; Lewis, N. S. Solar Water Splitting Cells. *Chem. Rev*. **2010**, *110*, 6446−6473.

(43) Lewis, N. S. Chemical Control of Charge Transfer and Recombination at Semiconductor Photoelectrode Surfaces. *Inorg. Chem*. **2005**, *44*, 6900−6911.

(44) Peter, L. M. Photocatal. Fundam. Perspect., edited by J. Schneider, D. Bahnemann, J. Ye, G.L. Puma, and D.D. Dionysiou, *Royal Society of Chemistry*, **2016**, 1–28.

(45) Peter, L. M. Energetics and kinetics of light-driven oxygen evolution at semiconductor electrodes: the example of hematite. *J. Solid State Electrochem*. **2013**. *17*, 315-326.

(46) Salvador, P. Semiconductors' photoelectrochemistry: a kinetic and thermodynamic analysis in the light of equilibrium and nonequilibrium models. *J. Phys. Chem. B*. **2001**, *105*, 6128-6141.

(47) Bard, A. J.; Bocarsly, A. B.; Fan, F. R. F.; Walton, E. G.; Wrighton, M. S. The Concept of Fermi Level Pinning at Semiconductor/Liquid Junctions. Consequences for Energy Conversion Efficiency and Selection of Useful Solution Redox Couples in Solar Devices. *J. Am. Chem. Soc.* **1980**, *102*, 3671–3677.

(48) Gärtner, W. W. Depletion-Layer Photoeffects in Semiconductors. *Phys. Rev.* **1959**, *116*, 84–87.

(49) Reichman, J. The current-voltage characteristics of semiconductor-electrolyte junction photovoltaic cells. *Appl. Phys. Lett*. **1980**, *36*, 574–577.

(50) McConnell, I.; Li, G.; Brudvig, G. W. Energy conversion in natural and artificial photosynthesis. *Chem. Biol.* **2010**, *17*, 434−447.

(51) Nakamura, Y.; Aratani, N.; Osuka, A. Cyclic porphyrin arrays as artificial photosynthetic antenna: synthesis and excitation energy transfer. *Chem. Soc. Rev*. **2007**, *36*, 831−845.

(52) Grätzel, M. Dye-sensitized solar cells. J. Photochem. *Photobiol.C Photochem. Rev.* **2003**, *4*, 145−153.

(53) Xiang, X.; Cao, X.; Sun, W.; Ding, Y. Recent Progress in Visible Light Driven Water Oxidation Using Semiconductors Coupled with Molecular Catalysts. *ChemCatChem* **2019**, *11*, 6190−6202.

(54) Bard, A. J. Photoelectrochemistry and heterogeneous photocatalysis at semiconductors. *J. Photochem*. **1979**, *10*, 59−75.

(55) Garnett, E.; Yang, P. Light Trapping in Silicon Nanowire Solar Cells. *Nano Lett*. **2010**, *10*, 1082−1087.

(56) Liu, C.; Dasgupta, N. P.; Yang, P. Semiconductor Nanowires for Artificial Photosynthesis. *Chem. Mater*. **2014**, *26*, 415−422.

(57) Tumas, B.; Dempsey, J. L.; Mallouk, T. E. Basic Energy Sciences Roundtable on Liquid Solar Fuels; U.S. Department of Energy, **2019**.

(58) Bard, A. J.; Memming, R.; Miller, B. Terminology in semiconductor electrochemistry and photoelectrochemical energy conversion. *Pure Appl. Chem*. **1991**, *63*, 569−596.

(59) Nielander, A. C.; Shaner, M. R.; Papadantonakis, K. M.; Francis, S. A.; Lewis, N. S. A taxonomy for solar fuels generators. *Energy Environ. Sci*. **2015**, *8*, 16−25.

(60) Nozik, A. J. Photochemical diodes. *Appl. Phys. Lett.* **1977**, *30*, 567−569.

CHAPTER 2 UNDERSTANDING AND CONTROLLING THE PERFORMANCE-LIMITING STEPS OF CATALYSTS-MODIFIED SEMICONDUCTORS.

Portions of this chapter are excerpted and reprinted with permission from:

Nguyen, N. P.; Wadsworth, B. L.; Nishiori, D.; Reyes Cruz, E. A.; Moore, G. F. Understanding and Controlling the Performance-Limiting Steps of Catalysts-Modified Semiconductors. *J. Phys. Chem. Lett*. **2021**, *12*, 199-203.

2.1 Introduction

Advances in interfacial chemistry and rational synthetic design have accelerated development of catalyst-modified semiconductors that convert energy between photonic, electronic, and chemical forms.[1-10] These constructs hold promise for unleashing renewable-energy technologies that convert sunlight to fuels and other value-added chemical products. However, the ability to effectively interface the required light harvesting and catalytic components remains challenging as there is an incomplete understanding of how charges move through these materials and what the bottleneck rate-limiting steps are that restrict their performance.

Understanding and controlling factors that restrict the rates of fuel-forming reactions are essential to designing effective catalyst-modified semiconductors for applications in solar-to-fuel technologies. In this chapter, I describe GaAs semiconductors featuring a polymeric coating that contains cobaloxime-type catalysts for photoelectrochemically powering hydrogen production. The activities of these electrodes (limiting current densities >20 mA cm^{-2} under 1-sun illumination) enable identification of fundamental performance-limiting bottlenecks encountered at relatively high rates of fuel formation. Experiments conducted under varying bias potential, pH, illumination intensity, and scan rate reveal two distinct mechanisms of photoelectrochemical hydrogen production.

2.1.1. Homogeneous and Heterogeneous Hydrogen Evolution Reaction using Cobaloxime-type catalyst

One of the most common and effective catalysts for activating the hydrogen evolution reaction is elemental platinum. However, availability and price concerns for future market demands for platinum and other rare-earth elements have prompted researchers to seek alternative catalysts for the production of hydrogen and other industrially relevant chemicals.[1,11,12] Molecular catalyst hold significant advantages thanks to high levels of tunability and selectivity. Tunability is especially a critical aspect of molecular catalyst, with various properties that can be synthetically designed and controlled. Choice of metal centers, and several ligands platforms, present seemingly endless opportunities for altering reactivities with binding abilities, electron withdrawing/donating effects, etc… The metal center is changeable, and the same set of ligands can be applied to different metals or the same metal in different oxidation states. These ligands can be replaced with a completely different molecule or slightly modified with a similar base structure. This allows researchers to explore and compare reactivity wide range of chemical and physical parameters affect catalysis, both homogeneously and heterogeneously. The ability to target a specific pathway or product in catalysis is particularly important in reactions that can have multiple undesired by products. Molecular catalysts' selectivity is shown by multiple sites for reactions as well as the choice of different reactive group on the ligand scaffold.[13-22]

Molecular catalysis of the HER reaction can proceed via a homolytic or a heterolytic pathway. In a homolytic pathway, the product is formed through a symmetrical bimolecular chemical step. Conversely, a heterolytic pathway involves the reaction of chemically distinct species. For example, the mechanism of HER catalysis by cobaloximes has been proposed to occur via several pathways.[23–26] After reduction of the cobalt center from Co(III) to Co(I), the Co(I) species is protonated to generate a cobalt hydride, Co(III). In the homolytic pathway, two cobalt hydride species react with one another to release hydrogen. Alternately, the HCo(III) generated in the initial protonation step can react with an acid in solution to generate hydrogen through a heterolytic pathway. It has also been proposed that the HCo(III) can be further reduced to HCo(II), which can then proceed to generate H_2 through a homolytic or heterolytic pathway.[26]

2.1.2. Cobaloxime-catalysts immobilization on III-V semiconductors

Leveraging the surface-grafting chemistry of olefins on GaP semiconductors, Moore and coworkers showcased the modularity of this strategy by modifying the ligand environment of the immobilized catalysts, the structure of the intervening polymer, and the crystal orientation of the underpinning (semi)conductor surface used to prepare the assemblies. They report successful immobilization of cobaloxime-type catalysts (Figure 2.1) on GaP and GaAs semiconductors via polyvinylpyridyl and polyvinylimmidazole polymer layers.[27-31] For example, GaP electrodes were prepared featuring surface-grafted polypyridyl coatings modified with cobaloxime catalysts (Figure 2.2) containing either a glyoximate capping group or an analog featuring a boron difluoride moiety.[28] For both constructs, successful surface attachment was confirmed via GATR-FTIRand XP spectroscopies, and photoelectrochemical characterization of the modified GaP photoelectrodes were conducted in pH 7 (0.1 M phosphate buffer) or pH 4.5 (0.1 M acetate buffer) under simulated AM 1.5 G illumination (100 mW cm^{-2}) using a Newport Oriel Apex light source. The pH response of the photoelectrochemical activity was consistent with results obtained from electrochemical studies conducted using analogous non-surface-attached catalysts dissolved in solution, meaning, a relatively lower pH was required to induce HER when using the electrodes modified with the difluoroboryl analog. These findings were attributed to a correlation between the $Co^{II/I}$ reduction potential and the basicity of Co^{I} species to form Co^{III} hydride species during the catalytic cycle[26,28] and show that incorporation of a cobaloxime with a ligand macrocycle that is modified at the molecular level affects the photoelectrochemical response observed at the construct level.

2.2 Results and Discussion

2.2.1 Materials Preparation

Materials

All reagents were purchased from Sigma-Aldrich. Methanol was freshly distilled before use. All aqueous solutions were prepared using Milli-Q water (18.2 MΩ·cm). Zn-doped p-type Gallium Arsenide (GaAs) (111)A and Gallium Phosphide (GaP) (111)A wafers were purchased from the Institute of Electronic Materials Technology, Poland. The crystalline wafers were single-side polished to an epi-ready finish. The GaAs (111)A wafers used in this report have a resistivity of 0.12 Ω·cm and a carrier concentration of 2.8 × 1017 cm^{-3}, with an etch pit density of less than 5.7 × 104 cm^{-2}. The p-type GaP (111)A wafers have a resistivity of 0.046 Ω·cm, a mobility of 50 $cm^2\ V^{-1}\ s^{-1}$, and a carrier concentration of 2.7 × 1018 cm^{-3}, with an etch pit density of less than 9.5 × 104 cm^{-2}.

Molecular Synthesis

All syntheses were carried out under an argon atmosphere using Schlenk techniques or in a nitrogen glovebox. All reagents were purchased from Aldrich. All solvents were stored over the appropriate molecular sieves prior to use. Milli-Q water (18.2 MΩ·cm) was used to prepare all aqueous solutions.

$Co(dmgH_2)(dmgH)Cl_2$. This complex was prepared following a previously reported procedure.[32] The molecular structure of this compound is shown in Figure 2.1a.

$Co(dmgH)_2PyCl$. This complex was prepared as previously described.[32,33] The molecular structure of this compound is shown in Figure 2.1b.

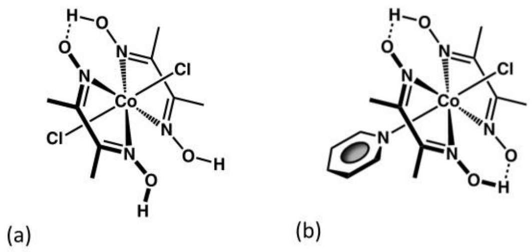

Figure 2.1. Molecular structures of (a) $Co(dmgH_2)(dmgH)Cl_2$ and (b) $Co(dmgH)_2PyCl$.

Wafer Preparation

All wafers were degreased with an acetone-soaked cotton swab. The wafers were further cleaned using consecutive ultrasonic treatments in a series of solvents (water, 2 min; methanol, 2 min; acetone, 2 min; methanol, 2 min; and water, 2 min), followed by 30 s of etching in concentrated sulfuric acid. The freshly etched wafers were put into quartz flasks containing argon-sparged 4-vinylpyridine and purged with argon for 5 min, after which they were placed into a UV chamber and irradiated with 254 nm UV light (using a Spectroline Model ENF-280C source operating at 115 Volts, 60 Hz, 0.20 A) for 2 h. The resulting polypyridyl-modified GaAs (PPy|GaAs) or polypyridyl-modified GaP (PPy|GaP) wafers were then rinsed with methanol followed by ultrasonic cleaning in methanol for 1 min, before drying under nitrogen and storing under vacuum. Cobaloxime functionalization was achieved by submerging the PPy|GaAs or PPy|GaP wafers in an argon-sparged solution of $Co(dmgH_2)(dmgH)Cl_2$ and triethylamine (1 mM in each) in methanol and allowing them to react overnight. The resulting cobaloxime|PPy|GaAs or cobaloxime|PPy|GaP wafers were then rinsed with methanol, followed by rinsing with isopropanol, and drying under nitrogen.[29,30]

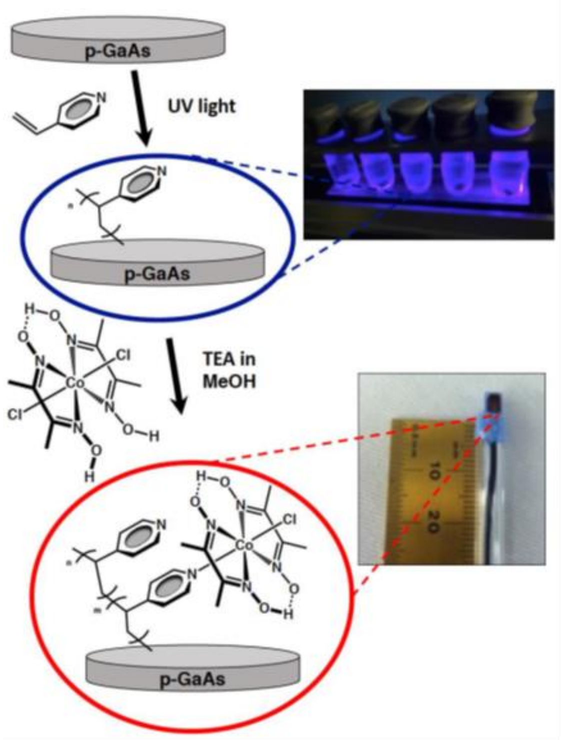

Figure 2.2. Schematic representation of the synthetic method used to prepare polypyridyl-modified GaAs electrodes (PPy|GaAs) alongside photos of the UV reaction apparatus (top image) and a custom-built working electrode (bottom image). In this scheme, assembly of the cobaloxime-type catalysts occurs by replacing one of the axial chloride ligands of the precursor complex, Co(dmgH$_2$)(dmgH)Cl$_2$, with a pyridyl functional group of the polymeric surface coating. Charge balance when replacing chloride, an anionic X-type ligand, with pyridyl, a neutral L-type ligand, is accounted for by the base-promoted conversion of the dimethylglyoxime ligand to the dimethylglyoximate monoanion.

Electrode Fabrication

GaAs or GaP and chemically-modified GaAs or chemically-modified GaP working electrodes were fabricated by applying an indium−gallium eutectic (Aldrich) to the unpolished/backside of the wafers before fixing a copper wire to the back of the wafers using a conductive silver epoxy (Circuit Works). The copper wire was passed through a glass tube, and the semiconductor wafer was insulated and attached to the glass tube with Loctite 615 Hysol Epoxi-patch adhesive. The epoxy was allowed to cure for approximately 24 h before performing experiments using the electrodes.

2.2.2 Surface Characterization of cobaloxime-polypyridyl-GaAs

Contact Angle

Contact angles using drops of deionized water on GaAs surfaces were conducted following surface modification steps (Figure 2.3). The increase in contact angles following each chemical-modification step indicates increased hydrophobicity of the resulting surfaces.

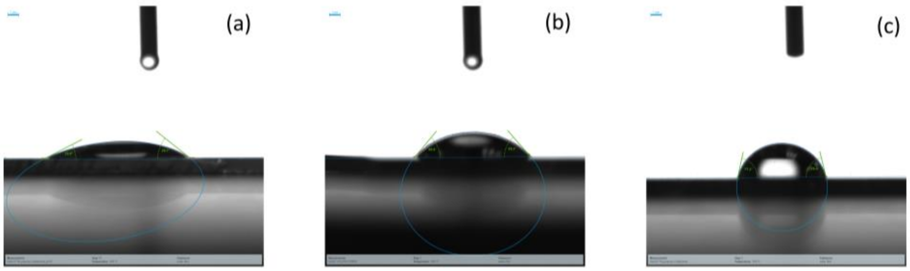

Figure 2.3. Photos collected during determination of contact angles using drops of deionized water on (a) GaAs (contact angle = 34 ± 1^{o}), (b) PPy|GaAs (contact angle = 50 ± 3^{o}), and (c) cobaloxime|PPy|GaAs (contact angle = 76 ± 1^{o}). The increase in contact angles (16^{o} increase after polypyridyl polymerization comparing to bare GaAs and 26^{o} increase after catalyst immobilization comparing to PPy|GaAs) following each chemical-modification step indicates increased hydrophobicity of the resulting surfaces, consisting

with successful immobilization of polymer and/or catalyst layer.

Ellipsometry

After polymer-functionalized, spectroscopic ellipsometry measurements were performed in air (Figure 2.4), indicating a polymer thickness of ≈ 1.97 ± 0.26 nm on GaAs(111)A surface (see Experimental section for details). This thickness is slightly higher than that previously reported using polypyridiyl (PPy) to functionalize GaP(100), which was 1.45 ± 0.17 nm.[29,30]

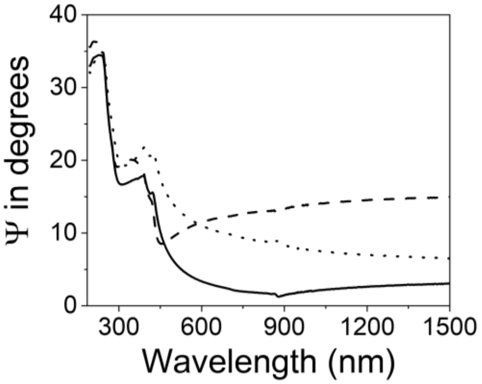

Figure 2.4. Ellipsometry spectra recorded using PPy|GaAs at incidence angles of 70° (dotted), 75° (solid), and 80° (dashed). Using these ellipsometry measurements, the thickness of the polypyridyl layer on GaAs was determined to be 2.0 ± 0.3 nm. Using the bulk polymer density of 1.15 g cm^{-3} and 4-vinylpyridine molecular weight of 105.14 g mol^{-1}, the related polypyridyl site density is 2.2 nmol cm^{-2}.

Cobalt catalyst loading on cobaloximePPy|GaAs surface using ICP-MS

Inductively coupled plasma mass spectrometry measurement results after acid digestion of bare GaAs and PPy|GaAs samples shows no significant presence of cobalt. For samples of cobaloxime|PPy|GaAs, the cobalt concentration is estimated to be 2.40 ± 0.04 nmol cm^{-2}.

Table 2.1. Total Cobalt Surface Loadings Determined using ICP-MS.[a]

Construct	**Cobalt Loading (nmol Co cm^{-2})**
GaAs	0.010 ± 0.001
PPy|GaAs	0.030 ± 0.003
Cobaloxime|PPy|GaAs	2.40 ± 0.04

X-ray Photoelectron Spectroscopy

Sample analysis using X-ray photoelectron spectroscopy (XPS) further confirms successful surface modification with polymer and catalyst moieties. Differences in N 1s core level XP spectra of bare GaAs, PPy|GaAs, and cobaloxime|PPy|GaAs are shown in Figure 2.5. Using the peak positions and fwhm of the two features identified in samples of GaAs, the N1s core level spectrum of cobaloxime|PPy|GaAs samples can be fit with an additional nitrogen component (Figure 2.5b). This extra contribution at 400.1 eV is assigned to the pyridyl nitrogens of the surface-grafted polymer coordinated with the cobalt centers of the cobaloxime and the nitrogrens of the glyoximate ligands. This feature's binding energy corresponds to the model compound $Co(dmgH)_2PyCl$ XPS spectrum previously reported[27] (Figure 2.5a). Inspection of the XPS spectrum of $Co(dmgH)_2PyCl$ powder samples reveals that N from glyoximate moieties of the ligand structure cannot be deconvoluted from the N contribution of Co-coordinated pyridine[27].

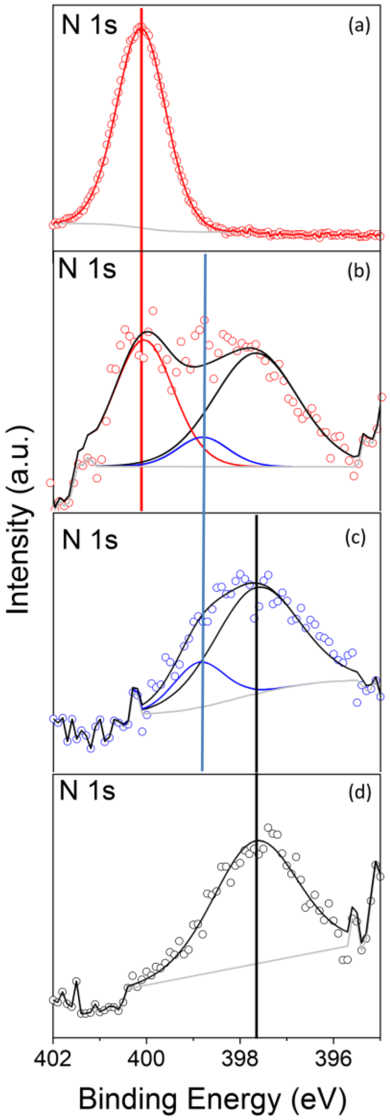

Figure 2.5. N 1s core level XP spectra of (a) a powder sample of Co(dmgH)$_2$PyCl, (b) cobaloxime|PPy|GaAs, (c) PPy|GaAs, and (d) GaAs. The circles are the spectral data, and the solid lines represent the backgrounds (light gray), a component fit associated with nitrogens bound to Co (red), a component fit associated with unbound pyridyl nitrogens (blue), and overall fits (black). The feature at 397.6 eV present in XP spectra of unmodified GaAs surfaces is assigned to a satellite feature of the Ga LMM Auger line at 393 eV. The peak position and full width at half maximum (fwhm) of this feature was used to guide the fitting and assist with identifying components in XP spectra of

PPy|GaAs. The XP spectrum of PPy|GaAs was fit with a component at 397.6 eV, assigned to a satellite feature of the Ga LMM Auger line, and an additional component at 398.8 eV, assigned to pyridyl nitrogens of the polymeric coating (Figure 2.5c). Using the peak positions and fwhm of these two components to guide the fitting of the N 1s core level spectrum of cobaloxime|PPy|GaAs, at least one additional nitrogen component could be fit to the data (Figure 2.5d). This additional contribution at 400.1 eV is ascribed to N atoms coordinated to Co ions, including pyridyl-type nitrogens as well as glyoximate- and glyoxime-type nitrogens. Inspection of the XP spectra collected using powder samples of Co(dmgH)$_2$PyCl and Co(dmgH$_2$)(dmgH)Cl$_2$ show the nitrogen signals arising from the glyoximate and glyoxime ligands overlap with the nitrogen contributions from Co-coordinated pyridine ligands (see Figure 2.6).

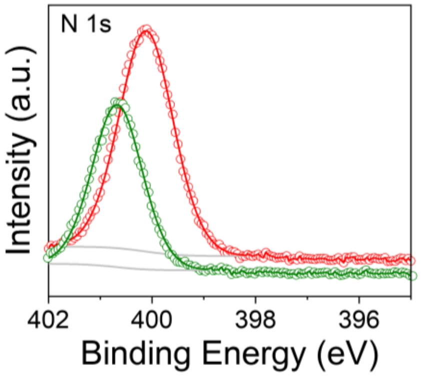

Figure 2.6. N 1s core level spectra collected using powder samples of either the model compound Co(dmgH)$_2$PyCl (red) or precursor compound Co(dmgH$_2$)(dmgH)Cl$_2$ (olive) (data taken from reference 27 in this Chapter).

Survey XP spectra of cobaloxime|PPy|GaAs (Figure 5.10) indicates the presence of Co elements associated with Cobaloxime catalyst. The Co 2p core level spectra of these samples show 2 peaks at 780 eV (2p3/2) and 795 eV (2p1/2), with a 2:1 ratio of branching, and no apparent shakeup satellite structures, confirming Co^{3+} species.[34,35]

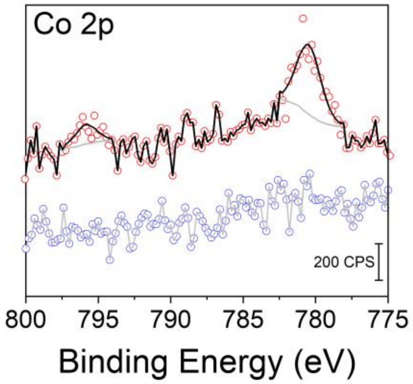

Figure 2.7. Co 2p core level XP spectra of PPy|GaAs (blue) and cobaloxime|PPy|GaAs (red). The circles are the spectral data, and the solid lines represent the background (light gray) and overall fit (black).

GATR-FTIR(Grazing angle attenuated total reflection Fourier transform infrared).

In order to confirm successful chemical functionalization of the GaAs(111A) surfaces with polypyridiyl polymer and molecular Cobaloxime catalyst layers, surface analysis using grazing angle attenuated total reflection Fourier transform infrared (GATR-FTIR) spectroscopy was employed. Transmission spectra of $Co(dmgH)_2PyCl$ recorded in a matrix of KBr display a relatively strong transmission band at 1240 cm^{-1} that is assigned to the NO- stretch of this complex. The frequency of this band is a diagnostic of cobaloxime complexes featuring axial coordination to pyridyl nitrogens. For comparison, the NO^- stretch of the precursor complex, $Co(dmgH_2)(dmgH)Cl_2$, is located at 1225 cm^{-1}. The frequencies of the polypyridyl infrared absorption bands on surfaces of PPy|GaAs samples measured using GATR-FTIRspectroscopy are similar to those previously reported on PPy|GaP surfaces[27-31, 36] and the absorption bands centered at 1600 cm^{-1} and 1419 cm^{-1} are assigned to C=N and C-N vibrational modes, respectively. Following treatment of PPy|GaP surfaces with $Co(dmgH_2)(dmgH)Cl_2$ (see Section 2.2.1 for further details) distinct absorption bands associated with cobaloxime-type catalysts are observed, including a strong absorption feature in the NO- region of the spectrum centered at ~ 1235 cm^{-1}. This apparent shift of the NO$^-$ absorption band to lower frequencies as compared to those measured for the model cobaloxime complex, and the relative broadness of this absorption band, are indicative of heterogenous contributions to this mode.

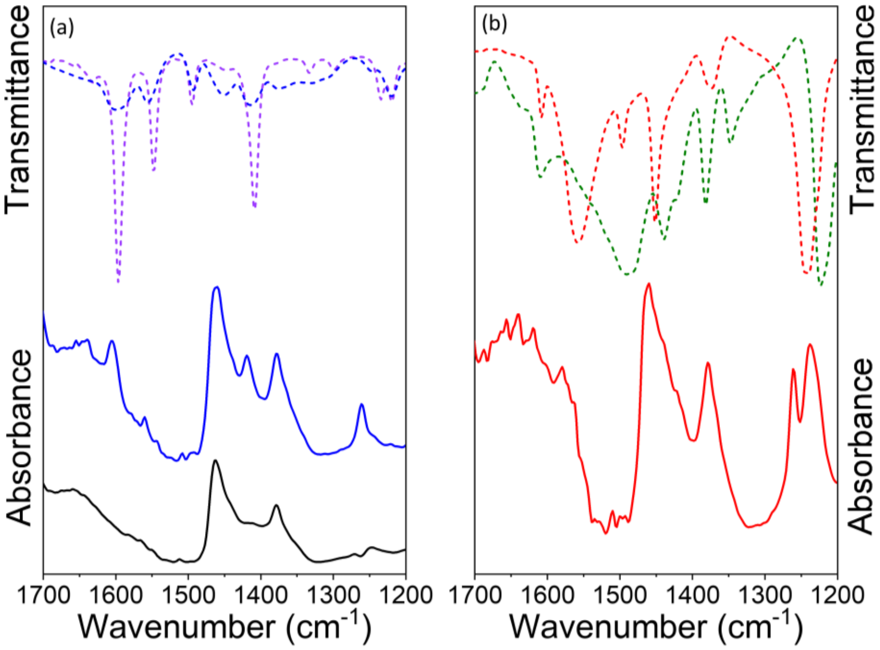

Figure 2.8. (a) GATR-FTIRabsorption spectra of GaAs (black solid line) and PPy|GaAs (blue solid line), as well as FTIR transmission spectra of 4-vinylpyridine in KBr (purple dashed line) and polyvinylpyridine in KBr (blue dashed line). (b) GATR-FTIRabsorption spectra of cobaloxime|PPy|GaAs (red solid line) as well as FTIR transmission spectra of the precursor complex, Co(dmgH$_2$)(dmgH)Cl$_2$, in KBr (olive dashed line) and the model cobaloxime complex, Co(dmgH)$_2$PyCl, in KBr (red dashed line).

The absorption feature at 1235 cm^{-1}, assigned to the NO$^-$ stretch of the immobilized cobaloxime units, is present in the GATR-FTIRspectra collected prior to and following photoelectrochemical experiments, indicating the immobilized catalysts present following these experiments are intact (Figure 2.9). This absorption band is particularly sensitive to the local coordination environment of cobaloximes[27] and in general, the results presented here using cobaloxime|PPy|GaAs electrodes are consistent with those previously reported using cobaloxime|PPy|GaP electrodes,[27-31] indicating that molecular cobalt sites, presumably at the periphery, and thus more loosely associated with the polymeric coating, detach from the polymer during redox cycling; however, the fraction that remains intact appears to maintain their molecular structural integrity. In order to exclude discrepancies in intensities arising from sample-to-sample variations in the degree of contact with the ATR crystal, we compared the ratios of absorption bands centered at 1600 cm^{-1} and at 1419 cm^{-1}, assigned to C=N and C-N vibrational modes of the polymer graft, to peaks assigned to the NO^- mode of the intact catalysts. We then used these ratios to obtain the fraction of catalyst species present in the polymer and information on the overall surface composition. These results are summarized in **Table 2.2** and indicate a decrease in the amount of cobaloximes remaining in the film following PEC testing. We estimate ~ 40% of the cobaloximes detach from the polymeric coating following our photoelectrochemical studies. These results are consistent with more detailed reports on this topic from our research group[11] indicating that cobaloximes loosely associated with the polymeric coating can detach during photoelectrochemical operation.

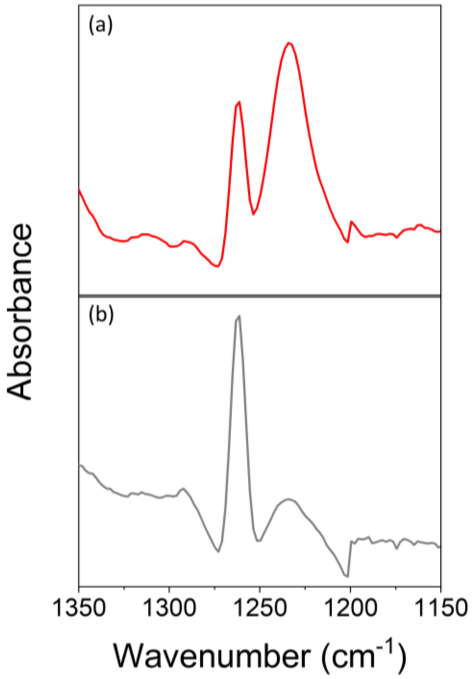

Figure 2.9. GATR-FTIRabsorption spectra of cobaloxime|PPy|GaAs collected (a) prior to and (b) following 3 cyclic voltammograms (scanning from +0.58 V vs RHE to -1.12 V versus RHE at a scan rate of 100 mV s^{-1}) recorded in pH 13 electrolyte (0.1 M NaOH) under simulated 1-sun illumination.

Table 2.2. Ratios of absorbance between NO^{-} stretch feature at 1235 cm^{-1} and features at 1600 cm^{-1} or 1419 cm^{-1} associated with the polymer.

Construct	**Ratio of Absorbance (1235 cm^{-1} : 1600 cm^{-1})**	**Ratio of Absorbance (1235 cm^{-1} : 1419 cm^{-1})**
Cobaloxime|PPy|GaAs (pre-PEC experiment)	1.21	1.02
Cobaloxime|PPy|GaAs (post-PEC experiment)	0.70	0.60

Ultraviolet-Visible-Near Infrared Spectroscopy Data

All solid-state optical measurements were performed using 400 μm thick cobaloxime|PPy|GaAs wafer.

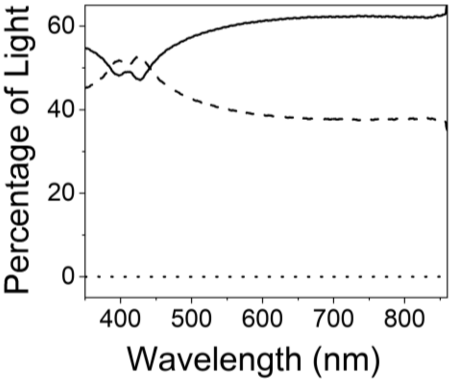

Figure 2.10. Plots of the percentage of light transmitted (dotted), reflected (dashed), or absorbed (solid) by cobaloxime|PPy|GaAs versus the wavelength of illumination. The percentage of light reflected is equal to the sum of the specular percent reflectance, collected at an incident angle of 5° to the normal of the sample surface, and diffuse percent reflectance. The data shown in this figure were used to prepare IQE plots from the related EQE plots.

2.2.3 Photoelectrochemical measurement and Mechanism for Hydrogen Evolution Reaction at Molecular-Modified Photoelectrode

Our use of GaAs semiconductors in this current work was prompted by studies of related molecular-catalyst-modified GaP electrodes.[27-31,36-37] Results previously published by Wadsworth *et al*.[37] shows that when these GaP-based constructs were illuminated at 1-sun intensity, the hydrogen evolution reaction (HER) activities were not limited by a chemical step (i.e., chemical catalysis / energy storage), but instead were limited by the incident photon flux and kinetics associated with charge transport (i.e., light capture and conversion steps).[37] These findings indicate that increasing the illumination intensity, or utilizing a semiconductor component that can harvest a larger portion of the solar spectrum, could enhance fuel-forming reaction rates. Based on their respective band gaps, GaAs can absorb photons with wavelengths up to 870 nm, while GaP can only absorb photons with wavelengths up to 549 nm (**Figure 2.11a**). Thus, if the overall incident photon-to-current efficiencies are similar, we hypothesize that GaAs-based constructs should achieve higher current densities and deliver charge carriers required for activating surface-immobilized catalysts at faster rates.

Synthesis of cobaloxime|PPy|GaAs assemblies was achieved via modification of a method previously developed for functionalizing GaP[27-31,36,37] and structural characterization, including contact angle measurements, ellipsometry, ICP-MS, XPS, and GATR-FTIR, provides converging lines of evidence for successful functionalization of the GaAs substrates (See Section 2.2.2). Voltammograms recorded using cobaloxime|PPy|GaAs, polypyridyl-modified GaAs (PPy|GaAs), and GaAs working electrodes immersed in 0.1 M phosphate buffered aqueous solutions (pH 7) are shown in Figures 2.11b & 2.12 (See Experimental section 5.1.1 – *Photoelectrochemistry*). Under simulated 1-sun illumination (100 mW cm^{-2}), the cobaloxime|PPy|GaAs electrodes produce a current density of 1.0 ± 0.4 mA cm^{-2} when polarized at the H^+/H_2 equilibrium potential and achieve a limiting current density of ~ 20 mA cm^{-2} when polarized at more negative potentials. For comparison, when studied under otherwise identical experimental conditions, the analogous GaP-based constructs (cobaloxime|PPy|GaP) achieve a current density of 1.08 ± 0.03 mA cm^{-2} when polarized at the H^+/H_2 equilibrium potential and approach a limiting current density that remains at ~ 1 mA cm^{-2} when polarizing to more negative potentials (**Figure 2.11c**).

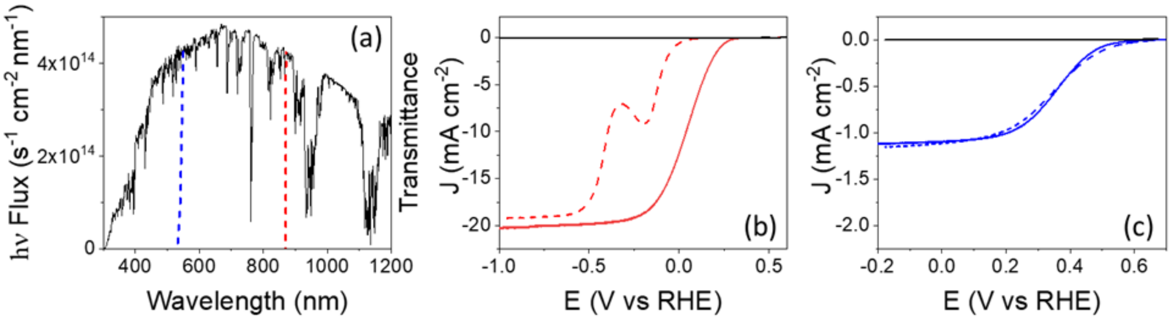

Figure 2.11. (a) The air mass 1.5 global tilt solar flux spectrum (black solid) as well as transmission spectra of the GaP (bandgap = 2.26 eV) (blue dash) and GaAs (bandgap = 1.43 eV) (red dash) semiconductors used in this work. (b) Linear sweep voltammograms recorded at a scan rate of 100 mV s^{-1} using cobaloxime-polypyridyl-modified GaAs (cobaloxime|PPy|GaAs) electrodes in pH 7 (dash traces) or pH 13 (solid traces) solutions under simulated 1-sun illumination (red traces) or in the dark (black traces). (c) Linear sweep voltammograms recorded at a scan rate of 100 mV s^{-1} using cobaloxime-polypyridyl-modified GaP (cobaloxime|PPy|GaP) electrodes in pH 7 (dash traces) or pH 13 (solid traces) solutions under simulated 1-sun illumination (blue traces) or in the dark (black traces).

Voltammograms recorded using cobaloxime|PPy|GaAs, polypyridyl-modified GaAs (PPy|GaAs), and GaAs working electrodes immersed in 0.1 M phosphate buffered aqueous solutions (pH 7) are shown in **Figures 2.12** for comparison of the photoelectrochemical activities of these hybrid constructs under otherwise identical experimental conditions. Under simulated 1-sun illumination (100 mW cm^{-2}), the cobaloxime|PPy|GaAs electrodes produce a current density of 1.0 ± 0.4 mA cm^{-2} when polarized at the H^+/H_2 equilibrium potential and achieve a limiting current density of ~ 20 mA cm^{-2} when polarized at more negative potentials (**Table 2.3**). For comparison, when studied under otherwise identical experimental conditions, the analogous GaP-based constructs (cobaloxime|PPy|GaP) achieve a current density of 1.08 ± 0.03 mA cm^{-2} when polarized at the H$^+$/H$_2$ equilibrium potential and approach a limiting current density that remains at ~ 1 mA cm^{-2} when polarizing to more negative potentials (Figure 2.11c).

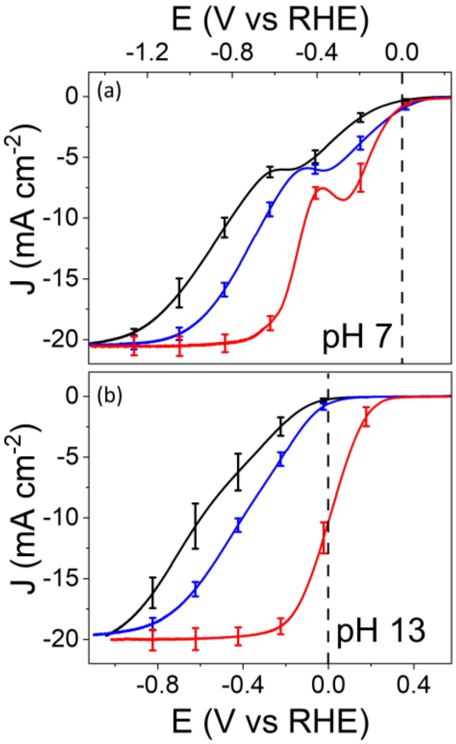

Figure 2.12. Linear sweep voltammograms recorded at 100 mV s^{-1} using either GaAs (black), PPy|GaAs (blue), or cobaloxime|PPy|GaAs (red) working electrodes under 100 mW cm^{-2} illumination in either (a) pH neutral (0.1 M phosphate buffer) or (b) pH 13 (0.1 M NaOH) electrolyte solutions. The black dashed lines represent the H$^+$/H$_2$ equilibrium potential.

Table 2.3. Open-circuit voltages, short-circuit current densities, maximum power points, and fill factors extracted from linear sweep voltammetry data recorded at a scan rate of 100 mV s^{-1} using PPy|GaAs or cobaloxime|PPy|GaAs working electrodes in 0.1 M phosphate buffer (pH 7) or 0.1 M NaOH (pH 13). All data were recorded under simulated 1-sun illumination.

Construct	**pH**	**Open-Circuit Voltage (V vs RHE)**	**Short-Circuit Current (mA cm^{-2})**	**Maximum Power Point (mA cm^{-2})**	**Fill Factor**
GaAs	7	0.289 ± 0.005	0.34 ± 0.05	0.011 ± 0.003	0.11 ± 0.02
PPy|GaAs	7	0.31 ± 0.02	1.1 ± 0.3	0.033± 0.009	0.099 ± 0.007
Cobaloxime|PPy|GaAs	7	0.35 ± 0.02	1.0 ± 0.4	0.028 ± 0.007	0.09 ± 0.06
GaAs	13	0.48 ± 0.03	0.24 ± 0.08	0.008 ± 0.002	0.08 ± 0.01
PPy|GaAs	13	0.48 ± 0.05	0.6 ± 0.2	0.015 ± 0.007	0.05 ± 0.01
Cobaloxime|PPy|GaAs	13	0.55 ± 0.06	10 ± 1	0.5 ± 0.1	0.09 ± 0.02

Unlike the voltammograms recorded using cobaloxime|PPy|GaP electrodes, which display single S-shaped waveforms, the voltammograms recorded using cobaloxime|PPy|GaAs electrodes in pH neutral aqueous solutions display two distinct regions of photoelectrosynthetic performance (i.e., dual-waveform voltammograms featuring two limiting current features). We term the region of photoelectrosynthetic performance at less negative bias potentials the *low polarization region*, and the region of photoelectrosynthetic performance at more negative bias potentials the *high polarization region*. The low polarization region spans from ~ –0.3 V vs RHE to more positive potentials and includes a limiting current peak feature centered at –0.2 V vs RHE, with an intensity of ~ 10 mA cm^{-2}, in voltammograms recorded at pH 7 under 100 mW cm^{-2} illumination. Sweeping the polarization to potentials negative of this peak feature results in decreasing currents (i.e., rates of charge transfer) despite the increasing applied bias potential (i.e., driving force), indicating that transport, and thus local concentration, of substrates other than electrons begins to limit the HER activity.[38] Conversely, in the high polarization region, which spans from ~ –0.3 V vs RHE to more negative potentials, the current response switches back to increasing with further negative polarization until reaching a limiting value that approaches ~ 20 mA cm^{-2}.

To further explore the dual-waveform nature of the GaAs based assemblies, photoelectrochemical experiments were also performed at elevated pH. Voltammograms recorded using cobaloxime|PPy|GaAs electrodes immersed in 0.1 M NaOH aqueous solutions (pH 13) are shown in **Figures 2.11b & 2.12**. Under these conditions, the cobaloxime|PPy|GaAs electrodes produce a current density of 10 ± 1 mA cm^{-2} when polarized at the H^+/H_2 equilibrium potential, and the current density steadily increases upon polarizing to more negative potentials until reaching a limiting value that again approaches ~ 20 mA cm^{-2}. In addition, the voltammograms recorded under basic conditions display a single S-shaped waveform (**Figure 2.11b, 2.12b, and 2.13**) and not the dual waveform observed in experiments performed at pH 7 (**Figure 2.14 and 2.15**). For comparison, at pH 13 (and otherwise identical experimental conditions) the analogous cobaloxime|PPy|GaP assemblies achieve a current density of only 1.08 ± 0.03

mA cm^{-2} when polarized at the H^+/H_2 equilibrium potential, and a limiting current density that remains at ~ 1 mA cm^{-2} when polarizing to more negative potentials (Figure 2.11c). Thus, unlike cobaloxime|PPy|GaAs, the current response versus the RHE potential (which adjusts for the nernstian pH response of the HER) shows relatively little to no difference in experiments performed at pH 7 versus 13 when using cobaloxime|PPy|GaP working electrodes.[27-30,37]

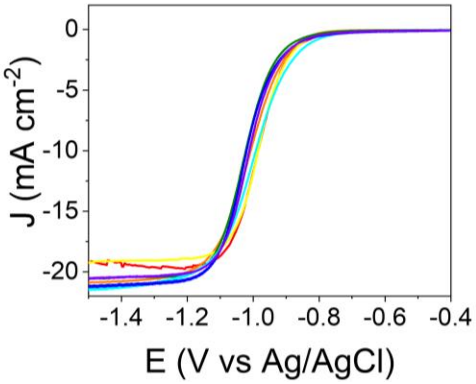

Figure 2.13. Linear sweep voltammograms recorded under 100 mW cm^{-2} illumination using cobaloxime|PPy|GaAs working electrodes in pH 13 (0.1 M NaOH) electrolyte solutions and the following scan rates: 10 (red), 50 (orange), 100 (yellow), 200 (green), 500 (cyan), 700 (blue) and 1000 (violet) mV s^{-1}.

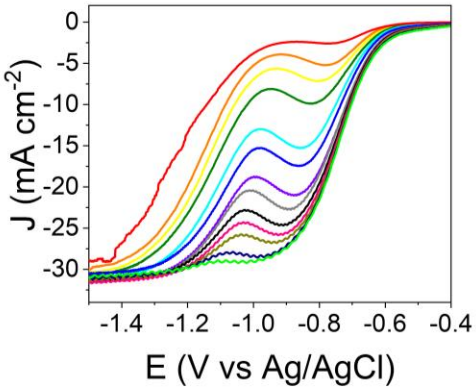

Figure 2.14. Linear sweep voltammograms recorded under 150 mW cm^{-2} illumination using cobaloxime|PPy|GaAs working electrodes in pH neutral (0.1 M phosphate buffer)

electrolyte solutions and the following scan rates: 10 (red), 50 (orange), 100 (yellow), 200 (olive), 500 (cyan), 700 (blue), 1000 (violet), 1200 (grey), 1500 (black), 1700 (pink), 2000 (dark yellow), 2500 (navy), and 3000 (green) mV s^{-1}.

The observation of dual-waveform voltammograms and changes in waveforms as a function of pH have been reported by Gerischer *et al.* in experiments involving unmodified-GaAs electrodes interfaced with a liquid electrolyte.[39] The authors proposed that currents at lower bias potentials are restricted by diffusion of solvated protons to the electrode surface, and at higher bias potentials the reduction of water becomes limited by the number of electron – hole pairs generated via illumination of the semiconductor.[39] To investigate if similar mechanisms are at play when using cobaloxime|PPy|GaAs, we also investigated their photoelectrosynthetic performance under varying illumination intensity and scan rate.

The limiting current at lower polarization is independent of illumination conditions when modifying them from 50 mW cm^{-2} up to 200 mW cm^{-2} (**Figures 2.15a, 2.15b, & 2.16**). However, the position of the peak feature shifts toward more positive potentials when increasing the light intensity. Juxtaposed to the invariance of the limiting current intensity in the low polarization region when modifying the illumination conditions, its value does increase when modifying the scan rate from 10 mV s^{-1} up to 500 mV s^{-1} (**Figure 2.15c & 2.15d**); whereupon, the limiting current becomes scan rate independent and saturates at a current density similar to that recorded at higher polarization (~ 20 mA cm^{-2}) (**Figure 2.17**). These results are consistent with limitations of the HER activity in the low polarization region due to diffusion of substrate protons (the second step in equation **Eq. 2.1**). This apparent shift of the current limiting peak feature to more positive potentials is attributed to a more rapid consumption of substrate protons at higher illumination conditions. In other words, the catalytic turnover frequency increases at higher illumination intensities, and the concentration of protons at the electrode surface becomes depleted earlier in the voltammogram scan, causing the peak feature to appear at more positive potentials. Conversely, the relative thickness of the diffusion layer, which is the region in the vicinity of an electrode where concentrations of chemical substrates are different from their values in the bulk solution,[40] depends on the time scale of the voltammogram scan. At faster scan rates, the thickness of the diffusion layer is narrower, enabling higher fluxes of chemical substrate to the electrode surface and hence higher currents.[41,42]

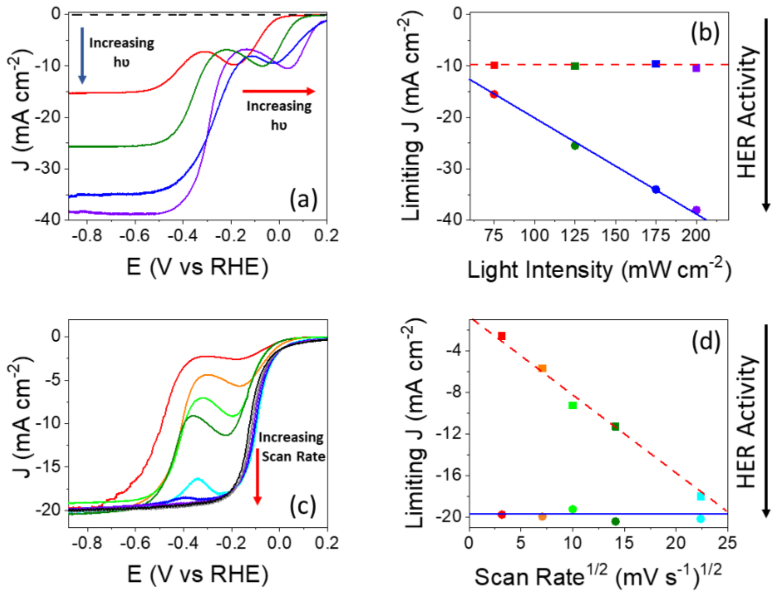

Figure 2.15. (a) Linear sweep voltammograms recorded at 100 mV s^{-1} using cobaloxime|PPy|GaAs electrodes in 0.1 M phosphate buffer (pH 7) and the following illumination intensities: 0 (black dash), 75 (red), 125 (olive), 175 (blue), and 200 (violet) mW cm^{-2}. (b) Plots of the limiting current densities recorded in the *low polarization region* (squares) and *high polarization region* (circles) versus the illumination intensity.

(c) Linear sweep voltammograms recorded under 100 mW cm^{-2} illumination using cobaloxime|PPy|GaAs electrodes in 0.1 M phosphate buffer (pH 7) and the following scan rates: 10 (red), 50 (orange), 100 (green), 200 (olive), 500 (cyan), 700 (blue), 1000 (violet), 1200 (grey), and 1500 (black) mV s^{-1}. (d) Plots of the limiting current densities recorded in the *low polarization region* (squares) and *high polarization region* (circles) versus the scan rate.

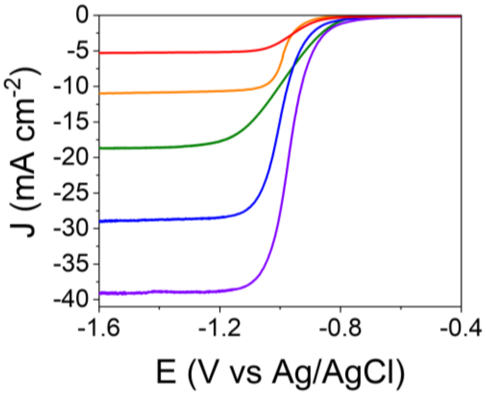

Figure 2.16. Linear sweep voltammograms recorded at a scan rate of 100 mV s^{-1} using cobaloxime|PPy|GaAs working electrodes in pH 13 (0.1 M NaOH) electrolyte solutions and the following illumination conditions: 25 (red), 50 (orange), 100 (olive), 150 (blue), and 200 (purple) mW cm^{-2}.

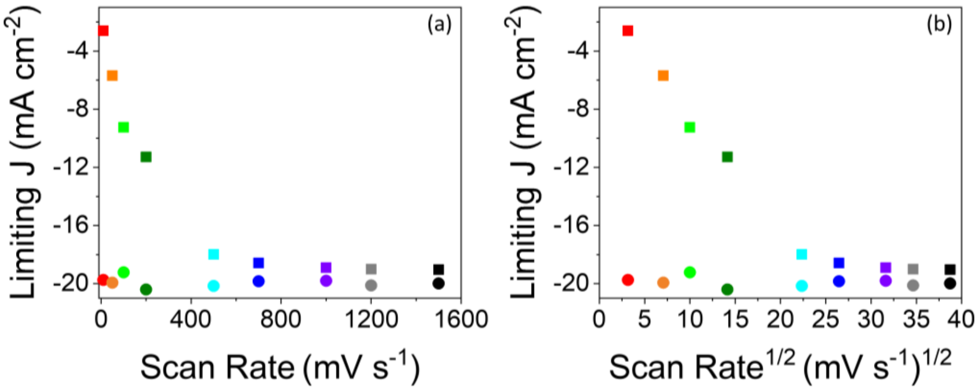

Figure 2.17. Plots of the limiting peak current densities versus (a) scan rate and (b) scan rate$^{1/2}$ recorded under 100 mW cm^{-2} illumination in the *low polarization region* (squares) and *high polarization region* (circles) using cobaloxime|PPy|GaAs working electrodes in pH neutral (0.1 M phosphate buffer) electrolyte solutions and the following scan rates: 10 (red), 50 (orange), 100 (green), 200 (olive), 500 (cyan), 700 (blue), 1000 (violet), 1200 (grey), and 1500 (black) mV s^{-1}.

In the high polarization region, the response of the limiting current to increasing light intensity and scan rate is counter to that observed in the low polarization region (**Figures 2.15b and 2.15d**), and the limiting current is instead proportional to the illumination intensity, yet invariant to increasing scan rate. These results are consistent with limitations of the HER activity related to the availability of photons at the electrode surface (the first step in **Eq. 2.2**). Under simulated 1-sun illumination, increasing the scan rate to improve mass transport, and thereby increase the availability of protons at the electrode surface, does not increase the limiting current and HER activity at high polarization because the electrode is photon starved. Further, at relatively high polarization, or high pH (**Figures 2.13 and 2.16**), the concentration of protons at the electrode surface is relatively low and water serves as a weak acid and reactant (the second step in equation **Eq. 2.2**).

Reduction of Protons at Relatively Low Polarization and Low pH:

Step 1: $h\nu + \text{semiconductor} \leftrightarrows e^- + h^+$

Step 2: $2H^+ + 2e^- \leftrightarrows H_2$ (Eq. 2.1)

Reduction of Water at Relatively High Polarization or High pH:

Step 1: $h\nu + \text{semiconductor} \leftrightarrows e^- + h^+$

Step 2: $2H_2O + 2e^- \leftrightarrows H_2 + 2OH^-$ (Eq. 2.2)

We continue utilizing this GaAs-based construct to better understand the mechanism of proton reduction and/or water reduction at the surface of a semiconductor interfaced with molecular catalysts. In particular, we aim to investigate the proton source for proton reduction at relatively low polarization to hydrogen, whether from solvated protons or from contributions from the buffer salts.

2.2.4 Quantum Efficiencies

External quantum efficiencies

External quantum efficiencies (EQE) were measured under a bias of 0 V vs RHE in the wavelength range of 300–550 nm for GaP and 300–900 nm for GaAs. The experimental setup consisted of a Biologic potentiostat and the QEPVSI-b Quantum Efficiency Measurement System from Newport Corporation, including a reference detector with NIST-traceable responsivity data, a 300 W Oriel Xenon lamp, and an Oriel Cornerstone 260 monochromator. Data were collected at 10 nm intervals. The current was collected at one point per second, and the data collected at each wavelength were averaged. The dark current was subtracted from the current produced under illumination. The photon flux (q_p) was determined using the voltage response of the reference detector in accordance with **Equation 2.6**:

$$q_{\mathrm{p}} = \frac{(V)}{(CR)(SR)(Gain)E(\lambda)} \qquad \text{(Eq. 2.6)}$$

where *V* is the detector voltage, *CR* is the correction multiplier of the AC measurement, *SR* is the spectral responsivity of the reference detector, *Gain* is the gain set for the detector, and *E* is the energy of a photon at a given wavelength.

External quantum efficiency (EQE) action spectra provide information on the number of charge carriers collected as current versus the number of photons incident on the working electrode surfaces. Analyses of the EQE action spectra recorded using cobaloxime|PPy|GaAs electrodes polarized at 0 V vs RHE (**Figures 2.12 & 2.18**) confirm these constructs are photoactive over wavelengths ranging from 300 to 870 nm. Conversely, cobaloxime|PPy|GaP electrodes are only photoactive over wavelengths ranging from 300 to 549 nm. These results corroborate our hypothesis that the GaAs-based constructs should be capable of delivering charge carriers required for activating surface-immobilized catalysts at significantly faster rates than those achieved analogous GaP-based constructs and facilitate mechanistic studies at relatively high rates of fuel formation.

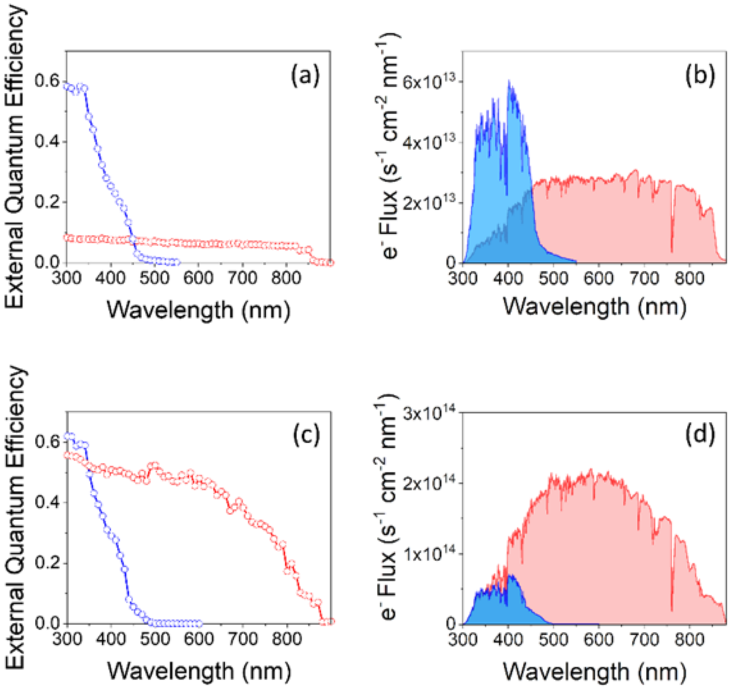

Figure 2.18. (a) External quantum efficiency (EQE) action spectra recorded at pH 7 using either cobaloxime|PPy|GaAs (red) or cobaloxime|PPy|GaP (blue) working electrodes polarized at 0 V vs RHE. (b) Electron flux spectra for cobaloxime|PPy|GaAs (red) and cobaloxime|PPy|GaP (blue) calculated using the EQE action spectra shown in Figure 3a and the solar flux spectrum shown in Figure 2.11. (c) EQE action spectra recorded at pH 13 using either cobaloxime|PPy|GaAs (red) or cobaloxime|PPy|GaP (blue) working electrodes polarized at 0 V vs RHE. (d) Electron flux spectra for cobaloxime|PPy|GaAs (red) and cobaloxime|PPy|GaP (blue) calculated using the EQE action spectra shown in Figure **2.18c** and the solar flux spectrum shown in **Figure 2.11a**.

Internal Quantum Efficiency

Internal quantum efficiencies (IQE) were calculated by dividing the measured EQE values by the light harvesting efficiency (LHE) at each wavelength of interest. LHEs were determined for GaAs and chemically-modified GaAs samples using Equations 2.7 and 2.8:

$$\Phi_{abs} = \text{LHE} = 1 - 10^{-A} \quad \text{(Eq. 2.7)}$$

$$A = \frac{\alpha * L}{\ln 10} \quad \text{(Eq. 2.8)}$$

where A is the absorbance, α is the wavelength-dependent absorption coefficient, and L is the pathlength or thickness of the GaAs wafer (400 µm).

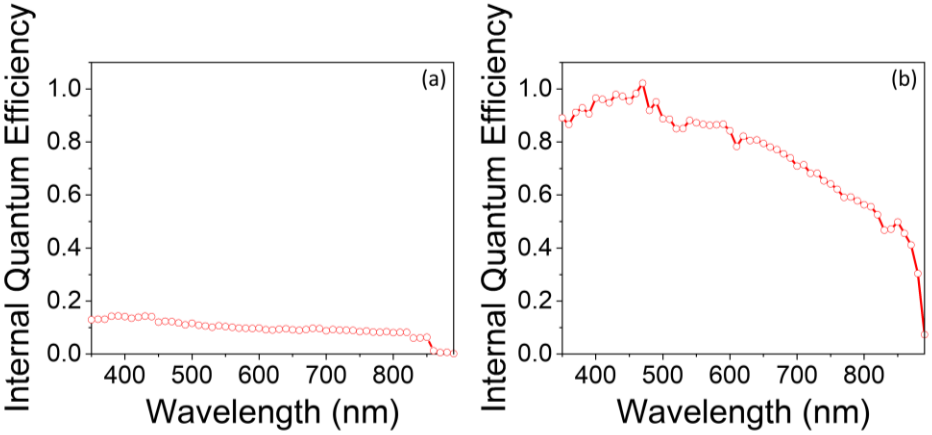

Figure 2.19. Internal quantum efficiency (IQE) action spectra of cobaloxime|PPy|GaAs working electrodes polarized at 0 V vs RHE in (a) 0.1 M phosphate buffer pH 7 (green) or (b) 0.1 M NaOH pH 13 (red). These IQE spectra were constructed using the related EQE spectra (**Figure 2.18**) and the plot of percentage of light absorbed by cobaloxime|PPy|GaAs (i.e., the light harvesting efficiency of cobaloxime|PPy|GaAs) versus the wavelength of illumination (solid line in **Figure 2.10**).

Spectral Profile of the LSC-100 Series Oriel Solar Simulator

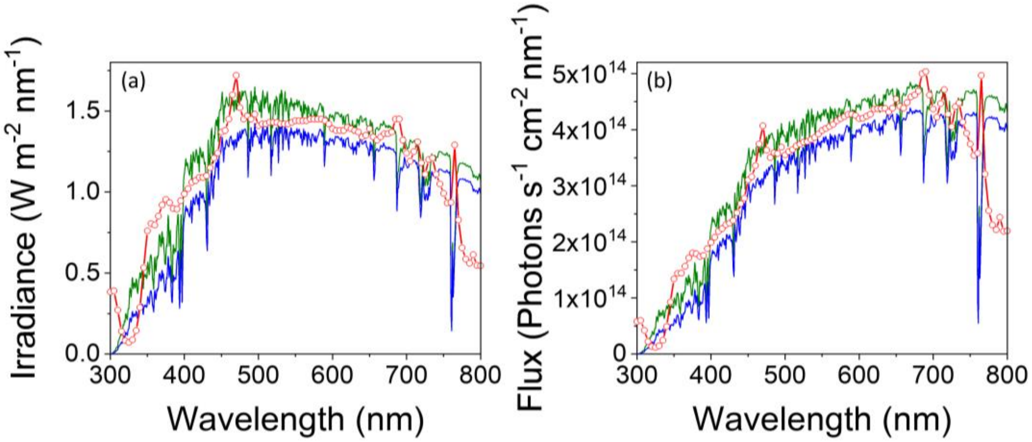

Figure 2.20. (a) Irradiance and (b) photon flux spectra of an LSC-100 Series Oriel Solar Simulator collected with an AM 1.5 G filter (red circles). For comparison, the air mass 1.5 global tilt (olive) and direct circumsolar (blue) irradiance and photon flux spectra are included.*

**At the time of writing, the air mass 1.5 global tilt (AM 1.5 G) spectrum from the ASTM G-173-03 data set is available online at hTTPs://www.nrel.gov/grid/solar-resource/spectra.html.*

2.2.5 Product detection

In addition, gas chromatography analyses of headspace gas samples taken from photoelectrochemical cells equipped with cobaloxime|PPy|GaP working electrodes polarized for 20 minutes at potentials in the high polarization region or low polarization region, and at pH 7 or pH 13, all confirm the production of hydrogen gas with near unity faradaic efficiency (**Figure 2.21**).

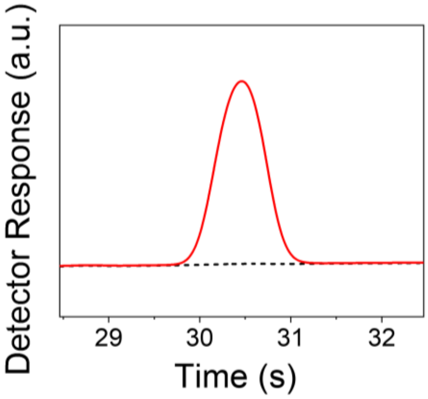

Figure 2.21. A representative gas chromatogram obtained from chromatography of a headspace gas sample taken from a sealed photoelectrochemical cell containing a cobaloxime|PPy|GaAs working electrode polarized at 0 V vs RHE in a pH 13 solution before (dashed line) and after (solid line) 20 min of illumination at 100 mW cm^{-2}. In these experiments, quantification of hydrogen confirmed near unity faradaic efficiencies when polarizing cobaloxime|PPy|GaAs working electrode at 0 V, -0.2 V, -0.58 V, -0.98 V, or -1.38 V vs RHE in pH 7 electrolyte solutions or at 0 V, -0.2 V, -0.52 V, or -1.92 V vs RHE in pH 13 electrolyte solutions.

2.2.6 Determination of Per Cobalt Hydrogen Evolution Reaction (HER) Activities

Per cobalt HER activities were determined using the total per geometric area cobalt surface loadings determined via ICP-MS and XPS measurements (2.4 ± 0.4 nmol cm-2) and the per geometric HER activities determined using photoelectrochemical experiments. This total cobalt surface loadings places an upper bound on the total cobaloxime surface loading. The presence of a broad infrared absorption feature located at 1235 cm^{-1} on surfaces of cobaloxime|PPy|GaAs (see **Figure 2.8**) could indicate the presence of remnant precursor complexes in addition to pyridyl-bound cobaloximes. If the per geometric area loading of active cobaloximes is lower than the upper bound set by ICP-MS and XPS measurements, the per cobalt HER activity values underestimate the related per cobaloxime site turnover frequencies.

In the absence of limitations due to diffusion of chemical substrates, the rate of a photoelectrosynthetic reaction (where J is the current density) occurring at a molecular-catalyst-modified semiconductor can be related to a rate constant for catalysis (where k_{cat} is a pseudo first-order rate constant which is the potential independent 'maximum' turnover frequency, $\mathrm{TOF}_{\mathrm{max}}$) and the concentration of immobilized catalysts present in their activated form ($\Gamma_{\mathrm{C}'}$) as indicated in Equation 2.9:[37]

$$J = \frac{\mathrm{nF}}{\mathrm{FE}} * \ k_{\mathrm{cat}}\,\Gamma_{\mathrm{C}'} \qquad \text{(Eq. 2.9)}$$

where n is the number of electrons required for the chemical transformation, F is the Faraday constant, FE is the faradaic efficiency. However, the results presented in this letter do not permit an accurate determination of the fraction of activated catalyst present on the semiconductor surfaces as the kinetics at low polarization and pH 7 are limited by diffusion of chemical substrate. In addition, the kinetics at high polarization and high pH are limited by the flux of photons. To the best of our knowledge, the $\mathrm{TOF}_{\mathrm{max}}$ associated with a molecular-modified semiconductor has not been reported for any assembly. Although the work described here sets the stage for achieving semiconductor immobilized catalysts that operate at relatively high activities, and thus closer to their maximum turnover frequencies, without an accurate determination of $\mathrm{TOF}_{\mathrm{max}}$ (k_{cat}), it is difficult to draw any firm conclusions regarding the enhanced activity at pH 13 for the constructs reported herein. Nonetheless, other reports describing enhanced hydrogen evolution activities at elevated pH have been reported in the literature for other molecular catalyst-modified semiconductors.[43,44]

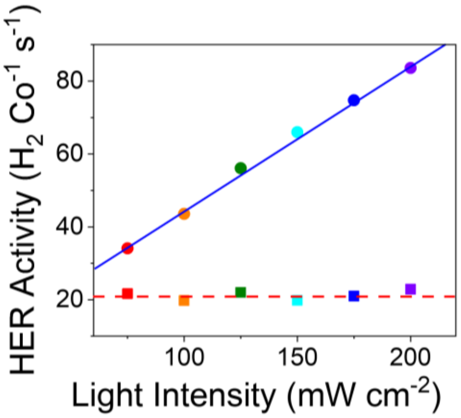

Figure 2.22. Plots of the limiting per cobalt site HER activity of cobaloxime|PPy|GaAs working electrodes in the *low polarization region* (squares) and *high polarization region* (circles) versus the illumination intensity when immersed in phosphate buffer (pH 7) and using a scan rate of 100 mV s^{-1} (see Experimental Methods for further details).

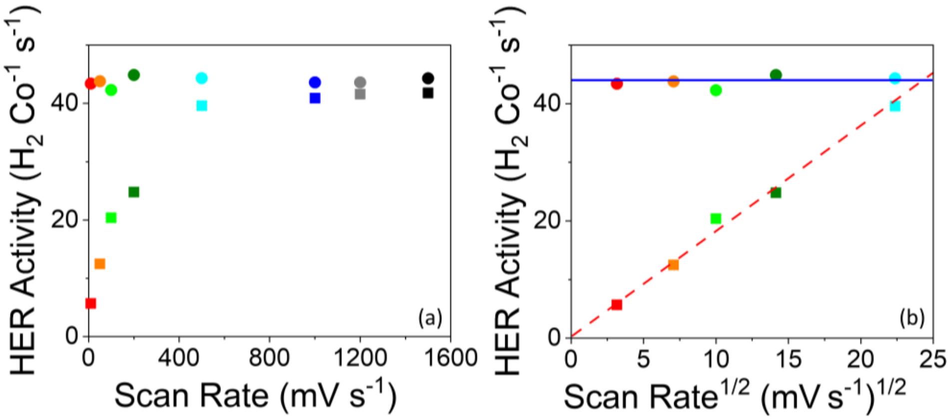

Figure 2.23. Plots of the limiting per cobalt site HER activity versus (a) scan rate and (b) scan rate$^{1/2}$ recorded under 100 mW cm^{-2} illumination in the *low polarization region* (squares) and *high polarization region* (circles) using cobaloxime|PPy|GaAs working electrodes in pH neutral (0.1 M phosphate buffer) electrolyte solutions and the following scan rates: 10 (red), 50 (orange), 100 (green), 200 (olive), 500 (cyan), 700 (blue), 1000 (violet), 1200 (grey), and 1500 (black) mV s^{-1}. The related linear sweep voltammetry data is shown in **Figure 2.15c**.

We have previously reported an equation connecting EQE and TOF (Eq 1.11).

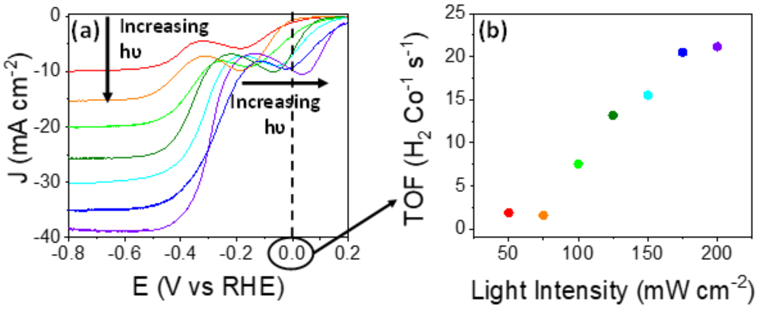

Figure 2.24. (a) Linear Sweep Voltammograms of cobaloxime|PPy|GaAs (red) recorded at 100 mV s^{-1}, under increasing illumination, in 0.1 M solution of phosphate buffer (pH 7). (b) Plot of the turnover frequency (TOF) recorded at 0 V vs RHE versus illumination intensity.

From the current densities collected in linear sweep experiments with varying illumination conditions, we can derive the TOF (H_2 molecule per Co site per second). A plot of this TOF versus the illumination intensity show that TOF increases linearly as the light intensity increase but eventually reach a maximum value of ~20 H_2 Co^{-1} s^{-1} under 200 mW cm^{-2} illumination (**Figure 2.24b**).

2.3 Conclusion

In conclusion, the higher activities achieved using the GaAs-based assemblies enable identification of the performance-limiting factors encountered at accelerated fuel-formation rates and reveal a hitherto unexplored switching of the rate-limiting steps and reagents required for driving photoelectrosynthetic reactions. In a longer-term view, a viable PEC device must be efficient, durable, and ultimately cost effective. To date no assembly effectively achieves this and thus there is a need for ongoing research addressing all of these aspects. The results described in this Chapter highlight the modularity of a polymeric-attachment strategy and provide insights for better understanding and controlling the rate-limiting steps of fuel-forming reactions at catalyst-modified semiconductors where photons, electrons, and protons are all required reagents.

2.4 References

(1) Ardo, S.; Fernandez Rivas, D. F.; Modestino, M. A.; Schulze Greiving, V. S.; Abdi, F. F.; Alarcon Llado, E. A.; Artero, V.; Ayers, K.; Battaglia, C.; Becker, J.-P.; Bederak, D.; Berger, A.; Buda, F.; Chinello, E.; Dam, B.; Di Palma, V.; Edvinsson, T.; Fujii, K.; Gardeniers, H.; Geerlings, H.; Hashemi, S. M. H.; Haussener, S.; Houle, F.; Huskens, J.; James, B. D.; Konrad, K.; Kudo, A.; Kunturu, P. P.; Lohse, D.; Mei, B.; Miller, E. L.; Moore, G. F.; Muller, J.; Orchard, K. L.; Rosser, T. E.; Saadi, F. H.; Schüttauf, J.-W.; Seger, B.; Sheehan, S. W.; Smith, W. A.; Spurgeon, J.; Tang, M. H.; van de Krol, R.; Vesborg, P. C. K.; Westerik, P. Pathways to Electrochemical Solar-Hydrogen Technologies. *Energy Environ. Sci.* **2018**, *11*, 2768−2783.

(2) Faunce, T. A.; Lubitz, W.; Rutherford, A. W.; MacFarlane, D.; Moore, G. F.; Yang, P.; Nocera, D. G.; Moore, T. A.; Gregory, D. H.; Fukuzumi, S.; Yoon, K. B.; Armstrong, F. A.; Wasielewski, M. R.; Styring, S. Energy and Environment Policy Case for a Global Project on Artificial Photosynthesis. *Energy Environ. Sci.* **2013**, *6*, 695−698.

(3) Blankenship, R. E.; Tiede, D. M.; Barber, J.; Brudvig, G. W.; Fleming, G.; Ghirardi, M.; Gunner, M. R.; Junge, W.; Kramer, D. M.; Melis, A.; Moore, T. A.; Moser, C. C.; Nocera, D. G.; Nozik, A. J.; Ort, D. R.; Parson, W. W.; Prince, R. C.; Sayre, R. T. Comparing Photosynthetic and Photovoltaic Efficiencies and Recognizing the Potential for Improvement. *Science* **2011**, *332*, 805−809.

(4) Walter, M. G.; Warren, E. L.; McKone J. R.; Boettcher, S. W.; Mi, Q.; Santori, E. A.; Lewis, N. S. Solar Water Splitting Cells. *Chem. Rev.* **2010**, *110*, 6446−6473.

(5) Gray, H. B, Powering the Planet with Solar Fuel. *Nat. Chem.* **2009**, *1*, 7.

(6) Khan, M. A.; Varadhan, P.; Ramalingam, V.; Fu, H.; Idriss, H.; He, J. Importance of Oxygen Measurements during Photoelectrochemical Water-Splitting Reactions. *ACS Energy Lett.* **2019**, *4*, 2712–2718.

(7) Holm, J., Jørgensen, H., Krogstrup, P. *et al.* Surface-passivated GaAsP single-nanowire solar cells exceeding 10% efficiency grown on silicon. *Nat. Commun.* **2013**, *4*, 1–5.

(8) Lewis, N. S.; Nocera, D. G. Powering the Planet: Chemical Challenges in Solar Energy Utilization. *Proc. Natl. Acad. Sci.* **2006**, *103*, 15729–15735.

(9) Wang, Y.; Wei, H.; Lv, H.; Chen, Z.; Zhang, J.; Yan, X.; Lee, L.; Wang, Z.M.; Chueh, Y. Highly Stable Three-Dimensional Nickel-Cobalt Hydroxide Hierarchical Heterostructures Hybridized with Carbon Nanotubes for High-Performance Energy Storage Devices. *ACS Nano* **2019**, *13*, 11235–11248.

(10) Manikandan, A.; Lee, L.; Wang, Y.; Chen, C.; Chen, Y.; Medina, H.; Tseng, J.; Wang, Z.M.; Chueh, Y. Graphene-coated copper nanowire networks as a highly stable transparent electrode in harsh environments toward efficient electrocatalytic hydrogen evolution reactions. *J. Mater. Chem. A* **2017**, *5*, 13320–13328.

(11) Vesborg, P. C. K.; Jaramillo, T. F. Addressing the Terawatt Challenge: Scalability in the Supply of Chemical Elements for Renewable Energy. *RSC Adv*. **2012**, *2* (21), 7933–7947.

(12) Chemical Sciences Roundtable. The Role of the Chemical Sciences in Finding Alternatives to Critical Resources: A Workshop Summary. Washington, D.C.: National Academies Press. 2012.

(13) Helm, M. L.; Stewart, M. P.; Bullock, R. M.; DuBois, M. R.; DuBois, D. L. A Synthetic Nickel Electrocatalyst with a Turnover Frequency Above 100,000 s^{-1} for H_2 Production. *Science* **2011**, *333* (6044), 863–866.

(14) Bacchi, M.; Berggren, G.; Niklas, J.; Veinberg, E.; Mara, M. W.; Shelby, M. L.; Poluektov, O. G.; Chen, L. X.; Tiede, D. M.; Cavazza, C.; Field, M. J.; Fontecave, M.; Artero, V. Cobaloxime-Based Artificial Hydrogenases. *Inorg. Chem.* **2014**, *53* (15), 8071–8082.

(15) Queyriaux, N.; Kaeffer, N.; Morozan, A.; Chavarot-Kerlidou, M.; Artero, V. Molecular Cathode and Photocathode Materials for Hydrogen Evolution in Photoelectrochemical Devices. *J. Photochem. Photobiol. C Photochem. Rev.* **2015**, *25*, 90–105.

(16) Ginovska-Pangovska, B.; Dutta, A.; Reback, M. L.; Linehan, J. C.; Shaw, W. J. Beyond the Active Site: The Impact of the Outer Coordination Sphere on Electrocatalysts for Hydrogen Production and Oxidation. *Acc. Chem. Res.* **2014**, *47* (8), 2621–2630.

(17) Dutta, A.; Ginovska, B.; Raugei, S.; Roberts, J. A. S.; Shaw, W. J. Optimizing Conditions for Utilization of an H_2 Oxidation Catalyst with Outer Coordination Sphere Functionalities. *Dalt. Trans.* **2016**, *45* (24), 9786–9793.

(18) Maher, A. G.; Passard, G.; Dogutan, D. K.; Halbach, R. L.; Anderson, B. L.; Gagliardi, C. J.; Taniguchi, M.; Lindsey, J. S.; Nocera, D. G. Hydrogen Evolution

Catalysis by a Sparsely Substituted Cobalt Chlorin. *ACS Catal.* **2017**, *7*(5), 3597–3606.

(19) Tsay, C.; Yang, J. Y. Electrocatalytic Hydrogen Evolution under Acidic Aqueous Conditions and Mechanistic Studies of a Highly Stable Molecular Catalyst. *J. Am. Chem. Soc.* **2016**, *138* (43), 14174–14177.

(20) Wiese, S.; Kilgore, U. J.; Ho, M.-H.; Raugei, S.; DuBois, D. L.; Bullock, R. M.; Helm, M. L. Hydrogen Production Using Nickel Electrocatalysts with Pendant Amines: Ligand Effects on Rates and Overpotentials. *ACS Catal*. **2013**, *3* (11), 2527–2535.

(21) Artero, V.; Saveant, J.-M. Toward the Rational Benchmarking of Homogeneous H2-Evolving Catalysts. *Energy Environ. Sci.* **2014**, *7* (11), 3808–3814.

(22) Costentin, C.; Savéant, J.-M. Multielectron, Multistep Molecular Catalysis of Electrochemical Reactions: Benchmarking of Homogeneous Catalysts. *ChemElectroChem* **2014**, *1* (7), 1226–1236

(23) Khusnutdinova, D.; Wadsworth, B. L.; Flores, M.; Beiler, A. M.; Reyes Cruz, E. A.; Zenkov, Y.; Moore, G. F. Electrocatalytic Properties of Binuclear Cu(II) Fused Porphyrins for Hydrogen Evolution. *ACS Catal*. **2018**, *8* (10), 9888–9898.

(24) Roberts, E. M.; Koski, W. S. An Electron Spin Resonance Study of Copper Etioporphyrin II1. *J. Am. Chem. Soc*. **1960**, *82* (12), 3006–3010.

(25) Blumberg, W. E.; Peisach, J. An Electron Spin Resonance Study of Copper Uroporphyrin III and Other Touraco Feather Components. *J. Biol. Chem*. **1965**, *240* (2), 870–876.

(26) Dempsey, J. L.; Brunschwig, B. S.; Winkler, J. R.; Gray, H. B. Hydrogen Evolution Catalyzed by Cobaloximes, *Acc. Chem. Res*. **2009**, *42*, 1995–2004.

(27) Krawicz, A.; Yang, J.; Anzenberg, E.; Yano, J.; Sharp, I. D.; Moore, G. F. Photofunctional Construct That Interfaces Molecular Cobalt-Based Catalysts for H2 Production to a Visible-Light-Absorbing Semiconductor. *J. Am. Chem. Soc*. **2013**, *135*, 11861−11868.

(28) Cedeno, D.; Krawicz, A.; Doak, P.; Yu, M.; Neaton, J. B.; Moore, G. F. A Noble-Metal-Free Hydrogen Evolution Catalyst Grafted to Visible Light-Absorbing Semiconductors. *J. Phys. Chem. Lett*. **2014**, *5*, 3222−3226.

(29) Beiler, A. M.; Khusnutdinova, D.; Jacob, S. I.; Moore, G. F. Solar Hydrogen Production Using Molecular Catalysts Immobilized on Gallium Phosphide (111)A and (111)B Polymer-Modified Photocathodes. *ACS Appl. Mater. Interfaces* **2016**, *8*, 10038−10047.

(30) Beiler, A. M.; Khusnutdinova, D.; Jacob, S. I.; Moore, G. F. Chemistry at the Interface: Polymer-Functionalized GaP Semiconductors for Solar Hydrogen Production. *Ind. Eng. Chem. Res.* **2016**, *55*, 5306−5314.

(31) Nguyen, N. P.; Wadsworth, B. L.; Nishiori, D.; Reyes Cruz, E. A.; Moore, G. F. Understanding and Controlling the Performance- Limiting Steps of Catalyst-Modified Semiconductors. *J. Phys. Chem. Lett*. **2021**, *12*, 199−203.

(32) Trogler, W.; Stewart, R. C; Epps, L. A.; Marzilli, L. G. Cis and Trans Effects on the Proton Magnetic Resonance Spectra of Cobaloxime. *Inorg Chem*. **1974**, *13*, 1564−1570.

(33) Costa, G.; Tauzher, G.; Puxeddu, A. Mechanism of Formation of trans-Chloro-Bisdimethylglyoximato-Tertiary Phosphine Cobalt(III) Complexes and Their Isomers 1:1 Electrolytes. *Inorg. Chim. Acta* **1969**, *3*, 45−48.

(34) Chuang, T. J.; Brundle, C. R.; Rice, D. W. Interpretation of the X-ray Photoemission Spectra of Cobalt Oxides and Cobalt Oxide Surfaces. *Surf. Sci.* **1976**, *59*, 413−429.

(35) Dillard, J. G.; Schenck, C. V.; Koppelman, M. H. Surface Chemistry of Cobalt in Calcined Cobalt-Kaolinite Materials. *Clays Clay Miner*. **1983**, *31*, 69−72.

(36) Beiler, A. M.; Khusnutdinova, D.; Wadsworth, B. L.; Moore, G. F. Cobalt Porphyrin-Polypyridyl Surface Coatings for Photoelectrosynthetic Hydrogen Production. *Inorg. Chem.* **2017**, *56*, 12178−12185.

(37) Wadsworth, B. L.; Beiler, A. M.; Khusnutdinova, D.; Reyes Cruz, E. A.; Moore, G. F. Interplay between Light Flux, Quantum Efficiency, and Turnover Frequency in Molecular-Modified Photoelectrosynthetic Assemblies. *J. Am. Chem. Soc.* **2019**, *141*, 15932−15941.

(38) Santangelo, P. G.; Miskelly, G. M.; Lewis, N. S. Voltammetry of Semiconductor Electrodes. 2. Cyclic Voltammetry of Freely Diffusing Redox Species and Rotating Semiconductor Disk Voltammetry. *J. Phys. Chem*. **1989**, *93*, 6128–6136.

(39) Gerischer, H.; Muller, N. On the Mechanism of Hydrogen Evolution at GaAs Electrodes. *J. Electroanal. Chem*. **1981**, *119*, 41–48.

(40) IUPAC. Compendium of Chemical Terminology, 2nd ed. (the "Gold Book"). Compiled by A. D. McNaught and A. Wilkinson. Blackwell Scientific

Publications, Oxford (1997). Online version (2019) created by S. J. Chalk. ISBN 0-9678550-9-8. hTTPs://doi.org/10.1351/goldbook.

(41) Bard, A. J.; Faulkner, L. R. Chapter 6: Potential Sweep Methods, In Electrochemical Methods: Fundamentals and Applications, 2nd ed., John Wiley & Sons, New York, 2001.

(42) Costentin, C.; Saveant, J.-M. Multielectron, Multistep Molecular Catalysis of Electrochemical Reactions: Benchmarking of Homogeneous Catalysts. *ChemElectroChem*. **2014**, *7*, 1226–1236.

(43) Gu, J.; Yan, Y.; Young, J. L.; Steirer K. X.; Neale, N. R.; Turner, J. A. Water Reduction by a p-$GaInP_2$ Photoelectrode Stabilized by an Amorphous TiO_2 Coating and a Molecular Cobalt Catalyst. *Nat. Mater.* **2016**, *15*, 456–460.

(44) Zhao, Y.; Anderson, N. C.; Ratzloff, M. W.; Mulder, D. W.; Zhu, K.; Turner, J. A.; Neale, N. R.; King, P. W.; Branz, H. M. Proton Reduction Using a Hydrogenase-Modified Nanoporous Black Silicon Photoelectrode. *ACS Appl. Mater. Interfaces* **2016**, *8*, 14481–14487.

CHAPTER 3 DEGRADE – REPAIR CYCLE OF A FUEL-FORMING PHOTOELECTRODE

Portions of this chapter are excerpted and reprinted with permission from:

Nguyen, N. P.; Hensleigh, L. K.; Nishiori, D.; Reyes Cruz, E. A.; Moore, G. F. Degrade-Repair Cycle of a Fuel-Forming Photoelectrode. *ACS Appl. Energy Mater.,* **2022**, *5*, 13128–13133.

3.1 Introduction

Artificial leaves that produce fuels using sunlight hold promise for sustainably powering the planet, but require advancements in energetic efficiency, cost effectiveness, and operational durability. Efficiency, however, is not enough for large-scale, global deployment. Scalability requires the component materials are also relatively low cost to manufacture, and durable. Nature offers some design aspirations in the process of biological photosynthesis, especially as they relate to using earth-abundant, low-cost elements and achieving durability via repair rather than inherent material stability.[1-4] In this Chapter, I showcase the application of combined surface-sensitive spectroscopic techniques to durability studies that characterize structural changes accompanying functional degradation and go beyond just observing changes in function over time. The photoelectrodes used in this work feature a polymeric surface coating functionalized with molecular complexes that catalyze the hydrogen evolution reaction. Using a polymeric layer to interface the light-harvesting component with catalytic sites enables reassembly of catalysts that detach during operation, establishing a degrade-repair cycle (**Figure 3.1**).

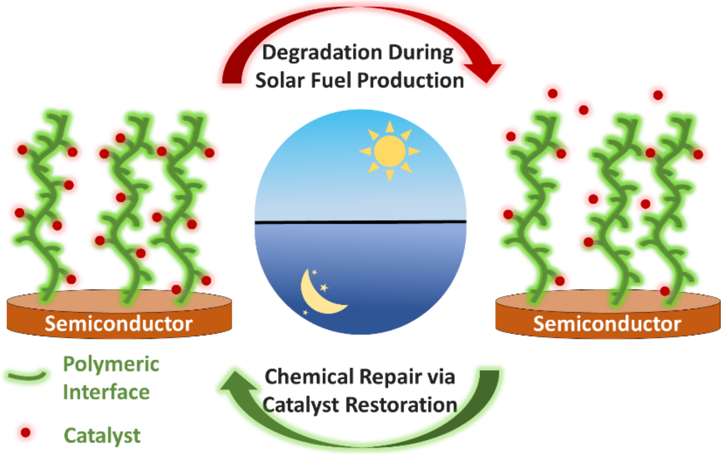

Figure 3.1. Schematic representations of a degrade-repair cycle for a molecular modified phototelectrode.

This chapter investigates the degradation in performance and structure of a photoelectrode featuring a polymeric coating applied to a visible-light-absorbing semiconductor. The surface coating provides a molecular interface, where catalysts are assembled at specific functional-group sites along the surface-grafted coating. This model system (Co|PPy|GaP) (**Figure 3.2**) is composed of a gallium phosphide (GaP) photocathode and a polypyridyl (PPy) surface coating that is used to assemble cobaloximes (Co), a relatively well studied class of molecular catalysts for the hydrogen evolution reaction.[5-9] Surface-sensitive structural characterization performed prior to and following degradation in rates of fuel formation indicates that detachment of catalysts, resulting from breaking of the pyridyl nitrogen–cobalt coordination during redox cycling, is responsible for the changes in function over time. We further show the polymeric architecture can be used to reassemble catalytic components that degrade during photoelectrosynthetic fuel production. These studies demonstrate that although coordinate bonds between a metal center and a polymeric functional group can be labile, they offer opportunities to explore the chemistry and engineering of achieving durably via repair rather than inherent material stability. In the context of producing *solar fuels,* this could involve operation by day and repair by night (**Figure 3.1**).

Previous work from our group describes synthetic methodologies for chemically grafting thin-film polymeric coatings onto conducting as well as semiconducting surfaces.[10-20] Overarching goals of these efforts include building protein-like, soft-material environments on solid-state electrode surfaces. This approach enables coordination of earth-abundant metal centers within the three-dimensional molecular coatings with the purpose of modulating, and ultimately controlling, the electronic and catalytic properties of the overall assembly. The grafting procedures leverage the UV-induced surface-attachment and polymerization chemistry of alkenes,[8,21-24] and provide model assemblies for studying the effects of polymeric-encapsulation on electrocatalytic[11,18,19] as well as photoelectrosynthetic[10,12-17,20] performance. Our previous work demonstrates: 1) the grafting method can be utilized on a range of oxide-terminated surfaces,[10-20] 2) the polymer grafting is not limited to a specific crystal-face orientation,[10,11] 3) the film thickness of the grafts –ranging from a few nano-meters to sub-microns– is sensitive to the reaction solvent conditions, illumination conditions, and chemical nature of the underpinning support (including doping levels in the case of semiconductors),[10-20] 4) the polymeric functional groups can be modified to control the (photo)electrosynthetic activity of the overall assembly,[12] 5) synthetic manipulation of the attached catalysts' ligand environment at the molecular level affects the photoelectrochemical response observed at the construct level,[13] and 6) the polymeric immobilization strategy is not limited to a single class of molecular catalysts, and thus provides a modular-assembly approach.[14,15]

3.2 Results and Discussion

3.2.1 Materials and Electrode Preparation

Materials

All reagents were purchased from Sigma-Aldrich. Methanol was freshly distilled over calcium hydride before use. All aqueous solutions were prepared using Milli-Q water (18.2 MΩ·cm). Zn-doped p-type Gallium Phosphide (GaP) (100) wafers were purchased from the Institute of Electronic Materials Technology, Poland. The crystalline wafers were single-side polished to an epi-ready finish. The GaP(100) wafers used in this report have a resistivity of 0.21-0.22 Ω·cm and a carrier concentration of 3.5×10^{17} to 3.7×10^{17} cm^{-3}, with an etch pit density of less than 4×10^4 cm^{-2}.

Molecular Synthesis

All syntheses were carried out under an argon atmosphere using Schlenk techniques, or under a nitrogen atmosphere in a glovebox (OMNI-Lab glove box from VAC), unless otherwise stated. All reagents were purchased from Aldrich. All solvents were stored over the appropriate molecular sieves prior to use. Milli-Q water (18.2 MΩ·cm) was used to prepare all aqueous solutions.

$Co(dmgH_2)(dmgH)Cl_2$ was prepared following a previously reported procedure.[25]

$Co(dmgH)_2PyCl$ was prepared as previously described.[25,26]

GaP Semiconductor Wafer Preparation

All wafers were degreased with an acetone-soaked cotton swab. The wafers were further cleaned using consecutive ultrasonic cleaning treatments (Cole-Parmer Ultrasonic Cleaner Model 08895-04) in a series of solvents (water, two minutes; methanol, two minutes; acetone, two minutes; methanol, two minutes; and water, two minutes), then exposed to an air-generated oxygen plasma (Harrick Plasma, U.S.) at 30 W for two minutes, followed by five minutes of etching in buffered hydrofluoric acid (6:1 HF/NH_4F in H_2O). The freshly etched wafers were put into quartz flasks containing argon-sparged 4-vinylpyridine and purged with argon for five minutes, after which they were placed into a custom-built UV-reaction chamber and irradiated with 254 nm light (using a Spectroline Model ENF-280C source operating at 115 V, 60 Hz, 0.20 A) for two hours. The resulting polypyridyl-modified GaP (PPy|GaP) wafers were then rinsed with methanol followed by ultrasonic cleaning in methanol for one minute, before drying under nitrogen and storing under vacuum. Cobaloxime functionalization was achieved by submerging the PPy|GaP wafers in an argon-sparged solution of $Co(dmgH_2)(dmgH)Cl_2$ and triethylamine (1 mM in each) in methanol and allowing them to react overnight. The resulting cobaloxime-modified PPy|GaP (Co|PPy|GaP) wafers were then rinsed with methanol, followed by rinsing with isopropanol, and drying under nitrogen (Figure 3.2).[9,12]

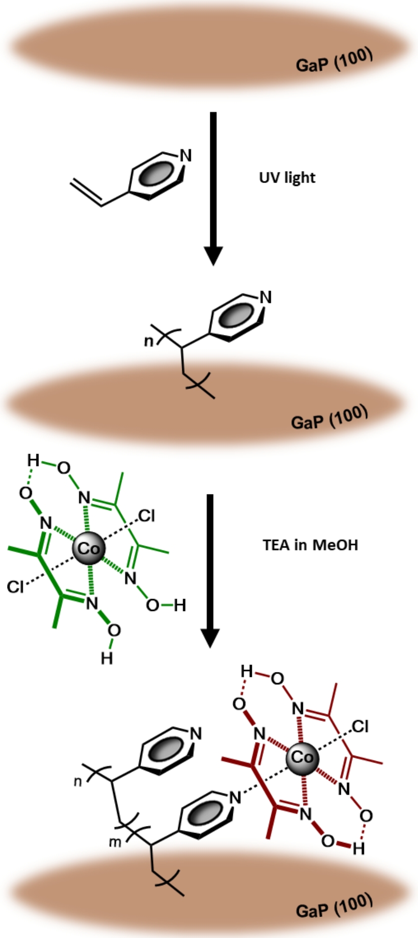

Figure 3.2. Schematic representation of the synthetic method used to prepare cobaloxime-polypyridyl-modified GaP electrodes (Co|PPy|GaP). In this scheme, assembly of the cobaloxime-type catalysts occurs by replacing one of the axial chloride ligands of the precursor complex, Co(dmgH$_2$)(dmgH)Cl$_2$, with a pyridyl functional group of the polymeric surface coating. Charge balance when replacing chloride, an anionic X-type ligand, with pyridyl, a neutral L-type ligand, is accounted for by the base-promoted conversion of the dimethylglyoxime ligand to the dimethylglyoximate monoanion.

Electrode Fabrication

GaP and chemically-modified GaP working electrodes were fabricated by applying an indium−gallium eutectic (Aldrich) to the unpolished face of the wafers. The electrodes were then installed into a customized photoelectrochemical cell featuring a spring-loaded mechanism for making electrical contact to the unpolished face of the wafers (**Figure 3.3**).

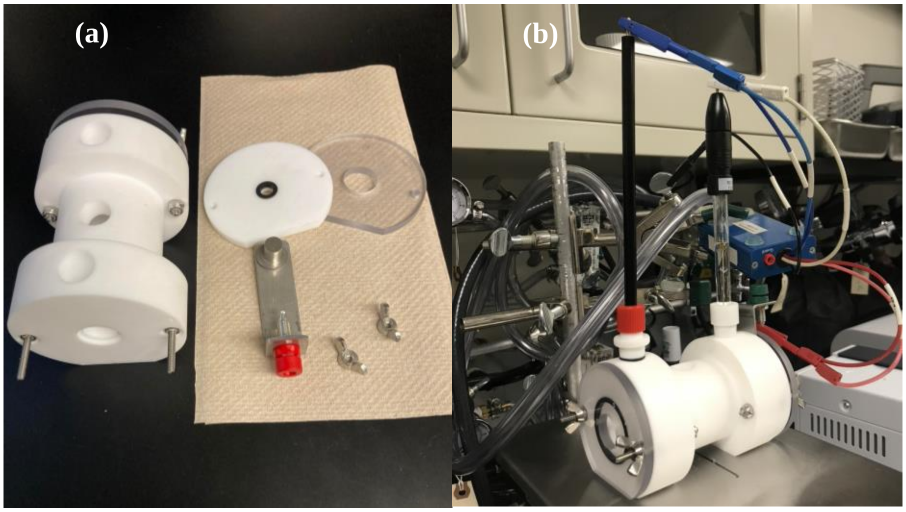

Figure 3.3. (a) Components of the customized photoelectrochemical cell used in this work and (b) the assembled cell in operation using a modified-GaP working electrode, a Pt counter electrode and Ag/AgCl reference electrode.

Electrode Chemical Repair Process

Following intial photoelectrochemical characterization experiments, the degraded wafers were unmounted from the photoelectrochemical cell, rinsed with Milli-Q water (18.2 MΩ·cm), and dried under N_2 gas before immersing them into an argon-sparged, methanolic solution of the cobalt-containing precursor complex, $Co(dmgH_2)(dmgH)Cl_2$, (1mM) and triethylamine (1 mM). Following overnight exposure, the wafers were removed from the methanolic solution, rinsed with methanol, rinsed with isopropanol, and dried under nitrogen to yield chemically-repaired, cobaloxime-modified PPy|GaP (Co|PPy|GaP) wafers. These repaired wafers were then used in *post-repair* structural characterization and photoelectrochemical experiments.

3.2.2 Workflow and processes used for surface characterization

Workflow and processing of GaP, PPy|GaP, and Co|PPy|GaP samples used for characterization via ellipsometry and GATR-FTIRspectroscopy

For the experiments reported in this communication, three samples of Co|PPy|GaP were initially characterized via ellipsometry and GATR-FTIRspectroscopy, before being subjected to photoelectrochemical experiments. The photoelectrochemical experiments included one linear sweep voltammogram recorded at a scan rate of 100 mV s^{-1}, scanning from 0.25 V to -1.5 V vs Ag/AgCl (from 0.873 V to -0.877 V vs RHE) under 1-sun illumination, followed by 15 minutes of controlled-potential electrolysis at 0 V vs RHE and then another linear sweep voltammogram scan performed under the same experimental conditions as the voltammogram recorded prior to the 15 minutes of controlled-potential electrolysis. All of these experiments were performed in a 0.1 M phosphate buffer solution at pH 7.

Following the photoelectrochemical experiments described above, the resulting *post-degrade* Co|PPy|GaP samples were then structurally characterized via ellipsometry and GATR-FTIRspectroscopy. These same *post-degrade* samples were then chemically repaired by placing them in a 1.0 mM methanolic solution of the cobalt-containing precursor $Co(dmgH_2)(dmgH)Cl_2$ for 18 hours, to yield the *post-repair* Co|PPy|GaP samples. The *post-repair* samples were then structurally characterized via ellipsometry and GATR-FTIRspectroscopy, before undergoing photoelectrochemical experiment of one linear sweep voltammogram scan under the same experimental conditions as the voltammograms recorded prior to and following the 15 minutes of controlled-potential electrolysis.

For control experiments, three samples of PPy|GaP and three samples of GaP underwent otherwise similar processing and characterization, but without the catalyst regeneration step and subsequent structural and photoelectrochemical characterization.

A summary of this overall workflow and processing of GaP, PPy|GaP, and Co|PPy|GaP samples used for characterization via ellipsometry and GATR-FTIRspectroscopy is illustrated in **Figure 3.4**.

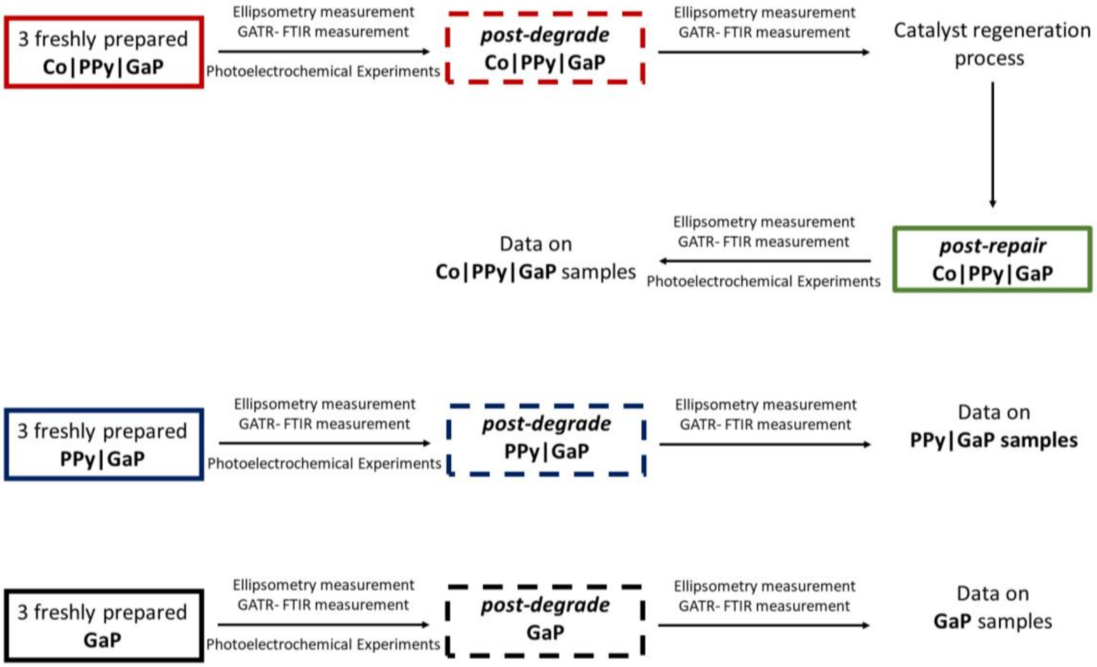

Figure 3.4. Work and processing scheme used for characterizing samples via GATR-FTIRand ellipsometry.

Workflow and processing of GaP, PPy|GaP, and Co|PPy|GaP samples used for characterization via XP spectroscopy

For the experiments reported in this communication, six separate Co|PPy|GaP samples were prepared.

Two of these samples were immediately characterized via XP spectroscopy, providing data on the *initial* Co|PPy|GaP samples.

Another two samples underwent a series of photoelectrochemical measurements consisting of linear sweep voltammetry, followed by 15 minutes of controlled-potential electrolysis and then another linear sweep voltammetry using the same electrochemical, experimental conditions as described above in the section titled: *"Workflow and processing of GaP, PPy|GaP, and Co|PPy|GaP samples used for characterization via ellipsometry and GATR-FTIRspectroscopy."* These *post-degrade* samples were then characterized by XP spectroscopy.

The final two samples underwent both photoelectrochemical measurement and catalyst regeneration process, before being characterized by XP spectroscopy, providing XP spectroscopy data on *post-repair* Co|PPy|GaP samples. A series of photoelectrochemical measurements consisted of linear sweep voltammetry, followed by 15 minutes of controlled-potential electrolysis and then another linear sweep voltammetry using the same electrochemical, experimental conditions as described above in the section titled *"Workflow and processing of GaP, PPy|GaP, and Co|PPy|GaP samples used for characterization via ellipsometry and GATR-FTIRspectroscopy."* These *post-degrade* samples were then chemically repaired via placing them in a 1.0 mM methanolic solution of the cobalt-containing precursor $Co(dmgH_2)(dmgH)Cl_2)$ for 18 hours, to yield the *post-repair* Co|PPy|GaP samples. The *post-repair* samples were then characterized by XP spectroscopy.

A summary of this overall workflow and processing of GaP, PPy|GaP, and Co|PPy|GaP samples used for characterization via XP spectroscopy is illustrated in **Figure 3.5**.

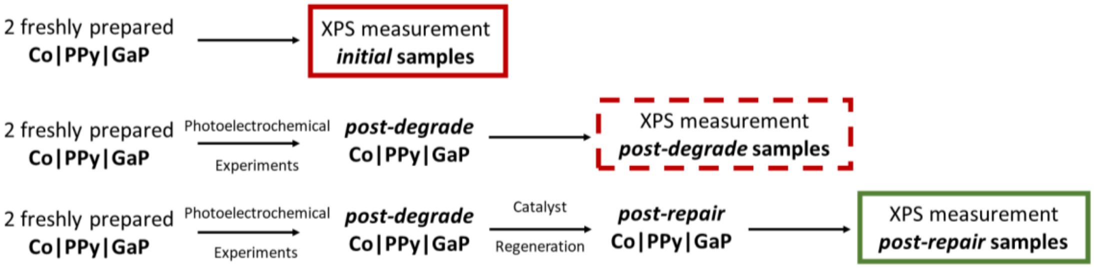

Figure 3.5. Work and processing scheme used for characterizing samples via XP spectroscopy.

3.2.3 Analysis of catalyst degradation and regeneration on Co|PPy|GaP surfaces via GATR-FTIR, XP spectroscopy, and ellipsometry

Fraction of total pyridyl-nitrogen sites coordinated to cobaloxime cobalt centers following catalyst degradation, as determined via GATR-FTIR

For this analysis all GATR-FTIRspectra were normalized to the absorbance at 1600 cm^{-1}. The percentage of initial cobaloxime catalyst that has degraded following photoelectrochemical operation were then evaluated by comparing the relative signal intensities of the absorption bands at 1240 cm^{-1} (assigned to the NO^{-} stretch of pyridyl coordinated cobaloxime catalysts) versus 1600 cm^{-1} (assigned to the C=N stretch of the polypyridyl layer) (ν_{1240}/ν_{1600}), recorded for the *post-degrade* versus *initial* samples as follows:

$$\%\,Degradation_{1600} = \frac{\nu_{1240}/\nu_{1600}\ initial - \nu_{1240}/\nu_{1600}\ post-degrade}{\nu_{1240}/\nu_{1600}\ initial} \times 100\% \qquad \text{(Eq. 3.1)}$$

A similar analysis is afforded by comparing the relative signal intensities of the absorption bands at 1240 cm^{-1} versus 1417 cm^{-1} feature (assigned to the C-N stretch of the polypyridyl layer) (ν_{1240}/ν_{1417}), recorded for the *post-degrade* versus *initial* samples as follows:

$$\% \, Degradation_{1417} = \frac{\nu_{1240}/\nu_{1417} \, initial - \nu_{1240}/\nu_{1417} \, post-degrade}{\nu_{1240}/\nu_{1417} \, initial} \times 100\%$$

(Eq.3.2)

Using this method, we obtain the % Degradation values indicated in **Table 3.1**.

Fraction of total pyridyl-nitrogen sites coordinated to cobaloxime cobalt centers following catalyst repair, as determined via GATR-FTIR

For this analysis all GATR-FTIRspectra were normalized to the absorbance at 1600 cm^{-1}. The percentage of initial cobaloxime catalyst restored via chemical repair was then evaluated by comparing the relative signal intensities of the absorption bands at 1240 cm^{-1} (assigned to the NO^{-} stretch of pyridyl coordinated cobaloxime catalysts) versus 1600 cm^{-1} (assigned to the C=N stretch of the polypyridyl layer) (ν_{1240}/ν_{1600}), recorded for the *post-degrade* versus *initial* samples as follows:

$$\% \, Repair_{1600} = \frac{\nu_{1240}/\nu_{1600} \, post-repair}{\nu_{1240}/\nu_{1600} \, initial} \times 100\% \qquad \text{(Eq. 3.3)}$$

A similar analysis is afforded by comparing the relative signal intensities of the absorption bands at 1240 cm^{-1} versus 1417 cm^{-1} feature (assigned to the C-N stretch of the polypyridyl layer) (ν_{1240}/ν_{1417}), recorded for the *post-repair* versus initial samples as follows:

$$\% \ Repair_{1417} = \frac{\nu_{1240}/\nu_{1417} \ post\text{-}repair}{\nu_{1240}/\nu_{1417} \ initial} \times 100\% \qquad \text{(Eq. 3.4)}$$

Using this method, we obtain the % Repair values indicated in **Table 3.1**.

Table 3.1. Percentage of initial cobaloximes that degrade following photoelectrochemical operation (% Degradation), and the percentage of initial cobaloximes present following chemical repair (% Repair), as determined via GATR-FTIRrelative peak intensity analysis.

Sample	**% Degradation or % Repair using ν_{1240}/ν_{1600}**	**% Degradation or % Repair using ν_{1240}/ν_{1417}**
Co|PPy|GaP *(post-degrade)*	74 ± 2% degradation of *initial* loading	74 ± 2% degradation of *initial* loading
Co|PPy|GaP (*post-repair*)	96 ± 4% repair of *initial* loading	95 ± 4% repair of *initial* loading

Fraction of total pyridyl-nitrogen sites coordinated to cobaloxime cobalt centers as determined via deconvolution of N 1s core level XP spectra

Spectra obtained using Co|PPy|GaP samples were deconvoluted using three components (see Figure 3.12). These include a component centered at 398.0 eV assigned to free-base pyridyl nitrogens (abbreviated as PyN), a component centered at 399.5 eV assigned to glyoximate nitrogens of the cobaloxime ligands (abbreviated as GlyN), and a component centered at 400.5 eV assigned to pyridyl nitrogens coordinated to the cobalt centers of cobaloximes (abbreviated as PyN-Co). Comparing the spectral intensity ratios of the PyN and PyN-Co components enables estimation of the fraction of total pyridyl-nitrogen sites coordinated to cobaloxime cobalt centers ($\frac{(\boldsymbol{PyN\text{-}Co})}{(\boldsymbol{PyN})+(\boldsymbol{PyN\text{-}Co})}$).

Comparing this fraction using *initial*, *post-degrade*, and *post-repair* samples of Co|PPy|GaP yields information on the percentage of initial cobaloximes that degrade following photoelectrochemical operation (% Degradation), and the percentage of initial cobaloximes present following chemical repair (% Repair), as determined via deconvolution of N 1s core level XP spectra.

Using this method, we obtain values indicated in **Table 3.2**.

Table 3.2. Fraction of total pyridyl-nitrogen sites coordinated to cobaloxime cobalt centers as determined via deconvolution of N 1s core level XP spectra.

Samples	$\frac{(\boldsymbol{PyN\text{-}Co})}{(\boldsymbol{PyN})+(\boldsymbol{PyN\text{-}Co})}$	**% Degradation/Repair of Cobaloximes**
Co|PPy|GaP (*initial*)	33.8 ± 0.3%	-
Co|PPy|GaP (*post-degrade*)	7.1 ± 0.2%	79 ± 1% degradation of *initial* loading
Co|PPy|GaP (*post-repair*)	32 ± 1%	95 ± 3% repair of *initial* loading

Fraction of total pyridyl-nitrogen sites coordinated to cobaloxime cobalt centers as determined via Co:N XP spectral intensity ratios

In this analysis, we define the fraction (x) of total pyridyl-nitrogen sites coordinated to the cobalt centers of cobaloximes, as follows:

$$x \equiv \frac{(PyN\text{-}Co)}{(PyN)+(PyN\text{-}Co)} \qquad \text{(Eq. 3.5)}$$

where PyN-Co is the number of pyridyl nitrogens coordinated to cobaloxime cobalt centers, and PyN is the number of free-base pyridyl nitrogens.

In addition, we define the fraction (y) of total nitrogen sites that are pyridyl nitrogens coordinated to cobaloxime cobalt centers, and use the cobalt 2p to nitrogen 1s spectral intensity ratio (Co:N) to approximate this value, as follows:

$$y \equiv \frac{(PyN\text{–}Co)}{(PyN)+(PyN\text{–}Co)+(GlyN)} \approx Co{:}N \qquad \text{(Eq. 3.6)}$$

where GlyN is the number of glyoximate nitrogens to cobaloxime cobalt centers. This approximation assumes the nitrogen signals arise from contributions of either free-base pyridyl nitrogens, pyridyl nitrogens coordinated to cobaloxime cobalt centers, or glyoximate nitrogens coordinated to cobaloxime cobalt centers, and cobalt signals arise from cobaloxime contributions only. These assumptions are consistent with spectral characterization via GATR-FTIRand N 1s as well as Co 2p core level XP spectroscopy.

Given the 4:1 stoichiometry of $PyN\text{–}Co$ to $GlyN$ for an individual cobaloxime unit, Eq. 3.7 can be expressed in terms of y, and the value of Co:N is used to approximate the value of x, as follows:

$$x \approx \frac{Co{:}N}{1-4Co{:}N} \qquad \text{(Eq. 3.7)}$$

Using this method, we obtain the relative cobaloxime loadings indicated in **Table 3.3**.

Table 3.3. Fraction of total pyridyl-nitrogen sites coordinated to cobaloxime cobalt centers as determined via Co:N XP spectral intensity ratios.

Samples	$\frac{(\boldsymbol{PyN\text{–}Co})}{(\boldsymbol{PyN})+(\boldsymbol{PyN\text{–}Co})}$	**% Degradation/Repair of Cobaloximes**
Co|PPy|GaP (*initial*)	31 ± 1%	-
Co|PPy|GaP (*post-degrade*)	5.2 ± 0.5%	84 ± 2% degradation of *initial* loading
Co|PPy|GaP (*post-repair*)	30 ± 1%	95 ± 4% repair of *initial* loading

Per-geometric-area loadings of cobaloximes as determined via ellipsometry and XP spectral measurement

By combining information on polymer thicknesses, as determined via ellipsometry, and fraction of total pyridyl-nitrogen sites coordinated to cobaloxime cobalt centers, obtained from XP spectroscopy, we estimate the per-geometric-area loadings of cobaloxime catalysts on Co|PPy|GaP surfaces.

We estimate a polypyridyl site density (ρ_{PPy}) of 2.53 ± 0.01 nmol cm^{-2} by using the polymer thickness (2.31 ± 0.01 nm as determined via ellipsometry measurement), the density of polyvinylpyridine (1.15 g cm^{-3}) and the molar mass of 4-vinylpyridine (105.14 g mol^{-1}) as follows:

$$\rho_{PPy} = \frac{1.15\ g\ cm^{-3}}{105.14\ g\ mol^{-1}} \times 2.31 \times 10^{-7} cm\ = 2.53\ nmol\ cm^{-2} \qquad \text{(Eq. 3.8)}$$

The fraction of total pyridyl-nitrogen sites coordinated to cobaloxime cobalt centers can be determined via N 1s core level XP spectra (33.8 ± 0.3 % - Table 3.2) or via Co:N XP spectral intensity ratios (31 ± 1 % - Table 3.3). The average value of relative Co loading calculated via the two methods is 32.4 ± 0.5 %.

Using this information on ρ_{PPy} and the fraction of total pyridyl-nitrogen sites coordinated to cobaloxime cobalt centers, we estimate the per-geometric-area cobaloximes loadings on Co|PPy|GaP surfaces as follows:

$$Per - geometric - area\ cobaloxime\ loading = \rho_{PPy} \times relative\ Co\ loading =$$

$$2.53 \pm 0.01\ nmol\ cm^{-2} \times 32.4 \pm 0.5\ \% = 0.82 \pm 0.01\ nmol\ Co\ cm^{-2}$$

(Eq. 3.9)

Using this method, we obtain the *initial* per-geometric-area cobaloxime loadings indicated in **Table 3.4**.

The *post-degrade* or *post-repair* per-geometric-area loadings of cobaloxime catalysts on Co|PPy|GaP surfaces are calculated from the *initial* loading with the average % degraded or repair determined via GATR-FTIR, N 1s core level XP spectra, or via Co:N XP spectral intensity ratios.

The average % degraded determined via GATR-FTIR(74 ± 2 % - Table S3.1), N 1s core level XP spectra (79 ± 1 % - Table S2), or via Co:N XP spectral intensity ratios (84 ± 2 % - Table S3) is 79 ± 1 %. This gives the average % of cobaloxime remained on the surface *post-degrade* as 21 ± 1 %. From this, the *post-degrade* per-geometric-area cobaloxime loadings can be calculated as:

$$Per - geometric - area\ cobaloxime\ loading_{\mathrm{post-degrade}} = initial\ loading \times$$

$$\%\ Co\ on\ the\ surafce\ post - degrade = 0.82 \pm 0.01\ nmol\ Co\ cm^{-2} \times 21 \pm$$

$$1\,\% \;=\; 0.172 \;\pm\; 0.009\, nmol\ Co\ cm^{-1} \qquad \text{(Eq. 3.10)}$$

Similarly, the average % repair determined via GATR-FTIR(96 ± 3 % - Table S1), N 1s core level XP spectra (95 ± 3 % - Table S2), or via Co:N XP spectral intensity ratios (95 ± 4 % - Table S3) is 95 ± 2 %. From this, the *post-repair* per-geometric-area cobaloxime loadings can be calculated as:

$$Per-geometric-area\ cobaloxime\ loading_{\mathrm{post-repair}} \;=\; initial\ loading \;\times\; \%\, Co\ on\ the\ surafce\ post-repair \;=\; 0.82 \;\pm\; 0.01\, nmol\ Co\ cm^{-2} \;\times\; 95 \;\pm\; 2\,\% \;=\; 0.78 \;\pm\; 0.02\, nmol\ Co\ cm^{-1} \qquad \text{(Eq. 3.11)}$$

From the calculations above, we obtain the *initial*, *post-degrade*, *and post-repair* per-geometric-area cobaloxime loadings indicated in **Table 3.4** shown in this chapter.

Table 3.4. Per-geometric-area Cobaloxime loadings[a]

Sample	**Cobaloxime Loading (nmol Co cm^{-2})**[a]
Co|PPy|GaP (*initial*)	0.82 ± 0.01
Co|PPy|GaP (*post-degrade*)	0.172 ± 0.009
Co|PPy|GaP (*post-repair*)	0.78 ± 0.02

[a] As determined via a combination of ellipsometry and XP spectroscopy.

3.2.4 Photoelectrochemical Performance

The photoelectrosynthetic performance of the GaP, PPy|GaP, and Co|PPy|GaP electrode assemblies was assessed via a combination of three-electrode voltammetry (**Figure 3.6c**) and controlled-potential electrolysis (**Figure 3.6d**) using aqueous solutions buffered at pH 7 (0.1 M phosphate buffer) and 100 mW cm^{-2} simulated-solar-illumination. Results from these experiments, including the short-circuit current densities (J_{SC}), open-circuit voltages (V_{OC}), and fill factors (*ff*), measured prior to and following 15 minutes of controlled-potential electrolysis at 0 V vs the reversible hydrogen electrode (RHE) potential, are summarized in Table 3.5. Following the initial voltammetry and controlled-potential electrolysis experiments recoded using the Co|PPy|GaP working electrodes, the J_{SC} decreased from 0.98 ± 0.01 mA cm^{-2} to 0.84 ± 0.04 mA cm^{-2} (corresponding to a 14 ± 3% decrease in activity). Likewise, the V_{OC} decreased from 0.718 ± 0.005 V vs RHE to 0.65 ± 0.03 V vs RHE (corresponding to a 10 ± 4% decrease), and the *ff* decreased from 0.17 ± 0.01 to 0.14 ± 0.02 (corresponding to a 20 ± 4% decrease). These electrodes also showed a decline in the steady-state photocurrent recorded during the 15 min of controlled-potential electrolysis, from an initial value of 1.05 ± 0.03 mA cm^{-2} to a final value of 0.63 ± 0.07 mA cm^{-2} (an overall 39 ± 6% decrease). Results from control experiments, performed using GaP and PPy|GaP as the working electrodes, are also included (**Table 3.5**).

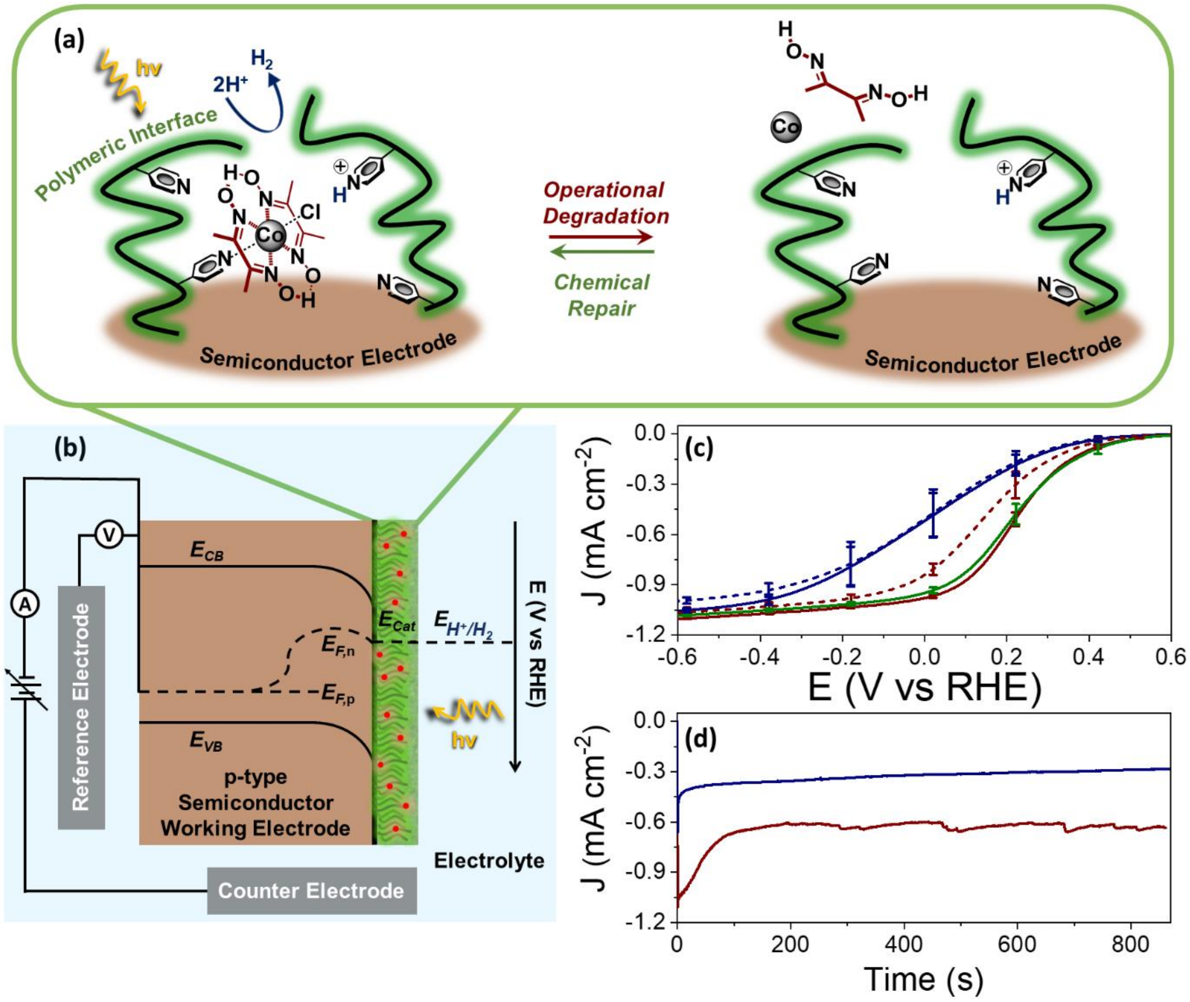

Figure 3.6. (a) Schematic representation of the Co|PPy|GaP degrade-repair cycle. (b) Schematic illustration of the three-electrode assembly featuring a molecular-modified p-type semiconductor working electrode under steady-state illumination at open-circuit conditions. E_{CB} is conduction band-edge potential and E_{VB} is valence band-edge potential, $E_{\mathrm{F,n}}$ is the electron quasi-Fermi level, $E_{\mathrm{F,p}}$ is the hole quasi-Fermi level, E_{cat} is the catalyst potential, $E_{\mathrm{H+/H2}}$ is the thermodynamic hydrogen potential, and V_{ph} is the photovoltage. (c) Voltammograms recorded using Co|PPy|GaP electrodes prior to (red) and following (red dash) degradation via controlled-potential electrolysis at 0 V vs RHE (see Figure 1d and related caption), as well as subsequent repair via wet-chemical

processing (green). Voltammograms recorded using PPy|GaP electrodes prior to (blue) and following (blue dash) the same controlled-potential electrolysis experiments are included for comparison. All voltammograms were recorded in 0.1 M phosphate buffer (pH 7) solution, at a scan rate of 100 mV s^{-1}, and under 100 mW cm^{-2} illumination. (d) Current density versus time plots obtained via 15 minutes of controlled-potential electrolysis at 0 V vs RHE using either Co|PPy|GaP (red) or PPy|GaP (blue) electrodes in 0.1 M phosphate buffer (pH 7), and under 100 mW cm^{-2} illumination.

Table 3.5. Open-circuit voltages, short-circuit current densities, maximum power points, and fill factors extracted from linear sweep voltammetry data recorded at a scan rate of 100 mV s^{-1} using GaP, PPy|GaP, and Co|PPy|GaP working electrodes in 0.1 M phosphate buffer (pH 7) before (indicated as *initial*) and after 15 minutes controlled-potential electrolysis (indicated as *post-degrade*), and after regeneration of catalyst (indicated as *post-repair*). All data were recorded under simulated 1-sun illumination.

Construct	**Open-Circuit Voltage (V vs RHE)**	**Short-Circuit Current (mA cm^{-2})**	**Maximum Power Point (mW cm^{-2})**	**Fill Factor**
GaP (*initial*)	0.62 ± 0.03	0.5 ± 0.1	0.026 ± 0.006	0.095 ± 0.005
GaP (*post-degrade*)	0.51 ± 0.03	0.27 ± 0.08	0.009 ± 0.003	0.069 ± 0.003
PPy|GaP (*initial*)	0.61 ± 0.06	0.42 ± 0.08	0.024 ± 0.007	0.10 ± 0.02
PPy|GaP (*post-degrade*)	0.63 ± 0.02	0.5 ± 0.2	0.04 ± 0.02	0.12 ± 0.01
Co|PPy|GaP (*initial*)	0.718 ± 0.005	0.98 ± 0.01	0.120 ± 0.008	0.17 ± 0.01
Co|PPy|GaP (*post-degrade*)	0.65 ± 0.03	0.84 ± 0.04	0.07 ± 0.02	0.14 ± 0.02

Co|PPy|GaP (*post-repair*)	0.71 ± 0.04	0.95 ± 0.02	0.114 ± 0.009	0.167 ± 0.008

It has not escaped our attention that the loss of photoelectrosynthetic activities described in this chapter, as observed during the 15 minutes of controlled-potential electrolysis experiments using Co|PPy|GaP working electrodes intentionally prepared with a relatively thin (~2.31 ± 0.01 nm) PPy coating, is not linear (see **Figure 3.6d**). In these experiments, there is an initial, more rapid loss of activity that occurs during the first ~150 s (with a 39 ± 6% decrease of current density from 1.05 ± 0.03 mA cm^{-2} to 0.64 ± 0.06 mA cm^{-2}). This is followed by a relatively more stable phase (with a 2 ± 14% change in the current density to a value of 0.63 ± 0.07 mA cm^{-2} at the end of the overall 15-minute experiment). We speculate the upfront loss in activity is a consequence of catalysts detachment at points loosely associated with the polymeric coating and/or at sites more directly exposed to the bulk electrolyte.

Further, as demonstrated by performing three successive degrade-repair cycles (**Figure 3.7**). the restoration of photoelectrochemical activity following chemical repair is not limited to a single cycle.

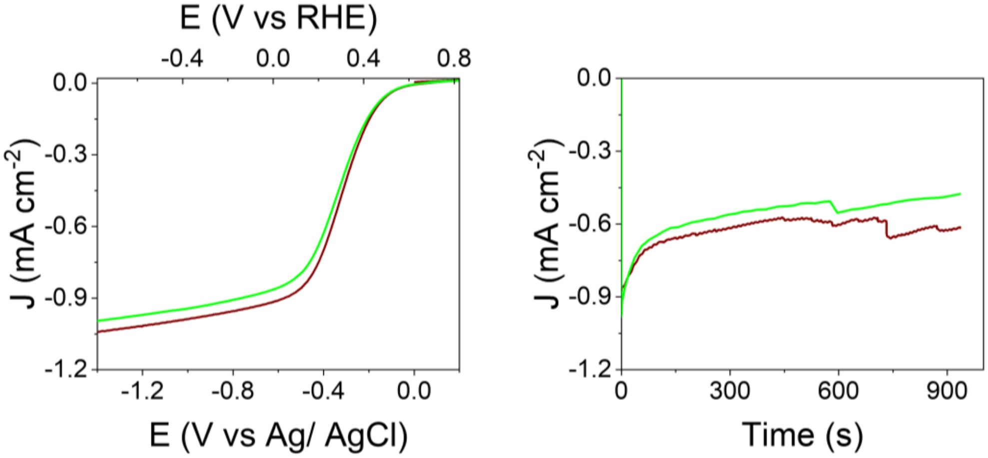

Figure 3.7. (a) Linear sweep voltammograms recorded at a scan rate of 100 mV s^{-1} using a Co|PPy|GaP working electrodes in 0.1 M phosphate buffer (pH 7), under 100 mW cm^{-2} before controlled-potential electrolysis experiment (red) and after the third *degrade-repair* cycle (light green). (b) Current density versus time plots obtained via 15 minutes of controlled-potential electrolysis at 0 V vs RHE using the electrodes described in (a).

3.2.5 Product Detection via Gas Chromatography

Product detection via gas chromatography experiments performed using *initial*, *post-degrade*, and *post-repair* electrodes confirms hydrogen production in the case of all samples (**Figures 3.8-3.11**).

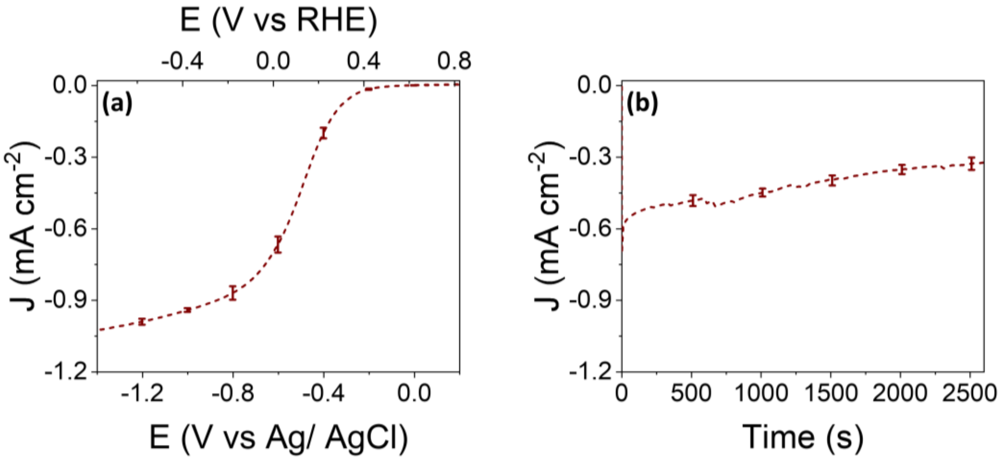

Figure 3.8. (a) Linear sweep voltammogram recorded using *post-degrade* Co|PPy|GaP samples (post controlled-potential electrolysis experiment) at a scan rate of 100 mV s^{-1} and a freshly prepared solution of 0.1 M phosphate buffer that was not previously exposed to the Co|PPy|GaP electrodes. These post-degrade electrodes showed near-unity faradaic efficiency at activities equal to those obtained in the initial phosphate buffer solutions (Fig. S3). This result indicates no photocatalysis in solution happening. (b) Current density versus time plots obtained during controlled-potential electrolysis at 0 V vs RHE for gas chromatography experiments. All data are averaged from three separate working electrodes.

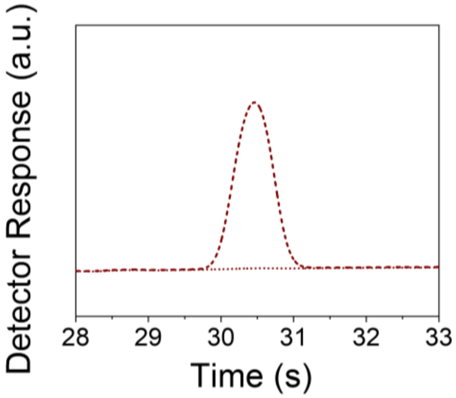

Figure 3.9. A representative gas chromatogram obtained from chromatography of a headspace gas sample taken from a sealed photoelectrochemical cell containing a *post-degrade* Co|PPy|GaP working electrode before (dotted) and after (dashed) 20 minutes of controlled-potential electrolysis at 0 V vs RHE in a pH 7 phosphate buffer solution, under illumination at 100 mW cm^{-2}.

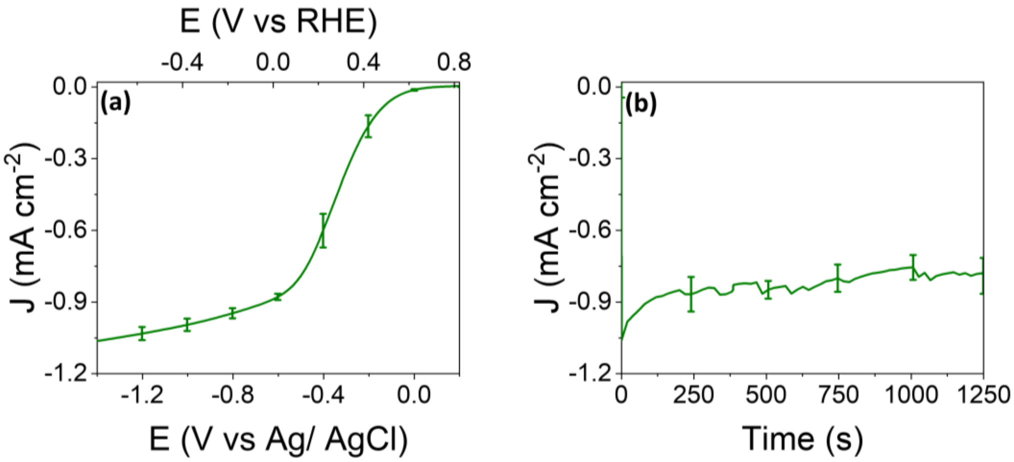

Figure 3.10. (a) Linear sweep voltammogram recorded using *post-repair* Co|PPy|GaP samples (post controlled-potential electrolysis experiment) at a scan rate of 100 mV s^{-1}. (b) Current density versus time plots obtained during controlled-potential electrolysis at 0 V vs RHE for gas chromatography experiments. All data are averaged from three separate working electrodes.

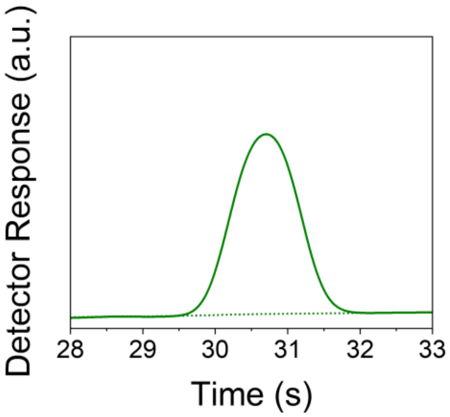

Figure 3.11. A representative gas chromatogram obtained from chromatography of a headspace gas sample taken from a sealed photoelectrochemical cell containing a *post-repair* Co|PPy|GaP working electrode before (dotted) and after (solid) 20 minutes of controlled-potential electrolysis at 0 V vs RHE in a pH 7 phosphate buffer solution, under illumination at 100 mW cm^{-2}.

3.2.6 Structural Characterization for degradation and repair mechanism

To facilitate comparisons between results obtained via grazing angle attenuated total reflection Fourier transform infrared (GATR-FTIR) –which probes up to micrometers in depth– and X-ray photoelectron (XP) spectroscopy –which probes only a few nanometers in depth– the polypyridyl-modified samples (PPy|GaP) described in this Chapter were intentionally prepared with a relatively thin PPy coating (~2.31 ± 0.01 nm, as determined by spectroscopic ellipsometry). Following post-synthetic modification of the PPy|GaP samples, via wet chemical processing with a 1.0 mM methanolic solution of the cobalt-containing precursor $Co(dmgH_2)(dmgH)Cl_2$ (see experimental methods and **Figure 3.2** for further details), 31 ± 1% of the pyridyl groups on the surface-graft are coordinated to a cobaloxime cobalt center (as determined via XP spectroscopy analysis, see **Table 3.3**). This yields a per-geometric-area cobaloxime loading of 1.75 ± 0.06 nmol cm^{-2} with a film thickness (as determined by spectroscopic ellipsometry) that increases to 5.16 ± 0.01 nm (**Figure 3.12**). These film thickness and loading conditions were also selected to facilitate structural characterization, performed prior to and following photoelectrosynthetic operation with minimized experimental times, and thus reduced risks of contaminating the samples. In addition, a customized photoelectrochemical cell that makes electrical contact with the unfunctionalized face of the semiconductors, and facilitates relatively rapid loading and unloading of electrode samples to and from the cell, was used in these experiments (**Figure 3.3**).

Ellipsometry Data

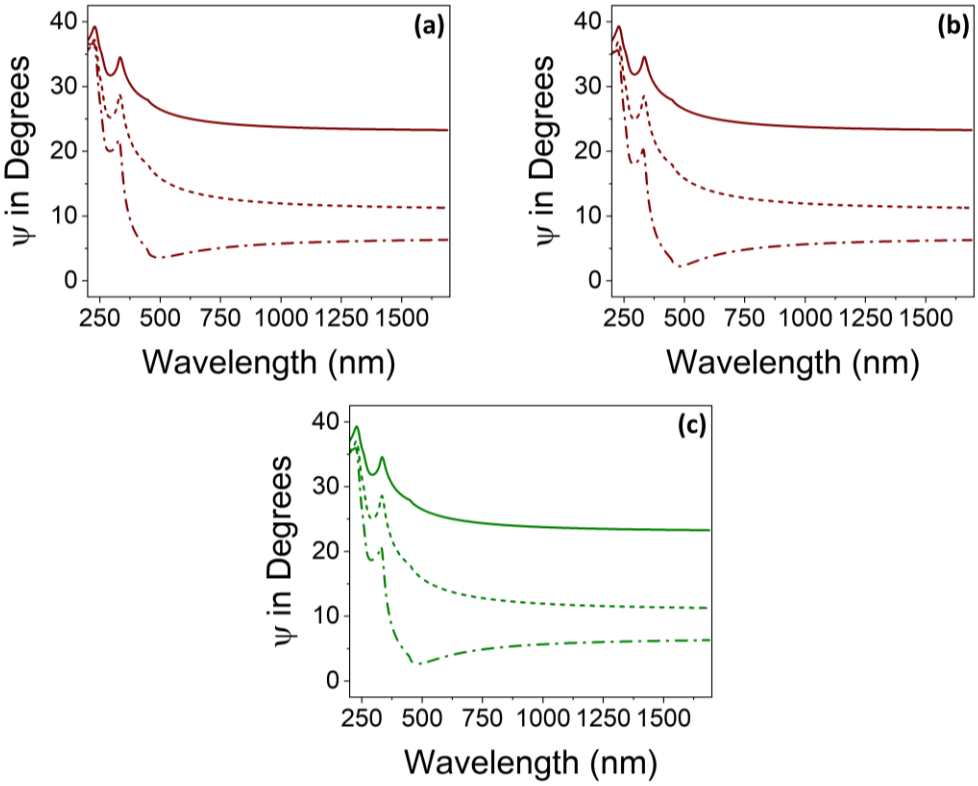

Figure 3.12. Ellipsometry spectra recorded using Co|PPy|GaP samples (a) prior to photoelectrochemical characterization/degradation, (b) following photoelectrochemical characterization/degradation and (c) following chemical repair. The spectra shown here are obtained from an average of measurements involving three separately prepared samples. All individual spectra were recorded at incidence angles of either 55° (solid), 65° (dashed), or 75° (dash-dot). The data was modeled in CompleteEase with a B-Spline layer to describe the polypyridyl film for all samples. Averaging between three samples, the thickness of the Co-polypyridyl layer on GaP was determined to be 5.16 ± 0.01 nm for the *initial* Co|PPy|GaP samples, 5.34 ± 0.03 nm for the *post-degrade* Co|PPy|GaP samples, and 3.96 ± 0.01 nm for the *post-repair* Co|PPy|GaP samples.

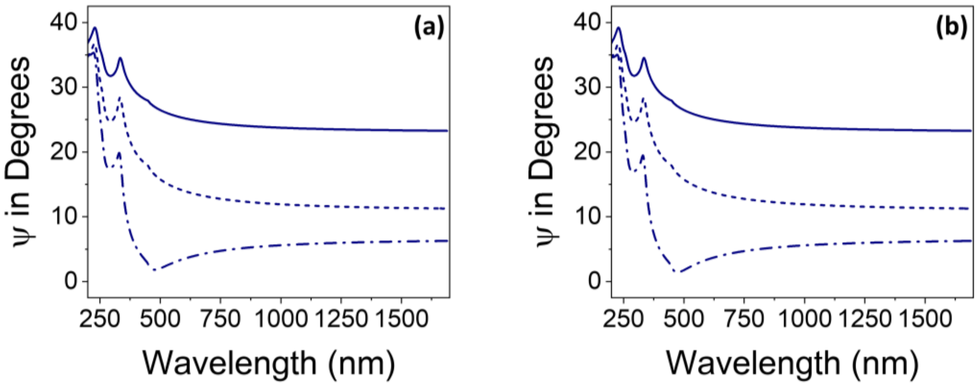

Figure 3.13. The PPy|GaP ellipsometry data was analyzed (a) prior to photoelectrochemical characterization/degradation and (b) following photoelectrochemical characterization/degradation. The plots shown here are obtained by averaging data from three separately prepared samples. All individual spectra were recorded at incidence angles of either 55° (solid), 65° (dashed), or 75° (dash-dot). The data was modeled in CompleteEase with a B-Spline layer to describe the polypyridyl film for all sample. Averaging between three samples, the thickness of the polypyridyl layer on GaP was determined to be 2.31 ± 0.01 nm for the *initial* PPy|GaP samples, and 3.56 ± 0.03 nm for the *post-degrade* PPy|GaP samples.

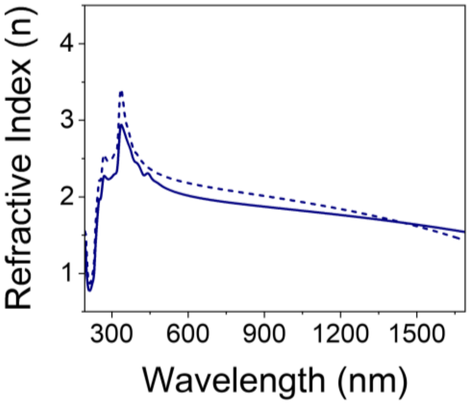

Figure 3.14. Refractive index of the polypyridyl layer on GaP for *initial* PPy|GaP (solid) and *post-degrade* PPy|GaP (dashed) samples.

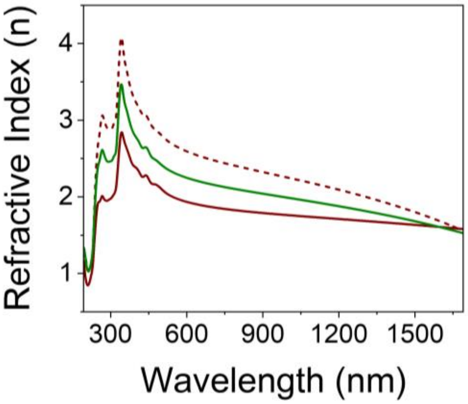

Figure 3.15. Refractive index of the cobaloxime-polypyridyl layer on GaP for *initial* Co|PPy|GaP (solid red), *post-degrade* PPy|GaP (dashed red) and *post-repair* Co|PPy|GaP (solid green) samples.

Spectroscopic measurements, including GATR-FTIRand XP spectroscopy, were performed prior to and following the series of voltammetry and controlled-potential electrolysis experiments to observe possible changes in structures of these hybrid photocathodes along with changes in photoelectrochemical activities.

GATR-FTIR(Grazing angle attenuated total reflection Fourier transform infrared).

GATR-FTIRwas used to monitor the relative intensity of absorption bands on the surfaces that are associated with vibrational modes of free-base pyridyl groups versus pyridyl groups coordinated to cobaloxime units (**Figures 3.16 and 3.17**). In particular, the relative intensity ratios of peaks assigned to the NO^- stretching mode of intact cobaloximes (1240 cm^{-1})[27] and those assigned to either the C=N (1600 cm^{-1}) or C-N (1417 cm^{-1}) vibrations of the polypyridyl layer were compared before and after photoelectrosynthetic operation.[26] Comparing relative intensity ratios, rather than absolute intensities, avoids sample-to-sample discrepancies in signal intensities arising from varying contact between the GaP semiconductor samples and the attenuated total reflectance crystal of the GATR-FTIRunit. These results are summarized in **Table 3.1** and indicate a 74 ± 2% reduction of the cobaloxime loadings following the series of voltammetry and controlled-potential experiments (**Table 3.1**).

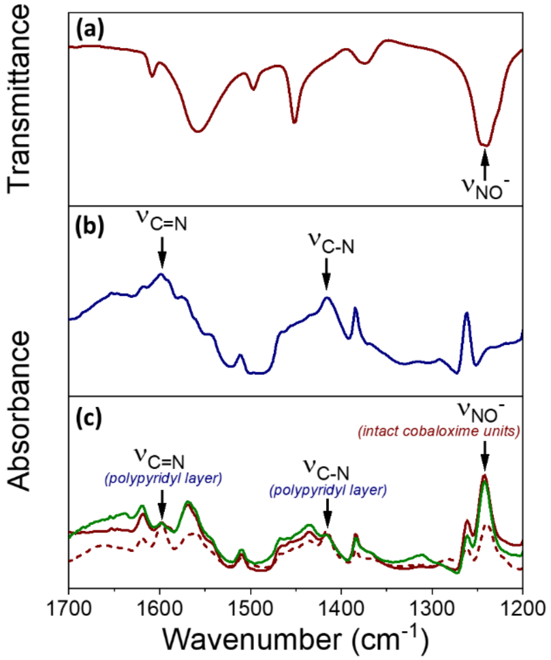

Figure 3.16. (a) FTIR transmission spectrum of the model cobaloxime complex, $\mathrm{Co(dmgH)_2PyCl}$, in KBr (red solid). (b) GATR-FTIR spectrum of PPy|GaP recorded using *initial* sample (blue solid). (c) GATR-FTIR spectra of Co|PPy|GaP samples recorded using *initial* (red solid), *post-degrade* (see Fig. 1d and related caption) (red dash), and *post-repair* (green solid) samples. All spectra are normalized to the absorbance peak at 1600 cm^{-1}.

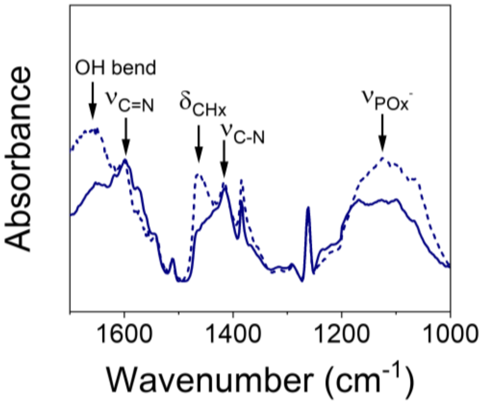

Figure 3.17. VariGATR-FTIRspectra of PPy|GaP samples recorded prior to (solid) and following (dashed) the controlled-potential electrolysis experiments. Spectral contributions at ~1126 cm^{-1}, 1464 cm^{-1} and at 1655 are attributed to bending of PO_x^- groups, stretching of CH_x groups from adventitious carbon and deformation/bending of OH groups, respectively, arising from air exposure and handling of the samples.

X-ray Photoelectron Spectroscopy

XP spectroscopy yields additional insights on the structural differences of the electrode coatings prior to and following photoelectrosynthetic operation, including evidence of changes in the amount of Co-N bonds between the catalyst and the polypyridyl layer. As compared with the N 1s core level XP spectra of PPy|GaP surfaces, which display a single N 1s feature assigned to pyridyl nitrogens of the surface graft,[12] the N 1s core level XP spectra of Co|PPy|GaP surfaces are more complex, with overlapping spectral features that are fit using three components **(Figure 3.18**). These include a component centered at 398.0 eV assigned to free-base pyridyl nitrogens (abbreviated as PyN), a component centered at 399.5 eV assigned to glyoximate nitrogens of the cobaloxime ligands (abbreviated as GlyN), and a component centered at 400.5 eV assigned to pyridyl nitrogens coordinated to cobalt centers of cobaloximes (abbreviated as PyN-Co).

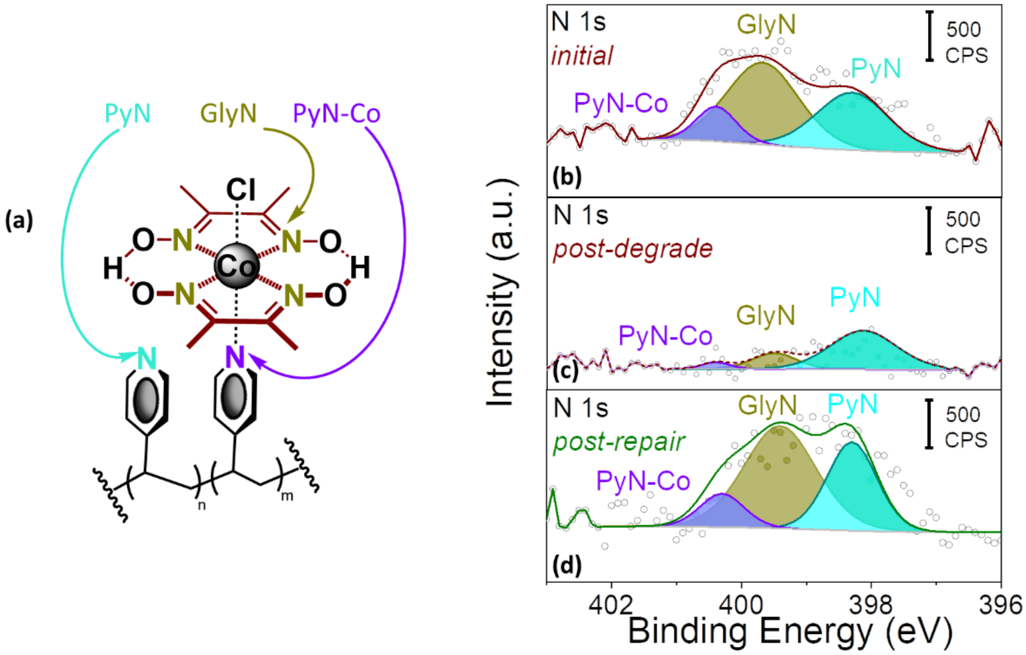

Figure 3.18. (a) Structure of the pyridyl and cobaloxime units of Co|PPy|GaP indicating the PyN, GlyN, and PyN-Co nitrogen sites. (b-d) N 1s core level XP spectra of Co|PPy|GaP recorded using (b) *initial*, (c) *post-degrade* (see **Figure 3.6d** and related caption), and (d) *post-repair* samples. Solid lines represent the background (gray) and indicated components (cyan for remnant pyridyl nitrogens (PyN), yellow for glyoximate nitrogens bound to cobalt centers (GlyN), and purple for pyridyl nitrogens bound to cobaloximes (PyN-Co)).

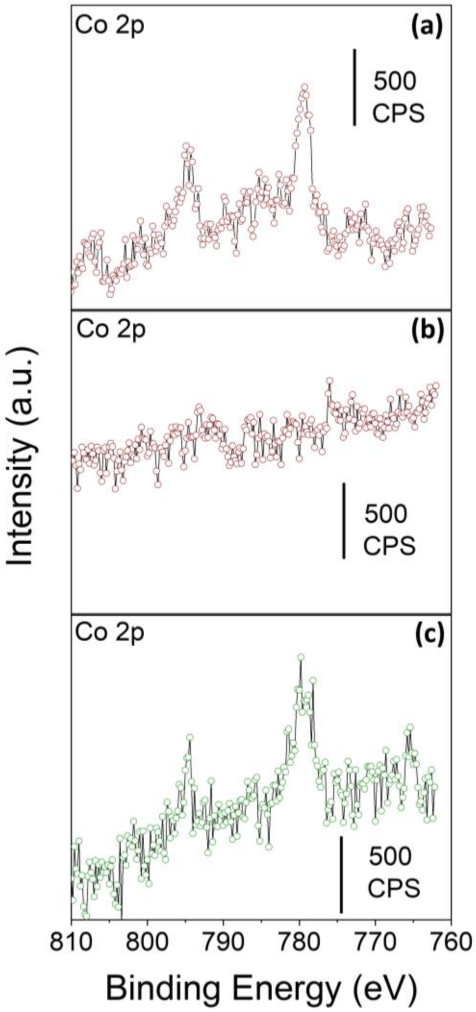

Figure 3.19. Co 2p core level spectra of Co|PPy|GaP recorded (a) prior to and (b) following degradation via controlled-potential electrolysis at 0 V vs RHE as well as (c) subsequent repair via wet-chemical processing. Circles represent the spectral data.

3.3 Conclusions

Considering the results described in this chapter (obtained using a model polypyridyl-cobaloxime-modified semiconductor assembly) and those of previous reports on the electrocatalytic performance and operational mechanisms of homogenous cobaloxime catalysts,[5-9,28-29] we postulate the loss of cobaloximes during photoelectrosynthetic operation is in part triggered by redox cycling and an associated breaking of pyridyl nitrogen-cobalt bonds during reduction of the cobalt centers from their Co^{II} to Co^{I} oxidation states. Although a redundancy of ligand sites and confinement effects associated with polymeric coatings appear to impart increased chemical stability of the cobaloxime units as compared to their homogenous counterparts,[11] fragments of the cobaloximes leach from the surface-immobilized polymer during photoelectrosynthetic operation. By comparison, related studies using porphyrins grafted to GaP surfaces via an intervening PPy coating[16-18] or via more covalent-based attachment strategies[14,15,18] show enhanced durability as measured by the decreases in their fuel-production activities over time. This suggests the nature of the catalysts, their chemical attachment, degree of solubility in the electrolyte, and thickness of the polymer coatings they are anchored to all affect the robustness of the attachment chemistry.

The relatively larger % loss of cobaloximes following operational degradation as compared to the % loss in fuel-production metrics implies not all of the lost Co complexes contributed, or contributed equally, to the initial photoelectrosynthetic performance.[11,17] In addition to degradation of cobaloxime catalysts, we cannot rule out that some fraction of the performance loss is due to damage induced at the underlying semiconductor (*e.g.*, formation of surface oxides, see Figure X) or intervening polymeric scaffold. Nonetheless, the nearly complete restoration of activity following repair of the electrodes by restoring the loading of cobaloximes indicates the overall performance loss is largely (i.e. within the error of the measurements reported in this research) associated with degradation of cobaloxime sites.

In summary, the polypyridyl-cobaloxime-modified semiconductors used in these experiments are purposefully designed for fundamental studies aimed at better understanding the structure-function relationships of hybrid interfaces involving hard- and soft- material components. These assemblies afford opportunities to study their photoelectrosynthetic performance, degradation, and accompanying structural changes. Consistent with the proposed mechanism of the activity loss being linked to structural degradation at cobaloxime catalyst sites, we show the activity can be restored by chemically repairing the cobaloximes. Although demonstration of a degrade-repair cycle is a promising feature in the context of developing schemes to generate solar fuels by day coupled with repair at night, further advancements are required for commercial-based applications. In general, designing, interfacing, and characterizing combinations of (semi)conducting and catalytic materials to effectively power chemical transformations remain outstanding challenges. Addressing this will likely require development of new materials and material interfaces, improved models for better understanding how charge carriers move across these hybrid assemblies, and standardized techniques for benchmarking their overall performance.[30]

3.4 References

(1) Faunce, T. A.; Lubitz, W.; Rutherford, A. W.; MacFarlane, D.; Moore, G. F.; Yang, P.; Nocera, D. G.; Moore, T. A.; Gregory, D. H.; Fukuzumi, S.; Yoon, K. B.; Armstrong, F. A.; Wasielewski, M. R.; Styring S. Energy and environment policy case for a global project on artificial photosynthesis. *Energy Environ. Sci.*, **2013**, *6*, 695–698.

(2) Ardo, S.; Fernandez Rivas, D. F.; Modestino, M. A.; Schulze Greiving, V. S.; Abdi, F. F.; Alarcon Llado, E. A.; Artero, V.; Ayers, K.; Battaglia, C.; Becker, J.-P.; Bederak, D.; Berger, A.; Buda, F.; Chinello, E.; Dam, B.; Di Palma, V.; Edvinsson, T.; Fujii, K.; Gardeniers, H.; Geerlings, H.; Hashemi, S. M. H.; Haussener, S.; Houle, F.; Huskens, J.; James, B. D.; Konrad, K.; Kudo, A.; Kunturu, P. P.; Lohse, D.; Mei, B.; Miller, E. L.; Moore, G. F.; Muller, J.; Orchard, K. L.; Rosser, T. E.; Saadi, F. H.; Schüttauf, J.-W.; Seger, B.; Sheehan, S. W.; Smith, W. A.; Spurgeon, J.; Tang, M. H.; van de Krol, R.; Vesborg, P. C. K.; Westerik, P. Pathways to Electrochemical Solar-Hydrogen Technologies. *Energy Environ. Sci.* **2018**, *11*, 2768−2783.

(3) Wadsworth, B. L.; Khusnutdinova, D.; Moore, G. F. Polymeric coatings for applications in electrocatalytic and photoelectrosynthetic fuel production. *J. Mater. Chem. A*, **2018**, *6*, 21654–2166.

(4) Reyes Cruz, E. A.; Nishiori, D.; Wadsworth, B. L.; Nguyen, N. P.; Hensleigh, L. K.; Khusnutdinova, D.; Beiler, A. M.; Moore, G. F. Molecular-Modified Photocathodes for Applications in Artificial Photosynthesis and Solar-to-Fuel Technologies. *Chem. Rev.*, **2022**, 16051–16109.

(5) Connolly, P.; Espenson, J. H. Cobalt-catalyzed evolution of molecular hydrogen. *Inorg. Chem.*, **1986**, *25*, 2684−2688.

(6) Razavet, M.; Artero, V.; Fontecave, M. Proton Electroreduction Catalyzed by Cobaloximes: Functional Models for Hydrogenases. *Inorg. Chem.*, **2005**, *44*, 4786−4795.

(7) Hu, X. L.; Cossairt, B. M.; Brunschwig, B. S.; Lewis N. S.; Peters, J. C. Electrocatalytic hydrogen evolution by cobalt difluoroboryl-diglyoximate complexes. *Chem. Commun.*, **2005**, *37*, 4723−4725.

(8) Krawicz, A.; Yang, J.; Anzenberg, E.; Yano, J.; Sharp, I. D.; Moore, G. F. Photofunctional Construct That Interfaces Molecular Cobalt-Based Catalysts for H_2 Production to a Visible-Light-Absorbing Semiconductor. *J. Am. Chem. Soc.*, **2013**, *135*, 11861–11868.

(9) Dempsey, J. L.; Brunschwig, B. S.; Winkler, J. R.; Gray, H. B. Hydrogen Evolution Catalyzed by Cobaloximes. *Acc. Chem. Res.*, **2009**, *42*, 1995–2004.

(10) Beiler, A. M.; Khusnutdinova, D.; Jacob, S. I.; Moore, G. F. Solar Hydrogen Production Using Molecular Catalysts Immobilized on Gallium Phosphide (111)A and (111)B Polymer-Modified Photocathodes. *ACS Appl. Mater. Interfaces*, **2016**, *8*, 10038–10047.

(11) Wadsworth, B. L.; Beiler, A. M.; Khusnutdinova, D.; Jacob, S. I.; Moore, G. F. Electrocatalytic and Optical Properties of Cobaloxime Catalysts Immobilized at a Surface-Grafted Polymer Interface. *ACS Catal.*, **2016**, *6*, 8048−8057.

(12) Beiler, A. M.; Khusnutdinova, D.; Jacob, S. I.; Moore, G. F. Chemistry at the Interface: Polymer-Functionalized GaP Semiconductors for Solar Hydrogen Production. *Ind. Eng. Chem. Res.*, **2016**, *55*, 5306–5314.

(13) Cedeno, D.; Krawicz, A.; Doak, P.; Yu, M.; Neaton, J. B.; Moore, G. F. A Noble-Metal-Free Hydrogen Evolution Catalyst Grafted to Visible Light-Absorbing

Semiconductors. *J. Phys. Chem. Lett.*, **2014**, *5*, 3222–3226.

(14) Khusnutdinova, D.; Beiler, A. M.; Wadsworth, B. L.; Jacob, S. I.; Moore, G. F. Metalloporphyrin-modified semiconductors for solar fuel production. *Chem. Sci.*, **2016**, *8*, 253–259.

(15) Nishiori, D.; Wadsworth, B. L.; Reyes Cruz, E. A.; Nguyen, N. P.; Hensleigh, L. K.; Karcher, T.; Moore, G. F. Photoelectrochemistry of metalloporphyrin-modified GaP semiconductors *Photosynth Res*, **2021**, *151*, 1-10.

(16) Beiler, A. M.; Khusnutdinova, D.; Wadsworth, B. L.; Moore, G. F. Cobalt Porphyrin–Polypyridyl Surface Coatings for Photoelectrosynthetic Hydrogen Production. *Inorg. Chem.*, **2017**, *56*, 12178–12185.

(17) Wadsworth, B. L.; Beiler, A. M.; Khusnutdinova, D.; Reyes Cruz E. A.; Moore, G. F. Interplay between Light Flux, Quantum Efficiency, and Turnover Frequency in Molecular-Modified Photoelectrosynthetic Assemblies. *J. Am. Chem. Soc.*, **2019**, *141*, 15932–15941.

(18) Wadsworth, B. L.; Khusnutdinova, D.; Urbine, J. M.; Reyes, A. S.; Moore, G. F. Expanding the Redox Range of Surface-Immobilized Metallocomplexes Using Molecular Interfaces. *ACS Appl. Mater. Interfaces*, **2020**, *12*, 3903–3911.

(19) Wadsworth, B. L.; Nishiori, D.; Nguyen, N. P.; Reyes Cruz, E. A.; Moore, G. F. Electrochemistry of Polymeric Cobaloxime-Containing Assemblies in Organic and Aqueous Solvents. *ECS J. Solid State Sci. Technol.*, **2020**, *9*, 061018.

(20) Nguyen, N. P.; Wadsworth, B. L.; Nishiori, D.; Reyes Cruz, E. A.; Moore, G. F. Understanding and Controlling the Performance-Limiting Steps of Catalyst-Modified Semiconductors. *J. Phys. Chem. Lett.*, **2021**, *12*, 199–203.

(21) Steenackers, M.; Küller, A.; Stoycheva, S.; Grunze M.; Jordan, R. Structured and Gradient Polymer Brushes from Biphenylthiol Self-Assembled Monolayers by Self-Initiated Photografting and Photopolymerization (SIPGP). *Langmuir*, **2009**, *25*, 2225–2231.

(22) Wang, X.; Ruther, R. E.; Streifer, J. A.; Hamers, R. J. UV-Induced Grafting of Alkenes to Silicon Surfaces: Photoemission versus Excitons. *J. Am. Chem. Soc.*, **2010**, *132*, 4048–4049.

(23) Seifert, M.; Koch, A. H. R.; Deubel, F.; Simmet, T.; Hess, L. H.; Stutzmann, M.; Jordan, R.; Garrido, J. A.; Sharp, I. D. Functional Polymer Brushes on Hydrogenated Graphene. *Chem. Mater.*, **2013**, *25*, 466–470.

(24) Moore, G. F.; Sharp, I. D. A Noble-Metal-Free Hydrogen Evolution Catalyst Grafted to Visible Light-Absorbing Semiconductors. *J. Phys. Chem. Lett.*, **2013,** *4*, 568–572.

(25) Trogler W.; Stewart R. C; Epps L. A.; Marzilli L. G. Cis and Trans Effects on the Proton Magnetic Resonance Spectra of Cobaloxime. Inorg Chem. 1974, 13, 1564−1570.

(26) Costa, G.; Tauzher, G.; Puxeddu, A. Mechanism of Formation of trans-Chloro-Bisdimethylglyoximato-Tertiary Phosphine Cobalt(III) Complexes and Their Isomers 1:1 Electrolytes. *Inorg. Chim. Acta* **1969**, *3*, 45−48.

(27) Yamazaki, N.; Hohokabe, Y. Studies on Cobaloxime Compounds. I. Synthesis of Various Cobaloximes and Investigation on Their Infrared and Far-Infrared Spectra. *Bull. Chem. Soc. Jpn.*, **1971**, *44,* 63–69.

(28) Muckerman, J. T.; Fujita, E. Theoretical studies of the mechanism of catalytic hydrogen production by a cobaloxime. *Chem. Commun.*, **2011**, *47*, 12456–12458.

(29) Veldkamp, B. S.; Han, W. S.; Dyar, S. M.; Eaton, S. W.; Ratner, M. A.; Wasielewski, M. R. Photoinitiated multi-step charge separation and ultrafast charge transfer induced dissociation in a pyridyl-linked photosensitizer–cobaloxime assembly. *Energy Environ. Sci.*, **2013**, *6*, 1917–1928.

(30) Nishiori, D.; Wadsworth, B. L.; Moore, G. F. Parallels between enzyme catalysis, electrocatalysis, and photoelectrosynthesis. *Chem Catal*., **2021**, *1*, 978–996.

CHAPTER 4 ADDRESSING THE ORIGIN OF PHOTOCURRENTS AND FUEL PRODUCTION ACTIVITIES IN CATALYST-MODIFIED SEMICONDUCTOR ELECTRODES

Portions of this chapter are excerpted and reprinted with permission from:

Wadsworth, B. L.; Nguyen, N. P.; Nishiori, D.; Beiler, A. M.; Moore, G. F. Addressing the Origin of Photocurrents and Fuel Production Activities in Catalyst-Modified Semiconductor Electrodes. *ACS Appl. Energy Mater*. **2020**, *8*, 7512-7519.

My contributions to this work included synthesizing the hybrid photocathodes used in External and Internal Quantum Efficiencies measurement as well as conducting the External Quantum Efficiencies measurements.

4.1 Introduction

Photoelectrosynthesis provides an approach to capture, convert, and store solar energy in the form of chemical bonds.[1–3] However, the ability to effectively interface electrocatalysts for activating multi-electron / multi-proton chemical transformations with materials that absorb sunlight and convert photons into charge carriers moving through a potential remains challenging.[4–8] Additionally, most electrocatalyst layers also absorb visible light, complicating analysis of these hybrid composite materials and determination of the components directly involved in energy harvesting.

4.1.1 Cobalt Porphyrin-modified photocathode for Hydrogen Evolution Reaction

We have previously reported synthetic methods for interfacing molecular cobalt porphyrin catalysts with (semi)conducting materials.[9–12] In one example, cobalt porphyrins are immobilized onto gallium phosphide (GaP) semiconductors using a two-step strategy involving initial UV-induced grafting of 4-vinylpyridine, to form polypyridyl coatings (PPy) on GaP surfaces, followed by wet-chemical processing with a solution of 5,10,15,20-tetra-*p*-tolylporphyrin cobalt(II) (CoTTP). This overall process yields samples where the porphyrin cobalt centers are coordinated to nitrogen sites along surface-grafted polypyridyl chains (**Figure 4.1**). A similar process was applied to prepare samples used in this Chapter.

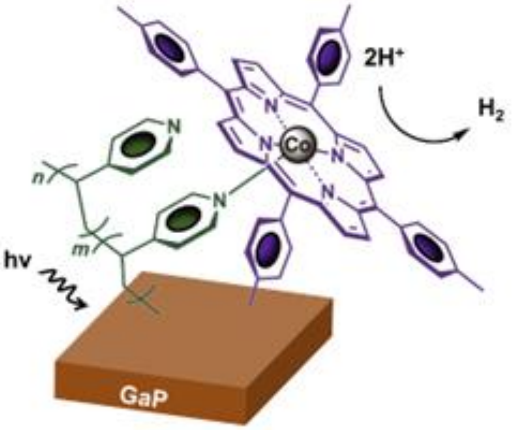

Figure 4.1. Schematic representation of the cobalt porphyrin-polypyridyl GaP photoelectrode (CoTTP|PPy|GaP).

Previous work from our group shows, that when wired in a three-electrode configuration with appropriate counter and reference electrodes (**Figure 4.2**), cobalt porphyrin-polypyridyl-modified GaP electrodes (CoTTP|PPy|GaP) use light to power the production of hydrogen gas from pH neutral aqueous solutions in the absence of sacrificial chemical reductants, and with no electrochemical forward biasing, at a rate of ~10 µL of H_2 min-1 cm^{-2}.[9] Complementary methods of ellipsometry, inductively coupled plasma mass spectrometry, and X-ray photoelectron spectroscopy were used to quantify the thickness of the polypyridyl films, the per geometric area loading of cobalt porphyrins, and the fraction of pyridyl sites coordinated to cobalt porphyrin centers.[9] Given this structural information and the near-unity faradaic efficiency determined by product analysis, the hydrogen production rate of 10 µL of H_2 min^{-1} cm^{-2} equates to a per-cobalt-site hydrogen evolution reaction (HER) activity of 17.6 H_2 molecules s^{-1} Co^{-1}.[9] More recently, we developed kinetic models relating the HER activity of these photoelectrodes to the fraction of catalysts present in their activated form under varying steady-state illumination.[11] Although the models described in that report focus on hydrogen evolution using metalloporphyrin-modified GaP semiconductors, we postulate the methods used in our analyses are likely applicable to a broader range of photoelectrosynthetic assemblies and thus provide a more general model for studying and better understanding photoelectrosynthetic performance. Herein, we now show that quantification of the per geometric area loading of molecular components can be coupled with information on their light harvesting efficiency (LHE) and overall external quantum efficiency (EQE) to quantify the fraction of photons absorbed by surface-grafted molecular coatings and address the effects this can have on overall photocurrent production and associated HER activity.

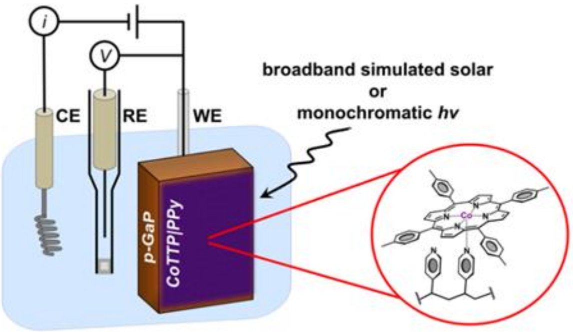

Figure 4.2. Schematic Diagram Highlighting the Molecular Structure of a Cobalt Porphyrin Coordinated to a Surface-Grafted Polypyridyl Chain on a CoTTP|PPy|GaP Working Electrode Wired in a Three-Electrode Configuration Under Illumination Using a Broadband or Monochromatic Light Source.

4.1.2 Photoelectrosynthesis vs. Screening vs. Dye-Sensitized Hole Injection

Porphyrins are effective electrocatalysts, capable of transforming protons to hydrogen or reducing carbon dioxide to carbon monoxide and other reduced forms of carbon.[13–18] For this latter reason, they have been utilized as components in electrocatalytic and photoelectrosynthetic assemblies.[8–12,19–21] The relatively high extinction coefficients of tetrapyrrolic macrocycles, including porphyrins (10^3 to 10^5 M^{-1} cm^{-1} across the visible region of the electromagnetic spectrum), have also made them useful as light-harvesting components in biological and technological systems, including applications in dye-sensitized solar cells.[22–29]

GaP has also been explored as a light-absorbing material for applications in photoelectrosynthesis.[30–38] Favorable aspects of GaP semiconductors include conduction band energetics (~ –1 V vs NHE at pH 1)[39] with sufficient redox poise for driving reductive chemical transformations, including proton and CO_2 reduction, but surface corrosion and ineffective transfer of minority carriers across the semiconductor|liquid interface limit its performance.[40] Although chemical modification of semiconductor surfaces has been employed as a strategy for improving rates of photoelectrosynthetic fuel production (**Figure 4.3a**), the addition of colored materials, which include myriad electrocatalysts, can have the undesirable effect of screening light from the underlying semiconductor (**Figure 4.3b**) through reflection or parasitic absorption of photons by the surface coating.[9–11,19–21,41–43]

Juxtaposed with more traditional approaches of maximizing the per geometric area loading of catalysts to achieve high activities, design approaches can be more nuanced in the case of photoelectrosynthetic assemblies where a relatively thick catalyst layer can hamper performance via screening light from reaching the underlying semiconductor and/or disfavoring accumulation of multiple redox equivalents at individual catalytic sites. For example, recent studies involving photoactivation of dye-sensitized semiconductors modified with a proxy for a molecular catalyst indicate relatively low loadings of catalytic sites could be beneficial.[44,45] Conversely, dye-sensitization processes involving the transfer of charge carriers between excited dyes and semiconductors (**Figure 4.3c**) have been reported as a strategy for extending the absorption range of semiconducting materials, including GaP, and thereby improving their photoelectrochemical performance.[46–51]

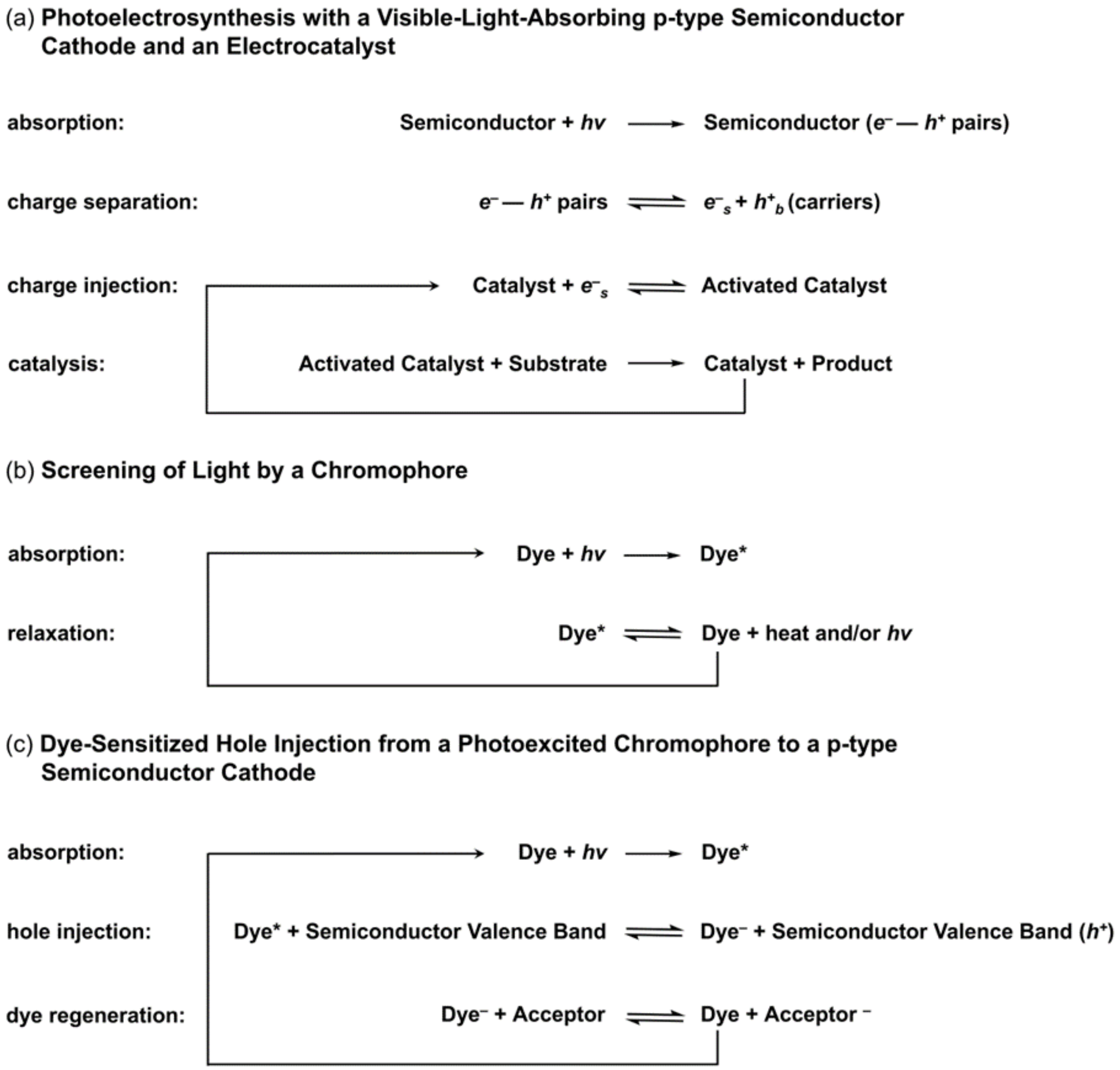

Figure 4.3. Photoelectrosynthesis vs. Screening vs. Dye-Sensitized Hole Injection*

* A photon could be absorbed by a semiconductor and initiate a photoelectrosynthesis process (as indicated in Scheme S1a). Alternatively, a photon could be captured by a chromophore giving rise to screening (where, as indicated in Scheme S1b, the excited state dye radiatively and/or thermally relaxes to its ground state electron configuration), or dye-sensitized hole injection from an excited state chromophore to a semiconductor valence band (as indicated in Scheme S1c).

4.2 Results and Discussion

4.2.1 Material Preparation

Materials

All reagents were purchased from Sigma-Aldrich. Toluene was freshly distilled before use. All aqueous solutions were prepared using Milli-Q water (18.2 MΩ·cm). Zn-doped p-type gallium phosphide (GaP) (100) wafers were purchased from Institute of Electronic Materials Technology (ITME). The single-side-polished, crystalline wafers had a 400 μm thickness, a resistivity of 0.053 – 0.045 Ω cm, a carrier concentration of $1.8 - 2.3 \times 10^{18}$ cm^{-3}, and an etch pit density of less than 2×10^{4} cm^{-2}.

Molecular Synthesis

All syntheses were carried out under an argon atmosphere using Schlenk techniques or in a nitrogen glovebox. All reagents were purchased from Aldrich. All solvents were stored over the appropriate molecular sieves prior to use. Milli-Q water (18.2 MΩ·cm) was used to prepare all aqueous solutions.

5,10,15,20-tetra-*p*-tolylporphyrin (TTP) This complex was prepared following a previously reported procedure.[10,52]

5,10,15,20-tetra-*p*-tolylporphyrin cobalt(II) (CoTTP). This complex was prepared following a previously reported procedure.[10,53]

Wafer Preparation

The functionalization of GaP with a polypyridyl coating containing cobalt porphyrin units coordinated to pyridyl nitrogen sites of the polymer has been previously reported.[9] Diced semiconductor samples were degreased by wiping the surface with an acetone-soaked cotton swab and ultrasonically cleaning in acetone and then isopropanol for 5 min each, followed by drying under nitrogen. Samples were then exposed to an air-generated oxygen plasma (Harrick Plasma, U.S.) at 30 W for 2 min. Surface oxide layers were then removed by immersion of the plasma-treated samples in buffered hydrofluoric acid (6:1 HF/NH_4F in H_2O) for 5 min, followed by rinsing with distilled methanol and drying under a stream of nitrogen. Freshly etched wafers were put into an argon-sparged solution of the neat monomer 4-vinylpyridine and exposed to 254 nm UV light for 2 h. After thoroughly rinsing with methanol, the wafers were dried under nitrogen and stored under vacuum. The polypyridyl-functionalized GaP samples were then soaked for 18 h in a 1 mM solution of cobalt (II) 5,10,15,20-tetra-*p*-tolylporphyrin in toluene. GaP and chemically-modified GaP working electrodes were fabricated by applying an indium−gallium eutectic (Aldrich) to the unpolished/backside of the wafers, then fixing a copper wire to the back of the wafer using a conductive silver epoxy (Circuit Works). The copper wire was passed through a glass tube, and the wafer was insulated and attached to the glass tube with Loctite 615 Hysol Epoxi-patch adhesive. The epoxy was allowed to cure for approximately 24 h before performing experiments using the electrodes.

Electrode Fabrication

GaP and chemically-modified GaP working electrodes were fabricated by applying an indium−gallium eutectic (Aldrich) to the unpolished/backside of the wafers before fixing a copper wire to the back of the wafers using a conductive silver epoxy (Circuit Works). The copper wire was passed through a glass tube, and the semiconductor wafer was insulated and attached to the glass tube with Loctite 615 Hysol Epoxi-patch adhesive.

The epoxy was allowed to cure for approximately 24 h before performing experiments using the electrodes.

4.2.2 Optical Characterization of cobalt porphyrin-modified-GaP

Measurements of the wavelength-resolved Φ_{abs}, probability of reflection (Φ_{ref}), and probability of transmission (Φ_{trans}) collected using samples of GaP, polypyridyl-modified GaP (PPy|GaP), or CoTTP|PPy|GaP, are indicated in **Figure 4.4**. For all three constructs, transmittance at wavelengths with corresponding energies greater than the indirect band gap of GaP (≤549 nm, ≥2.26 eV) is ~0. Further, the reflectance and absorption spectra recorded in this spectral region are nearly identical (that is with values that overlap within the error of the measurements), except for relatively small differences in the values of Φ_{ref} and Φ_{abs}. recorded at 440 nm (where the values are as follows: 0.336 ± 0.007 and 0.664 ± 0.007 for samples of GaP, 0.342 ± 0.001 and 0.658 ± 0.001 for samples of PPy|GaP, and 0.347 ± 0.001 and 0.653 ± 0.001 for samples of CoTTP|PPy|GaP, respectively) (**Figure 4.5**). These results indicate the differences in both Φ_{ref} and Φ_{abs} recorded at 440 nm using samples of CoTTP|PPy|GaP as compared to those recorded using samples of either PPy|GaP or GaP is <1%.

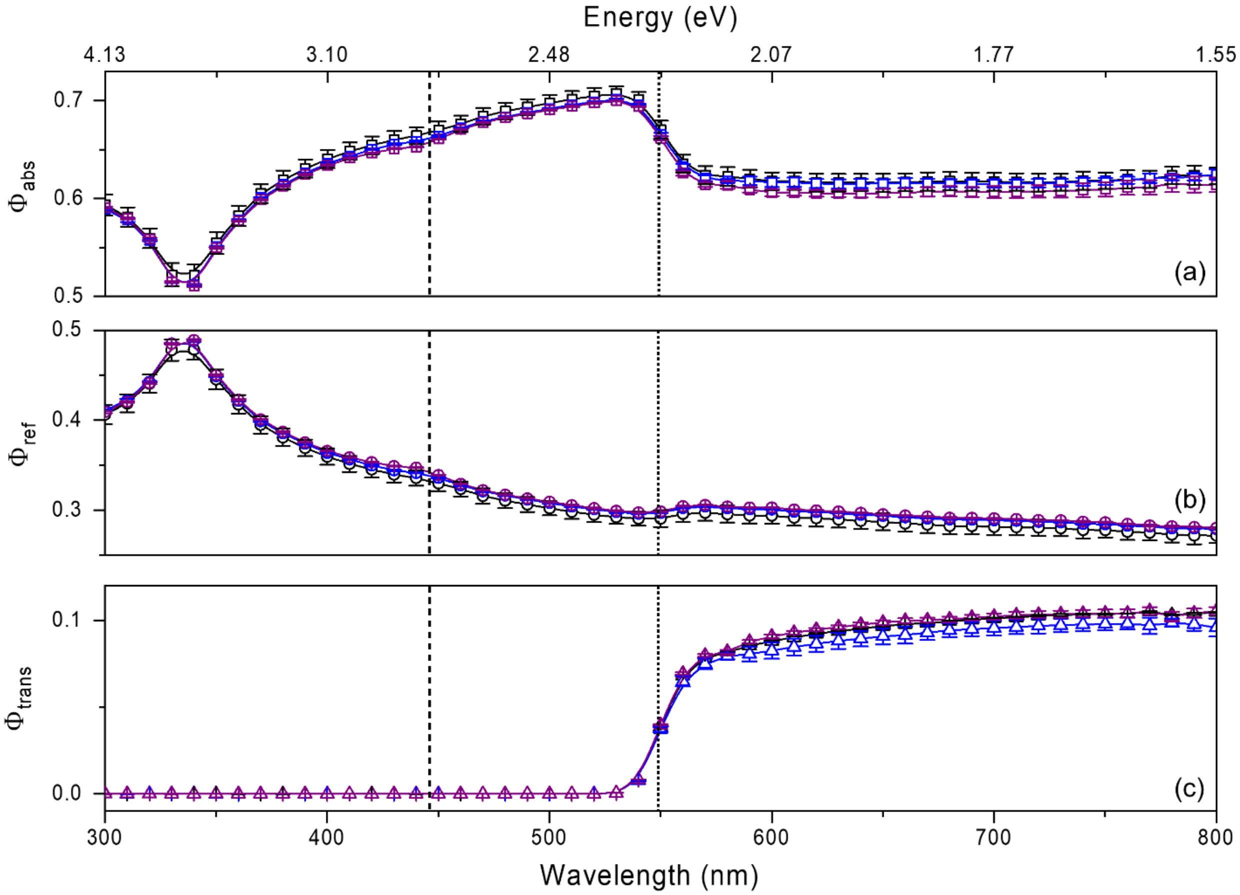

Figure 4.4. Plots of the probabilities of (a) absorption (Φ_{abs}) (squares), (b) reflection (Φ_{ref}) (circles), and (c) transmission (Φ_{trans}) (triangles) for GaP (black), PPy|GaP (blue), and CoTTP|PPy|GaP (purple). The dashed and dotted black lines indicate energies associated with the direct and indirect bandgaps of GaP, respectively.

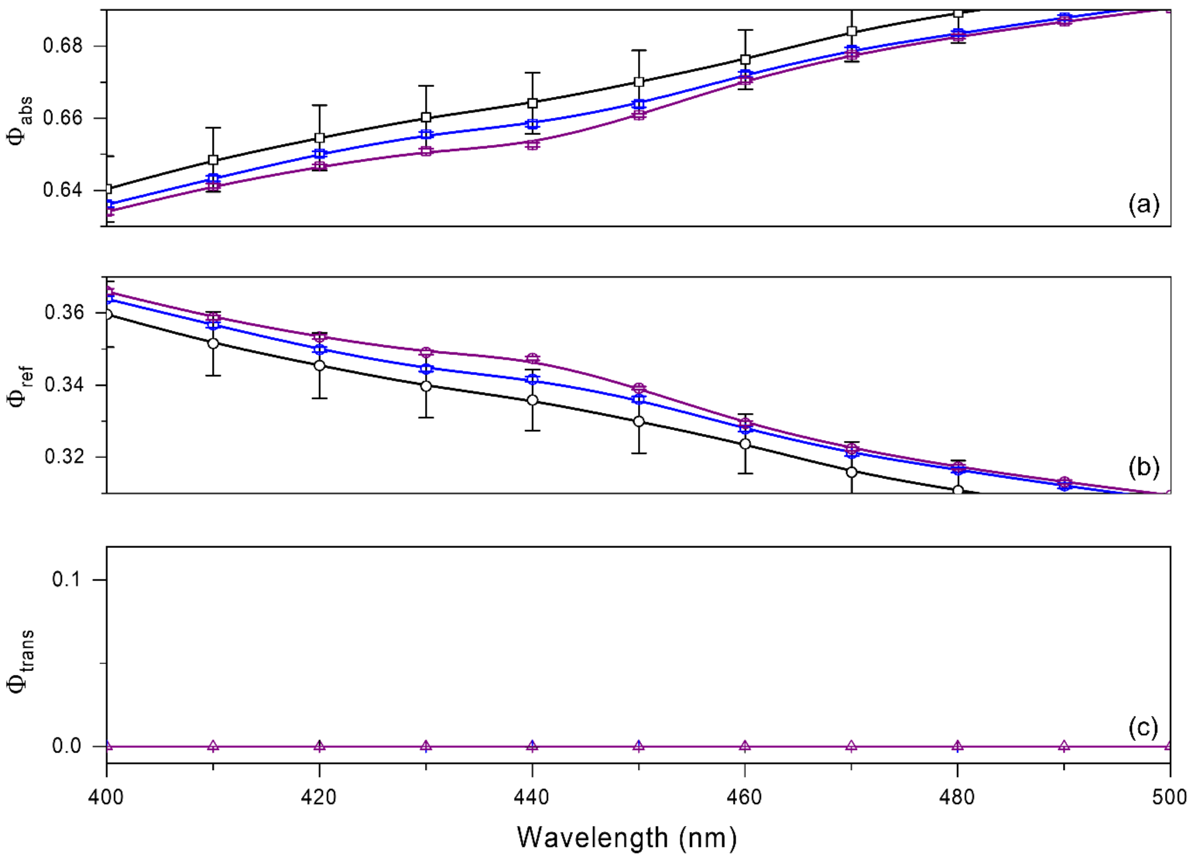

Figure 4.5. Plots of the probabilities of (a) absorption (Φ_{abs}) (squares), (b) reflection (Φ_{ref}) (circles), and (c) transmission (Φ_{trans}) (triangles) measured using samples of GaP (black), PPy|GaP (blue), and CoTTP|PPy|GaP (purple).

Optical measurements performed at wavelengths from 549 nm up to 800 nm show the Φ_{trans} values of all three constructs approach 11% at relatively longer wavelengths (**Figure 4.4**). Further, the Φ_{abs} values recorded in this spectral region are non-zero, even though photons at these wavelengths have corresponding energies less than the indirect band gap of GaP. Absorption at these longer wavelengths is attributed to free-carrier (holes in the case of this p-type semiconductor) absorption in GaP.[54] Related to this, the absorption coefficients of CoTTP|PPy|GaP samples at wavelengths >549 nm are significantly lower than those measured using samples of GaP or PPy|GaP (**Figure 4.6**), indicating there is a reduction in the free-carrier population following immobilization of the porphyrins. Because porphyrins are redox active and p-type doping of a semiconductor introduces free-carrier holes that are associated with an increase in the potential of the semiconductor Fermi level, we postulate this decrease in sub-bandgap absorption coefficients results in part from an equilibration of the potentials associated with the isolated p-type semiconductor and cobalt porphyrin layer. During this equilibration, carriers flow between the semiconductor and porphyrin layer until equilibrium is established and there is no potential difference across the interface.

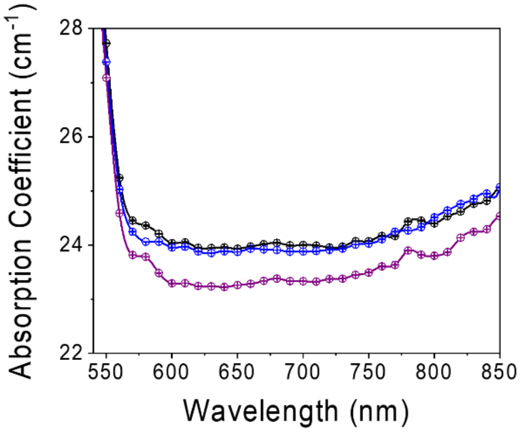

Figure 4.6. Plots of the absorption coefficients for unmodified GaP (black), PPy|GaP (blue), and CoTTP|PPy|GaP (purple) from 540 to 850 nm. Error bars are included for each data point shown.

4.2.3 Photoelectrochemical Characterization

Linear sweep voltammograms recorded under broadband simulated solar illumination using working electrodes immersed in pH neutral aqueous conditions (0.1 M phosphate buffer) are shown in **Figure 4.7**. Under these experimental conditions, electrodes constructed from samples of GaP, PPy|GaP, and CoTTP|PPy|GaP yield current densities of 0.50 ± 0.07 mA cm^{-2}, 0.68 ± 0.06 mA cm^{-2}, and 0.84 ± 0.04 mA cm^{-2}, respectively, when operating at the equilibrium potential of the H^+/H_2 couple (0 V vs the reversible hydrogen electrode (RHE)). Additional metrics, including open-circuit potentials and associated fill factors, are included in **Table 4.1**.

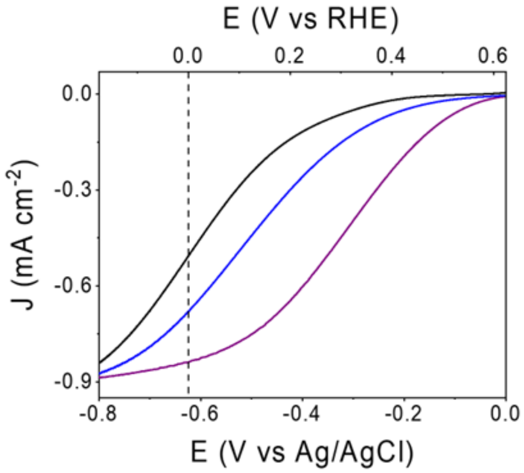

Figure 4.7. Linear sweep voltammograms recorded using a GaP (black solid), PPy|GaP (blue solid), or CoTTP|PPy|GaP (purple solid) electrode in 0.1 M phosphate buffer (pH 7) under simulated 1-sun illumination. The vertical dashed line at 0 V vs RHE indicates the equilibrium potential of the H^+/H_2 couple.

Table 4.1. Open-circuit voltages, short-circuit current densities, maximum power points, and fill factors recorded using GaP, PPy|GaP, or CoTTP|PPy|GaP electrodes in 0.1 M phosphate buffer (pH 7) under simulated 1-sun illumination.

Construct	**Open-Circuit Voltage (V vs RHE)**	**Short-Circuit Current (mA cm^{-2})**	**Maximum Power Point (mW cm^{-2})**	**Fill Factor**
GaP	0.57 ± 0.03	0.50 ± 0.07	0.03 ± 0.01	0.10 ± 0.03
PPy|GaP	0.66 ± 0.01	0.68 ± 0.06	0.06 ± 0.02	0.13 ± 0.02
CoTTP|PPy|GaP	0.67 ± 0.01	0.84 ± 0.04	0.14 ± 0.04	0.25 ± 0.04

In addition to measurements performed under broadband illumination, wavelength-resolved external quantum efficiencies were recorded using either PPy|GaP or CoTTP|PPy|GaP working electrodes (**Figure 4.8**) polarized at 0 V vs RHE in pH neutral aqueous conditions (EQE action spectra of unmodified GaP samples are not included due to the instability of these samples on the timescales required to conduct EQE measurements). Under these experimental conditions, the photocurrents recorded when illuminating either PPy|GaP or CoTTP|PPy|GaP electrodes at wavelengths ≤549 nm are non-zero (consistent with the 2.26 eV indirect band gap of GaP) and rise sharply when illuminating at wavelengths <446 nm, where the transition from the indirect to the direct band gap occurs (2.78 eV). Further, the EQE action spectra of both PPy|GaP and CoTTP|PPy|GaP reach maxima at 300 nm, albeit with values of 50% and 59%, respectively. The EQEs and LHEs measured using PPy|GaP and CoTTP|PPy|GaP electrodes enable construction of IQE plots (**Figure 4.8b**) that both display maxima at 330 nm, with values of 88% for PPy|GaP and 100% for CoTTP|PPy|GaP.

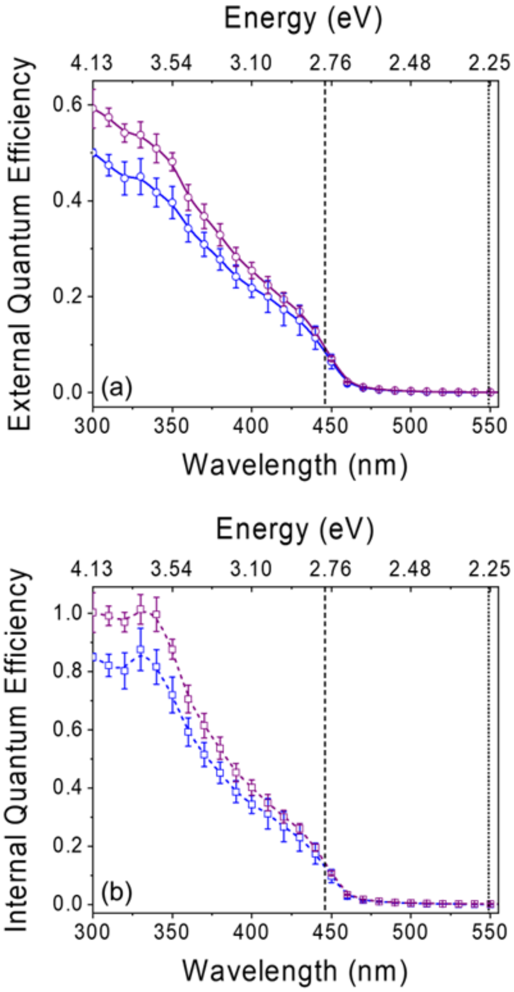

Figure 4.8. Wavelength-resolved (a) external (circles) and (b) internal (squares) quantum efficiency plots recorded using PPy|GaP (blue) or CoTTP|PPy|GaP (purple) electrodes polarized at 0 V vs RHE in 0.1 M phosphate buffer (pH 7). The dashed and dotted black lines indicate energies associated with the direct and indirect bandgaps of GaP.

To confirm the current densities recorded under monochromatic lighting conditions and constant potential polarization (0 V vs RHE) are consistent with those measured under broadband illumination when sweeping the applied potential, wavelength-resolved electron flux plots were generated using the EQE data shown in Figure 4.8a and considering illumination conditions of either 1) the photon flux associated with the AM 1.5 global tilt spectrum[55] (**Figure 4.9**) or 2) the photon flux associated with the spectral profile of the solar simulator used in our experiments. Integration of the electron flux plots associated with AM 1.5 global tilt illumination conditions yield values of 0.71 ± 0.06 mA cm^{-2} for the PPy|GaP electrodes and 0.83 ± 0.05 mA cm^{-2} for the CoTTP|PPy|GaP electrodes. Integration of the electron flux plots associated with the simulated solar conditions yield values 0.77 ± 0.06 mA cm^{-2} for the PPy|GaP electrodes and 0.90 ± 0.05 mA cm^{-2} for the CoTTP|PPy|GaP electrodes. Thus, the current densities obtained from integration of the electron flux plots are consistent when using either AM 1.5 global tilt conditions or the lamp spectrum of the solar simulator used in our experiments (**Table 4.2**). Further, within the experimental error of these measurements, the current densities determined by integration of the wavelength resolved electron flux plots are consistent with those measured in linear sweep voltammograms recorded using broadband simulated solar illumination.

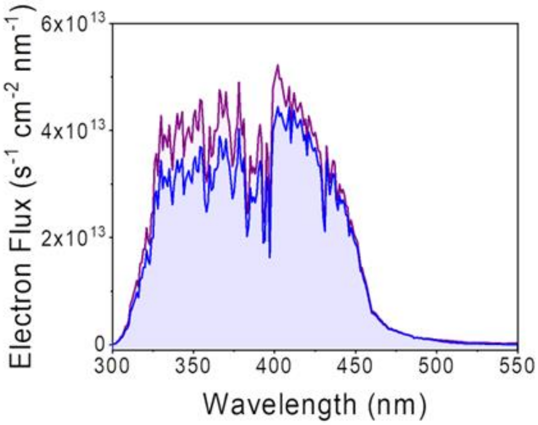

Figure 4.9. Plots of wavelength-resolved electron flux associated with PPy|GaP (blue) or CoTTP|PPy|GaP (purple) electrodes polarized at 0 V vs RHE in 0.1 M phosphate buffer (pH 7). All plots were generated using related EQE data and considering illumination under AM1.5 global tilt solar flux. At the equilibrium potential (0 V vs RHE) the activities associated with both the PPy|GaP and CoTTP|PPy|GaP electrodes are approaching their limiting values (see Figure 4.5).

Table 4.2. Current densities associated with PPy|GaP or CoTTP|PPy|GaP electrodes polarized at 0 V vs RHE in 0.1 M phosphate buffer (pH 7) determined using three different methods.

Construct	**Current Density at 0 V vs RHE (mA cm^{-2}) Simulated Broadband Illumination**[a]	**Current Density at 0 V vs RHE (mA cm^{-2}) Wavelength-Resolved: AM 1.5 Global Tilt Spectrum**[b]	**Current Density at 0 V vs RHE (mA cm^{-2}) Wavelength-Resolved: Solar Simulator with AM 1.5 Filter**[c]
PPy|GaP	0.68 ± 0.06	0.71 ± 0.06	0.77 ± 0.06
CoTTP|PPy|GaP	0.84 ± 0.04	0.83 ± 0.05	0.90 ± 0.05

[a] Current densities recorded from linear sweep voltammograms collected under broadband simulated solar illumination

[b] Current densities calculated from integration of wavelength-resolved electron fluxes generated using EQE action spectra and the AM 1.5 Global Tilt Spectrum*

[c] Current densities calculated from integration of wavelength-resolved electron fluxes generated using EQE action spectra and the photon flux associated with the spectral profile of the solar simulator.

** At the time of writing, the air-mass 1.5 global tilt (AM 1.5G) spectrum from the ASTM G-173-03 data set is available online at hTTPs://www.nrel.gov/grid/solar-resource/spectra.html.*

4.2.4 Comparisons between Heterogeneous-Homogeneous Semiconductor Electrodes and Homogeneous Solutions Containing the Molecular Electrocatalyst.

Wavelength-resolved LHEs and EQEs of GaP prior to and following porphyrin modification were also compared with absorption spectra recorded using solutions of CoTTP in chloroform in the absence and presence of pyridine (**Figures 4.10 – 4.12, Table 4.3**). These comparisons yield insights regarding to what extent and at what wavelengths the presence of cobalt porphyrin units immobilized on GaP surfaces could attenuate the photon flux reaching the underlying GaP semiconductor and possibly contribute to photocurrent densities at wavelengths outside the absorption range of GaP.

LHEs associated with cobalt porphyrin-polypyridyl layers (CoTTP|PPy) were approximated using information on the optical properties of CoTTP in chloroform recorded in the absence or presence of ~1 equivalent of pyridine13 as expressed in Equation 4.1:

$$\text{LHE of CoTTP|PPy} \approx 1 - 10^{-\varepsilon lc} \qquad \text{(Eq. 4.1)}$$

where ε is the wavelength dependent extinction coefficient (in units of M-1 cm-1) of CoTTP in chloroform recorded in the absence or presence of ~1 equivalent of pyridine, l is the thickness (in units of cm) of the polypyridyl layer measured on the surfaces of CoTTP|PPy|GaP, and c is the concentration (in units of M) of cobalt porphyrins immobilized on the surfaces of CoTTP|PPy|GaP.

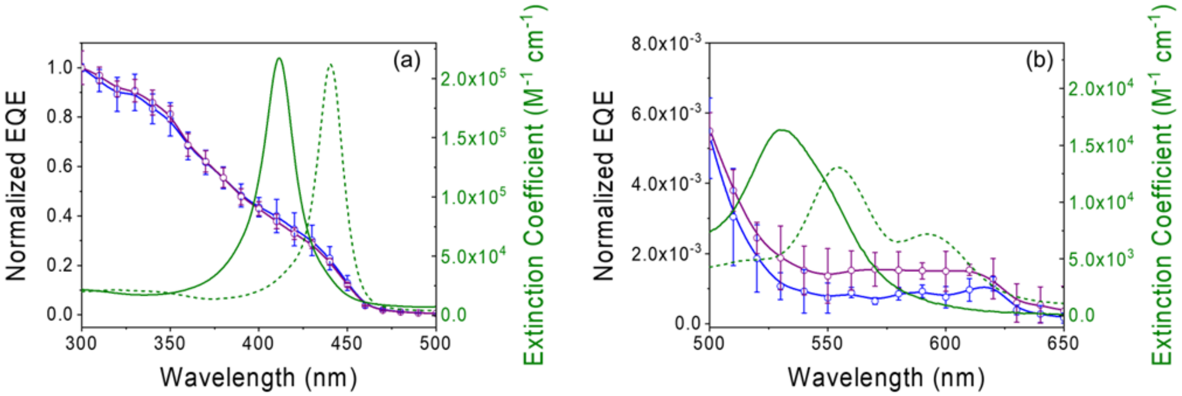

Figure 4.10. External quantum efficiency action spectra collected using PPy|GaP (blue) or CoTTP|PPy|GaP (purple) electrodes polarized at 0 V vs RHE in 0.1 M phosphate buffer (pH 7) normalized at 300 nm as well as absorption spectra of 5,10,15,20-tetra-p-tolylporphyrin cobalt(II) (CoTTP) recorded in chloroform in the absence (solid green) and presence of ~1 equivalent of pyridine (dashed green) in the wavelength ranges where the porphyrin (a) Soret absorption band (300 to 500 nm) and (b) Q-type absorption bands (500 to 650 nm) occur.

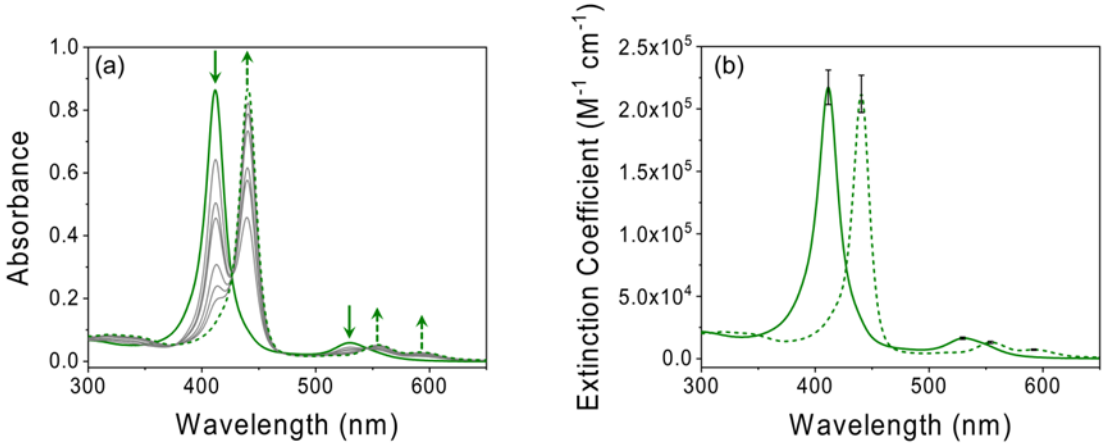

Figure 4.11. (a) Absorption spectra of 5,10,15,20-tetra-p-tolylporphyrin cobalt(II) (CoTTP) in chloroform recorded prior to (solid green) and following 26 hours after the addition of ~1 equivalent of pyridine (dashed green). The gray lines show data recorded following 5 min, 1 h, 2h, 7h, 10h, and 12h after the addition of ~1 equivalent of pyridine.

(b) Extinction coefficients of CoTTP in chloroform recorded prior to (solid green) and following 26 hours after the addition of ~1 equivalent of pyridine (dashed green).

Table 4.3. Soret and Q-type absorption bands (λ_{abs}) as well as associated extinction coefficients (ε) of 5,10,15,20-tetra-p-tolylporphyrin cobalt(II) (CoTTP) in chloroform recorded prior to and following 26 hours after the addition of ~1 equivalent of pyridine.

Complex	**Soret Absorption Band** **λ_{abs} (nm);** **ε (x 10^5 M^{-1} cm^{-1})**	**Q-type Absorption Band(s)** **λ_{abs} (nm);** **ε (x 10^4 M^{-1} cm^{-1})**
CoTTP	412; 2.2 ± 0.1	530; 1.6 ± 0.1
CoTTP with ~1 equivalent of pyridine	441; 2.1 ± 0.2	554; 1.3 ± 0.1 and 592; 0.72 ± 0.05

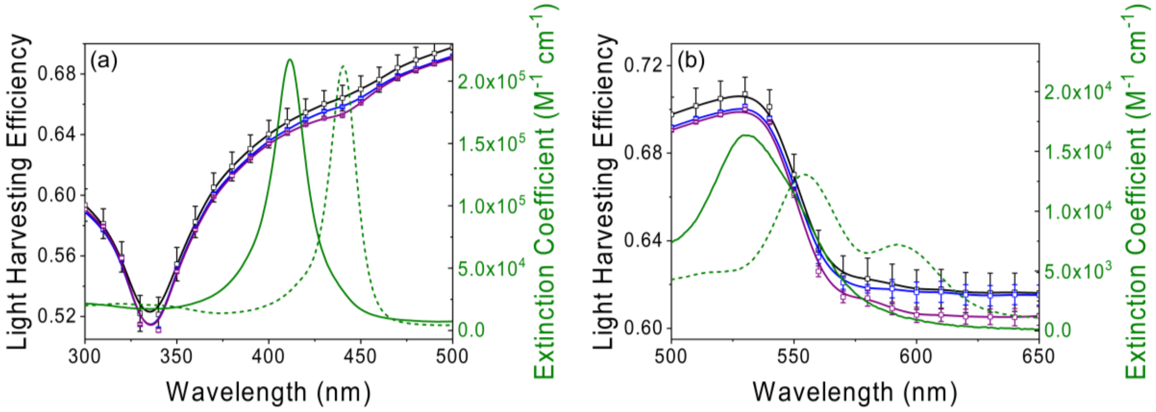

Figure 4.12. Wavelength-resolved LHE plots collected using GaP (black), PPy|GaP (blue), or CoTTP|PPy|GaP (purple) electrodes as well as extinction coefficients of CoTTP in chloroform recorded in the absence (solid green) or presence of ~1 equivalent of pyridine (dashed green). The data were collected at wavelengths where porphyrin (a)

Soret absorption bands (300 to 500 nm) occur and (b) Q-type absorption bands (500 to 650 nm) occur.

Absorption spectra of CoTTP in chloroform are characterized by a relatively strong Soret absorption at 412 nm (2.2 ± 0.1 x 10^5 M^{-1} cm^{-1}) and a weaker Q-type absorption band at 530 nm (1.6 ± 0.1 x 10^4 M^{-1} cm^{-1}) with both absorption bands appearing at wavelengths where the underlying GaP is photoactive (**Figure 4.11 and Table 4.3**). In contrast with absorption spectra of CoTTP recorded in neat chloroform, spectra of CoTTP recorded in chloroform following the addition of ~1 equivalent of pyridine show two Q-type absorption bands with maxima at 554 nm(1.3 ± 0.1 x 10^4 M^{-1} cm^{-1}) and 592 nm (7.2 ± 0.5 x 10^3 M^{-1} cm^{-1}) (wavelengths with corresponding energies that are lower than the 2.26 eV bandgap of GaP) and a Soret absorption band centered at 441 nm (2.1 ± 0.2 x 10^5 M^{-1} cm^{-1}) (**Figure 4.3, Figure 4.11, and Table 4.3**).[56] The Soret absorption band occurs at a wavelength where there is a relatively small difference (0.5 ± 0.1%) in LHEs at 440 nm recorded using samples of PPy|GaP or CoTTP|PPy|GaP (**Figure 4.12**).[57] In addition to the optical data presented in this Chapter, obtained using either heterogeneous-homogeneous samples of cobalt porphyrin-modified GaP semiconductors or homogeneous solutions of cobalt porphyrins, we have previously reported on the optical and electrochemical properties of heterogeneous-homogeneous samples of cobalt porphyrins immobilized on transparent conducting oxide materials.[10] These previous studies indicate the optical properties of the heterogeneous-homogeneous samples (including wavelengths of the Soret and Q-type absorption bands and their corresponding extinction coefficients) track closely with those recorded using homogeneous solutions of cobalt porphyrin and pyridine (**Figure 4.14 and Table 4.4**).

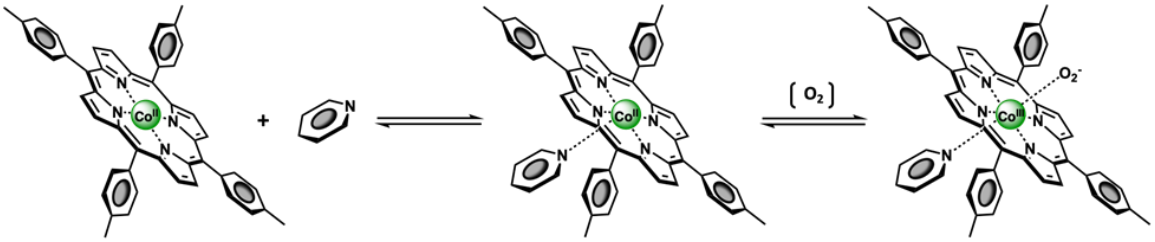

Figure 4.13. Schematic representation of the CoTTP, CoTTP-pyridine, and CoTTP-pyridine-O_2 equilibria. Oxygen binds to the cobalt center to form a CoTTP-pyridine-O2 complex, where the oxygen exists formally as a superoxide ion.[58-60]

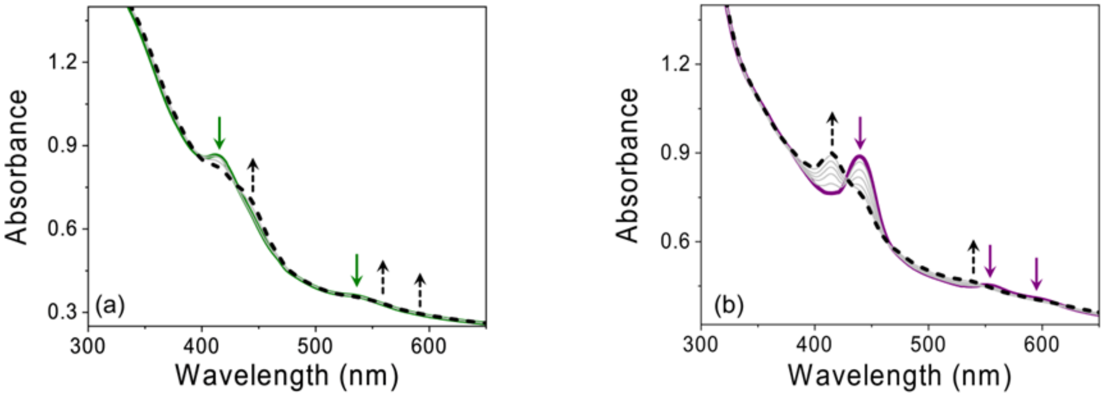

Figure 4.14. Absorption spectra of (a) cobalt porphyrin-modified nanostructured indium tin oxide (CoP|NanoITO) at open circuit potential (green solid) and polarized at potentials required to generate the Co^{III} species (grey solid and black dashed) as well as (b) cobalt porphyrin-polyvinylpyridine-modified nanostructured indium tin oxide (CoTTP|PVP|NanoITO) at open circuit potential (purple solid) and polarized at potentials required to generate the Co^{II} species (grey solid and black dashed). The black dashed traces in both panels represent spectra of CoP|NanoITO and CoTTP|PVP|NanoITO electrodes that no longer change upon further biasing the applied potential. This data is taken from reference 12 of this Chapter.

Table 4.4. Soret and Q-type absorption bands (λabs) as well as associated extinction coefficients (ε) recorded using CoP|NanoITO or CoTTP|PVP|NanoITO electrodes in propylene carbonate as described in reference 12 of this Chapter.

Heterogeneous-Homogeneous Construct	**Soret Absorption Band λ_{abs} (nm); ε (x 10^4 M^{-1} cm^{-1})**	**Q-type Absorption Band(s) λ_{abs} (nm); ε (x 10^4 M^{-1} cm^{-1})**
CoP|NanoITO	414; 6.1 ± 0.3	533; 1.5 ± 0.1
CoTTP|PVP|NanoITO	439; 2.8 ± 0.6	555; 0.45 ± 0.09 and 592; 0.36 ± 0.07

The fraction of light absorbed by surface-grafted cobalt porphyrins in samples of CoTTP|PPy|GaP was approximated using the extinction coefficients recorded for homogeneous solutions of CoTTP in chloroform following the addition of ~1 equivalent of pyridine ($2.1 \pm 0.2 \times 10^5$ M^{-1} cm^{-1} for the Soret absorption band and $1.3 \pm 0.1 \times 10^4$ M^{-1} cm^{-1} and $7.2 \pm 0.5 \times 10^3$ M^{-1} cm^{-1} for the Q-type absorption bands), the per geometric area loading of cobalt porphyrin in samples of CoTTP|PPy|GaP (~1 nmol cm^{-2}), and the polypyridyl film thickness (4 ± 1 nm). Analyses of these approximated LHEs associated with the cobalt porphyrin-polypyridyl surface coating indicate the immobilized porphyrins attenuate ~39% of the light at the maximum absorbance of the Soret absorption band (441 nm) and ~3% of the light at the maximum absorbance of the most intense Q-type absorption band (554 nm) (**Figure 4.15**). Despite this attenuation of light by the porphyrins, the overall photocurrents and related EQEs measured using

CoTTP|PPy|GaP working electrodes are higher than those measured using PPy|GaP electrodes.

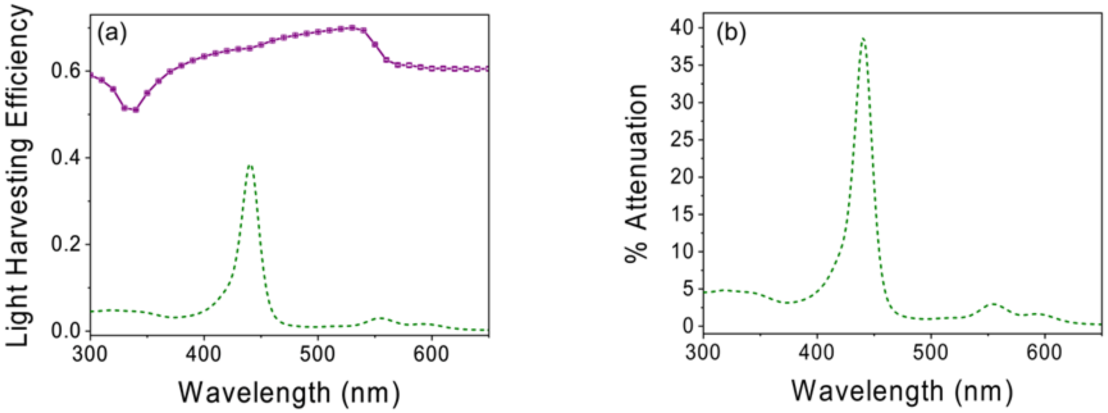

Figure 4.15. (a) Plots of the wavelength-resolved LHE measured using CoTTP|PPy|GaP electrodes (purple solid) and an approximated LHE associated with the CoTTP|PPy layer (green dashed). (b) Plot of the percent of light attenuated by the cobalt porphyrin-polypyridyl coating of the CoTTP|PPy|GaP assemblies (green dashed).

As expressed in Eq. 4.1, the LHE associated with the CoTTP|PPy layer is approximated using the measured per geometric area loading of cobalt porphyrins on CoTTP|PPy|GaP surfaces (1 nmol cm^{-2}), the polypyridyl layer thickness on CoTTP|PPy|GaP surfaces (~4 nm), and the extinction coefficients of CoTTP in chloroform recorded in the presence of ~1 equivalent of pyridine. Using the LHE values associated with the CoTTP|PPy layer from panel a, the percent of light attenuated by the cobalt porphyrin-polypyridyl coating is estimated to be ~39% at the wavelength associated with the Soret absorption band at 441 nm, ~3% at the wavelength associated with the Q-type absorption band at 554 nm, and ~2% at the wavelength associated with the Q-type absorption band at 592 nm.

Comparisons of the spectral profiles associated with the wavelength-resolved EQEs recorded using PPy|GaP or CoTTP|PPy|GaP electrodes should address to what extent the porphyrin coating may enhance photoelectrosynthetic performance by mechanisms involving dye sensitization. Following normalization at 300 nm, a wavelength that is well resolved from the cobalt porphyrin Soret and Q-type absorption bands, and where EQEs of PPy|GaP and CoTTP|PPy|GaP are at maximum values, these plots show no significant differences (i.e. outside the error of the measurements) in spectral intensities at wavelengths associated with cobalt porphyrin Soret absorption bands (**Figure 4.10a**) as well as the Q-type absorption band of CoTTP (**Figure 4.10b**). Although cobalt porphyrin complexes featuring coordination to axial pyridyl moieties display Q-type absorption bands at wavelengths with energies lower than the band gap of GaP (>549 nm, <2.26 eV),[12,58–60] there is an absence of prominent sub-band-gap features in EQE action spectra recorded using CoTTP|PPy|GaP samples. Although, analysis of EQEs recorded in the 570 nm to 610 nm range does indicate a slight (i.e. outside the error of the measurements) increase of the normalized signal intensity associated with the porphyrin-modified GaP electrodes (**Figure 4.10b**), this difference in signal accounts for only 0.05% of the total current density measured under broadband illumination conditions. Although it is true the electronic spectra of porphyrins recorded in the absence of polarization may not be indicative of the steady-state concentration of porphyrin species present on GaP surfaces under the conditions in which EQEs are measured (i.e. steady-state-illumination and polarization at 0 V vs RHE in the presence of chemical substrates), these results confirm the immobilized porphyrins serve relatively little role in extending the photoactivity of the hybrid assemblies to wavelengths outside the actinic range of GaP.

4.2.5. Apparent Dye-Sensitization Efficiencies

Information on the LHE associated with the cobalt porphyrin-polypyridyl surface coating was also used to generate hypothetical EQE plots. These plots are constructed assuming the immobilized porphyrins serve strictly as light- screening pigments or as dye-sensitizers (not catalysts). Thus, these hypothetical EQE plots represent extreme conditions where all cobalt porphyrins screen the flux of photons reaching the underlying GaP (i.e. when the absorbed photon-to-current dye-sensitization efficiency is 0%) or where all excited state cobalt porphyrins transfer carriers to the underlying GaP (i.e. when the absorbed photon-to-current dye-sensitization efficiency is 100%) (**Figures 4.16 – 4.18**).

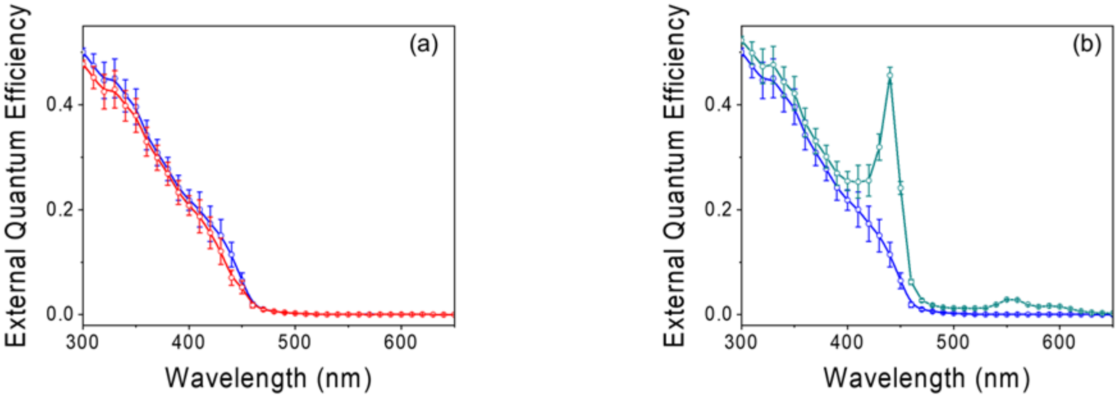

Figure 4.16. (a) External quantum efficiency action spectra calculated for a cobalt porphyrin-polypyridyl-modified GaP electrode assuming the immobilized porphyrins serve strictly as light-screening pigments (not catalysts) and all photons absorbed by the porphyrin layer are screened from the underlying GaP semiconductor (red). (b) External quantum efficiency action spectra calculated for a cobalt porphyrin-polypyridyl-modified GaP electrode assuming the immobilized porphyrins serve strictly as dye-sensitizers (not catalysts) and all photons absorbed by the porphyrin layer contribute to production of

photocurrent via a dye-sensitization mechanism (teal). For comparison, the external quantum efficiency action spectrum collected using PPy|GaP electrodes polarized at 0 V vs RHE in 0.1 M phosphate buffer (blue) is included in both panels (a) and (b).

Hypothetical EQE action spectra associated with CoTTP|PPy|GaP electrodes (red and teal spectra in **Figures 4.17 and 4.18**) were constructed assuming the immobilized porphyrins serve strictly as pigments or dye sensitizers and not catalysts.

Hypothetical EQE Action Spectra Assuming 0% Dye-Sensitization Efficiency

The hypothetical EQE of CoTTP|PPy|GaP if the absorbed photon-to-current dye-sensitization efficiency (DSE) is 0% (hypothetical $\text{EQE}_{0\%\text{DSE}}$) was constructed by multiplying the EQE of PPy|GaP (blue action spectrum in **Figure 4.8a**) by one minus the LHE associated with the CoTTP|PPy layer (dashed green spectrum in **Figure 4.15a**) as expressed in **Equation 4.2**:

$$\text{Hypothetical EQE}_{0\%\ \text{DSE}} \approx \text{EQE of PPy|GaP} \bullet (1 - \text{LHE of CoTTP|PPy}) \qquad \text{(Eq. 4.2)}$$

When the DSE is 0%, every photon absorbed by the CoTTP|PPy layer is screened from the underlying GaP and thus do not contribute to production of current.

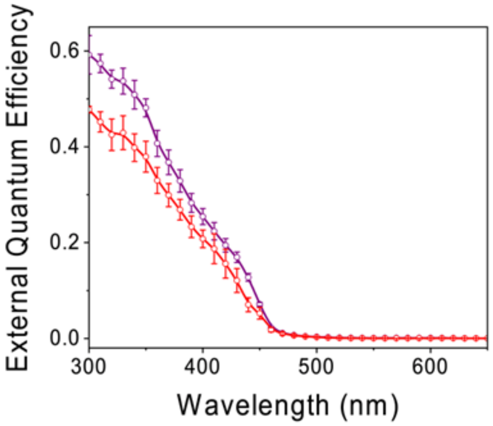

Figure 4.17. EQE action spectrum collected using CoTTP|PPy|GaP electrodes polarized at 0 V vs RHE in 0.1 M phosphate buffer (pH 7) (purple) and a hypothetical EQE action spectrum of CoTTP|PPy|GaP electrodes assuming the immobilized porphyrins serve strictly as pigments, not catalysts, and that all photons absorbed by the porphyrin layer are screened from the underlying GaP and do not contribute to production of current (i.e. the DSE is 0%) (red).

Hypothetical EQE Action Spectra Assuming 100% Dye-Sensitization Efficiency

The hypothetical EQE of CoTTP|PPy|GaP if the DSE is 100% (hypothetical $\mathrm{EQE}_{100\%\mathrm{DSE}}$) was constructed by summing the hypothetical $\mathrm{EQE}_{0\%\mathrm{DSE}}$ and the hypothetical EQE associated with the CoTTP|PPy layer as expressed in **Equation 4.3**:

$$\text{Hypothetical EQE}_{100\%\ \mathrm{DSE}} \approx \text{Hypothetical EQE of CoTTP|PPy} + \text{Hypothetical EQE}_{0\%\ \mathrm{DSE}} \qquad \text{(Eq. S3)}$$

where the hypothetical EQE of CoTTP|PPy is the product of the LHE of CoTTP|PPy (dashed green spectrum in Figure S6a) and the DSE of CoTTP|PPy as defined according to **Equation 4.3**:

$$\text{Hypothetical EQE of CoTTP|PPy} = \text{LHE of CoTTP|PPy} \bullet \text{DSE} \qquad \text{(Eq. S4)}$$

When the DSE is 100%, the hypothetical EQE of CoTTP|PPy is equal to the LHE of CoTTP|PPy, and every photon absorbed by the CoTTP|PPy layer is screened from the underlying GaP but contributes to production of current via a dye-sensitization mechanism.

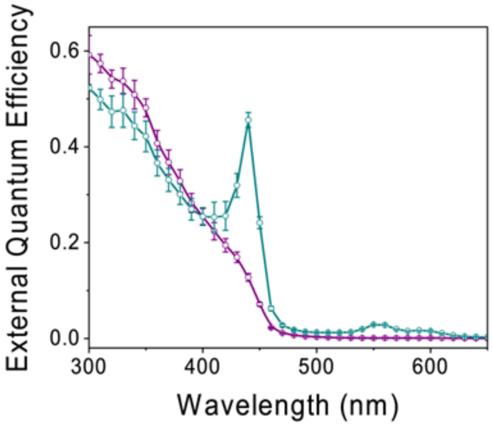

Figure 4.18. EQE action spectrum collected using CoTTP|PPy|GaP electrodes polarized at 0 V vs RHE in 0.1 M phosphate buffer (pH 7) (purple) and a hypothetical EQE action spectrum of CoTTP|PPy|GaP electrodes assuming the immobilized porphyrins serve strictly as pigments, not catalysts, and that all photons absorbed by the porphyrin layer are screened from the underlying GaP but contribute to production of current via a dye-sensitization mechanism (i.e. the DSE is 100%) (teal).

These results further demonstrate the measured enhancements in EQE following porphyrin modification cannot be accounted for by porphyrin dye sensitization. For example, the apparent absorbed photon-to-current dye-sensitization efficiency required to achieve the EQEs measured following porphyrin modification at wavelengths between 300 and 400 nm would be almost 250% (**Figure 4.19**). Thus, the enhancement in EQE following porphyrin modification is inconsistent with a mechanism involving dye-sensitization. Although the results reported here clearly demonstrate an increase in the ratio of incident photon flux to electron flux measured as current following porphyrin modification in such hybrid assemblies, it can be difficult to deconvolute enhancements in photoelectrochemical activity arising from improvements due to chemical catalysis versus changes in surface energetics.[61–65]

Apparent Dye-Sensitization Efficiencies

The EQE measured using samples of CoTTP|PPy|GaP can be expressed as a sum of hypothetical EQEs associated with the CoTTP|PPy and GaP components in accordance with **Equation 4.5**:

$$\text{EQE of CoTTP|PPy|GaP} \approx \text{Hypothetical EQE of CoTTP|PPy} + \text{Hypothetical EQE}_{0\%\ \text{DSE}} \qquad \text{(Eq. 4.5)}$$

If the measured enhancements in EQE following porphyrin modification are indeed solely due to dye sensitization, **Equation 4.5** can be re-expressed (using the relationship given in **Equation 4.4**) in terms of an apparent DSE required to afford the measured EQE values, as indicated in **Equation 4.6**:

$$\text{EQE of CoTTP|PPy|GaP} \approx (\text{LHE of CoTTP|PPy} \bullet \text{Apparent DSE}) + \text{Hypothetical EQE}_{0\%\ \text{DSE}} \qquad \text{(Eq. 4.6)}$$

This apparent DSE is approximated by rearranging Equation 4.6 to yield Equation 4.7:

$$\text{Apparent DSE} \approx \frac{\text{EQE of CoTTP|PPy|GaP} - \text{Hypothetical EQE}_{0\%\ \text{DSE}}}{\text{LHE of CoTTP|PPy}} \qquad \text{(Eq. 4.7)}$$

In principle, the analysis described in this work could be applied to other molecular-modified semiconductor assemblies if information is available regarding the EQE and LHE of the molecular-modified semiconductor assembly as well as the surface loading and extinction coefficients of the light absorbing components.

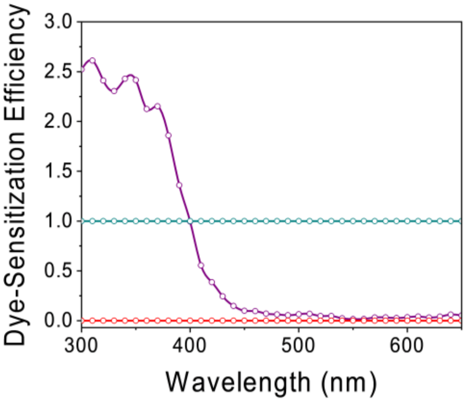

Figure 4.19. A plot of the apparent DSE (as defined in Equation 4.7) required to achieve the EQEs measured using CoTTP|PPy|GaP electrodes (purple). For comparisons, the DSEs used to construct the hypothetical EQE action spectra shown in **Figure 4.17**, where the DSE of the CoTTP|PPy|GaP electrodes is 0%, (red) and **Figure 4.18**, where the DSE of the CoTTP|PPy|GaP electrodes is 100% (teal) are also included. These results further demonstrate that enhancements in EQE following porphyrin modification cannot be accounted for by porphyrin dye sensitization. For example, the apparent DSE required to achieve the EQEs measured following porphyrin modification at wavelengths between 300 and 400 nm would be almost 250%.

4.3 Conclusion

In conclusion, optical and photoelectrochemical measurements, including measurements of light harvesting efficiencies and in operando wavelength-resolved quantum efficiencies associated with hydrogen production, were performed using unmodified and chemically modified GaP working electrodes. Our results indicate the immobilized porphyrins contribute relatively little to extending the photoactivity of these assemblies to wavelengths outside the actinic range of GaP yet are essential to improving the overall photocurrent density. Although the studies described in this report focus on hydrogen evolution using metalloporphyrin-modified GaP semiconductors, the analysis techniques (including quantification of catalyst loading coupled with determination of the LHEs, EQEs, and IQEs obtained from measurements performed prior to and following surface modification chemistry) are likely applicable to a broader range of photoelectrosynthetic assemblies and chemical transformations. Thus, this approach highlights a general yet useful strategy for better understanding the activity of photoelectrosynthetic assemblies containing molecular electrocatalysts that absorb visible light.

4.4 References

(1) Ardo, S.; Rivas, D. F.; Modestino, M. A.; Greiving, V. S.; Abdi, F. F.; Llado, E. A.; Artero, V.; Ayers, K.; Battaglia, C.; Becker, J.-P.; Bederak, D.; Berger, A.; Buda, F.; Chinello, E.; Dam, B.; Di Palma, V.; Edvinsson, T.; Fuji, K.; Gardeniers, H.; Geerlings, H.; Hashemi, S. M. H.; Haussener, S.; Houle, F.; Huskens, J.; James, B. D.; Konrad, K.; Kudo, A.; Kunturu, P. P.; Lohse, D.; Mei, B.; Miller, E. L.; Moore, G. F.; Muller, J.; Orchard, K. L.; Rosser, T. E.; Saadi, F. H.; Schüttauf, J.-W.; Seger, B.; Sheehan, S. W.; Smith, W. A.; Spurgeon, J.; Tang, M. H.; van de Krol, R.; Vesborg, P. C. K.; Westerik, P. Pathways to Electrochemical Solar-Hydrogen Technologies. *Energy Environ. Sci.* **2018**, *11*, 2768–2783.

(2) Faunce, T. A.; Lubitz, W.; Rutherford, A. W.; MacFarlane, D.; Moore, G. F.; Yang, P.; Nocera, D. G.; Moore, T. A.; Gregory, D. H.; Fukuzumi, S.; Yoon, K. B.; Armstrong, F. A.; Wasielewski, M. R.; Styring, S. Energy and Environment Policy Case for a Global Project on Artificial Photosynthesis. *Energy Environ. Sci.* **2013**, *6*, 695–698.

(3) Hambourger, M.; Moore, G. F.; Kramer, D. M.; Gust, D.; Moore, A. L.; Moore, T. A. Biology and Technology for Photochemical Fuel Production. *Chem. Soc. Rev.* **2009**, *38*, 25−35.

(4) McKone, J. R.; Marinescu, S. C.; Brunschwig, B. S.; Winkler, J. R.; Gray, H. B. Earth-Abundant Hydrogen Evolution Electrocatalysts. *Chem. Sci.* **2014**, *5*, 865–878.

(5) Wadsworth, B. L.; Khusnutdinova, D.; Moore, G. F. Polymeric Coatings for Applications in Electrocatalytic and Photoelectrosynthetic Fuel Production. *J. Mater. Chem. A* **2018**, *6*, 21654–21665.

(6) Ye, R.; Zhao, J.; Wickemeyer, B. B.; Toste, F. D.; Somorjai, G. A. Foundations and Strategies of the Construction of Hybrid Catalysts for Optimized Performances. *Nat. Catal.* **2018**, *1*, 318–325.

(7) Queyriaux, N.; Kaeffer, N.; Morozan, A.; Chavarot-Kerlidou, M.; Artero, V. Molecular Cathode and Photocathode Materials for Hydrogen Evolution in Photoelectrochemical Devices. *J. Photochem. Photobiol. C Photochem. Rev.* **2015**, *25*, 90–105.

(8) Bullock, R. M.; Das, A. K.; Appel, A. M. Surface Immobilization of Molecular Electrocatalysts for Energy Conversion. *Chem. – Eur. J.* **2017**, *23*, 7626–7641.

(9) Beiler, A. M.; Khusnutdinova, D.; Wadsworth, B. L.; Moore, G. F. Cobalt Porphyrin–Polypyridyl Surface Coatings for Photoelectrosynthetic Hydrogen Production. *Inorg. Chem.* **2017**, *56*, 12178–12185.

(10) Khusnutdinova, D.; Beiler, A. M.; Wadsworth, B. L.; Jacob, S. I.; Moore, G. F. Metalloporphyrin-Modified Semiconductors for Solar Fuel Production. *Chem. Sci.* **2017**, *8*, 253–259.

(11) Wadsworth, B. L.; Beiler, A. M.; Khusnutdinova, D.; Reyes Cruz, E. A.; Moore, G. F. Interplay between Light Flux, Quantum Efficiency, and Turnover Frequency in Molecular-Modified Photoelectrosynthetic Assemblies. *J. Am. Chem. Soc.* **2019**, *141*, 15932–15941.

(12) Wadsworth, B. L.; Khusnutdinova, D.; Urbine, J. M.; Reyes, A. S.; Moore, G. F. Expanding the Redox Range of Surface-Immobilized Metallocomplexes using Molecular Interfaces. *ACS Appl. Mater. Interfaces* **2020**, 12, 3903–3911.

(13) Ladomenou, K.; Natali, M.; Iengo, E.; Charalampidis, G.; Scandola, F.; Coutsolelos, A. G. Photochemical Hydrogen Generation with Porphyrin-Based Systems. *Coord. Chem. Rev.* **2015**, *304*, 38–54.

(14) Costentin, C.; Robert, M.; Savéant, J. M. Current Issues in Molecular Catalysis Illustrated by Iron Porphyrins as Catalysts of the CO_2-to-CO Electrochemical Conversion. *Acc. Chem. Res.* **2015**, *48*, 2996–3006.

(15) Manbeck, G. F.; Fujita, E. A Review of Iron and Cobalt Porphyrins, Phthalocyanines and Related Complexes for Electrochemical and Photochemical Reduction of Carbon Dioxide. *J. Porphyrins Phthalocyanines* **2015**, *19*, 45–64.

(16) Morris, A. J.; Meyer, G. J.; Fujita, E. Molecular Approaches to the Photocatalytic Reduction of Carbon Dioxide for Solar Fuels. *Acc. Chem. Res.* **2009**, *42*, 1983–1994.

(17) Losse, S.; Vos, J. G.; Rau, S. Catalytic Hydrogen Production at Cobalt Centres. *Coord. Chem. Rev.* **2010**, *254*, 2492–2504.

(18) Collin, J. P.; Sauvage, J. P. Electrochemical Reduction of Carbon Dioxide Mediated by Molecular Catalysts. *Coord. Chem. Rev.* **1989**, *93*, 245–268.

(19) Dalle, K. E.; Warnan, J.; Leung, J. J.; Reuillard, B.; Karmel, I. S.; Reisner, E. Electro-and Solar-Driven Fuel Synthesis with First Row Transition Metal Complexes. *Chem. Rev.* **2019**, *119*, 2752–2875.

(20) Zhang, B.; Sun, L. Artificial Photosynthesis: Opportunities and Challenges of Molecular Catalysts. *Chem. Soc. Rev.* **2019**, *48*, 2216–2264.

(21) Morikawa, T.; Sato, S.; Sekizawa, K.; Arai, T.; Suzuki, T. M. Molecular Catalysts Immobilized on Semiconductor Photosensitizers for Proton Reduction toward Visible-Light-Driven Overall Water Splitting. *ChemSusChem* **2019**, *12*, 1807–1824.

(22) Auwärter, W.; Écija, D.; Klappenberger, F.; Barth, J. V. Porphyrins at Interfaces. *Nat. Chem.* **2015**, *7*, 105–120.

(23) Gust, D.; Moore, T. A.; Moore, A. L. Solar Fuels via Artificial Photosynthesis. *Acc. Chem. Res.* **2009**, *42*, 1890–1898.

(24) Lindsey, J. S.; Bocian, D. F. Molecules for Charge-Based Information Storage. *Acc. Chem. Res.* **2011**, *44*, 638–650.

(25) Swierk, J. R.; Méndez-Hernández, D. D.; McCool, N. S.; Liddell, P.; Terazono, Y.; Pahk, I.; Tomlin, J. J.; Oster, N. V.; Moore, T. A.; Moore, A. L.; Gust, D. Metal-Free Organic Sensitizers for Use in Water-Splitting Dye-Sensitized Photoelectrochemical Cells. *Proc. Nat. Acad. Sci.* **2015**, *112*, 1681–1686.

(26) Higashino, T.; Imahori, H. Porphyrins as Excellent Dyes for Dye-Sensitized Solar Cells: Recent Developments and Insights. *Dalton Trans.* **2015**, *44*, 448–463.

(27) Mathew, S.; Yella, A.; Gao, P.; Humphry-Baker, R.; Curchod, B.F.; Ashari-Astani, N.; Tavernelli, I.; Rothlisberger, U.; Nazeeruddin, M. K.; Grätzel, M. Dye-Sensitized Solar Cells with 13% Efficiency Achieved through the Molecular Engineering of Porphyrin Sensitizers. *Nat. Chem.* **2014**, *6*, 242–247.

(28) Walter, M. G.; Rudine, A. B.; Wamser, C. C. Porphyrins and Phthalocyanines in Solar Photovoltaic Cells. *J. Porphyrins Phthalocyanines* **2010**, *14*, 759–792.

(29) Li, L. L.; Diau, E. W. G. Porphyrin-Sensitized Solar Cells. *Chem. Soc. Rev.* **2013**, *42*, 291–304.

(30) Standing, A.; Assali, S.; Gao, L.; VeRHEijen, M. A.; Van Dam, D.; Cui, Y.; Notten, P. H.; Haverkort, J. E.; Bakkers, E. P. Efficient Water Reduction with Gallium Phosphide Nanowires. *Nat. Commun.* **2015**, *6*, 7824.

(31) Liu, C.; Sun, J.; Tang, J.; Yang, P. Zn-Doped p-Type Gallium Phosphide Nanowire Photocathodes from a Surfactant-Free Solution Synthesis. *Nano Lett.* **2012**, *12*, 5407–5411.

(32) Barton, E. E.; Rampulla, D. M.; Bocarsly, A. B. Selective Solar-Driven Reduction of CO_2 to Methanol Using a Catalyzed p-GaP Based Photoelectrochemical Cell. *J. Am. Chem. Soc.* **2008**, *130*, 6342–6344.

(33) Grätzel, M. Photoelectrochemical Cells. *Nature* **2001**, *414*, 338–344.

(34) Butler, M. A.; Ginley, D. S. P-Type GaP as a Semiconducting Photoelectrode. *J. Electrochem. Soc.* **1980**, *127*, 1273–1278.

(35) Halmann, M. Photoelectrochemical Reduction of Aqueous Carbon Dioxide on p-Type Gallium Phosphide in Liquid Junction Solar Cells. *Nature* **1978**, *275*, 115–116.

(36) Tomkiewicz, M.; Woodall, J. M. Photoassisted Electrolysis of Water by Visible Irradiation of a p-Type Gallium Phosphide Electrode. *Science* **1977**, *196*, 990–991.

(37) Bockris, J. M.; Uosaki, K. The Rate of the Photoelectrochemical Generation of Hydrogen at p-Type Semiconductors. *J. Electrochem. Soc.* **1977**, *124*, 1348–1355.

(38) Krawicz, A.; Yang, J.; Anzenberg, E.; Yano, J.; Sharp, I. D.; Moore, G. F. Photofunctional Construct that Interfaces Molecular Cobalt-Based Catalysts for H_2 Production to a Visible-Light-Absorbing Semiconductor. *J. Am. Chem. Soc.* **2013**, *135*, 11861–11868.

(39) Gleria, M.; Memming, R. Charge Transfer Processes at Large Band Gap Semiconductor Electrodes: Reactions at SiC-Electrodes. *J. Electroanal. Chem.* **1975**, *65*, 163–175.

(40) Memming, R.; Schwandt, G. Electrochemical Properties of Gallium Phosphide in Aqueous Solutions. *Electrochim. Acta* **1968**, *13*, 1299–1310.

(41) Liang, X.; Cao, X.; Sun, W.; Ding, Y. Recent Progress in Visible Light Driven Water Oxidation using Semiconductors Coupled with Molecular Catalysts. *ChemCatChem* **2019**, *11*, 6190–6202.

(42) Trotochaud, L.; Mills, T. J.; Boettcher, S. W. An Optocatalytic Model for Semiconductor–Catalyst Water-Splitting Photoelectrodes Based on in situ Optical Measurements on Operational Catalysts. *J. Phys. Chem. Lett.* **2013**, *4*, 931–935.

(43) Kempler, P. A.; Gonzalez, M. A.; Papadantonakis, K. M.; Lewis, N. S. Hydrogen Evolution with Minimal Parasitic Light Absorption by Dense Co–P Catalyst Films on Structured p-Si Photocathodes. *ACS Energy Lett.* **2018**, *3*, 612–617.

(44) Chen, H. Y.; Ardo, S. Direct Observation of Sequential Oxidations of a Titania-Bound Molecular Proxy Catalyst Generated Through Illumination of Molecular Sensitizers. *Nat. Chem.* **2018**, *10*, 17–23.

(45) Beiler, A. M.; Moore, G. F. Multi-Electron Transfer Photochemistry: Caught in the Act. *Nat. Chem.* **2018**, *10*, 3–4.

(46) Willkomm, J.; Orchard, K. L.; Reynal, A.; Pastor, E.; Durrant, J. R.; Reisner, E. Dye-Sensitised Semiconductors Modified with Molecular Catalysts for Light-Driven H_2 Production. *Chem. Soc. Rev.* **2016**, *45*, 9–23.

(47) Ashford, D. L.; Gish, M. K.; Vannucci, A. K.; Brennaman, M. K.; Templeton, J. L.; Papanikolas, J. M.; Meyer, T. J. Molecular Chromophore–Catalyst Assemblies for Solar Fuel Applications. *Chem. Rev.* **2015**, *115*, 13006–13049.

(48) Brennaman, M. K.; Dillon, R. J.; Alibabaei, L.; Gish, M. K.; Dares, C. J.; Ashford, D. L.; House, R. L.; Meyer, G. J.; Papanikolas, J. M.; Meyer, T. J. Finding the Way to Solar Fuels with Dye-Sensitized Photoelectrosynthesis Cells. *J. Am. Chem. Soc.* **2016**, *138*, 13085–13102.

(49) Ilic, S.; Brown, E. S.; Xie, Y.; Maldonado, S.; Glusac, K. D. Sensitization of p-GaP with Monocationic Dyes: The Effect of Dye Excited-State Lifetime on Hole Injection Efficiencies. *J. Phys. Chem. C* **2016**, *120*, 3145–3155.

(50) Memming, R.; Tributsch, H. Electrochemical Investigations on the Spectral Sensitization of Gallium Phosphide Electrodes. *J. Phys. Chem.* **1971**, *75*, 562–570.

(51) Hammarström, L. Accumulative Charge Separation for Solar Fuels Production: Coupling Light-Induced Single Electron Transfer to Multielectron Catalysis. *Acc. Chem. Res.* **2015**, *48*, 840–850.

(52) Lee, C. H.; Lindsey, J. S. One-Flask Synthesis of Meso-Substituted Dipyrromethanes and Their Application in the Synthesis of Trans-Substituted Porphyrin Building Blocks. *Tetrahedron* **1994**, *50*, 11427–11440.

(53) Chizhova, N. V.; Kumeev, R. S.; Mamardashvili, N. Z. Synthesis and Spectral Properties of Cobalt (II) and Cobalt (III) Tetraarylporphyrinates. *Russ. J. Inorg. Chem*. **2013**, *58*, 740–743.

(54) Chen, Z.; Jaramillo, T. F.; Deutsch, T. G.; Kleiman-Shwarsctein, A.; Forman, A. J.; Gaillard, N.; Garland, R.; Takanabe, K.; Heske, C.; Sunkara, M.; McFarland, E. W. Accelerating Materials Development for Photoelectrochemical Hydrogen Production: Standards for Methods, Definitions, and Reporting Protocols. *J. Mater. Res.* **2010**, *25*, 3–16.

(55) Döscher, H.; Young, J. L.; Geisz, J. F.; Turner, J. A.; Deutsch, T. G. Solar-to-Hydrogen Efficiency: Shining Light on Photoelectrochemical Device Performance. *Energy Environ. Sci.* **2016**, *9*, 74–80.

(56) Lacey, S. D. The Absorption Coefficient of Gallium Phosphide in the Wavelength Region 530 to 1100 nm. *Solid State Commun.* **1970**, *8*, 1115–1118.

(57) At the time of writing, the air-mass 1.5 global tilt (AM 1.5G) spectrum from the ASTM G-173-03 data set is available online at hTTPs://www.nrel.gov/grid/solar-resource/spectra.html.

(58) Changes in the electronic spectra of cobalt porphyrins when in the presence of pyridine and oxygen have been previously reported and ascribed to axial coordination of a pyridine unit and a superoxide ion.

(59) Given the value of Φ_{trans} is ~0 at 440 nm for all samples and LHE is not directly measured but is determined from reflectance and transmittance measurements, any differences in LHE at 440 nm correspond to changes in reflection properties following porphyrin modification. Nonetheless, the LHE data indicate any decrease in LHE at 440 nm following porphyrin modification is limited to <1%.

(60) Walker, F. A. Electron Spin Resonance Study of Coordination to the Fifth and Sixth Positions of α,β,γ,δ-Tetra(p-methoxyphenyl)porphinatocobalt (II). *J. Am. Chem. Soc.* **1970**, *92*, 4235−4244.

(61) Walker, F. A. Steric and Electronic Effects in the Coordination of Amines to a Cobalt (II) Porphyrin. *J. Am. Chem. Soc.* **1973**, *95*, 1150−1153.

(62) Walker, F. A. Reactions of Monomeric Cobalt-Oxygen Complexes. I. Thermodynamics of Reaction of Molecular Oxygen with Five-and Six-Coordinate Amine Complexes of a Cobalt Porphyrin. *J. Am. Chem. Soc.* **1973**, *95*, 1154−1159.

(63) Barroso, M.; Cowan, A. J.; Pendlebury, S. R.; Grätzel, M.; Klug, D. R.; Durrant, J. R. The Role of Cobalt Phosphate in Enhancing the Photocatalytic Activity of α-Fe_2O_3 Toward Water Oxidation. *J. Am. Chem. Soc.* **2011**, *133*, 14868−14871.

(64) Barroso, M.; Mesa, C. A.; Pendlebury, S. R.; Cowan, A. J.; Hisatomi, T.; Sivula, K.; Grätzel, M.; Klug, D. R; Durrant, J. R. Dynamics of Photogenerated Holes in Surface Modified α-Fe_2O_3 Photoanodes for Solar Water Splitting. *Proc. Nat. Acad. Sci.* **2012**, *109*, 15640−15645.

(65) Li, W.; He, D.; Sheehan, S. W.; He, Y.; Thorne, J. E.; Yao, X.; Brudvig, G. W.; Wang, D. Comparison of Heterogenized Molecular and Heterogeneous Oxide Catalysts for Photoelectrochemical Water Oxidation. *Energy Environ. Sci.* **2016**, *9*, 1794−1802.

(66) Thorne, J. E.; Jang, J. W.; Liu, E. Y.; Wang, D. Understanding the Origin of Photoelectrode Performance Enhancement by Probing Surface Kinetics. *Chem. Sci.* **2016**, *7*, 3347−3354.

(67) Klahr, B.; Gimenez, S.; Fabregat-Santiago, F.; Bisquert, J.; Hamann, T. W. Electrochemical and Photoelectrochemical Investigation of Water Oxidation with Hematite Electrodes. *Energy Environ. Sci.* **2012**, *5*, 7626−7636.

CHAPTER 5 EXPERIMENTAL METHODS

5.1 Experimental Methods for Chapter 2

5.1.1 Experimental Methods

Contact Angle Measurements

Contact angle measurements were performed using a KRÜSS Contact Angle Model DSA 10 analyzer. The software program used was Drop Shape Analyzer 25 Basic Advance. The liquid sessile drop method was used to determine the contact angle of unmodified, polymer-modified, and catalyst-polymer-modified samples. Images were recorded using a video camera following a waiting period of 5 s.

Ellipsometry

Film thickness (FT) was determined using a J. A. Woollam variable angle spectroscopic ellipsometer with a spectral range of 190−2000 nm. Measurements were taken at 70°, 75°, and 80° incidence angles, and analysis was done using VASE software. The model used to determine the FT of surface-grafted polypyridyl films was composed of a GaAs (111)A substrate layer (Aspnes) and a Cauchy layer for the polypyridyl film of each sample. The Cauchy coefficients for GaAs (111)A were $A = 1.937$ and $B = 0.00842$ with an MSE of 1.967. The film thickness of the Cauchy layer was determined to be 2.0 ± 0.3 nm.

Inductively Coupled Plasma Mass Spectrometry

Inductively coupled plasma mass spectrometry (ICP-MS) was performed on a Thermo-Finnigan Neptune ICP-MS. The samples were run in kinetic-energy discrimination (KED) mode. The ICP-MS samples were prepared by immersing a cobaloxime|PPy|GaAs wafer into 1000 μL of concentrated Omni trace H_2SO_4 solution and heating the solution at 60 °C for 20 min, followed by sonicating the solution for 1 h. The solution was then diluted to 0.5 M H_2SO_4 by taking 108 μL of the 1000 μL solution and diluting to 4000 μL. Three different wafers of cobaloxime|PPy|GaAs were analyzed and three different wafers of PPy|GaAs as well as three different wafers of unmodified GaAs substrates were analyzed as controls.

Fourier Transform Infrared Spectroscopy

Grazing angle attenuated total reflection Fourier transform Infrared Spectroscopy (GATR-FTIR) was performed using a VariGATR accessory with a Ge crystal plate (Harrick Scientific) installed in a Vertex 70 Fourier Transform Infrared (FTIR) spectrometer (Bruker). Samples were pressed against the Ge crystal to ensure effective optical coupling. Spectra were collected at 4 cm^{-1} resolution using 256 scans, a dry nitrogen purge, GloBar MIR source, a broadband KBr beamsplitter, and a liquid nitrogen cooled MCT detector. Background measurements (also collected using 256 scans) were obtained from the bare Ge crystal, and all data were processed using OPUS software. GATR-FTIRmeasurements were baselined using the rubber band correction method. Spectra of model compounds in pressed KBr pellets were collected using 64 scans in transmission mode with a resolution of 1 cm^{-1}.

X-ray Photoelectron Spectroscopy

X-ray photoelectron spectroscopy (XPS) was performed using a monochromatized Al Kα source (hν = 1486.6 eV), operated at 63 W, on a Vacuum Generators 220i-XL (Thermo Fisher) system at a takeoff angle of 0° relative to the surface normal and a pass energy for narrow scan spectra of 20 eV, at an instrument resolution of approximately 700 meV. Survey spectra were collected with a pass energy of 150 eV. Spectral fitting was performed using Casa XPS analysis software. Spectral positions were corrected by shifting the primary C 1s core level position to 284.8 eV, and curves were fit with quasi-Voigt lines following Shirley background subtraction. All N 1s fits were constrained to a full width at half maximum (fwhm) value of less than 1.3 eV.

Photoelectrochemistry

Photoelectrochemical (PEC) experiments were performed using a 100 W Oriel Solar Simulator equipped with an air mass 1.5 filter. All linear sweep voltammetry and chronoamperometry experiments were performed with a Biologic SP-300 potentiostat using a platinum coil counter electrode and a Ag/AgCl reference electrode in a modified cell containing a quartz window. The supporting electrolytes were either 0.1 M NaOH solution (pH 13) or 0.1 M phosphate buffer (pH 7). The resistance of the solution between a working electrode and the reference electrode (also called the uncompensated resistance, Ru) was determined using the zero internal resistance (ZIR) technique. To compensate for the solution resistance, the ZIR technique was performed before other experiments and 85% of the uncompensated resistance was accounted for in the following experiments. All linear sweep voltammograms were recorded under a continuous flow of forming gas (5% hydrogen in nitrogen). Open-circuit photovoltages were taken as the zero-current value in the linear sweep voltammograms.

Gas Chromatography Analysis

Confirmation of hydrogen generation was performed via gas chromatography using an Agilent 490 Micro gas chromatograph equipped with a 5 Å MolSieve column at a temperature of 80 °C and argon as the carrier gas. Gas samples were syringe-injected using 5 mL aliquots of headspace gas collected with a gastight Hamilton syringe from a sealed PEC cell both prior to and following 20 min of three-electrode photoelectrochemical operation using a cobaloxime|PPy|GaAs working electrode polarized at 0 V, -0.2 V, -0.58 V, -0.98 V, or -1.38 V vs RHE in pH 7 electrolyte solutions or at 0 V, -0.2 V, -0.52 V, or -1.92 V vs RHE in pH 13 electrolyte solutions (E vs RHE = E vs NHE + (0.05916 V × pH) = E vs Ag/AgCl + (0.05916 V × pH) + 0.21 V). Prior to the experiment, the photoelectrochemical cell was purged for 30 min with argon and 5 mL of 99.9% methane was injected into the cell as an internal standard before sealing. The retention time of hydrogen was confirmed using a known source of hydrogen obtained from a standard lecture bottle containing a hydrogen and nitrogen mixture (100 ppm hydrogen in nitrogen) (Scotty).

Ultraviolet-Visible-Near Infrared Spectroscopy

All optical spectra were recorded using a SolidSpec-3700 Ultraviolet-Visible-Near Infrared (UV-VIS-NIR) spectrophotometer (Shimadzu, Kyoto, Japan) with a D_2 (deuterium) lamp for the ultraviolet range and a WI (halogen) lamp for the visible and near-infrared ranges. All solution measurements were collected in chloroform at 0.5 nm intervals. All solid-state optical measurements were performed using 400 μm thick GaAs wafers prior to and following all chemical modification steps. The transmittance and reflectance of GaAs samples were measured using an integrating sphere at 10 nm intervals. Specular reflectance measurements were collected at an incident angle of 5^{o} to the normal of the surface using a Specular Reflectance Attachment from Shimadzu and referenced to a STAN-SSH-reference mirror (OceanOptics). Absorption coefficients for GaAs and chemically-modified GaAs samples were calculated using Equation 5.1:

$$\alpha = -\ln\left[\frac{(\%T+\%R)}{100}\right] / L \qquad \text{(Eq. 5.1)}$$

where α is the wavelength-dependent absorption coefficient, L is the pathlength or thickness of the GaAs wafer (400 μm), $\%T$ represents the percent transmittance collected at normal incidence, and $\%R$ represents the sum of the measured specular percent reflectance, collected at an incident angle of 5° to the normal of the surface, and diffuse percent reflectance.

Determination of Cobalt Surface Loadings

Determination of the total cobalt surface concentration takes into account that the synthetic method used to prepare the chemically-modified semiconductors (i.e., UV-induced grafting followed by post synthetic manipulation) yields samples with cobaloximes assembled on both sides of the GaAs (111)A wafers.[1,2] XP spectroscopic analysis indicates the surface cobalt concentration on the non-directly illuminated side of the wafer (i.e., the unpolished side) is 33% lower than the surface cobalt concentration on the directly illuminated side of the wafer (i.e., the polished side). The total cobalt concentration, including contributions from the front and back sides of the GaAs wafer and as measured by ICP-MS following acid digestion of cobaloxime|PPy|GaAs samples, is 4.0 ± 0.4 nmol cm^{-2}, indicating the cobalt concentration on the polished side of the wafer (i.e., the directly illuminated side during photo-deposition of the polymeric layer as well as the solution facing side during photoelectrochemical experiments), is 2.4 ± 0.4 nmol cm^{-2}.

Determination of the Ratio of Pyridyl Nitrogens to Cobalt

Using the total areas of N 1s and Co 2p signals recorded in XP spectra collected using samples of cobaloxime|PPy|GaAs, and after considering the relative sensitivity factors for each element, the N:Co ratio on cobaloxime|PPy|GaAs surfaces is 5:1. Using the thickness of the surface-grafted polypyridyl layer obtained from ellipsometry (2.0 ± 0.3 nm), the total cobalt surface loading determined using ICP-MS and XPS (2.4 ± 0.4 nmol cm^{-2}), and assuming the density of the polymeric layer is the same as the bulk polymer's (1.15 g cm^{-3}), the ratio of pyridyl nitrogens to cobalt is 1:1

.

5.1.2 X-ray Photoelectron Spectroscopy Data

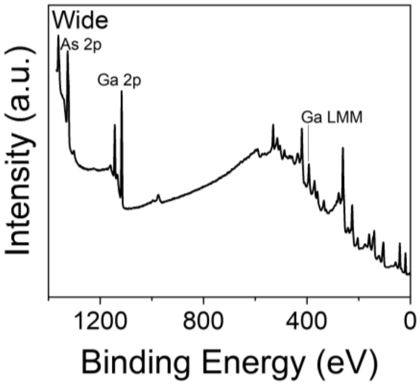

Figure 5.1. XP survey spectrum of GaAs (111)A.

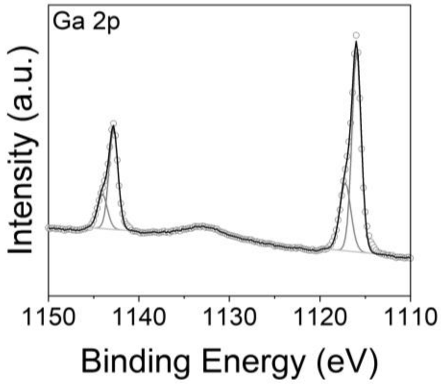

Figure 5.2. Ga 2p core level XP spectrum of GaAs (111)A. The circles are the spectral data, and the solid lines represent the background (light gray), component fits (dark gray), and overall fit (black)

.

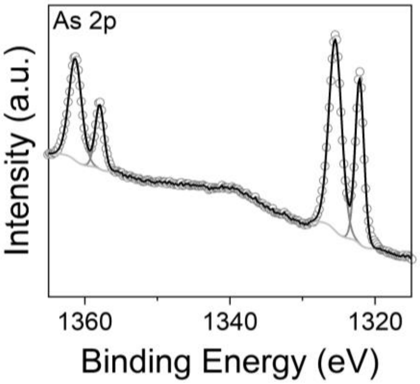

Figure 5.3. As 2p core level XP spectrum of GaAs (111)A. The circles are the spectral data, and the solid lines represent the background (light gray), component fits (dark gray), and overall fit (black).

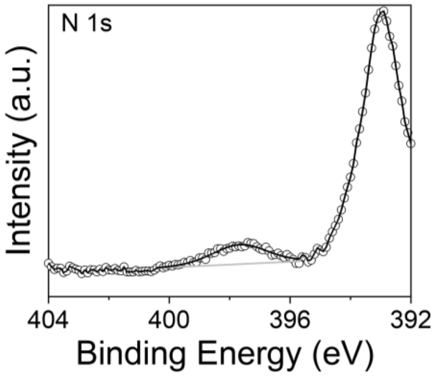

Figure 5.4. N 1s core level XP spectrum of GaAs (111)A. The circles are the spectral data, and the solid lines represent the background (light gray) and overall fit (black).

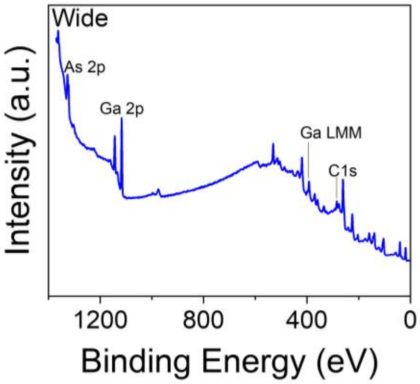

Figure 5.5. XP survey spectrum of PPy|GaAs.

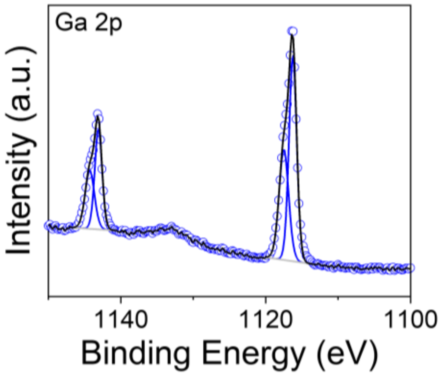

Figure 5.6. Ga 2p core level XP spectrum of PPy|GaAs. The circles are the spectral data, and the solid lines represent the background (light gray), component fits (blue), and overall fit (black).

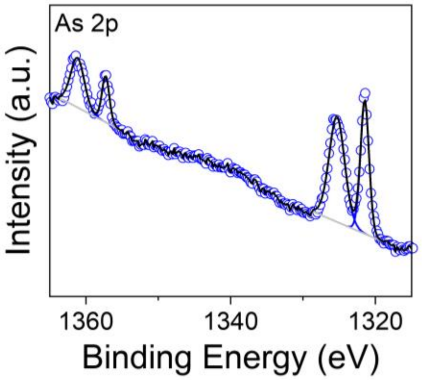

Figure 5.7. As 2p core level XP spectrum of PPy|GaAs. The circles are the spectral data, and the solid lines represent the background (light gray), component fits (blue), and overall fit (black).

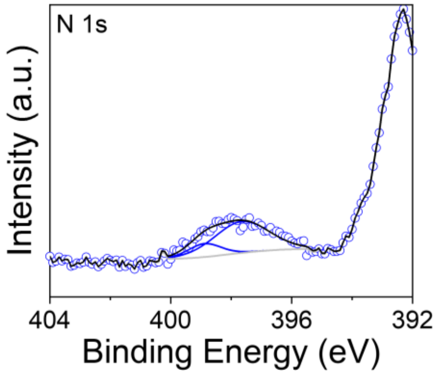

Figure 5.8. N 1s core level XP spectrum of PPy|GaAs. The circles are the spectral data, and the solid lines represent the background (light gray), component fits (blue), and overall fit (black).

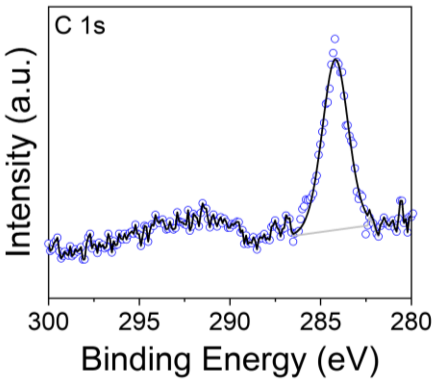

Figure 5.9. C 1s core level XP spectrum of PPy|GaAs. The circles are the spectral data, and the solid lines represent the background (light gray) and overall fit (black).

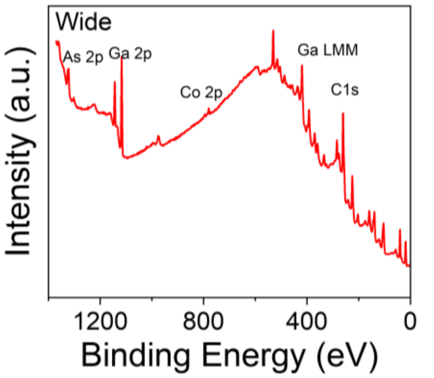

Figure 5.10. XP survey spectrum of cobaloxime|PPy|GaAs.

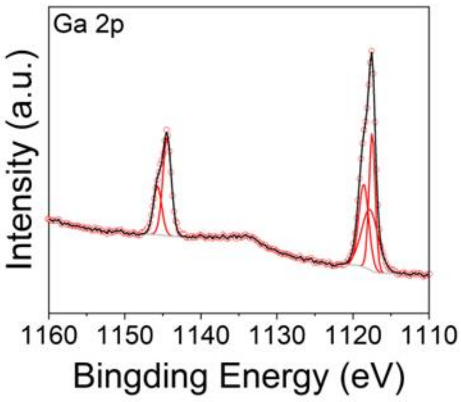

Figure 5.11. Ga 2p core level XP spectrum of cobaloxime|PPy|GaAs. The circles are the spectral data, and the solid lines represent the background (light gray), component fits (red), and overall fit (black).

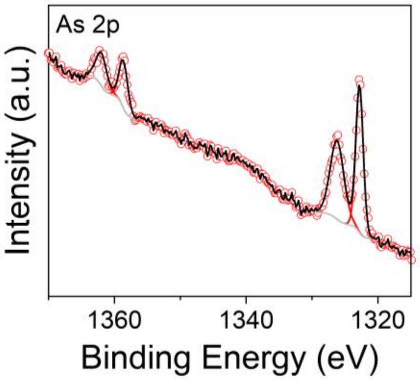

Figure 5.12. As 2p core level XP spectrum of cobaloxime|PPy|GaAs. The circles are the spectral data, and the solid lines represent the background (light gray), component fits (red), and overall fit (black).

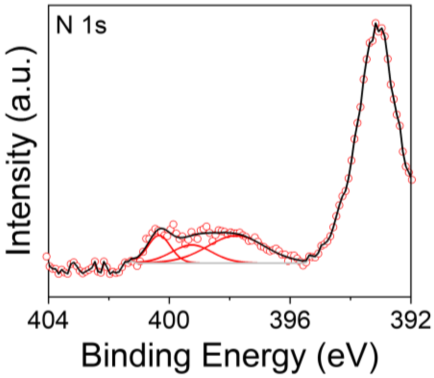

Figure 5.13. N 1s core level XP spectrum of cobaloxime|PPy|GaAs. The circles are the spectral data, and the solid lines represent the background (light gray), component fits (red), and overall fit (black).

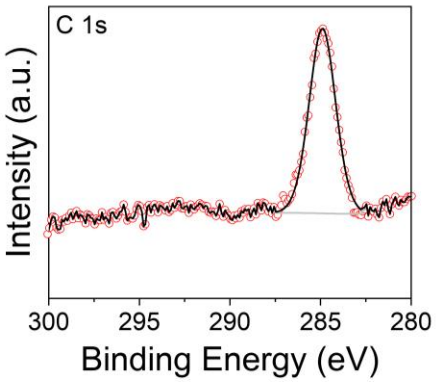

Figure 5.14. C 1s core level XP spectrum of cobaloxime|PPy|GaAs. The circles are the spectral data, and the solid lines represent the background (light gray) and overall fit (black).

5.1.3 Photoelectrochemistry Data

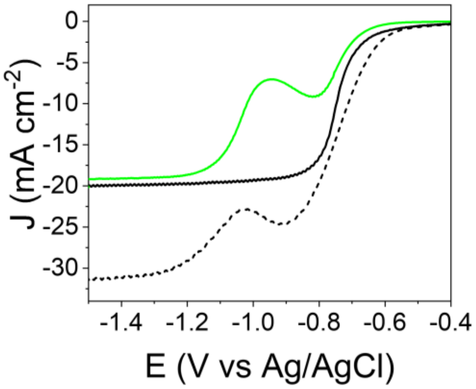

Figure 5.15. Linear sweep voltammograms recorded using cobaloxime|PPy|GaAs working electrodes in pH neutral (0.1 M phosphate buffer) electrolyte solutions under 100 mW cm^{-2} illumination at scan rates of 100 (green) and 1500 (black) mV s^{-1} as well as under 150 mW cm^{-2} illumination at a scan rate of 1500 mV s^{-1} (black dashed).

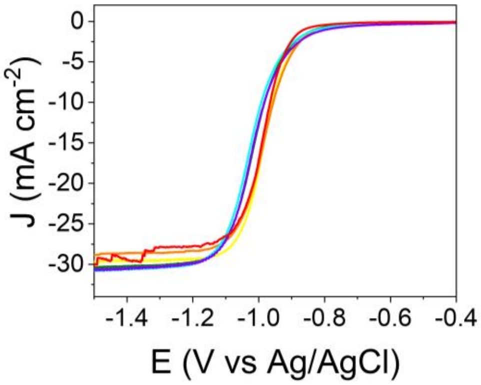

Figure 5.16. Linear sweep voltammograms recorded under 150 mW cm^{-2} illumination using cobaloxime|PPy|GaAs working electrodes in pH 13 (0.1 M NaOH) electrolyte solutions and the following scan rates: 10 (red), 50 (orange), 100 (yellow), 200 (olive), 500 (cyan), and 1000 (violet) mV s^{-1}.

5.1.4 References

(1) Beiler, A. M.; Khusnutdinova, D.; Jacob, S. I.; Moore, G. F. Chemistry at the Interface: Polymer-functionalized GaP Semiconductors for Solar Hydrogen Production. *Ind. Eng. Chem. Res*. **2016**, *55*, 5306−5314.

(2) Beiler, A. M.; Khusnutdinova, D.; Jacob, S. I. and Moore, G. F. Solar Hydrogen Production Using Molecular Catalysts Immobilized on Gallium Phosphide (111)A and (111)B Polymer-Modified Photocathodes. *ACS Appl. Mater. Interfaces* **2016**, *8*, 10038−10047.

5.2 Experimental Methods for Chapter 3

5.2.1 Experimental Methods

Ellipsometry

Samples were measured on a J. A. Woollam M2000 spectroscopic ellipsometer using a spectral range of 193-1690 nm and three different incident angles, 55°, 65°, and 75°. Film thickness (FT) was determined by modeling in CompleteEase using a B-Spline layer to describe the polypyridyl film for all samples. The film thicknesses of the B-Spline layer for different constructs are reported in Section 8 of this Supporting Information file.

Fourier Transform Infrared Spectroscopy

Grazing angle attenuated total reflection Fourier transform infrared (GATR-FTIR) spectroscopy was performed using a VariGATR accessory with a Ge crystal plate (Harrick Scientific) installed in a Vertex 70 Fourier Transform Infrared (FTIR) spectrometer (Bruker). Samples were pressed against the Ge crystal to ensure effective optical coupling. Spectra were collected at 4 cm^{-1} resolution using 256 scans, a dry nitrogen purge, a GloBar MIR source, a broadband KBr beamsplitter, and a liquid nitrogen-cooled MCT detector. Background measurements (also collected using 256 scans) were obtained using the bare Ge crystal, and all data were processed using OPUS software. GATR-FTIRmeasurements were baseline corrected using the rubber band correction method. Spectra of model, homogenous molecular compounds were obtained in a matrix of pressed KBr and collected using 64 scans in transmission mode with a resolution of 1 cm^{-1}.

X-ray Photoelectron Spectroscopy

X-ray photoelectron (XP) spectroscopy was performed using a monochromatized Al Kα source (hν = 1486.6 eV), operated at 63 W, on a Vacuum Generators 220i-XL (Thermo Fisher) system at a takeoff angle of 0° relative to the surface normal and a pass energy for narrow scan spectra of 20 eV, at an instrument resolution of approximately 700 meV. Survey spectra were collected with a pass energy of 150 eV. Spectral fitting was performed using Casa XPS analysis software. Spectral positions were corrected by shifting the primary C 1s core-level position to 284.8 eV, and curves were fit with quasi-Voigt lines following Shirley background subtraction. All N 1s fits were constrained to a full width at half maximum (fwhm) value of less than 1.3 eV. Further details on the characterization of Co|PPy|GaP surfaces via XP spectroscopy are described in Chapter 3.

Photoelectrochemistry

Photoelectrochemical experiments were performed using a 100 W Oriel Solar Simulator equipped with an air mass (AM) 1.5 filter. All voltammetry and controlled-potential electrolysis experiments were performed with a Biologic SP-300 potentiostat using a platinum coil counter electrode and a Ag/AgCl (3M NaCl) reference electrode in a modified cell containing a quartz window. The supporting electrolyte was 0.1 M phosphate buffer (pH 7). The resistance of the solution between the working electrode and the reference electrode (also called the uncompensated resistance, R_u) was determined using the zero internal resistance (ZIR) technique before linear sweep voltammetry and controlled-potential electrolysis experiments, and 85% of the uncompensated resistance was accounted for during the experiments. All voltammetry and controlled-potential electrolysis experiments were performed using a continuous flow of forming gas (5% hydrogen in nitrogen). Open-circuit photovoltages were taken as the voltage at which net zero-current passes during a linear sweep voltammetry experiment.

Gas Chromatography Analysis

Confirmation of hydrogen generation was performed via gas chromatography using an Agilent 490 Micro gas chromatograph equipped with a 5 Å MolSieve column at a temperature of 80 °C and argon as the carrier gas. Gas samples were syringe-injected using 5 mL aliquots of headspace gas collected with a gastight Hamilton syringe from a sealed photoelectrochemical (PEC) cell. Prior to the experiment, the PEC cell was purged for 30 minutes with argon and 5 mL of 99.9% methane was injected into the sealed cell as an internal standard. The retention time of hydrogen was confirmed using a known source of hydrogen obtained from standard lecture bottles containing a hydrogen and nitrogen mixture (100 ppm and 1% hydrogen in nitrogen) (Scotty).

5.2.2 Fourier Transform Infrared Spectroscopy Data

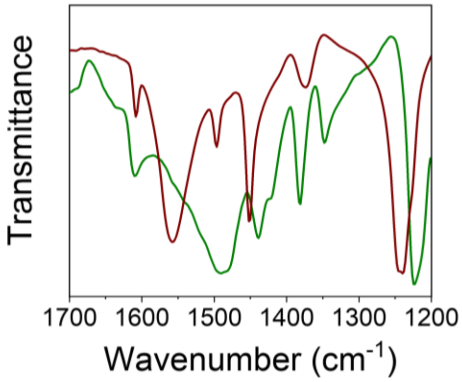

Figure 5.17. FTIR transmission spectra of the precursor complex, Co(dmgH_2)(dmgH)Cl_2, in KBr (green) and the model cobaloxime complex, Co$(dmgH)_2$PyCl, in KBr (red). Transmission spectra of Co$(dmgH)_2$PyCl display a relatively strong transmission band at 1240 cm^{-1} that is assigned to the NO$^-$ stretch of this complex. The frequency of this band is diagnostic of cobaloxime complexes featuring axial coordination to pyridyl nitrogens. For comparison, the NO$^-$ stretch of the precursor complex, Co(dmgH_2)(dmgH)Cl_2, is located at 1225 cm^{-1}.

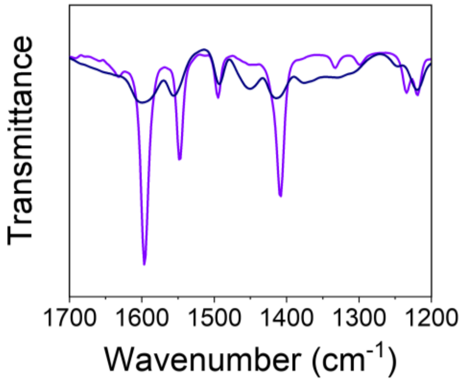

Figure 5.18. FTIR transmission spectra of 4-vinylpyridine in KBr (purple) and polyvinylpyridine in KBr (blue). The absorption bands centered at 1600 cm^{-1} and 1417 cm^{-1} are assigned to C=N and C-N vibrational modes, respectively. The feature observed

at 1453 cm^{-1} in the polyvinylpyridine spectrum (blue) is indicative of the planar deformation vibration of the CH_2 groups along the polymer chain backbone.

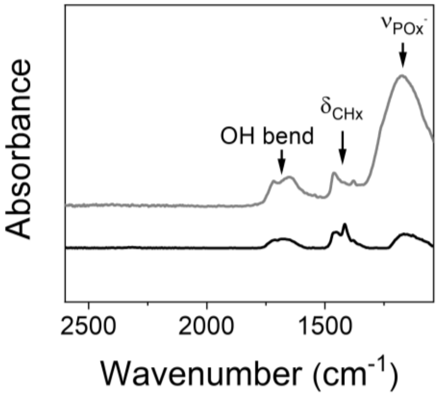

Figure 5.19. GATR-FTIRabsorbance spectra of unmodified GaP before (gray) and after (black) etching with buffered hydrofluoric acid (6:1 HF/NH_4F in H_2O) for five minutes. In this figure, ν and δ denote stretching and deformation (bending) vibrational modes, respectively (figure adapted from reference 1).

5.2.3 X-ray Photoelectron Spectroscopy Data

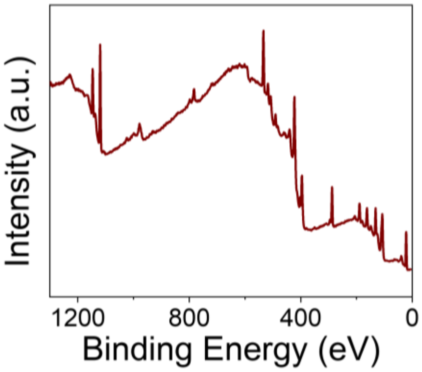

Figure 5.20. XP survey spectrum of an *initial* Co|PPy|GaP sample.

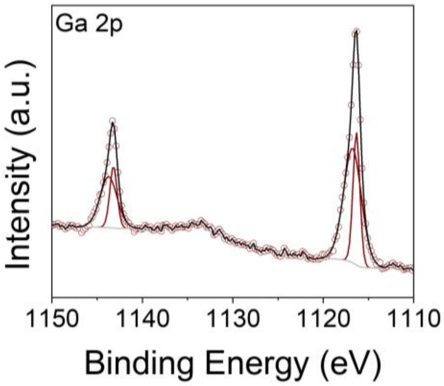

Figure 5.21. Ga 2p core-level XP spectrum of an *initial* Co|PPy|GaP sample. The circles are the spectral data, the solid lines represent the background (light gray), component fit (red), and overall fit (black).

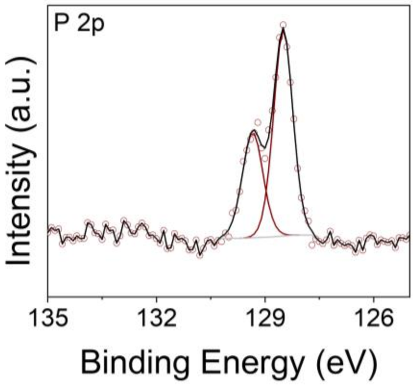

Figure 5.22. P 2p core-level XP spectrum of the of an *initial* Co|PPy|GaP sample collected prior to photoelectrochemical characterization and associated degradation. The circles are the spectral data, and the solid lines represent the background (light gray), component fit (red), and overall fit (black).

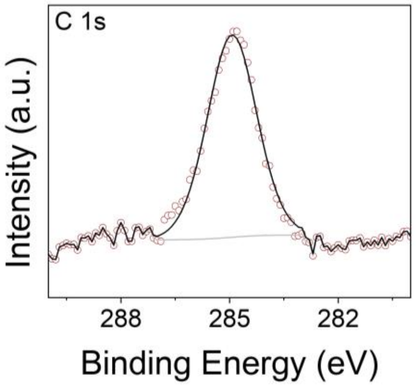

Figure 5.23. C 1s core-level XP spectrum of an *initial* Co|PPy|GaP sample. The circles are the spectral data, and the solid lines represent the background (light gray), and overall fit (black).

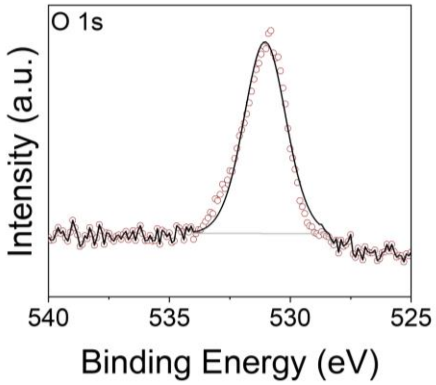

Figure 5.24. O 1s core-level XP spectrum of an *initial* Co|PPy|GaP sample. The circles are the spectral data, and the solid lines represent the background (light gray), and overall fit (black).

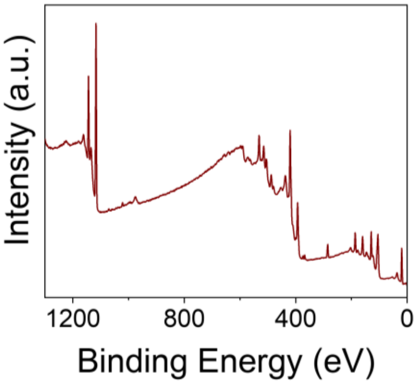

Figure 5.25. XP survey spectrum of a *postdegrade* Co|PPy|GaP sample.

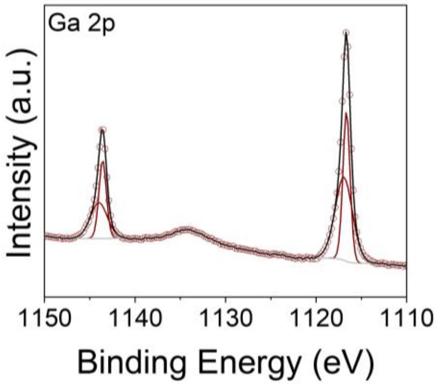

Figure 5.26. Ga 2p core-level XP spectrum of a *postdegrade* Co|PPy|GaP sample. The circles are the spectral data, and the solid lines represent the background (light gray), component fit (red), and overall fit (black).

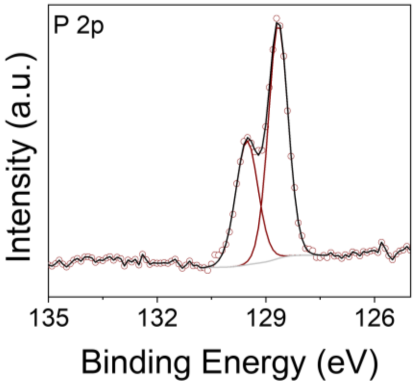

Figure 5.27. P 2p core-level XP spectrum of a *postdegrade* Co|PPy|GaP sample. The circles are the spectral data, and the solid lines represent the background (light gray), component fit (red), and overall fit (black).

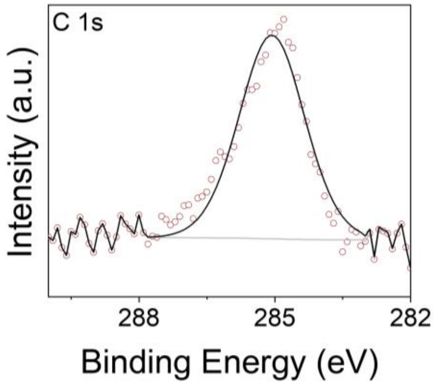

Figure 5.28. C 1s core-level XP spectrum of a *postdegrade* Co|PPy|GaP sample. The circles are the spectral data, and the solid lines represent the background (light gray), and overall fit (black).

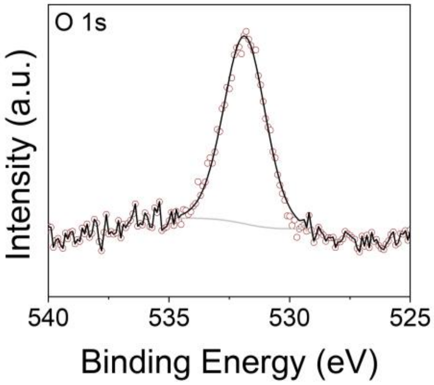

Figure 5.29. O 1s core-level XP spectrum of a *postdegrade* Co|PPy|GaP sample. The circles are the spectral data, and the solid lines represent the background (light gray), and overall fit (black).

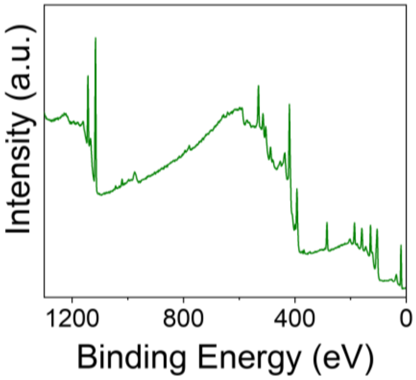

Figure 5.30. XP survey spectrum of a *postrepair* Co|PPy|GaP sample.

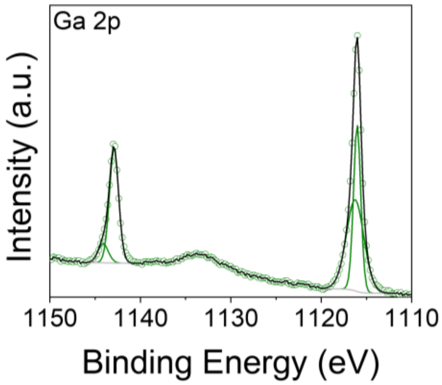

Figure 5.31. Ga 2p core-level XP spectrum of a *postrepair* Co|PPy|GaP sample. The circles are the spectral data, the solid lines represent the background (light gray), component fit (green), and overall fit (black).

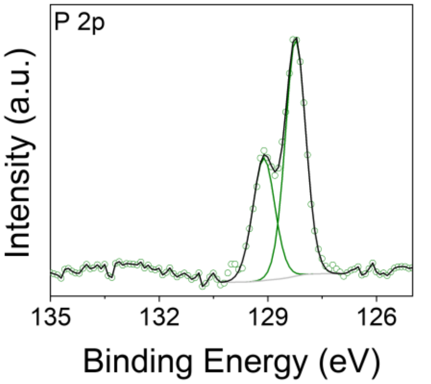

Figure 5.32. P 2p core-level XP spectrum of a *postrepair* Co|PPy|GaP sample. The circles are the spectral data, and the solid lines represent the background (light gray), component fit (green), and overall fit (black).

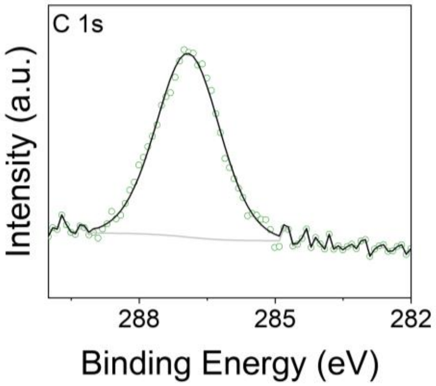

Figure 5.33. C 1s core-level XP spectrum of a *postrepair* Co|PPy|GaP sample. The circles are the spectral data, and the solid lines represent the background (light gray), and overall fit (black).

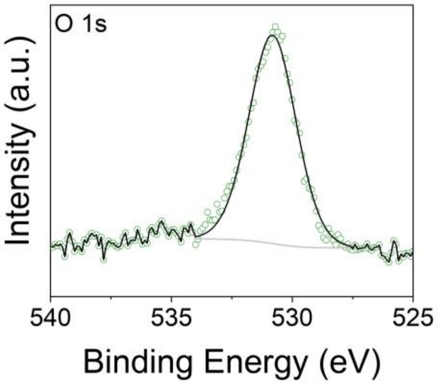

Figure 5.34. O 1s core-level XP spectrum of a *postrepair* Co|PPy|GaP sample. The circles are the spectral data, and the solid lines represent the background (light gray), and overall fit (black).

5.2.4 Photoelectrochemical Data

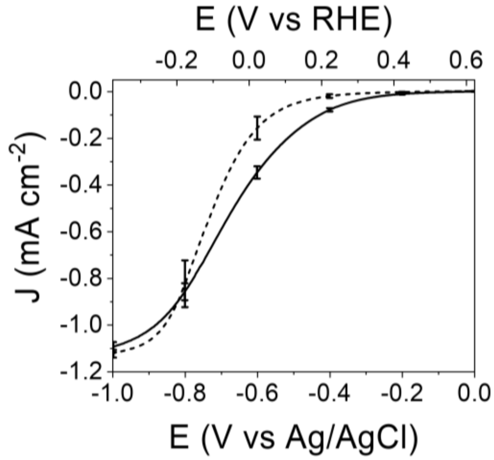

Figure 5.35. Linear sweep voltammograms recorded at a scan rate of 100 mV s^{-1} using unmodified GaP working electrodes prior to (solid) and following (dashed) controlled-potential electrolysis experiments. All data are averages obtained using three separate unmodified GaP working electrodes in 0.1 M phosphate buffer (pH 7) as the electrolyte and 100 mW cm^{-2} illumination conditions.

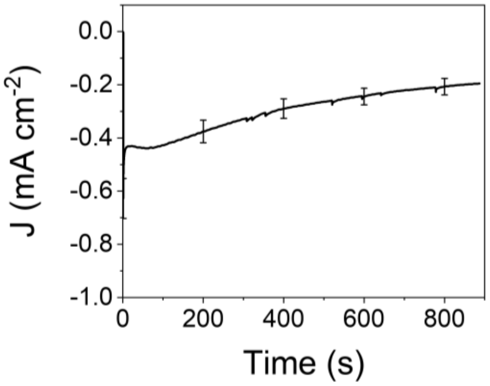

Figure 5.36. Current density versus time plot obtained during 15 minutes of controlled-potential electrolysis at 0 V vs RHE using unmodified GaP working electrodes. All data are averages obtained using three separate unmodified GaP working electrodes in 0.1 M phosphate buffer (pH 7) as the electrolyte and 100 mW cm^{-2} illumination conditions.

Table 5.1. Open-circuit voltages, short-circuit current densities, maximum power points, and fill factors extracted from linear sweep voltammetry data recorded at a scan rate of 100 mV s^{-1} using GaP, PPy|GaP, and Co|PPy|GaP working electrodes in 0.1 M phosphate buffer (pH 7) in the dark.

Construct	Open-Circuit Voltage (V vs RHE)	Short-Circuit Current ($\mu A\ cm^{-2}$)	Maximum Power Point ($\mu W\ cm^{-2}$)	Fill Factor
GaP	0.52 ± 0.02	0.049 ± 0.006	0.019 ± 0.001	0.76 ± 0.09
PPy|GaP	0.56 ± 0.03	0.03 ± 0.02	0.01 ± 0.01	0.5 ± 0.4
Co|PPy|GaP	0.556 ± 0.008	0.048 ± 0.004	0.022 ± 0.002	0.83 ± 0.02

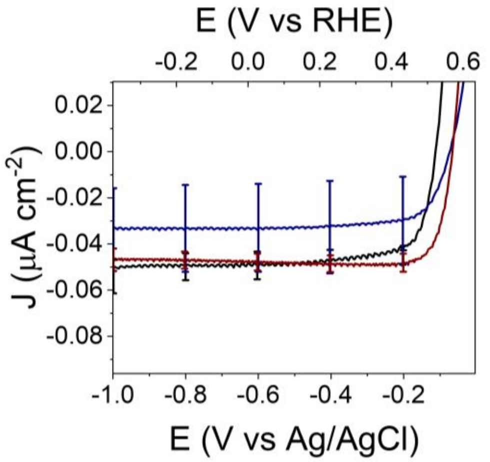

Figure 5.37. Linear sweep voltammograms recorded at a scan rate of 100 mV s^{-1} using GaP (black), PPy|GaP (blue), or Co|PPy|GaP (red) working electrodes in 0.1 M phosphate buffer (pH 7) in the dark. All data are averages obtained using three separately prepared working electrodes.

5.2.5 References

(1) Beiler, A. M.; Khusnutdinova, D.; Wadsworth, B. L.; Moore, G. F. Cobalt Porphyrin–Polypyridyl Surface Coatings for Photoelectrosynthetic Hydrogen Production. *Inorg. Chem.* **2017**, *56*, 12178–12185.

5.3 Experimental Methods for Chapter 4

5.3.1. Experimental Methods

Synthesis

5,10,15,20-tetra-*p*-tolylporphyrin. A similar method was previously reported.[1,2] A solution of 5-(4-methylphenyl)-dipyrromethane (1.417 g, 6 mmol) and *p*-tolyl aldehyde (707 µL, 6 mmol) in chloroform (600 mL) was purged for 15 min with argon before adding $BF_3(OEt)_2$ (792 µL of 2.5 M stock solution in chloroform, final concentration was 3.3 µM). After stirring for 12 h, 2,3-dichloro-5,6-dicyano-1,4-benzoquinone (2.04 g, 9 mmol) was added and the mixture was stirred for an additional 3 h before adding 7.5 mL of triethylamine. The mixture was filtered through an alumina pad and the solvent was evaporated at reduced pressure. The crude product was purified by column chromatography on silica using a mixture of 2:1 chloroform and hexanes as the eluent to yield the desired product (45%). ^1H NMR (400 MHz, $CDCl_3$): δ -2.77 (2H, s, NH), 2.70 (12H, s, CH_3), 7.55 (8H, d, *J* = 7.8 Hz, ArH), 8.09 (8H, d, *J* = 7.8 Hz, ArH) 8.85 (8H, s, βH); MALDI-TOF-MS *m/z* calcd. for $C_{48}H_{38}N_4$ 670.31, obsd. 670.46; UV-Vis (Toluene) 420, 516, 550, 593, 651 nm.

5,10,15,20-tetra-*p*-tolylporphyrin cobalt(II). A similar method was previously reported.[1,3] 5,10,15,20-tetra-*p*- tolylporphyrin (25 mg, 0.03 mmol) and cobalt (II) acetate (53 mg, 0.3 mmol) were dissolved in dimethylformamide (35 mL) and brought to reflux. The mixture was refluxed for 20 min before evaporating the solvent at reduced pressure. The product was purified on an alumina column using dichloromethane as eluent and recrystallized from dichloromethane/methanol to give the desired product (98%). UV-Vis

(Toluene) 416, 530 nm.

CoTTP|PPy|GaP Sample Preparation

The GaP ingot used to prepare the samples described in this report has different physical characteristics (doping density, charge mobility, and resistance (see Experimental Section in the main text for details) than those used to prepare samples described in previous reports from our group.[1,4–8] For the polymer-modified electrodes assembled from these wafers, the polypyridyl coatings are 4 ± 1 nm thick as determined using spectroscopic ellipsometry. X-ray photoelectron spectroscopy and inductively coupled plasma mass spectrometry measurements indicate 25% of the pyridyl sites are coordinated to a cobalt center following the porphyrin attachment chemistry,[4] yielding a per geometric area surface concentration of cobalt of approximately 1 nmol cm^{-2}.

UV-Vis-NIR

Spectra of 5,10,15,20-tetra-*p*-tolylporphyrin cobalt(II)

Aliquots taken from a stock solution of 5,10,15,20-tetra-*p*-tolylporphyrin cobalt(II) (CoTTP) in chloroform (5.5 μM) were diluted with chloroform to prepare solutions at five additional concentrations (0.55 μM, 1.1 μM, 2.2 μM, 3.3 μM and 4.4 μM). Absorption spectra of each solution were collected using a quartz cuvette (pathlength of 1 cm) sealed under air, and associated extinction coefficients were obtained from the slope of a concentration versus absorbance plot. This entire process was repeated using two other CoTTP stock solutions (5.5 μM), and the extinction coefficients were reported as averaged values.

Spectra of 5,10,15,20-tetra-*p*-tolylporphyrin cobalt(II) with ~ 1 Equivalent of Pyridine

A mixture of 5,10,15,20-tetra-*p*-tolylporphyrin cobalt(II) (CoTTP) in chloroform with ~1 equivalent of pyridine per porphyrin was prepared by mixing 2 mL of 9 μM CoTTP in chloroform with 2 mL of 11 μM pyridine in chloroform and adjusting the volume of the mixture to 5 mL in total by adding chloroform. Absorption spectra of this mixture were recorded at varying time intervals (5 min, 1 h, 2h, 7h, 10h, and 12h after the addition of ~1 equivalent of pyridine) using a quartz cuvette (pathlength of 1 cm) sealed under air. The extinction coefficients of the complex formed after 26 hours (assigned as a CoTTP-pyridine-O_2 complex)[9,10] was obtained by multiplying the extinction coefficients determined at selected wavelengths in the absence of pyridine by the ratio of the absorbance values measured at the same selected wavelength prior to and following 26 h after the addition of pyridine. This entire process was repeated two additional times, and the extinction coefficients were reported as averaged values.

5.3.2 Electrochemical data

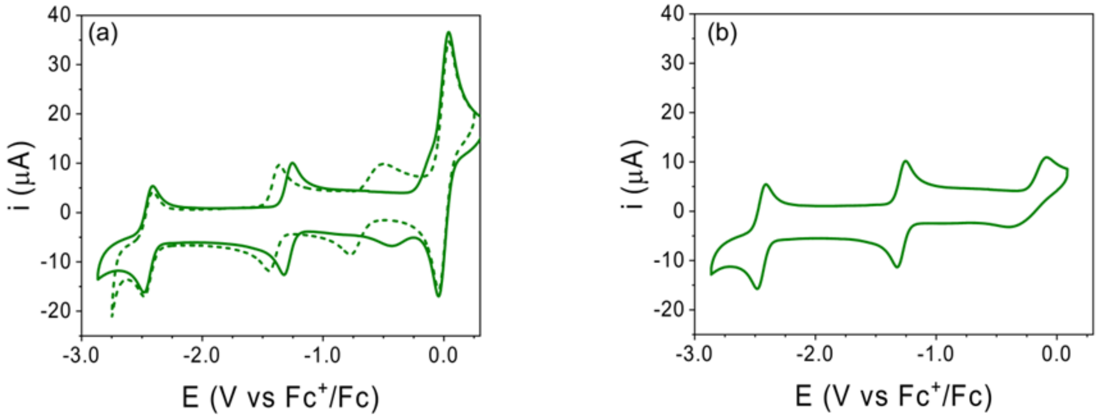

Figure 5.38. (a) Cyclic voltammograms of 5,10,15,20-tetra-*p*-tolylporphyrin cobalt(II) (CoTTP) (0.34 mM) recorded in dimethylformamide containing 0.1 M tetrabutylammonium hexafluorophosphate (TBAPF6) as the supporting electrolyte, ferrocene as an internal standard, and 0 (solid green) or 2,282 (dashed green) equivalents of pyridine. (b) Cyclic voltammogram of CoTTP recorded in dimethylformamide containing 0.1 M TBAPF6 in the absence of ferrocene. This voltammogram is included for comparison given the overlap between the ferrocenium/ferrocene (Fc^+/Fc) redox couple and the redox feature assigned to the $Co^{III/II}$ couple of CoTTP. All voltammograms were collected at room temperature under an argon atmosphere using a 3 mm diameter glassy carbon working electrode and referenced to the ferrocenium/ferrocene redox couple.

Table 5.2. Midpoint potentials for the reduction and oxidation ($^{n}E_{1/2}$) of 5,10,15,20-tetra-*p*-tolylporphyrin cobalt(II) (CoTTP) in the presence of 0 and 2,282 equivalents of pyridine as determined by cyclic voltammetry. Peak-to-peak separations (ΔE_p) are reported in parentheses. For irreversible redox couples, the anodic peak potential ($^{n}E_a$) and/or cathodic peak potential ($^{n}E_c$) is reported. All voltammograms were recorded in dimethylformamide containing 0.1 M TBAPF6 as the supporting electrolyte under argon using a 3 mm diameter glassy carbon working electrode at room temperature and the ferrocenium/ferrocene redox couple as an internal reference.

Complex	**$^{II}E_{1/2}$ (V vs Fc^+/Fc)**	**$^{I}E_{1/2}$ (V vs Fc^+/Fc)**	**$^{i}E_a$ (V vs Fc^+/Fc)**	**$^{i}E_c$ (V vs Fc^+/Fc)**
CoTTP	-2.45 (72)	-1.29(69)	-0.09	-0.40
CoTTP with excess pyridine (2282 equivalents)	-2.45(74)	-1.41(83)	-0.50	-0.77

5.3.3 References

(1) Khusnutdinova, D.; Beiler, A. M.; Wadsworth, B. L.; Jacob, S. I.; Moore, G. F. Metalloporphyrin-Modified Semiconductors for Solar Fuel Production. *Chem. Sci.* **2017**, *8*, 253–259.

(2) Lee, C. H.; Lindsey, J. S. One-Flask Synthesis of Meso-Substituted Dipyrromethanes and Their Application in the Synthesis of Trans-Substituted Porphyrin Building Blocks. *Tetrahedron* **1994**, *50*, 11427–11440.

(3) Chizhova, N. V.; Kumeev, R. S.; Mamardashvili, N. Z. Synthesis and Spectral Properties of Cobalt (II) and Cobalt (III) Tetraarylporphyrinates. *Russ. J. Inorg. Chem.* **2013**, *58*, 740–743.

(4) Beiler, A. M.; Khusnutdinova, D.; Wadsworth, B. L.; Moore, G. F. Cobalt Porphyrin–Polypyridyl Surface Coatings for Photoelectrosynthetic Hydrogen Production. *Inorg. Chem.* **2017**, *56*, 12178–12185.

(5) Krawicz, A.; Yang, J.; Anzenberg, E.; Yano, J.; Sharp, I. D.; Moore, G. F. Photofunctional Construct that Interfaces Molecular Cobalt-Based Catalysts for H_2 Production to a Visible-Light-Absorbing Semiconductor. *J. Am. Chem. Soc.* **2013**, *135*, 11861–11868.

(6) Cedeno, D.; Krawicz, A.; Doak, P.; Yu, M.; Neaton, J. B.; Moore, G. F. Using Molecular Design to Control the Performance of Hydrogen-Producing Polymer-Brush-Modified Photocathodes. *J. Phys. Chem. Lett.* **2014**, *5*, 3222–3226.

(7) Beiler, A. M.; Khusnutdinova, D.; Jacob, S. I.; Moore, G. F. Solar Hydrogen Production Using Molecular Catalysts Immobilized on Gallium Phosphide (111)A and (111)B Polymer-Modified Photocathodes. *ACS Appl. Mater. Interfaces* **2016**, *8*, 10038–

10047.

(8) Beiler, A. M.; Khusnutdinova, D.; Jacob, S. I.; Moore, G. F. Chemistry at the Interface: Polymer-Functionalized GaP Semiconductors for Solar Hydrogen Production. *Ind. Eng. Chem. Res.* **2016**, *55*, 5306–5314.

(9) Walker, F. A. Electron Spin Resonance Study of Coordination to the Fifth and Sixth Positions of α,β,γ,δ-Tetra(p-methoxyphenyl)porphinatocobalt (II). *J. Am. Chem. Soc.* **1970**, *92*, 4235−4244.

(10) Walker, F. A. Reactions of Monomeric Cobalt-Oxygen Complexes. I. Thermodynamics of Reaction of Molecular Oxygen with Five-and Six-Coordinate Amine Complexes of a Cobalt Porphyrin. *J. Am. Chem. Soc.* **1973**, *95*, 1154–1159.

BIBLIOGRAPHY

(1) Hemminger, J.; Fleming, G. R.; Ratner, M. A. Directing Matter and Energy: Five Challenges for Science and the Imagination; U.S. Government Printing Office: Washington, DC, 2007.

(2) Ort, D. R.; Merchant, S. S.; Alric, J.; Barkan, A.; Blankenship, R. E.; Bock, R.; Croce, R.; Hanson, M. R.; Hibberd, J. M.; Long, S. P.; Moore, T. A.; Moroney, J.; Niyogi, K. K.; Parry, M. A. J.; Peralta-Yahya, P. P.; Prince, R. C.; Redding, K. E.; Spalding, M. H.; van Wijk, K. J.; Vermaas, W. F. J.; von Caemmerer, S.; Weber, A. P. M.; Yeates, T. O.; Yuan, J. S.; Zhu, X. G. Redesigning Photosynthesis to Sustainably Meet Global Food and Bioenergy Demand. Proc. *Natl. Acad. Sci*. **2015**, *112* (28), 8529–8536.

(3) Smil, V. Harvesting the Biosphere: The Human Impact. *Popul. Dev. Rev*. **2011**, *37* (4), 613–636.

(4) Ardo, S.; Rivas, D. F.; Modestino, M. A.; Greiving, V. S.; Abdi, F. F.; Llado, E. A.; Artero, V.; Ayers, K.; Battaglia, C.; Becker, J.-P.; Bederak, D.; Berger, A.; Buda, F.; Chinello, E.; Dam, B.; Di Palma, V.; Edvinsson, T.; Fuji, K.; Gardeniers, H.; Geerlings, H.; Hashemi, S. M. H.; Haussener, S.; Houle, F.; Huskens, J.; James, B. D.; Konrad, K.; Kudo, A.; Kunturu, P. P.; Lohse, D.; Mei, B.; Miller, E. L.; Moore, G. F.; Muller, J.; Orchard, K. L.; Rosser, T. E.; Saadi, F. H.; Schüttauf, J.-W.; Seger, B.; Sheehan, S. W.; Smith, W. A.; Spurgeon, J.; Tang, M. H.; van de Krol, R.; Vesborg, P. C. K.; Westerik, P. Pathways to Electrochemical SolarHydrogen Technologies. *Energy Environ. Sci.* **2018**, *11*(10), 2768–2783.

(5) Faunce, T. A.; Lubitz, W.; Rutherford, A. W.; MacFarlane, D.; Moore, G. F.; Yang, P.; Nocera, D. G.; Moore, T. A.; Gregory, D. H.; Fukuzumi, S.; Yoon, K. B.; Armstrong, F. A.; Wasielewski, M. R.; Styring, S. Energy and Environment Policy Case for a Global Project on Artificial Photosynthesis. *Energy Environ. Sci*. **2013**, *6* (3), 695–698.

(6) Faunce, T.; Styring, S.; Wasielewski, M. R.; Brudvig, G. W.; Rutherford, A. W.; Messinger, J.; Lee, A.F.; Hill, C.L.; Degroot, H.; Fontecave, M.;

MacFarlane, D. R.; Hankamer, B.; Nocera, D. G.; Tiede, D. M.; Dau, H.; Hiller, W.; Wang, L.; Amal, R. Artificial Photosynthesis as a Frontier Technology for Energy Sustainability. *Energy Environ. Sci.* **2013,** *6* (4), 1074–1076.

(7) Gray, H. B, Powering the Planet with Solar Fuel. *Nat. Chem*. **2009**, *1*, 7.

(8) Najafpour, M. M.; Barber, J.; Shen, J.-R.; Moore, G. F. Running on Sun. *Chem. World* **2012**, 43.

(9) Hambourger, M.; Moore, G. F.; Kramer, D. M.; Gust, D.; Moore, A. L.; Moore, T. A. Biology and Technology for Photochemical Fuel Production. *Chem. Soc. Rev*. **2009**, *38* (1), 25–35.

(10) Lewis, N. S. Research Opportunities to Advance Solar Energy Utilization. *Science* **2016**, *351* (6271), aad1920.

(11) Blankenship, R. E.; Tiede, D. M.; Barber, J.; Brudvig, G. W.; Fleming, G.; Ghirardi, M.; Gunner, M. R.; Junge, W.; Kramer, D. M.; Melis, A; Moore, T. A.; Moser, C. C.; Nocera, D. G.; Nozik, A. J.; Ort, D. R.; Parson, W. W.; Prince, R. C.; Sayre, R. T. Comparing Photosynthetic and Photovoltaic Efficiencies and Recognizing the Potential for Improvement. *Science* **2011**, *332* (6031), 805–809.

(12) Lewis, N. S., and Nocera, D. G., Powering the planet: Chemical challenges in solar energy utilization, *Proc. Natl. Acad. Sci.* **2006**, *103*, 15729 – 15735.

(13) Ciamician, G. The Photochemistry of the Future. Science 1912, 36, 385−394.

(14) Tran, P. D.; Wong, L. H.; Barber, J.; Loo, J. S. C. Recent Advances in Hybrid Photocatalysts for Solar Fuel Production. *Energy Environ. Sci.* **2012**, *5*, 5902-5918.

(15) Woolerton, T. W.; Sheard, S.; Chaudhary, Y. S.; Armstrong, F. A. Enzymes and Bio-Inspired Electrocatalysts in Solar Fuel Devices. *Energy Environ. Sci*. **2012**, *5* (6), 7470–7490.

(16) Nozik, A. J. Photoelectrochemistry: Applications to Solar Energy Conversion. *Annu. Rev. Phys. Chem*. **1978**, *29* (1), 189–222.

(17) Bard, A. J.; Fox, M. A. Artificial Photosynthesis: Solar Splitting of Water to Hydrogen and Oxygen. *Acc. Chem. Res.* **1995**, *28* (3), 141–145.

(18) Gust, D.; Moore, T. A.; Moore, A. L. Solar Fuels via Artificial Photosynthesis. *Acc. Chem. Res.* **2009**, *42* (12), 1890–1898.

(19) Moore, G. F.; Brudvig, G. W. Energy Conversion in Photosynthesis: A Paradigm for Solar Fuel Production. *Annu. Rev. Condens. Matter Phys*. **2011**, *2* (1), 303– 327.

(20) Modestino, M. A. and Haussener, S. An Integrated Device View on Photo-Electrochemical Solar-Hydrogen Generation. *Annu. Rev. Chem. Biomol. Eng*., **2015**, *6*, 13-34.

(21) Alcala-Torano, R.; Sommer, D. J.; Bahrami Dizicheh, Z.; Ghirlanda, G. Methods in Enzymology, Volume 580: Peptide, Protein and Enzyme Design; Academic Press: Cambridge, **2016**; p 389−416.

(22) Sakimoto, K. K.; Kornienko, N.; Yang, P. Cyborgian Material Design for Solar Fuel Production: The Emerging Photosynthetic Biohybrid Systems. *Acc. Chem. Res.* **2017**, *50*, 476−481.

(23) Berggren, G.; Adamska, A.; Lambertz, C.; Simmons, T. R.; Esselborn, J.; Atta, M.; Gambarelli, S.; Mouesca, J. M.; Reijerse, E.; Lubitz, W.; et al. Biomimetic assembly and activation of [FeFe]-hydrogenases. *Nature* **2013**, *499*, 66−69.

(24) Slater, J. W.; Marguet, S. C.; Monaco, H. A.; Shafaat, H. S. Going beyond Structure: Nickel-Substituted Rubredoxin as a Mechanistic Model for the [NiFe] Hydrogenases. *J. Am. Chem. Soc*. **2018**, *140*, 10250−10262.

(25) Helm, M. L.; Stewart, M. P.; Bullock, R. M.; Dubois, M. R.; Dubois, D. L. A Synthetic Nickel Electrocatalyst with a Turnover Frequency Above 100,000 s−1 for H_2 Production. *Science* **2011**, *333*, 863−866.

(26) Das, A. K.; Engelhard, M. H.; Bullock, R. M.; Roberts, J. A. S. A Hydrogen-Evolving $Ni(P_2N_2)_2$ Electrocatalyst Covalently Attached to a Glassy Carbon Electrode: Preparation, Characterization, and Catalysis. Comparisons with the Homogeneous Analogue. *Inorg. Chem*. **2014**, *53*, 6875−6885.

(27) Leung, J. J.; Warnan, J.; Nam, D. H.; Zhang, J. Z.; Willkomm, J.; Reisner, E. Photoelectrocatalytic H2 evolution in water with molecular catalysts immobilised on p-Si via a stabilising mesoporous TiO_2 interlayer. *Chem. Sci.* **2017**, *8*, 5172−5180.

(28) Reback, M. L.; Ginovska-Pangovska, B.; Ho, M. H.; Jain, A.; Squier, T. C.; Raugei, S.; Roberts, J. A. S.; Shaw, W. J. The Role of a Dipeptide Outer-Coordination Sphere on H_2-Production Catalysts: Influence on Catalytic Rates and Electron Transfer. *Chem. Eur. J.* **2013**, *19*, 1928−1941.

(29) Ginovska-Pangovska, B.; Dutta, A.; Reback, M. L.; Linehan, J. C.; Shaw, W. J. Beyond the Active Site: The Impact of the Outer Coordination Sphere on Electrocatalysts for Hydrogen Production and Oxidation. *Acc. Chem. Res*. **2014**, *47*, 2621−2630.

(30) Gust, D.; Moore, T. A.; Makings, L. R.; Liddell, P. A.; Nemeth, G. A.; Moore, A. L. Photodriven Electron Transfer in Triad Molecules: A Two-Step Charge Recombination Reaction. *J. Am. Chem. Soc*. **1986**, *108*, 8028−8031.

(31) Yang, J.; Yoon, M. C.; Yoo, H.; Kim, P.; Kim, D. Excitation energy transfer in multiporphyrin arrays with cyclic architectures: Towards artificial light-harvesting antenna complexes. *Chem. Soc. Rev*. **2012**, *41*, 4808−4826.

(32) Rudolf, M.; Kirner, S. V.; Guldi, D. M. A multicomponent molecular approach to artificial photosynthesis - the role of fullerenes and endohedral metallofullerenes. *Chem. Soc. Rev*. **2016**, *45*, 612−630.

(33) Kosco, J.; Moruzzi, F.; Willner, B.; McCulloch, I. Photocatalysts Based on Organic Semiconductors with Tunable Energy Levels for Solar Fuel Applications. *Adv. Energy Mater.* **2020**, *10*, 2001935.

(34) Cheng, Y.-Z.; Ding, X.; Han, B.-H. Porous Organic Polymers for Photocatalytic Ca Carbon Dioxide Reduction. *ChemPhotoChem* **2021**,*5*, 406−417.

(35) X.; Fan, K.; Li, F.; Sun, L. Molecular Engineering of Photocathodes based on Polythiophene Organic Semiconductors for Photoelectrochemical Hydrogen Generation. *ACS Appl. Mater. Interfaces* **2021**, *13*, 40602−40611.

(36) Guldi, D. M. Fullerene-porphyrin architectures; photosynthetic antenna and reaction center models. *Chem. Soc. Rev*. **2002**, *31*, 22−36.

(37) Alstrum-Acevedo, J. H.; Brennaman, M. K.; Meyer, T. J. Chemical Approaches to Artificial Photosynthesis. 2. *Inorg. Chem*. **2005**, *44*, 6802−6827.

(38) Memming, R, Semiconductor Electrochemistry, 2nd Ed, *John Wiley & Sons, Incorporated*, **2015**, 169–266.

(39) Alverty, R. A, and Silbey, and R.J. Physical Chemistry, 1st Ed. *Wiley & Sons*, **1992**.

(40) Ramette. R. W., *J. Chem. Edu*. **1987**, *64*, 885.

(41) Osterloh, F. E. Photocatalysis versus Photosynthesis: A Sensitivity Analysis of Devices for Solar Energy Conversion and Chemical Transformations. *ACS Energy Lett*. **2017**, *2*, 445−453.

(42) Walter, M. G.; Warren, E. L.; McKone, J. R.; Boettcher, S. W.; Mi, Q.; Santori, E. A.; Lewis, N. S. Solar Water Splitting Cells. *Chem. Rev*. **2010**, *110*, 6446−6473.

(43) Lewis, N. S. Chemical Control of Charge Transfer and Recombination at Semiconductor Photoelectrode Surfaces. *Inorg. Chem*. **2005**, *44*, 6900−6911.

(44) Peter, L. M. Photocatal. Fundam. Perspect., edited by J. Schneider, D. Bahnemann, J. Ye, G.L. Puma, and D.D. Dionysiou, *Royal Society of Chemistry*, **2016**, 1–28.

(45) Peter, L. M. Energetics and kinetics of light-driven oxygen evolution at semiconductor electrodes: the example of hematite. *J. Solid State Electrochem*. **2013**. *17*, 315-326.

(46) Salvador, P. Semiconductors' photoelectrochemistry: a kinetic and thermodynamic analysis in the light of equilibrium and nonequilibrium models. *J. Phys. Chem. B*. **2001**, *105*, 6128-6141.

(47) Bard, A. J.; Bocarsly, A. B.; Fan, F. R. F.; Walton, E. G.; Wrighton, M. S. The Concept of Fermi Level Pinning at Semiconductor/Liquid Junctions.

Consequences for Energy Conversion Efficiency and Selection of Useful Solution Redox Couples in Solar Devices. *J. Am. Chem. Soc.* **1980**, *102*, 3671–3677.

(48) Gärtner, W. W. Depletion-Layer Photoeffects in Semiconductors. *Phys. Rev.* **1959**, *116*, 84–87.

(49) Reichman, J. The current-voltage characteristics of semiconductor-electrolyte junction photovoltaic cells. *Appl. Phys. Lett*. **1980**, *36*, 574–577.

(50) McConnell, I.; Li, G.; Brudvig, G. W. Energy conversion in natural and artificial photosynthesis. *Chem. Biol.* **2010**, *17*, 434−447.

(51) Nakamura, Y.; Aratani, N.; Osuka, A. Cyclic porphyrin arrays as artificial photosynthetic antenna: synthesis and excitation energy transfer. *Chem. Soc. Rev*. **2007**, *36*, 831−845.

(52) Grätzel, M. Dye-sensitized solar cells. J. Photochem. *Photobiol.C Photochem. Rev*. **2003**, *4*, 145−153.

(53) Xiang, X.; Cao, X.; Sun, W.; Ding, Y. Recent Progress in Visible Light Driven Water Oxidation Using Semiconductors Coupled with Molecular Catalysts. *ChemCatChem* **2019**, *11*, 6190−6202.

(54) Bard, A. J. Photoelectrochemistry and heterogeneous photocatalysis at semiconductors. *J. Photochem*. **1979**, *10*, 59−75.

(55) Garnett, E.; Yang, P. Light Trapping in Silicon Nanowire Solar Cells. *Nano Lett*. **2010**, *10*, 1082−1087.

(56) Liu, C.; Dasgupta, N. P.; Yang, P. Semiconductor Nanowires for Artificial Photosynthesis. *Chem. Mater*. **2014**, *26*, 415−422.

(57) Tumas, B.; Dempsey, J. L.; Mallouk, T. E. Basic Energy Sciences Roundtable on Liquid Solar Fuels; U.S. Department of Energy, **2019**.

(58) Bard, A. J.; Memming, R.; Miller, B. Terminology in semiconductor electrochemistry and photoelectrochemical energy conversion. *Pure Appl. Chem*. **1991**, *63*, 569−596.

(59) Nielander, A. C.; Shaner, M. R.; Papadantonakis, K. M.; Francis, S. A.; Lewis, N. S. A taxonomy for solar fuels generators. *Energy Environ. Sci*. **2015**, *8*, 16−25.

(60) Nozik, A. J. Photochemical diodes. *Appl. Phys. Lett.* **1977**, *30*, 567−569.

(61) Khan, M. A.; Varadhan, P.; Ramalingam, V.; Fu, H.; Idriss, H.; He, J. Importance of Oxygen Measurements during Photoelectrochemical Water-Splitting Reactions. *ACS Energy Lett.* **2019**, *4*, 2712–2718.

(62) Holm, J., Jørgensen, H., Krogstrup, P. *et al.* Surface-passivated GaAsP single-nanowire solar cells exceeding 10% efficiency grown on silicon. *Nat. Commun.* **2013**, *4*, 1–5.

(63) Wang, Y.; Wei, H.; Lv, H.; Chen, Z.; Zhang, J.; Yan, X.; Lee, L.; Wang, Z.M.; Chueh, Y. Highly Stable Three-Dimensional Nickel-Cobalt Hydroxide Hierarchical Heterostructures Hybridized with Carbon Nanotubes for High-Performance Energy Storage Devices. *ACS Nano* **2019**, *13*, 11235–11248.

(64) Manikandan, A.; Lee, L.; Wang, Y.; Chen, C.; Chen, Y.; Medina, H.; Tseng, J.; Wang, Z.M.; Chueh, Y. Graphene-coated copper nanowire networks as a highly stable transparent electrode in harsh environments toward efficient electrocatalytic hydrogen evolution reactions. *J. Mater. Chem. A* **2017**, *5*, 13320–13328.

(65) Vesborg, P. C. K.; Jaramillo, T. F. Addressing the Terawatt Challenge: Scalability in the Supply of Chemical Elements for Renewable Energy. *RSC Adv*. **2012**, *2* (21), 7933–7947.

(66) Chemical Sciences Roundtable. The Role of the Chemical Sciences in Finding Alternatives to Critical Resources: A Workshop Summary. Washington, D.C.: National Academies Press. 2012.

(67) Bacchi, M.; Berggren, G.; Niklas, J.; Veinberg, E.; Mara, M. W.; Shelby, M. L.; Poluektov, O. G.; Chen, L. X.; Tiede, D. M.; Cavazza, C.; Field, M. J.; Fontecave, M.; Artero, V. Cobaloxime-Based Artificial Hydrogenases. *Inorg. Chem*. **2014**, *53* (15), 8071–8082.

(68) Queyriaux, N.; Kaeffer, N.; Morozan, A.; Chavarot-Kerlidou, M.; Artero, V. Molecular Cathode and Photocathode Materials for Hydrogen Evolution in Photoelectrochemical Devices. *J. Photochem. Photobiol. C Photochem. Rev*. **2015**, *25*, 90–105.

(69) Dutta, A.; Ginovska, B.; Raugei, S.; Roberts, J. A. S.; Shaw, W. J. Optimizing Conditions for Utilization of an H_2 Oxidation Catalyst with Outer Coordination Sphere Functionalities. *Dalt. Trans.* **2016**, *45* (24), 9786–9793.

(70) Maher, A. G.; Passard, G.; Dogutan, D. K.; Halbach, R. L.; Anderson, B. L.; Gagliardi, C. J.; Taniguchi, M.; Lindsey, J. S.; Nocera, D. G. Hydrogen Evolution Catalysis by a Sparsely Substituted Cobalt Chlorin. *ACS Catal.* **2017**, *7*(5), 3597– 3606.

(71) Tsay, C.; Yang, J. Y. Electrocatalytic Hydrogen Evolution under Acidic Aqueous Conditions and Mechanistic Studies of a Highly Stable Molecular Catalyst. *J. Am. Chem. Soc.* **2016**, *138* (43), 14174–14177.

(72) Wiese, S.; Kilgore, U. J.; Ho, M.-H.; Raugei, S.; DuBois, D. L.; Bullock, R. M.; Helm, M. L. Hydrogen Production Using Nickel Electrocatalysts with Pendant Amines: Ligand Effects on Rates and Overpotentials. *ACS Catal*. **2013**, *3* (11), 2527–2535.

(73) Artero, V.; Saveant, J.-M. Toward the Rational Benchmarking of Homogeneous H2-Evolving Catalysts. *Energy Environ. Sci.* **2014**, *7* (11), 3808–3814.

(74) Costentin, C.; Savéant, J.-M. Multielectron, Multistep Molecular Catalysis of Electrochemical Reactions: Benchmarking of Homogeneous Catalysts. *ChemElectroChem* **2014**, *1* (7), 1226–1236.

(75) Khusnutdinova, D.; Wadsworth, B. L.; Flores, M.; Beiler, A. M.; Reyes Cruz, E. A.; Zenkov, Y.; Moore, G. F. Electrocatalytic Properties of Binuclear Cu(II) Fused Porphyrins for Hydrogen Evolution. *ACS Catal*. **2018**, *8* (10), 9888–9898.

(76) Roberts, E. M.; Koski, W. S. An Electron Spin Resonance Study of Copper Etioporphyrin II1. *J. Am. Chem. Soc*. **1960**, *82* (12), 3006–3010.

(77) Blumberg, W. E.; Peisach, J. An Electron Spin Resonance Study of Copper Uroporphyrin III and Other Touraco Feather Components. *J. Biol. Chem*. **1965**, *240* (2), 870–876.

(78) Dempsey, J. L.; Brunschwig, B. S.; Winkler, J. R.; Gray, H. B. Hydrogen Evolution Catalyzed by Cobaloximes, *Acc. Chem. Res*. **2009**, *42*, 1995–2004.

(79) Krawicz, A.; Yang, J.; Anzenberg, E.; Yano, J.; Sharp, I. D.; Moore, G. F. Photofunctional Construct That Interfaces Molecular Cobalt-Based Catalysts for H2 Production to a Visible-Light-Absorbing Semiconductor. *J. Am. Chem. Soc*. **2013**, *135*, 11861−11868.

(80) Cedeno, D.; Krawicz, A.; Doak, P.; Yu, M.; Neaton, J. B.; Moore, G. F. A Noble-Metal-Free Hydrogen Evolution Catalyst Grafted to Visible Light-Absorbing Semiconductors. *J. Phys. Chem. Lett*. **2014**, *5*, 3222−3226.

(81) Beiler, A. M.; Khusnutdinova, D.; Jacob, S. I.; Moore, G. F. Solar Hydrogen Production Using Molecular Catalysts Immobilized on Gallium Phosphide (111)A and (111)B Polymer-Modified Photocathodes. *ACS Appl. Mater. Interfaces* **2016**, *8*, 10038−10047.

(82) Beiler, A. M.; Khusnutdinova, D.; Jacob, S. I.; Moore, G. F. Chemistry at the Interface: Polymer-Functionalized GaP Semiconductors for Solar Hydrogen Production. *Ind. Eng. Chem. Res.* **2016**, *55*, 5306−5314.

(83) Nguyen, N. P.; Wadsworth, B. L.; Nishiori, D.; Reyes Cruz, E. A.; Moore, G. F. Understanding and Controlling the Performance- Limiting Steps of Catalyst-Modified Semiconductors. *J. Phys. Chem. Lett*. **2021**, *12*, 199−203.

(84) Trogler, W.; Stewart, R. C; Epps, L. A.; Marzilli, L. G. Cis and Trans Effects on the Proton Magnetic Resonance Spectra of Cobaloxime. *Inorg Chem*. **1974**, *13*, 1564−1570.

(85) Costa, G.; Tauzher, G.; Puxeddu, A. Mechanism of Formation of trans-Chloro-Bisdimethylglyoximato-Tertiary Phosphine Cobalt(III) Complexes and Their Isomers 1:1 Electrolytes. *Inorg. Chim. Acta* **1969**, *3*, 45−48.

(86) Chuang, T. J.; Brundle, C. R.; Rice, D. W. Interpretation of the X-ray Photoemission Spectra of Cobalt Oxides and Cobalt Oxide Surfaces. *Surf. Sci.* **1976**, *59*, 413−429.

(87) Dillard, J. G.; Schenck, C. V.; Koppelman, M. H. Surface Chemistry of Cobalt in Calcined Cobalt-Kaolinite Materials. *Clays Clay Miner*. **1983**, *31*, 69−72.

(88) Beiler, A. M.; Khusnutdinova, D.; Wadsworth, B. L.; Moore, G. F. Cobalt Porphyrin-Polypyridyl Surface Coatings for Photoelectrosynthetic Hydrogen Production. *Inorg. Chem.* **2017**, *56*, 12178−12185.

(89) Wadsworth, B. L.; Beiler, A. M.; Khusnutdinova, D.; Reyes Cruz, E. A.; Moore, G. F. Interplay between Light Flux, Quantum Efficiency, and Turnover Frequency in Molecular-Modified Photoelectrosynthetic Assemblies. *J. Am. Chem. Soc.* **2019**, *141*, 15932−15941.

(90) Santangelo, P. G.; Miskelly, G. M.; Lewis, N. S. Voltammetry of Semiconductor Electrodes. 2. Cyclic Voltammetry of Freely Diffusing Redox Species and Rotating Semiconductor Disk Voltammetry. *J. Phys. Chem*. **1989**, *93*, 6128–6136.

(91) Gerischer, H.; Muller, N. On the Mechanism of Hydrogen Evolution at GaAs Electrodes. *J. Electroanal. Chem*. **1981**, *119*, 41–48.

(92) IUPAC. Compendium of Chemical Terminology, 2nd ed. (the "Gold Book"). Compiled by A. D. McNaught and A. Wilkinson. Blackwell Scientific Publications, Oxford (1997). Online version (2019) created by S. J. Chalk. ISBN 0-9678550-9-8. hTTPs://doi.org/10.1351/goldbook.

(93) Bard, A. J.; Faulkner, L. R. Chapter 6: Potential Sweep Methods, In Electrochemical Methods: Fundamentals and Applications, 2nd ed., John Wiley & Sons, New York, 2001.

(94) Gu, J.; Yan, Y.; Young, J. L.; Steirer K. X.; Neale, N. R.; Turner, J. A. Water Reduction by a p-GaInP$_2$ Photoelectrode Stabilized by an Amorphous TiO$_2$ Coating and a Molecular Cobalt Catalyst. *Nat. Mater*. **2016**, *15*, 456–460.

(95) Zhao, Y.; Anderson, N. C.; Ratzloff, M. W.; Mulder, D. W.; Zhu, K.; Turner, J. A.; Neale, N. R.; King, P. W.; Branz, H. M. Proton Reduction Using a Hydrogenase-Modified Nanoporous Black Silicon Photoelectrode. *ACS Appl. Mater. Interfaces* **2016**, *8*, 14481–14487.

(96) Wadsworth, B. L.; Khusnutdinova, D.; Moore, G. F. Polymeric coatings for applications in electrocatalytic and photoelectrosynthetic fuel production. *J. Mater. Chem. A*, **2018**, *6*, 21654–2166.

(97) Reyes Cruz, E. A.; Nishiori, D.; Wadsworth, B. L.; Nguyen, N. P.; Hensleigh, L. K.; Khusnutdinova, D.; Beiler, A. M.; Moore, G. F. Molecular-Modified Photocathodes for Applications in Artificial Photosynthesis and Solar-to-Fuel Technologies. *Chem. Rev.*, **2022**, 16051–16109.

(98) Connolly, P.; Espenson, J. H. Cobalt-catalyzed evolution of molecular hydrogen. *Inorg. Chem.*, **1986**, *25*, 2684−2688.

(99) Razavet, M.; Artero, V.; Fontecave, M. Proton Electroreduction Catalyzed by Cobaloximes: Functional Models for Hydrogenases. *Inorg. Chem.*, **2005**, *44*, 4786−4795.

(100) Hu, X. L.; Cossairt, B. M.; Brunschwig, B. S.; Lewis N. S.; Peters, J. C. Electrocatalytic hydrogen evolution by cobalt difluoroboryl-diglyoximate complexes. *Chem. Commun.*, **2005**, *37*, 4723−4725.

(101) Wadsworth, B. L.; Beiler, A. M.; Khusnutdinova, D.; Jacob, S. I.; Moore, G. F. Electrocatalytic and Optical Properties of Cobaloxime Catalysts Immobilized at a Surface-Grafted Polymer Interface. *ACS Catal.*, **2016**, *6*, 8048−8057.

(102) Khusnutdinova, D.; Beiler, A. M.; Wadsworth, B. L.; Jacob, S. I.; Moore, G. F. Metalloporphyrin-modified semiconductors for solar fuel production. *Chem. Sci.*, **2016**, *8*, 253–259.

(103) Nishiori, D.; Wadsworth, B. L.; Reyes Cruz, E. A.; Nguyen, N. P.; Hensleigh, L. K.; Karcher, T.; Moore, G. F. Photoelectrochemistry of metalloporphyrin-modified GaP semiconductors *Photosynth Res*, **2021**, *151*, 1-10.

(104) Wadsworth, B. L.; Khusnutdinova, D.; Urbine, J. M.; Reyes, A. S.; Moore, G. F. Expanding the Redox Range of Surface-Immobilized Metallocomplexes Using Molecular Interfaces. *ACS Appl. Mater. Interfaces*, **2020**, *12*, 3903–3911.

(105) Wadsworth, B. L.; Nishiori, D.; Nguyen, N. P.; Reyes Cruz, E. A.; Moore, G. F. Electrochemistry of Polymeric Cobaloxime-Containing Assemblies in Organic and Aqueous Solvents. *ECS J. Solid State Sci. Technol.*, **2020**, *9*, 061018.

(106) Steenackers, M.; Küller, A.; Stoycheva, S.; Grunze M.; Jordan, R. Structured and Gradient Polymer Brushes from Biphenylthiol Self-Assembled Monolayers by Self-Initiated Photografting and Photopolymerization (SIPGP). *Langmuir*, **2009**, *25*, 2225–2231.

(107) Wang, X.; Ruther, R. E.; Streifer, J. A.; Hamers, R. J. UV-Induced Grafting of Alkenes to Silicon Surfaces: Photoemission versus Excitons. *J. Am. Chem. Soc.*, **2010**, *132*, 4048–4049.

(108) Seifert, M.; Koch, A. H. R.; Deubel, F.; Simmet, T.; Hess, L. H.; Stutzmann, M.; Jordan, R.; Garrido, J. A.; Sharp, I. D. Functional Polymer Brushes on Hydrogenated Graphene. *Chem. Mater.*, **2013**, *25*, 466–470.

(109) Moore, G. F.; Sharp, I. D. A Noble-Metal-Free Hydrogen Evolution Catalyst Grafted to Visible Light-Absorbing Semiconductors. *J. Phys. Chem. Lett.*, **2013,** *4*, 568–572.

(110) Yamazaki, N.; Hohokabe, Y. Studies on Cobaloxime Compounds. I. Synthesis of Various Cobaloximes and Investigation on Their Infrared and Far-Infrared Spectra. *Bull. Chem. Soc. Jpn.*, **1971**, *44,* 63–69.

(111) Muckerman, J. T.; Fujita, E. Theoretical studies of the mechanism of catalytic hydrogen production by a cobaloxime. *Chem. Commun.*, **2011**, *47*, 12456–12458.

(112) Veldkamp, B. S.; Han, W. S.; Dyar, S. M.; Eaton, S. W.; Ratner, M. A.; Wasielewski, M. R. Photoinitiated multi-step charge separation and ultrafast

charge transfer induced dissociation in a pyridyl-linked photosensitizer–cobaloxime assembly. *Energy Environ. Sci.*, **2013**, *6*, 1917–1928.

(113) Nishiori, D.; Wadsworth, B. L.; Moore, G. F. Parallels between enzyme catalysis, electrocatalysis, and photoelectrosynthesis. *Chem Catal*., **2021**, *1*, 978–996.

(114) McKone, J. R.; Marinescu, S. C.; Brunschwig, B. S.; Winkler, J. R.; Gray, H. B. Earth-Abundant Hydrogen Evolution Electrocatalysts. *Chem. Sci.* 2**014**, *5*, 865–878.

(115) Ye, R.; Zhao, J.; Wickemeyer, B. B.; Toste, F. D.; Somorjai, G. A. Foundations and Strategies of the Construction of Hybrid Catalysts for Optimized Performances. *Nat. Catal.* **2018**, *1*, 318–325.

(116) Bullock, R. M.; Das, A. K.; Appel, A. M. Surface Immobilization of Molecular Electrocatalysts for Energy Conversion. *Chem. – Eur. J.* **2017**, *23*, 7626–7641.

(117) Ladomenou, K.; Natali, M.; Iengo, E.; Charalampidis, G.; Scandola, F.; Coutsolelos, A. G. Photochemical Hydrogen Generation with Porphyrin-Based Systems. *Coord. Chem. Rev.* **2015**, *304*, 38–54.

(118) Costentin, C.; Robert, M.; Savéant, J. M. Current Issues in Molecular Catalysis Illustrated by Iron Porphyrins as Catalysts of the CO_2-to-CO Electrochemical Conversion. *Acc. Chem. Res.* **2015**, *48*, 2996–3006.

(119) Manbeck, G. F.; Fujita, E. A Review of Iron and Cobalt Porphyrins, Phthalocyanines and Related Complexes for Electrochemical and Photochemical Reduction of Carbon Dioxide. *J. Porphyrins Phthalocyanines* **2015**, *19*, 45–64.

(120) Morris, A. J.; Meyer, G. J.; Fujita, E. Molecular Approaches to the Photocatalytic Reduction of Carbon Dioxide for Solar Fuels. *Acc. Chem. Res.* **2009**, *42*, 1983–1994.

(121) Losse, S.; Vos, J. G.; Rau, S. Catalytic Hydrogen Production at Cobalt Centres. *Coord. Chem. Rev.* **2010**, *254*, 2492–2504.

(122) Collin, J. P.; Sauvage, J. P. Electrochemical Reduction of Carbon Dioxide Mediated by Molecular Catalysts. *Coord. Chem. Rev.* 1989, *93*, 245–268.

(123) Dalle, K. E.; Warnan, J.; Leung, J. J.; Reuillard, B.; Karmel, I. S.; Reisner, E. Electro-and Solar-Driven Fuel Synthesis with First Row Transition Metal Complexes. *Chem. Rev.* **2019**, *119*, 2752–2875.

(124) Zhang, B.; Sun, L. Artificial Photosynthesis: Opportunities and Challenges of Molecular Catalysts. *Chem. Soc. Rev.* **2019**, *48*, 2216–2264.

(125) Morikawa, T.; Sato, S.; Sekizawa, K.; Arai, T.; Suzuki, T. M. Molecular Catalysts Immobilized on Semiconductor Photosensitizers for Proton Reduction toward Visible-Light-Driven Overall Water Splitting. *ChemSusChem* **2019**, *12*, 1807–1824.

(126) Auwärter, W.; Écija, D.; Klappenberger, F.; Barth, J. V. Porphyrins at Interfaces. *Nat. Chem.* **2015**, *7*, 105–120.

(127) Lindsey, J. S.; Bocian, D. F. Molecules for Charge-Based Information Storage. *Acc. Chem. Res.* **2011**, *44*, 638–650.

(128) Swierk, J. R.; Méndez-Hernández, D. D.; McCool, N. S.; Liddell, P.; Terazono, Y.; Pahk, I.; Tomlin, J. J.; Oster, N. V.; Moore, T. A.; Moore, A. L.; Gust, D. Metal-Free Organic Sensitizers for Use in Water-Splitting Dye-Sensitized Photoelectrochemical Cells. *Proc. Nat. Acad. Sci.* **2015**, *112*, 1681–1686.

(129) Higashino, T.; Imahori, H. Porphyrins as Excellent Dyes for Dye-Sensitized Solar Cells: Recent Developments and Insights. *Dalton Trans.* **2015**, *44*, 448–463.

(130) Mathew, S.; Yella, A.; Gao, P.; Humphry-Baker, R.; Curchod, B.F.; Ashari-Astani, N.; Tavernelli, I.; Rothlisberger, U.; Nazeeruddin, M. K.; Grätzel, M. Dye-Sensitized Solar Cells with 13% Efficiency Achieved through the Molecular Engineering of Porphyrin Sensitizers. *Nat. Chem.* **2014**, *6*, 242–247.

(131) Walter, M. G.; Rudine, A. B.; Wamser, C. C. Porphyrins and Phthalocyanines in Solar Photovoltaic Cells. *J. Porphyrins Phthalocyanines* 2010, *14*, 759–792.

(132) Li, L. L.; Diau, E. W. G. Porphyrin-Sensitized Solar Cells. *Chem. Soc. Rev.* **2013**, *42*, 291–304.

(133) Standing, A.; Assali, S.; Gao, L.; VeRHEijen, M. A.; Van Dam, D.; Cui, Y.; Notten, P. H.; Haverkort, J. E.; Bakkers, E. P. Efficient Water Reduction with Gallium Phosphide Nanowires. *Nat. Commun.* **2015**, *6*, 7824.

(134) Liu, C.; Sun, J.; Tang, J.; Yang, P. Zn-Doped p-Type Gallium Phosphide Nanowire Photocathodes from a Surfactant-Free Solution Synthesis. *Nano Lett.* **2012**, *12*, 5407–5411.

(135) Barton, E. E.; Rampulla, D. M.; Bocarsly, A. B. Selective Solar-Driven

Reduction of CO_2 to Methanol Using a Catalyzed p-GaP Based Photoelectrochemical Cell. *J. Am. Chem. Soc.* **2008**, *130*, 6342–6344.

(136) Grätzel, M. Photoelectrochemical Cells. *Nature* **2001**, *414*, 338–344.

(137) Butler, M. A.; Ginley, D. S. P-Type GaP as a Semiconducting Photoelectrode. *J. Electrochem. Soc.* **1980**, *127*, 1273–1278.

(138) Halmann, M. Photoelectrochemical Reduction of Aqueous Carbon Dioxide on p-Type Gallium Phosphide in Liquid Junction Solar Cells. *Nature* **1978**, *275*, 115–116.

(139) Tomkiewicz, M.; Woodall, J. M. Photoassisted Electrolysis of Water by Visible Irradiation of a p-Type Gallium Phosphide Electrode. *Science* **1977**, *196*, 990–991.

(140) Bockris, J. M.; Uosaki, K. The Rate of the Photoelectrochemical Generation of Hydrogen at p-Type Semiconductors. *J. Electrochem. Soc.* **1977**, *124*, 1348–1355.

(141) Gleria, M.; Memming, R. Charge Transfer Processes at Large Band Gap Semiconductor Electrodes: Reactions at SiC-Electrodes. *J. Electroanal. Chem.* **1975**, *65*, 163–175.

(142) Memming, R.; Schwandt, G. Electrochemical Properties of Gallium Phosphide in Aqueous Solutions. *Electrochim. Acta* **1968**, *13*, 1299–1310.

(143) Trotochaud, L.; Mills, T. J.; Boettcher, S. W. An Optocatalytic Model for Semiconductor–Catalyst Water-Splitting Photoelectrodes Based on in situ Optical Measurements on Operational Catalysts. *J. Phys. Chem. Lett.* **2013**, *4*, 931–935.

(144) Kempler, P. A.; Gonzalez, M. A.; Papadantonakis, K. M.; Lewis, N. S. Hydrogen Evolution with Minimal Parasitic Light Absorption by Dense Co–P Catalyst Films on Structured p-Si Photocathodes. *ACS Energy Lett.* **2018**, *3*, 612–617.

(145) Chen, H. Y.; Ardo, S. Direct Observation of Sequential Oxidations of a Titania-Bound Molecular Proxy Catalyst Generated Through Illumination of Molecular Sensitizers. *Nat. Chem.* **2018**, *10*, 17–23.

(146) Beiler, A. M.; Moore, G. F. Multi-Electron Transfer Photochemistry: Caught in the Act. *Nat. Chem.* **2018**, *10*, 3–4.

(147) Willkomm, J.; Orchard, K. L.; Reynal, A.; Pastor, E.; Durrant, J. R.; Reisner, E. Dye-Sensitised Semiconductors Modified with Molecular Catalysts for

Light-Driven H_2 Production. *Chem. Soc. Rev.* **2016**, *45*, 9–23.

(148) Ashford, D. L.; Gish, M. K.; Vannucci, A. K.; Brennaman, M. K.; Templeton, J. L.; Papanikolas, J. M.; Meyer, T. J. Molecular Chromophore–Catalyst Assemblies for Solar Fuel Applications. *Chem. Rev.* **2015**, *115*, 13006–13049.

(149) Brennaman, M. K.; Dillon, R. J.; Alibabaei, L.; Gish, M. K.; Dares, C. J.; Ashford, D. L.; House, R. L.; Meyer, G. J.; Papanikolas, J. M.; Meyer, T. J. Finding the Way to Solar Fuels with Dye-Sensitized Photoelectrosynthesis Cells. *J. Am. Chem. Soc.* **2016**, *138*, 13085–13102.

(150) Ilic, S.; Brown, E. S.; Xie, Y.; Maldonado, S.; Glusac, K. D. Sensitization of p-GaP with Monocationic Dyes: The Effect of Dye Excited-State Lifetime on Hole Injection Efficiencies. *J. Phys. Chem. C* **2016**, *120*, 3145–3155.

(151) Memming, R.; Tributsch, H. Electrochemical Investigations on the Spectral Sensitization of Gallium Phosphide Electrodes. *J. Phys. Chem.* **1971**, *75*, 562–570.

(152) Hammarström, L. Accumulative Charge Separation for Solar Fuels Production: Coupling Light-Induced Single Electron Transfer to Multielectron Catalysis. *Acc. Chem. Res.* **2015**, *48*, 840–850.

(153) Lee, C. H.; Lindsey, J. S. One-Flask Synthesis of Meso-Substituted Dipyrromethanes and Their Application in the Synthesis of Trans-Substituted Porphyrin Building Blocks. *Tetrahedron* **1994**, *50*, 11427–11440.

(154) Chizhova, N. V.; Kumeev, R. S.; Mamardashvili, N. Z. Synthesis and Spectral Properties of Cobalt (II) and Cobalt (III) Tetraarylporphyrinates. *Russ. J. Inorg. Chem*. **2013**, *58*, 740–743.

(155) Chen, Z.; Jaramillo, T. F.; Deutsch, T. G.; Kleiman-Shwarsctein, A.; Forman, A. J.; Gaillard, N.; Garland, R.; Takanabe, K.; Heske, C.; Sunkara, M.; McFarland, E. W. Accelerating Materials Development for Photoelectrochemical Hydrogen Production: Standards for Methods, Definitions, and Reporting Protocols. *J. Mater. Res.* 2010, *25*, 3–16.

(156) Döscher, H.; Young, J. L.; Geisz, J. F.; Turner, J. A.; Deutsch, T. G. Solar-to-Hydrogen Efficiency: Shining Light on Photoelectrochemical Device Performance. *Energy Environ. Sci.* 2016, *9*, 74–80.

(157) Lacey, S. D. The Absorption Coefficient of Gallium Phosphide in the Wavelength Region 530 to 1100 nm. *Solid State Commun.* 1970, *8*, 1115–1118.

(158) At the time of writing, the air-mass 1.5 global tilt (AM 1.5G) spectrum from the ASTM G-173-03 data set is available online at

hTTPs://www.nrel.gov/grid/solar-resource/spectra.html.

(159) Changes in the electronic spectra of cobalt porphyrins when in the presence of pyridine and oxygen have been previously reported and ascribed to axial coordination of a pyridine unit and a superoxide ion.

(160) Given the value of Φ_{trans} is ~0 at 440 nm for all samples and LHE is not directly measured but is determined from reflectance and transmittance measurements, any differences in LHE at 440 nm correspond to changes in reflection properties following porphyrin modification. Nonetheless, the LHE data indicate any decrease in LHE at 440 nm following porphyrin modification is limited to <1%.

(161) Walker, F. A. Electron Spin Resonance Study of Coordination to the Fifth and Sixth Positions of α,β,γ,δ-Tetra(p-methoxyphenyl)porphinatocobalt (II). *J. Am. Chem. Soc.* 1970, *92*, 4235−4244.

(162) Walker, F. A. Steric and Electronic Effects in the Coordination of Amines to a Cobalt (II) Porphyrin. *J. Am. Chem. Soc.* 1973, *95*, 1150−1153.

(163) Walker, F. A. Reactions of Monomeric Cobalt-Oxygen Complexes. I. Thermodynamics of Reaction of Molecular Oxygen with Five-and Six-Coordinate Amine Complexes of a Cobalt Porphyrin. *J. Am. Chem. Soc.* 1973, *95*, 1154−1159.

(164) Barroso, M.; Cowan, A. J.; Pendlebury, S. R.; Grätzel, M.; Klug, D. R.; Durrant, J. R. The Role of Cobalt Phosphate in Enhancing the Photocatalytic Activity of α-Fe_2O_3 Toward Water Oxidation. *J. Am. Chem. Soc.* 2011, *133*, 14868−14871.

(165) Barroso, M.; Mesa, C. A.; Pendlebury, S. R.; Cowan, A. J.; Hisatomi, T.; Sivula, K.; Grätzel, M.; Klug, D. R; Durrant, J. R. Dynamics of Photogenerated Holes in Surface Modified α-Fe_2O_3 Photoanodes for Solar Water Splitting. *Proc. Nat. Acad. Sci.* 2012, *109*, 15640−15645.

(166) Li, W.; He, D.; Sheehan, S. W.; He, Y.; Thorne, J. E.; Yao, X.; Brudvig, G. W.; Wang, D. Comparison of Heterogenized Molecular and Heterogeneous Oxide Catalysts for Photoelectrochemical Water Oxidation. *Energy Environ. Sci.* 2016, *9*, 1794−1802.

(167) Thorne, J. E.; Jang, J. W.; Liu, E. Y.; Wang, D. Understanding the Origin of Photoelectrode Performance Enhancement by Probing Surface Kinetics. *Chem. Sci.* 2016, *7*, 3347−3354.

(168) Klahr, B.; Gimenez, S.; Fabregat-Santiago, F.; Bisquert, J.; Hamann, T. W. Electrochemical and Photoelectrochemical Investigation of Water Oxidation

with Hematite Electrodes. *Energy Environ. Sci.* 2012, *5*, 7626−7636.

APPENDIX A

ACKNOWLEDGEMENTS FOR PERMISSION TO REPRODUCE PORTIONS OF CHAPTER 1 FROM JOULE.

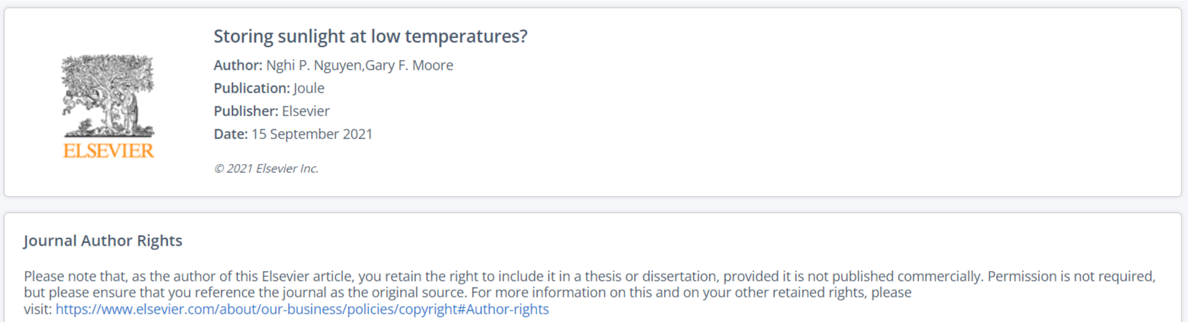

Storing sunlight at low temperatures?

Author: Nghi P. Nguyen,Gary F. Moore
Publication: Joule
Publisher: Elsevier
Date: 15 September 2021

© 2021 Elsevier Inc.

Journal Author Rights

Please note that, as the author of this Elsevier article, you retain the right to include it in a thesis or dissertation, provided it is not published commercially. Permission is not required, but please ensure that you reference the journal as the original source. For more information on this and on your other retained rights, please visit: https://www.elsevier.com/about/our-business/policies/copyright#Author-rights

Reprint with permission from Nguyen, N. P.; Moore, G. F. Storing Sunlight at Low Temperatures? *Joule* **2021**, *5*, 2254-2256 with permission from The Royal Society of Chemistry.

APPENDIX B

ACKNOWLEDGEMENTS FOR PERMISSION TO REPRODUCE PORTIONS OF CHAPTER 1 FROM ACS CHEMICAL REVIEWS.

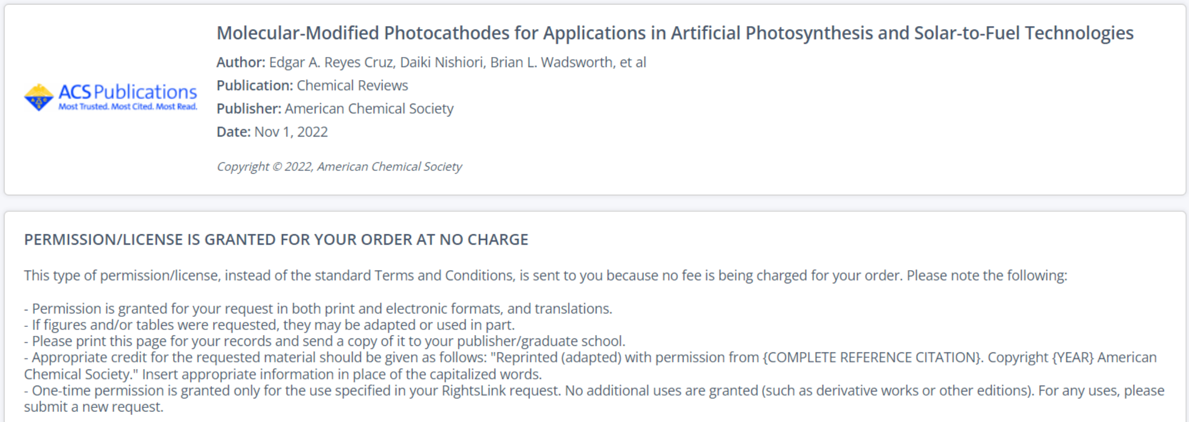

Molecular-Modified Photocathodes for Applications in Artificial Photosynthesis and Solar-to-Fuel Technologies

Author: Edgar A. Reyes Cruz, Daiki Nishiori, Brian L. Wadsworth, et al
Publication: Chemical Reviews
Publisher: American Chemical Society
Date: Nov 1, 2022

Copyright © 2022, American Chemical Society

PERMISSION/LICENSE IS GRANTED FOR YOUR ORDER AT NO CHARGE

This type of permission/license, instead of the standard Terms and Conditions, is sent to you because no fee is being charged for your order. Please note the following:

- Permission is granted for your request in both print and electronic formats, and translations.
- If figures and/or tables were requested, they may be adapted or used in part.
- Please print this page for your records and send a copy of it to your publisher/graduate school.
- Appropriate credit for the requested material should be given as follows: "Reprinted (adapted) with permission from {COMPLETE REFERENCE CITATION}. Copyright {YEAR} American Chemical Society." Insert appropriate information in place of the capitalized words.
- One-time permission is granted only for the use specified in your RightsLink request. No additional uses are granted (such as derivative works or other editions). For any uses, please submit a new request.

Reprint with permission from Reyes Cruz, E. A.; Nishiori, D.; Wadsworth, B. L.; Nguyen, N. P.; Hensleigh, L. K.; Khusnutdinova, D.; Beiler, A. M.; Moore, G. F. Molecular-Modified Photocathodes for Applications in Artificial Photosynthesis and Solar-to-Fuel Technologies. *Chem. Rev*. **2022**, *122*, 16051-16109 with permission from The American Chemical Society.

APPENDIX C

ACKNOWLEDGEMENTS FOR PERMISSION TO REPRODUCE PORTIONS OF CHAPTER 2 FROM ACS C JOURNAL OF PHYSICAL CHEMISTRY LETTERS.

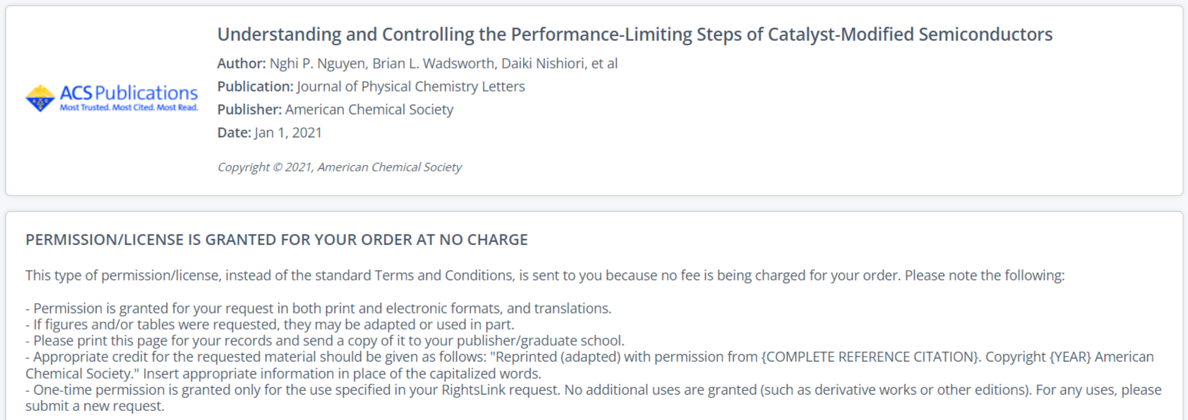

Understanding and Controlling the Performance-Limiting Steps of Catalyst-Modified Semiconductors

Author: Nghi P. Nguyen, Brian L. Wadsworth, Daiki Nishiori, et al
Publication: Journal of Physical Chemistry Letters
Publisher: American Chemical Society
Date: Jan 1, 2021

PERMISSION/LICENSE IS GRANTED FOR YOUR ORDER AT NO CHARGE

This type of permission/license, instead of the standard Terms and Conditions, is sent to you because no fee is being charged for your order. Please note the following:

- Permission is granted for your request in both print and electronic formats, and translations.
- If figures and/or tables were requested, they may be adapted or used in part.
- Please print this page for your records and send a copy of it to your publisher/graduate school.
- Appropriate credit for the requested material should be given as follows: "Reprinted (adapted) with permission from {COMPLETE REFERENCE CITATION}. Copyright {YEAR} American Chemical Society." Insert appropriate information in place of the capitalized words.
- One-time permission is granted only for the use specified in your RightsLink request. No additional uses are granted (such as derivative works or other editions). For any uses, please submit a new request.

Reprint with permission from Nguyen, N. P.; Wadsworth, B. L.; Nishiori, D.; Reyes Cruz, E. A.; Moore, G. F. Understanding and Controlling the Performance-Limiting Steps of Catalysts-Modified Semiconductors. *J. Phys. Chem. Lett*. **2021**, *12*, 199-203.

APPENDIX D

ACKNOWLEDGEMENTS FOR PERMISSION TO REPRODUCE PORTIONS OF CHAPTER 3 FROM ACS APPLIED ENERGY MATERIALS.

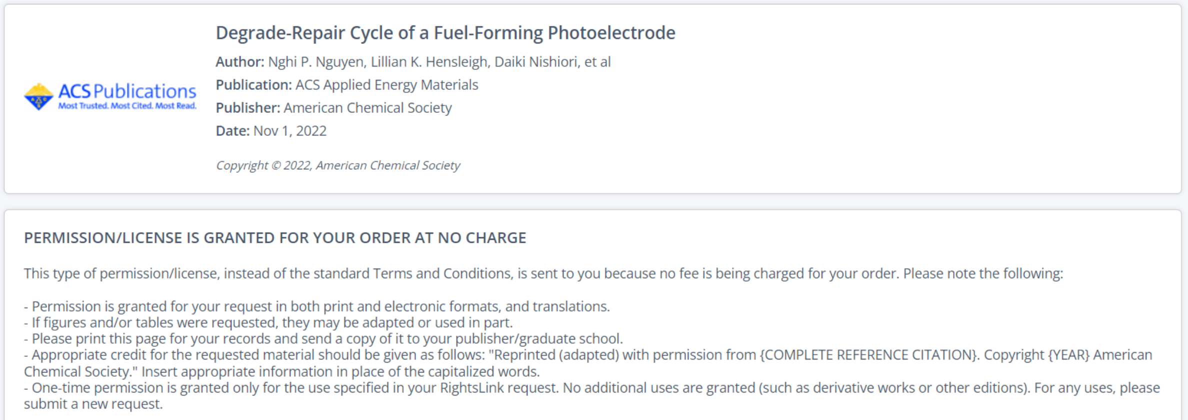

Degrade-Repair Cycle of a Fuel-Forming Photoelectrode

Author: Nghi P. Nguyen, Lillian K. Hensleigh, Daiki Nishiori, et al

Publication: ACS Applied Energy Materials

Publisher: American Chemical Society

Date: Nov 1, 2022

PERMISSION/LICENSE IS GRANTED FOR YOUR ORDER AT NO CHARGE

This type of permission/license, instead of the standard Terms and Conditions, is sent to you because no fee is being charged for your order. Please note the following:

- Permission is granted for your request in both print and electronic formats, and translations.
- If figures and/or tables were requested, they may be adapted or used in part.
- Please print this page for your records and send a copy of it to your publisher/graduate school.
- Appropriate credit for the requested material should be given as follows: "Reprinted (adapted) with permission from {COMPLETE REFERENCE CITATION}. Copyright {YEAR} American Chemical Society." Insert appropriate information in place of the capitalized words.
- One-time permission is granted only for the use specified in your RightsLink request. No additional uses are granted (such as derivative works or other editions). For any uses, please submit a new request.

Reprint with permission from Nguyen, N. P.; Hensleigh, L. K.; Nishiori, D.; Reyes Cruz, E. A.; Moore, G. F. Degrade-Repair Cycle of a Fuel-Forming Photoelectrode. *ACS Appl. Energy Mater.*, **2022**, *5*, 13128–13133.

APPENDIX E

ACKNOWLEDGEMENTS FOR PERMISSION TO REPRODUCE PORTIONS OF CHAPTER 4 FROM ACS APPLIED ENERGY MATERIALS.

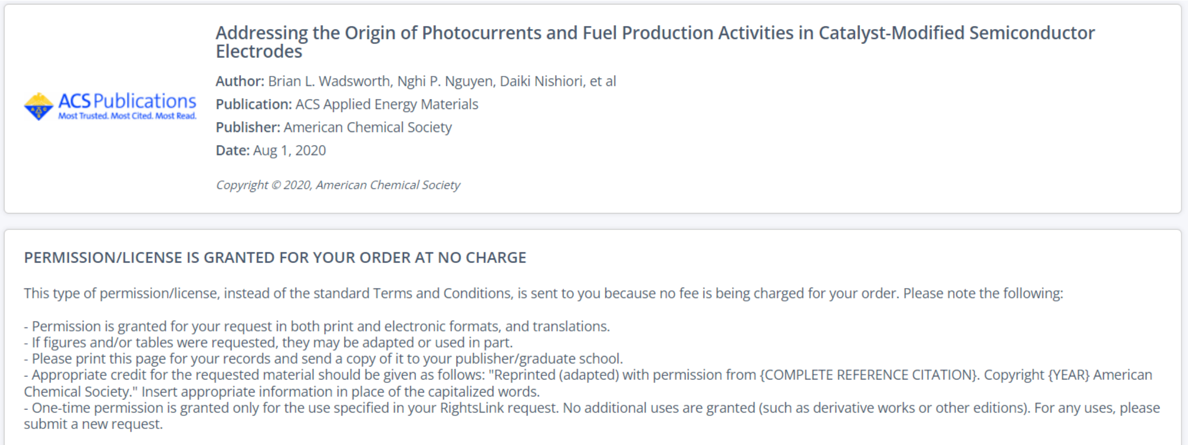

Addressing the Origin of Photocurrents and Fuel Production Activities in Catalyst-Modified Semiconductor Electrodes

Author: Brian L. Wadsworth, Nghi P. Nguyen, Daiki Nishiori, et al
Publication: ACS Applied Energy Materials
Publisher: American Chemical Society
Date: Aug 1, 2020

Copyright © 2020, American Chemical Society

PERMISSION/LICENSE IS GRANTED FOR YOUR ORDER AT NO CHARGE

This type of permission/license, instead of the standard Terms and Conditions, is sent to you because no fee is being charged for your order. Please note the following:

- Permission is granted for your request in both print and electronic formats, and translations.
- If figures and/or tables were requested, they may be adapted or used in part.
- Please print this page for your records and send a copy of it to your publisher/graduate school.
- Appropriate credit for the requested material should be given as follows: "Reprinted (adapted) with permission from {COMPLETE REFERENCE CITATION}. Copyright {YEAR} American Chemical Society." Insert appropriate information in place of the capitalized words.
- One-time permission is granted only for the use specified in your RightsLink request. No additional uses are granted (such as derivative works or other editions). For any uses, please submit a new request.

Reprint with permission from Wadsworth, B. L.; Nguyen, N. P.; Nishiori, D.; Beiler, A. M.; Moore, G. F. Addressing the Origin of Photocurrents and Fuel Production Activities in Catalyst-Modified Semiconductor Electrodes. *ACS Appl. Energy Mater*. **2020**, *8*, 7512-7519.